TAMPEREEN TEKNILLINEN YLIOPISTO
TAMPERE UNIVERSITY OF TECHNOLOGY

Mahmoud Abdelaziz

Reduced-complexity Digital Predistortion in Flexible Radio Spectrum Access

Julkaisu 1489 • Publication 1489

Tampere 2017

Tampereen teknillinen yliopisto. Julkaisu 1489
Tampere University of Technology. Publication 1489

Mahmoud Abdelaziz

Reduced-complexity Digital Predistortion in Flexible Radio Spectrum Access

Thesis for the degree of Doctor of Science in Technology to be presented with due permission for public examination and criticism in Sähkötalo Building, lecture room SJ204, at Tampere University of Technology, on the 12th of September 2017, at 12 noon.

Tampereen teknillinen yliopisto - Tampere University of Technology
Tampere 2017

Doctoral candidate: Mahmoud Abdelaziz
Faculty of Computing and Electrical Engineering
Tampere University of Technology
Tampere, Finland

Supervisor: Mikko Valkama, D.Sc. (Tech.), Professor
Faculty of Computing and Electrical Engineering
Tampere University of Technology
Tampere, Finland

Instructor: Lauri Anttila, D.Sc. (Tech.)
Faculty of Computing and Electrical Engineering
Tampere University of Technology
Tampere, Finland

Pre-examiners: Anding Zhu, Ph.D., Professor
School of Electrical and Electronic Engineering
University College Dublin (UCD)
Dublin, Ireland

Mohamed Helaoui, Ph.D., Associate Professor
Department of Electrical and Computer Engineering
University of Calgary
Alberta, Canada

Opponent: Magnus Isaksson, Ph.D., Professor
Department of Electronics, Mathematics, and Natural Sciences
University of Gävle
Gävle, Sweden

ISBN 978-952-15-3988-6 (printed)
ISBN 978-952-15-3998-5 (PDF)
ISSN 1459-2045

Abstract

Wireless communications is nowadays seen as one of the main foundations of technological advancements in, e.g., healthcare, education, agriculture, transportation, computing, personal communications, media, and entertainment. This requires major technological developments and advances at different levels of the wireless communication systems and networks. In particular, it is required to utilize the currently available frequency spectrum in a more and more efficient way, while also adopting new spectral bands. Moreover, it is required that cheaper and smaller electronic components are used to build future wireless communication systems to facilitate increasingly cost-effective solutions. Meanwhile, energy efficiency becomes extremely important in wide scale deployments of the networks both from a running cost point of view, and from an environmental impact point of view. This is the big picture, or the so called 'bird's eye view' of the challenges that are yet to be met in this very interesting and fast developing field of science.

The power amplifier (PA) is the most power-hungry component in most RF transmitters. Consequently, its energy efficiency significantly contributes to the overall energy efficiency of the transmitter, and in fact the whole wireless network. Unfortunately, energy efficiency enhancement implies operating the PA closer to its saturation region, which typically results in severe nonlinear distortion that can deteriorate the signal quality and cause interference to neighboring users, both of which negatively impact the system spectral efficiency. Moreover, in flexible spectrum access scenarios, which are essential for improving the spectral efficiency, particular in the form of non-contiguous radio spectrum access, the nonlinear distortion due to the PA becomes even more severe and can significantly impact the overall network performance. For example, in noncontiguous carrier aggregation (CA) in LTE-Advanced, it has been demonstrated that in addition to the classical in-band distortion and regrowth around the main carriers, harmful spurious emission components are generated which can easily violate the spurious emission limits even in the case of user equipment (UE) transmitters.

Technological advances in the digital electronics domain have enabled us to approach this problem from a digital signal processing point of view in the form of widely-adopted and researched digital predistortion (DPD) technology. However, when the signal

bandwidth gets larger, and flexible or non-contiguous spectrum access is introduced, the complexity of the DPD increases and the power consumed in the digital domain by the DPD itself becomes higher and higher, to the extent that it might be close to, or even surpass, the energy savings achieved from using a more efficient PA. The problem becomes even more challenging at the UE side which has relatively limited computational capabilities and lower transmit power. This dilemma can be resolved by developing novel reduced-complexity DPD solutions in such flexible spectrum access and/or wide bandwidth scenarios while not sacrificing the DPD performance, which is the main topic area that this thesis work contributes to.

The first contribution of this thesis is the development of a spur-injection based sub-band DPD structure for spurious emission mitigation in noncontiguous transmission scenarios. A novel and effective learning algorithm is also introduced, for the proposed sub-band DPD, based on the decorrelation principle. Mathematical models of the unwanted emissions are formulated based on realistic PA models with memory, followed by developing an efficient DPD structure for mitigating these emissions with reduced-complexity in both the DPD main processing and learning paths while providing excellent spurious emission suppression. In the special case when the spurious emissions overlap with the own RX band in frequency division duplexing (FDD) transceivers, a novel sub-band DPD solution is also developed that uses the main RX for DPD learning without requiring any additional observation RX, thus further reducing the DPD complexity.

The second contribution is the development of a novel reduced-complexity concurrent DPD, with a single-feedback receiver path, for carrier aggregation-like scenarios. The proposed solution is based on a simple and flexible DPD structure with decorrelation-based parameter learning. Practical simulations and RF measurements demonstrate that the proposed concurrent DPD provides excellent linearization performance, in terms of in-band error vector magnitude (EVM) and adjacent channel leakage ratio (ACLR), when compared to state-of-the-art concurrent DPD solutions, despite its reduced computational complexity in both the DPD main path processing and parameter learning.

The third contribution is the development of a new and novel frequency-optimized DPD solution which can tailor its linearization capabilities to any particular regions of the spectrum. Detailed mathematical expressions of the power spectrum at the PA output as a function of the DPD coefficients are formulated. A Newton-Raphson optimization routine is then utilized to optimize the suppression of unwanted emissions at arbitrary pre-specified frequencies at the PA output. From a complexity reduction perspective, this means that for a given linearization performance at a particular frequency range, an optimized and reduced-complexity DPD can be used.

Detailed quantitative complexity analysis, of all the proposed DPD solutions, is performed in this thesis. The complexity and linearization performance are also compared

to state-of-the-art DPD solutions in the literature to validate and demonstrate the complexity reduction aspect without sacrificing the linearization performance. Moreover, all the DPD solutions developed in this thesis are tested in practical RF environments using real cellular power amplifiers that are commercially used in the latest wireless communication systems, both at the base station side and at the mobile terminal side. These experiments, along with the strong theoretical foundation of the developed DPD solutions prove that they can be commercially used as such to enhance the performance, energy efficiency, and cost effectiveness of next generation wireless transmitters.

Preface

The research work reported in this thesis was carried out during the years 2013 – 2017 at the Department of Electronics and Communications Engineering, Faculty of Computing and Electrical Engineering, Tampere University of Technology, Tampere, Finland.

I would like to express my sincere gratitude to my supervisors Prof. Mikko Valkama and Dr. Lauri Anttila for their great support, guidance, and encouragement during my Doctoral studies. I also want to thank Prof. Markku Renfors for creating an inspiring working environment at the Department. I would also like to thank Prof. Joseph Cavallaro and his team for their wonderful hospitality and support during my research visit at Rice University, Houston, USA, in spring 2016.

I am grateful to my thesis pre-examiners Prof. Anding Zhu from University College Dublin, Ireland, and Prof. Mohamed Helaoui from University of Calgary, Canada, for their valuable comments that helped me to improve my thesis. I also wish to thank Prof. Magnus Isaksson from University of Gävle, Sweden, for agreeing to act as my opponent.

The thesis was financially supported by the Finnish Funding Agency for Technology and Innovation (Tekes), the Academy of Finland, the Linz Center of Mechatronics (LCM), TDK-EPCOS, Pulse Finland, Sasken Finland, Huawei Technologies Finland, and Nokia Bell Labs. I would like to thank all of them for their generous financial contribution.

I would also like to thank all my colleagues, administrative staff, and professors at

Tampere University of Technology for creating such a wonderful and pleasant working environment. I also want to thank all my friends in Tampere for being kind and supportive all the way long.

I want to thank all my family members, especially my dear parents, wife, children, and brother for their continuous support, prayers, care, and love.

Tampere, August 2017

Mahmoud Abdelaziz

Table of Contents

List of Publications

This thesis is a compound thesis based on the following seven publications.

[P1] M. Abdelaziz, Z. Fu, L. Anttila, A. M. Wyglinski, and M. Valkama, "Digital predistortion for mitigating spurious emissions in spectrally agile radios," *IEEE Communications Magazine*, vol. 54, no. 3, pp. 60-69, March 2016.

[P2] M. Abdelaziz, L. Anttila, C. Tarver, K. Li, J. Cavallaro, and M. Valkama, "Low-complexity Subband Digital Predistortion for Spurious Emission Suppression in Noncontiguous Spectrum Access," *IEEE Transactions on Microwave Theory and Techniques*, vol. 64, no. 11, pp. 3501-3517, Nov. 2016.

[P3] M. Abdelaziz, L. Anttila, A. Kiayani, and M. Valkama, "Decorrelation-based concurrent digital predistortion with a single feedback path," *IEEE Transactions on Microwave Theory and Techniques*, vol. PP, no. 99, pp. 1-14, June 2017.

[P4] Z. Fu, L. Anttila, M. Abdelaziz, M. Valkama, and A. M. Wyglinski, "Frequency-Selective Digital Predistortion for Unwanted Emission Reduction," *IEEE Transactions on Communications*, vol. 63, no. 1, pp. 254-267, Jan. 2015.

[P5] M. Abdelaziz, L. Anttila, A. Mohammadi, F. Ghannouchi, and M. Valkama, "Reduced-complexity power amplifier linearization for carrier aggregation mobile transceivers," in *Proc. IEEE International Conference on Acoustics, Speech and Signal Processing (ICASSP)*, Florence, 2014, pp. 3908-3912.

[P6] M. Abdelaziz, L. Anttila, J. R. Cavallaro, S. S. Bhattacharyya, A. Mohammadi, F. Ghannouchi, M. Juntti, and M. Valkama, "Low-complexity digital predistortion for reducing power amplifier spurious emissions in spectrally-agile flexible radio," in *Proc. International Conference on Cognitive Radio Oriented Wireless Networks and Communications (CROWNCOM)*, Oulu, 2014, pp. 323-328.

[P7] M. Abdelaziz, L. Anttila, and M. Valkama, "Digital predistortion for mitigating transmitter-induced receiver desensitization in carrier aggregation FDD transceivers," in *Proc. IEEE Global Conference on Signal and Information Processing (GlobalSIP)*, Washington, DC, 2016, pp. 694-698.

Abbreviations

3G	Third generation
3GPP	3^{rd} generation partnership project
4G	Fourth generation
5G	Fifth generation
AC	Adjacent channel
ACLR	Adjacent channel leakage ratio
ADC	Analog-to-digital converter
BOM	Bill of materials
BS	Base station
CA	Carrier aggregation
CAPEX	Capital expenditure
CC	Component carrier
CC1	First component carrier
CC2	Second component carrier
CMOS	Complementary metal oxide semiconductor
DAC	Digital-to-analog converter
DL	Downlink
DLA	Direct learning architecture
DPD	Digital predistortion
DSP	Digital signal processing
EVM	Error vector magnitude
FBMC	Filter bank multi-carrier
FCC	Federal communications commission
FDD	Frequency division duplexing

FFT	Fast Fourier transform
FIR	Finite impulse response
FLOP	Floating point operations
FLOP/s	Floating point operations per second
FPGA	Field programmable gate array
I/Q	In-phase/quadrature
IEEE	Institute of Electrical and Electronics Engineers
IF	Intermediate frequency
ILA	Indirect learning architecture
ILC	Iterative learning control
IM	Intermodulation
IM3	Third-order intermodulation
IM5	Fifth-order intermodulation
IM7	Seventh-order intermodulation
IMD	Intermodulation distortion
ITU	International telecommunications union
LAA	Licensed-assisted access
LASSO	Least absolute shrinkage and selection operator
LMS	Least mean square
LNA	Low noise amplifier
LO	Local oscillator
LPF	Lowpass filter
LS	Least squares
LTE	Long term evolution
LTE-A	Long term evolution advanced
MIMO	Multiple-input multiple-output
MMSE	Minimum mean square error
mmWave	Millimeter wave
MP	Memory polynomial
MPR	Maximum Power Reduction
MSPS	Mega samples per second
NLMS	Normalized LMS
NMSE	Normalized mean square error
OFDM	Orthogonal frequency division multiplexing
OOB	Out-of-band
OPEX	Operational expenditure
PA	Power amplifier
PAPR	Peak-to-average power ratio
PH	Parallel Hammerstein

PSD	Power spectral density
QAM	Quadrature amplitude modulation
QPSK	Quadrature phase shift keying
RF	Radio frequency
RX	Receiver
SC-FDMA	Single carrier frequency division multiple access
SINR	Signal-to-interference-and-noise ratio
SNL	Static non-linear
SNR	Signal-to-noise ratio
SRR	Spurious emission rejection ratio
SVD	Singular value decomposition
TX	Transmitter
UE	User equipment
UL	Uplink
VSA	Vector signal analyzer
VSG	Vector signal generator
VST	Vector signal transceiver

CHAPTER 1

Introduction

1.1 Thesis Motivation and Scope

The exponentially increasing demand for new applications, higher peak data rates, and new devices in wireless communication systems necessitates major technological breakthroughs that allow for a more efficient utilization of the available radio spectrum and energy resources. Consequently, spectral efficiency and energy efficiency enhancements are two of the most important objectives in the ongoing development in wireless communications, in particular 5G, [16, 38, 51, 63, 66, 138]. Moreover, from an economical perspective, spectral efficiency enhancement leads to better usage of the available spectrum, and thus more potential revenue. On the other hand, enhancing the energy efficiency can significantly reduce the operational expenditure (OPEX) of the wireless network as well as the carbon footprint, and thus benefit our environment. Additionally, reducing the capital expenditure (CAPEX) by using fewer, smaller, and cheaper components, e.g., in the RF transmitter, is also very important and economically relevant for both telecommunications operators and semiconductor manufacturers. The wider objective of this thesis is to develop novel solutions that can contribute to achieving a good compromise among the above requirements, in particular from the RF transmitter perspective, whether on the base station (BS) side, or on the user equipment (UE) side.

Flexible spectrum access through carrier aggregation (CA) in the transmitter is an effective means for improving peak data rates and spectral efficiency in wireless communication systems [26, 42, 103, 115]. This is achieved by combining multiple component carriers (CCs) from different frequencies/bands in order to increase the utilized bandwidth, which is practically not available as a contiguous portion of spectrum [129].

On the other hand, in order to enhance the energy efficiency of such flexible transmitters, the component carriers should be combined before the power amplifier (PA), whenever it is technologically feasible, to avoid the combiner loss after the PA [23]. This also has the advantage of reducing the bill of materials (BOM) by using a single dual-band PA instead of two PAs while aggregating two CCs, for example. However, this leads to three kinds of unwanted emissions. The first are emitted in-band, right on top of each CC, thus degrading the in-band error vector magnitude (EVM). The second kind of emissions are out-of-band (OOB) emissions which are emitted in the adjacent channels, thus degrading the adjacent channel leakage ratio (ACLR). The third kind of unwanted emissions are those emitted in the spurious domain, beyond the adjacent channel region. Moreover, multicarrier transmissions, with high spectral efficiency, exhibit very large peak-to-average power ratios (PAPRs) which can further increase the level of these unwanted spectral emissions.

The levels of these unwanted emissions are mandated and enforced by international and national regulators, such as the US Federal Communications Commission (FCC; see, e.g., [2]). On the base station (BS) transmitter side, mitigating these unwanted emissions in flexible spectrum access scenarios has received a lot of attention in both academia and industry, especially in the past decade [24, 34, 86, 106, 110]. Most of these works focus on the EVM and ACLR aspects, while some fewer works also focus on mitigating the spurious emissions. Recently, it has also been demonstrated in the context of LTE-Advanced UE with non-contiguous intraband CA or multicluster type transmissions, that spurious emissions due to the PA nonlinearity can violate the given spectrum emission limits [8, 99, 100, 103], or lead to own receiver desensitization in frequency-division duplexing (FDD) systems [47, 72, 103, 125]. This implies the need for solutions for these problems at the UE side as well, which is limited in terms of its computational capacity when compared to the BS, and thus makes the problem more challenging.

One straight forward solution to decrease the levels of unwanted emissions is to back off the transmit power from the PA saturation region. However, this is not an attractive solution since it requires using larger PAs operating in the linear region. As a result, the cost and size of the transmitter PA will increase, i.e., CAPEX will increase, and the energy efficiency will decrease, which directly translates to an increased running cost in terms of power supply and cooling, i.e., higher OPEX. This is known in the literature as the linearity efficiency tradeoff of power amplifiers [81]. A better solution is to use a smaller and more efficient PA in combination with a low complexity linearization method to mitigate the PA nonlinear distortion.

Digital predistortion (DPD) is considered one of the most widely used and effective linearization techniques, in terms of performance and flexibility [58, 76]. However,

developing low complexity DPD solutions in such flexible spectrum access scenarios is not an easy task. This is mainly because of the wide aggregated bandwidth of CA signals, which naturally increases the cost and complexity of classical DPD solutions, thus possibly becoming not suitable for smaller devices such as mobile terminals and small cell base stations.

In summary, we want to achieve higher spectral efficiency through flexible spectrum access, while achieving higher energy efficiency and lower CAPEX and OPEX through using inexpensive nonlinear PAs in the transmitter. This challenging combination causes severe unwanted emissions that can degrade the transmit signal quality, violate emission limits, and potentially desensitize the own receiver in FDD systems. Classical DPD solutions require high complexity to mitigate these unwanted emissions. Thus, the challenge lies in developing novel DPD solutions with reduced-complexity for such flexible spectrum access scenarios, which is the main scope of this thesis.

1.2 Thesis Objectives

The ultimate objective of this thesis is to facilitate the implementation of more energy efficient transmitters, with lower cost and size, particularly for modern multi-band and spectrally-agile flexible radio networks. This requires the usage of small, energy efficient, and therefore highly nonlinear power amplifiers in the transmitters. Towards this end, the goal is to develop novel reduced-complexity DPD techniques, structures, and algorithms in flexible spectrum access scenarios in order to mitigate the PA nonlinear distortion in such challenging scenarios. The DPD complexity reduction is achieved on different fronts, starting from reduced-complexity DPD main path processing structures, to reduced-complexity in the feedback observation receiver hardware, and ending with novel digital signal processing (DSP) and optimization techniques to reduce the DPD parameter estimation and real-time running complexity. Finally, the performance of the developed DPD algorithms is tested, verified, and compared to state-of-the-art DPD methods using realistic simulations as well as comprehensive RF measurements.

1.3 Thesis Contributions and Structure

The main contributions of this thesis are: developing a novel spur-injection based sub-band DPD solution for spurious emission mitigation incorporating decorrelation type of closed-loop parameter learning [P1], [P2], [P5], and [P6] (reviewed in Chapter 4 of this thesis); developing a novel sub-band DPD algorithm for protecting the own receiver from transmitter induced emissions without requiring an extra observation receiver [P7] (reviewed in Chapter 4); developing a novel concurrent DPD algorithm for

linearizing the main carrier(s) in carrier aggregation scenarios incorporating a simple and novel decorrelation-based learning concept [P3] (reviewed in Chapter 5); developing a novel frequency-optimized DPD algorithm that can tune its linearization to a particular frequency or band of interest [P4] (reviewed in Chapter 6). These DPD solutions have the capability to significantly reduce the complexity of the DPD while providing excellent linearization performance, in terms of EVM, ACLR, and spurious emission suppression, when compared to other state-of-the-art DPD methods. Three main strategies have been used to accomplish this objective. The first is based on developing reduced-complexity DPD structures that aim at partitioning the wide band spectrum into a set of so called *sub-bands*. Each sub-band uses a smaller, cheaper, and significantly more energy efficient DPD unit operating at a much lower sample rate. The second strategy is built on developing simple yet effective adaptive DPD learning solutions that do not require computationally demanding operations and can thus significantly cut the cost of the DPD in terms of the amount of digital processing required. The third strategy is based on optimizing the DPD parameter estimation such that the most critical emissions are given highest priority. From a complexity reduction perspective, this means that for a given linearization performance at a particular frequency range, an optimized and reduced-complexity DPD can be used.

The DPD solutions developed in this thesis are all adaptive, and therefore can adapt to changes in the transmitter operating conditions. These solutions are also waveform independent and can thus be applied to any of the current 3G and 4G mobile communication standards, or future networks, primarily 5G mobile communication systems. They can, in principle, also be applied to any wireless transmitter, e.g., fronthaul/backhaul, satellites, etc. Additionally, the proposed DPD algorithms can be applied on the transmitter side of the mobile terminal, or the base station. They can also be extended and applied to multiple input multiple output (MIMO) transmitter architectures whether in the sub-6 GHz range or in the millimeter wave range.

Several supplementary articles related to the thesis scope have also been published by the author together with his supervisors and colleagues. A conference paper [116] introduced some further developments to the sub-band DPD in [P2] that can both enhance its performance and further reduce its complexity. Another conference paper [12] applied the filtered basis functions concept to the decorrelation-based closed loop DPD for the main carrier, and also extended the DPD learning and processing to mitigate the I/Q modulator impairments in addition to the PA nonlinearity. Four additional conference papers, related to hardware implementation of the developed reduced-complexity DPD solutions on different platforms, have also been published [13, 14, 54, 83]. Three further conference papers and one book chapter are related to DPD for spectrally-contained 5G waveforms, e.g., FBMC, filtered-OFDM, etc., [10, 11, 33, 43].

The thesis is organized as follows: Chapter 2 describes and reviews the transmitter linearity challenges in flexible spectrum access. Chapter 3 introduces the digital predistortion fundamentals including nonlinear models, DPD main path processing architectures, and DPD learning architectures. A summary of reduced-complexity DPD state-of-the-art is also presented in Chapter 3. The main contributions of the thesis are presented in Chapters 4, 5, and 6. Chapter 4 summarizes the sub-band DPD for spurious emission mitigation in [P1], [P2], [P5] - [P7]. Chapter 5 then summarizes the concurrent DPD in [P3]. Chapter 6 summarizes the frequency-optimized DPD in [P4]. Finally, Chapter 7 presents the conclusions of the thesis and prospective future work.

1.4 Author's Contribution to the Publications

The research topic of developing reduced-complexity digital predistortion solutions for spurious emission mitigation in carrier aggregation transmitters was proposed by Prof. Mikko Valkama. The impact of such spurious emissions, and the associated linearity requirements in LTE-A mobile transmitters, were quantified in the M.Sc. thesis of M.Sc. Toni Lähteensuo [78], under Prof. Mikko Valkama's supervision. The study in [78] set the motivation for the development of the sub-band DPD for spurious emission mitigation in [P1], [P2], [P5], [P6], as solutions to relax the linearity requirements in LTE-A CA transmitters with reduced-complexity processing. The DPD algorithms in [P1], [P2], [P5], [P6] were all developed by the author. The modeling, derivations, complexity analysis, simulations, and RF measurements in these publications were all done by the author. The writing of the publications was mostly done by the author, however, Dr. Lauri Anttila and Prof. Mikko Valkama both significantly contributed to the final appearance and structure of these publications, especially the earlier ones.

The idea of developing a sub-band DPD solution specifically for mitigating transmitter induced receiver desensitization in CA FDD transceivers was proposed by Prof. Mikko Valkama, and lead to the development of the work in [P7]. The actual algorithm development, modeling, analysis, and simulations in [P7] were all done by the author. The writing of [P7] was done mainly by the author, while Prof. Mikko Valkama and Dr. Lauri Anttila both contributed to the final appearance of the publication.

The idea of developing a reduced-complexity concurrent DPD for the main carriers in CA transmitters was initially proposed by the author and lead to the development of the work in [P3]. The modeling, derivations, complexity analysis, simulations, and RF measurements in [P3] were all done by the author. The writing of [P3] was done mainly by the author, while Prof. Mikko Valkama and Dr. Lauri Anttila both contributed to the final appearance and structure of the publication.

The idea of developing the frequency-optimized DPD in [P4] was initially proposed by Dr. Lauri Anttila. The initial version of the modeling, analysis and derivations were done by Dr. Zhu Fu as a part of a research collaboration project with Worcester Polytechnic Institute (WPI), USA. The modeling, analysis, and derivations were then extensively revised jointly by the author and Dr. Lauri Anttila, which then lead to the final algorithm development of [P4]. The simulations, RF measurements, and complexity analysis in [P4] were all done by the author. The writing of [P4] was a joint effort between the author, Prof. Mikko Valkama, Dr. Lauri Anttila, Dr. Zhu Fu, and Prof. Alex Wyglinski.

CHAPTER 2

Transmitter Linearity Challenges in Flexible Spectrum Access

Wireless communications is facilitating new applications in almost every aspect of our lives, from healthcare, to education, entertainment, transportation, etc. These applications require wider spectral bandwidths, up to hundreds of MHz in both the downlink (DL) and the uplink (UL). Such wide bandwidths are practically unavailable as a contiguous portion of the spectrum, particularly in the sub-6 GHz range of frequencies. Many wireless communication standards have evolved in a way that satisfies such new requirements by adding features that support flexible spectrum access. An example of such standard developments is the carrier aggregation (CA) feature in 3GPP LTE-Advanced (LTE-A), also known as LTE-Advanced Pro since its recent Release 13 [6, 8, 64, 82, 84]. Other examples include the noncontiguous transmission feature in the IEEE 802.11ac WiFi standard [3], and the channel bonding feature in the IEEE 802.22 standard [4], also known as the cognitive radio standard. This flexibility in spectrum access comes at the expense of increased linearity challenges in the transmitter, particularly due to the transmitter power amplifier (PA).

In this Chapter, we mostly focus on the challenges in LTE-A CA, as a practical example for flexible spectrum access. We start the Chapter by shortly reviewing the evolution of CA in LTE-A in Section 2.1, followed by a discussion regarding possible CA transmitter architectures in Section 2.2. The challenges associated with noncontiguous CA transmission with respect to the PA nonlinearity are then introduced in Section 2.3. Section 2.4 then mentions the different methods for PA linearization. Finally,

reduced-complexity DPD concepts are shortly discussed in Section 2.5 as an efficient solution for the problem at hand.

2.1 Carrier Aggregation in 3GPP Cellular Network Evolution

3GPP began introducing carrier aggregation from Release 10 onwards, which is also the first release where the technology is called LTE-Advanced. In general, CA allows for combining several component carriers (CCs) in a contiguous or noncontiguous manner whether in the DL, or in the UL. Each CC may possess a bandwidth of any single-carrier bandwidth defined within the LTE specifications [6,8]. These CCs can be within the same RF band, i.e., intraband CA, or in different RF bands, i.e., interband CA. Currently, the RF specifications allow the aggregation of two CCs in intraband CA, and up to four CCs in interband CA [5, 6, 8, 9].

On the DL side, Release 10 introduced intraband contiguous CA and interband noncontiguous CA, followed by Release 11 which introduced intraband noncontiguous CA. A new set of frequency bands and band combinations were then added in Release 12, along with the possibility of aggregating FDD and TDD carriers. Release 13, which is also the first release where the technology is called LTE-Advanced Pro, introduced a new feature to further boost the DL network capacity namely licensed-assisted access (LAA) [97]. In LAA, CA can occur between licensed and unlicensed bands where the carrier in the licensed band coordinates the link, thus providing a reliable connection between the terminal and the base station, while more bandwidth can be opportunistically obtained from an unlicensed band [5, 6].

On the UL side, Release 10 introduced contiguous CA. Release 11 then introduced so-called multicluster transmission, which means that non-contiguous resource allocation can be performed within a single UL carrier. Release 12 yielded two additional major updates, as non-contiguous intraband CA and interband CA were introduced, where the LTE-A UE can be allocated UL resources across aggregated spectrum consisting of two or more component carriers [8, 9].

2.2 Carrier Aggregation Transmitter Architectures

The complexity and challenges of the CA transmitter architecture depend on where the CCs are combined in the transmitter. Considering the dual-carrier scenario, as a practical example, there are three possible options to combine the first CC, namely CC1, and the second CC, namely CC2, as shown in Fig. 2.1.

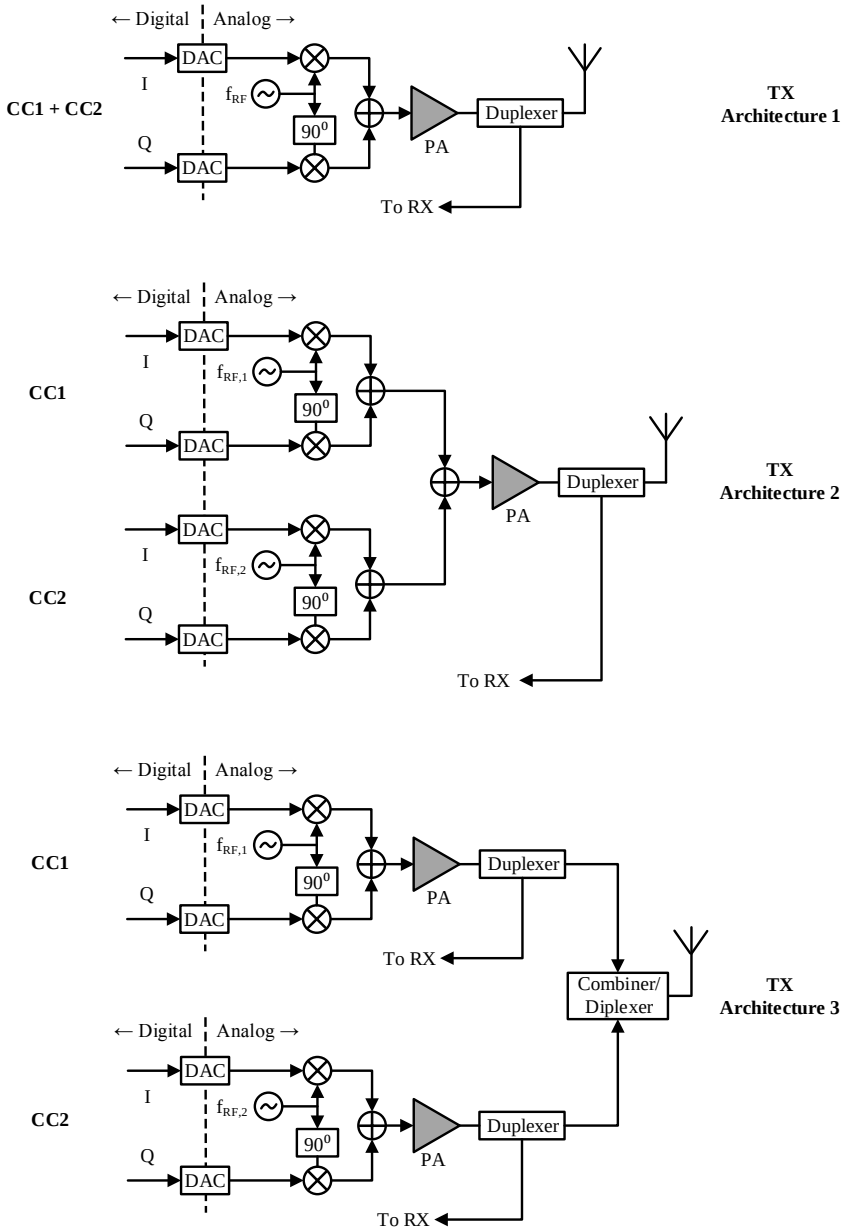

Figure 2.1: Three possible TX architectures for CA in LTE-A in the dual-carrier case. The I/Q upconversion based architecture is assumed per TX chain.

- Combining CC1 and CC2 already at digital front-end. This is suitable for intraband contiguous CA. In principle, it is possible also in intraband noncontiguous CA, but will require higher sample rates.

- Combining CC1 and CC2 at RF, before the transmitter PA. This is suitable for non-contiguous intraband CA. It can also be used in interband CA when the bands are not very far from each other, and hence using a single dual-band PA is feasible.
- Combining CC1 and CC2 at RF, after the per-CC PA stages. This is suitable for non-contiguous intraband or interband CA.

In the case of aggregating more than two CCs, a combination of these options can be used, depending on the frequency spacing between the aggregated bands, and also the computing and cost constraints of the considered TX.

Due to the excessively high complexity of TX architecture 1 in noncontiguous CA scenarios, it will most likely not be feasible, especially for computing-limited devices such as mobile terminals and small cell basestations. TX architecture 2 then has two advantages over TX architecture 3 in noncontiguous CA scenarios, whenever feasible. The first is that power efficiency of the overall transmitter is typically better with a single multi-band PA when compared to the multiple PA-based architecture, due to the combining loss at the PA output in TX architecture 3 [23]. The second advantage is that the bill of materials (BOM) in TX architecture 2 is lower than in TX architecture 3 due to fewer number of RF components. However, the nonlinearity of the multi-band PA in architecture 2 may result in severe intermodulation distortion (IMD) at the PA output with drastic effects, as will be shown in more details in the next section.

2.3 PA Nonlinear Distortion Quantification and Challenges in CA Transmitters

When a noncontiguous CA signal is applied at the input of a single nonlinear PA, three kinds of unwanted emissions result that affect three different regions of the spectrum. The first is emitted in-band, right on top of each CC, thus degrading the transmit signal quality, or in other words degrading the in-band error vector magnitude (EVM). The second kind of emissions are out-of-band (OOB) emissions which are emitted in the adjacent channels, thus possibly causing interference to neighboring users, or in other words degrading the adjacent channel leakage ratio (ACLR). The third kind of unwanted emissions are those emitted in the spurious domain, beyond the adjacent channel region, as demonstrated in Fig. 2.2. These spurious emissions can violate emission limits and/or desensitize the own RX in FDD transceivers. More details regarding the quantification of the PA nonlinear distortion in these three regions will be provided next.

Here and in the continuation, we refer to the frequency location of the different distortion terms as *sub-bands*. For example, in the dual carrier scenario shown in Fig. 2.2, 8 sub-bands are present. The first two sub-bands at $\pm \triangle f/2$ from the carrier frequency

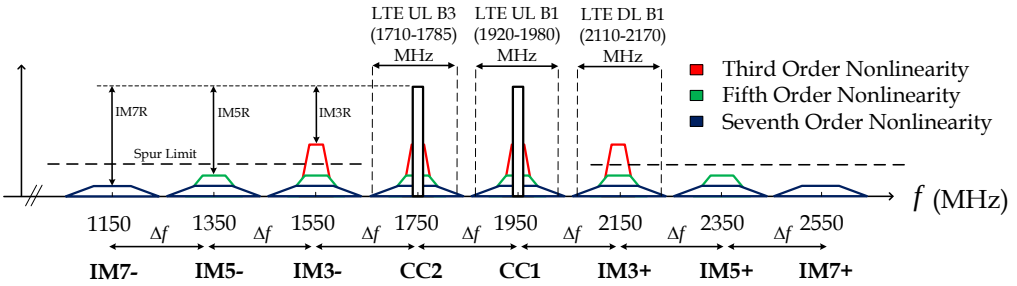

Figure 2.2: Illustration of the distortion components created by a nonlinear PA when excited with a non-contiguous CA signal with two component carriers. In this LTE-A interband CA UL example, the CCs are at bands 1 and 3 respectively. The spur at IM3+ sub-band overlaps with the own RX band of CC1.

contain the main carriers, where $\triangle f$ is defined as the frequency separation between the aggregated carriers. The sub-bands at $\triangle f$ from the center of the appropriate component carrier are denoted by the IM3$\pm$ sub-bands. Similarly, sub-bands at $2\triangle f$ from the center of the appropriate component carrier are denoted by the IM5$\pm$ sub-bands, and so on, as also illustrated in Fig. 2.2.

2.3.1 In-band Distortion Quantification

The in-band transmit waveform purity is typically measured through the EVM metric, which is defined as

$$EVM_{\%} = \sqrt{\frac{P_{error}}{P_{ref}}} \times 100\%, \tag{2.1}$$

where P_{error} is the power of the error signal, defined as the difference between the ideal symbol values and the corresponding symbol rate complex samples at the PA output, both normalized to the same average power, while P_{ref} is the reference power of the ideal symbol constellation. Typically in EVM evaluations, linear distortion of the transmit chain is equalized prior to calculating the error signal [42]. In the dual-carrier example shown in Fig. 2.2, EVM is calculated separately for the two CCs.

2.3.2 Out-of-band Distortion Quantification

The OOB emissions are usually quantified as the unwanted emissions at the immediate adjacent channels, and are measured with the ACLR metric. The ACLR is defined as the ratio of the transmitted powers within the wanted channel (P_{wanted}) and the

adjacent channel ($P_{adjacent}$), respectively [7], namely

$$ACLR_{dB} = 10\log_{10}\frac{P_{wanted}}{P_{adjacent}}, \tag{2.2}$$

and it can be calculated separately for left and right adjacent channels. Notice also that in general, depending on the system specifications, the evaluation or measurement bandwidth of the adjacent channel power can be different than that of the wanted signal power [6, 8]. In the dual-carrier example shown in Fig. 2.2, ACLR is calculated separately for the two CCs.

2.3.3 Spurious Emissions Quantification and Challenges

Following the ITU-R recommendations [2] for frequencies between 1 - 12.75 GHz, we quantify the spurious emissions as the integrated power over a 1 MHz measurement bandwidth/window, at frequencies beyond the OOB range. While this gives an absolute power measure for the spurious emissions within the measurement bandwidth, we also define the relative spurious emission rejection as the ratio of the in-band wanted channel power and the spurious emission power (over the 1 MHz measurement bandwidth) at the considered frequency/sub-band. For example, at the IM3, IM5, and IM7 sub-bands, these spurious emission rejection ratios read

$$IM3R_{dB} = 10\log_{10}\frac{P_{wanted,CC}}{P_{IM3}}, \tag{2.3}$$

$$IM5R_{dB} = 10\log_{10}\frac{P_{wanted,CC}}{P_{IM5}}, \tag{2.4}$$

$$IM7R_{dB} = 10\log_{10}\frac{P_{wanted,CC}}{P_{IM7}}. \tag{2.5}$$

These emissions can seriously violate the given spurious emission limits [8, 99, 100, 103]. Furthermore, in FDD devices, the generated spurious components can also overlap with the device's own receive band, causing receiver desensitization [47, 71, 72, 103, 125], as will be explained in more details in the following.

Spurious Emission Limit Violation

The levels of different unwanted emissions are, in general, regulated by the standardization bodies and ITU-R [2]. It has been recently demonstrated that in the context of LTE-Advanced with noncontiguous CA or multicluster type transmission, the PA nonlinearities lead to spurious emissions that can seriously violate the given spectrum and spurious emission limits if not properly controlled [8, 78, 99, 100, 103]. The most significant emissions are those emitted at the IM3± sub-bands, but in general, the

emissions at the other IM sub-bands can be harmful as well. One obvious solution to decrease the levels of unwanted emissions is to back off the transmit power from its saturation region. In 3GPP UE terminology, this is known as Maximum Power Reduction (MPR), and MPR values up to 18 dB are allowed in some use cases for mobile terminals [8]. Several numerical examples demonstrating that high MPR values are required in certain CA scenarios are shown in [13, 73, 78], [P1], and [P2]. This comes at the expense of lower UL coverage, and energy efficiency, as well as more expensive and less compact RF transmitters with larger PAs.

TX Induced Leakage at own RX

In FDD devices, in addition to violating the general spurious emission limits, the generated spurious components can also overlap with the device's own receive band, causing own receiver desensitization [47, 72, 103, 125]. Considering an LTE-A inter-band CA UL example, shown in Fig. 2.2, in which the two CCs are at bands 1 and 3 respectively, and are applied into a single dual band PA, the spur at the IM3+ sub-band falls on the own RX band of CC1, and therefore potentially desensitizing its own receiver. Two straight forward solutions to this problem are: increasing the duplexer isolation, and reducing the TX power. However, increasing the duplexer isolation, significantly increases the cost, complexity, and size of the duplexer filters, which becomes impractical, especially for mobile devices. Reducing the TX power, on the other hand, will end up yielding a significantly lower PA efficiency, as well as a substantial reduction in the network coverage.

Thus, there is a clear need for other solutions to these problems that do not have such drawbacks. That is why one of the main objectives of this thesis is to develop reduced-complexity PA linearization solutions that can mitigate particular spurious IMD components, as well as in-band and out-of-band distortion components resulting from the PA nonlinearity.

2.4 PA Linearization Techniques

PA linearization techniques include feedback linearization, feedforward linearization, RF predistortion, and baseband digital predistortion (DPD) [67, 70]. Analog feedback linearization techniques rely on a closed-loop feedback from the PA output to its input in order to reduce the emissions, and are limited in terms of bandwidth [67]. Feedforward linearization is an inherently wideband technique, but requires considerable additional RF hardware. The accuracy, flexibility, as well as practical bandwidth of feedforward linearization are all limited by the analog components [67]. RF predistortion is a wideband linearization technique, but its fidelity is rather limited due to the analog

implementation. Digital predistortion, on the other hand, is probably the most effective and cost efficient among all linearization techniques. It has the greatest flexibility, reconfigurability, and also performance in most cases. Its bandwidth is mostly limited by the digital hardware, and will therefore benefit from the scaling of CMOS technology.

For the above reasons, DPD is the PA linearization method of choice in this thesis where the focus is to develop reduced-complexity DPD methods that can be used for wideband and CA scenarios in 4G and 5G wireless communication systems. Particularly, the DPD solutions where complexity reduction is sought are likely to be important in 5G systems where the envisioned carrier bandwidths can be even in the order of 1-2 GHz, especially at mmWave bands.

2.5 Reduced-complexity DPD Concepts

There have been substantial research efforts in the past 20 years in developing ever more efficient and elaborate DPD techniques, mostly for high-end macro base-station type of devices. The conventional DPD approaches seek to linearize the full composite transmit signal, and we thus refer to such solutions as full-band DPD. However, the reason why such classical DPD techniques might be considered highly complex for wideband and CA scenarios is primarily due to the large additional complexity in terms of the required baseband processing and sample rates in the transmitter main path, as well as the feedback receiver used for DPD parameter estimation. Three main philosophies are thus used in this thesis in order to reduce the complexity of the DPD.

1. Dividing the overall wide transmit band into sub-bands, and using a lower complexity DPD structure for each sub-band, as explained in more details in Chapters 4 and 5. In Chapter 4, this idea is used to mitigate spurious emissions. While in Chapter 5, the main focus is on mitigating in-band and out-of-band emissions.

2. Tuning the DPD to particular frequencies/bands where linearization is more necessary, using optimization techniques. Thus, for a given linearization performance at such frequencies/bands, a reduced-complexity DPD, in terms of the DPD main processing path, can be used. These aspects are explained in more details in Chapter 6.

3. Developing novel DSP algorithms for DPD parameter estimation with reduced complexity in the DPD main path processing and in the feedback path. These aspects are explained in more details in Chapters 4, 5, and 6.

CHAPTER 3

Digital Predistortion Fundamentals and State-of-the-art

In general, any DPD system can be divided into two main paths as illustrated also in Fig. 3.1: the DPD main processing path and the DPD learning path which updates the DPD coefficients in the main path. Since the PA is nonlinear by nature, therefore the behavioral models which describe either the PA or the DPD are also nonlinear models. Section 3.1 summarizes some of the most common nonlinear models used in the literature for PA modeling and/or DPD processing. Section 3.2 then introduces the DPD main path processing approaches, followed by Section 3.3 which introduces the four basic DPD learning architectures available in the literature as per the author's knowledge to date. Finally, Section 3.4 presents a summary of state-of-the-art reduced-complexity DPD techniques available in the literature.

3.1 Nonlinear Models

PA nonlinear models can be divided into physical models and behavioral models [53, 65, 104]. Physical models use the equivalent circuit of the PA which relates the voltages and currents at the PA input and output using nonlinear equations. On the other hand, behavioral models consider the PA as a black box whose input-output relation is specified by a certain mathematical function that models its behavior, and are generally less accurate than physical models. However, in this thesis behavioral models are considered for two reasons: the first is that they are simpler to use, and the second is because the

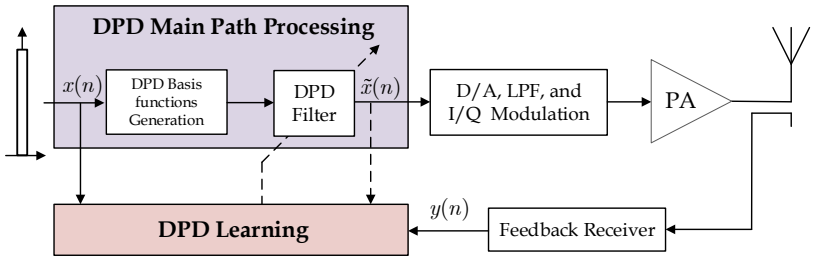

Figure 3.1: Generic DPD block diagram illustrating the DPD main path processing and the DPD learning path.

main focus is on DPD more than PA modeling, and in fact DPD is digital by nature and its nonlinear models are usually obtained by inverting the baseband equivalent PA model, as will be shown in Sections 3.2 and 3.3. Thus, behavioral models are considered a good fit for DPD.

Polynomial based models and artificial neural networks (ANN) are two of the most widely used behavioral models for nonlinear system identification [104]. However, ANN are nonlinear in their parameters and thus require more sophisticated nonlinear parameter extraction algorithms when compared to polynomial based models that can be described in a linear-in-parameters format. That is why polynomial based models are more widely used in PA modeling and DPD since they are both easy to use and at the same time have good approximation capabilities for various nonlinear functions [53, 79], and thus we will limit our discussion to such models. We start with the memoryless polynomial models, and then move to the more general and also widely used polynomial-based models with memory.

3.1.1 Memoryless Polynomial Models

Assuming a memoryless P^{th}-order polynomial model, the RF PA output signal reads

$$y_{RF}(t) = \sum_{p=1}^{P} \bar{f}_p \, x_{RF}^{p}(t), \tag{3.1}$$

where $x_{RF}(t)$ and $y_{RF}(t)$ are the RF bandpass PA input and output signals, respectively, and $\bar{f}_p$ is the RF PA p^{th}-order polynomial coefficient. The discrete time baseband equivalent PA output then reads [133]

$$y(n) = \sum_{\substack{p=1 \\ p \text{ odd}}}^{P} f_p \, |x(n)|^{p-1} x(n), \tag{3.2}$$

where $x(n)$ and $y(n)$ are the discrete time baseband equivalent (lowpass) PA input and output signals, respectively, and f_p is the p^{th}-order polynomial coefficient. Only the odd order intermodulation terms are included in the baseband equivalent model in (3.2). The harmonics and even order intermodulations are generally far away from the carrier frequency and can thus be easily filtered out by the TX RF filter(s), unless the signal bandwidth is very large with respect to the carrier frequency, which is usually not the case in most commercial wireless communication systems.

3.1.2 Polynomial-based Models with Memory

The Volterra model is the most general polynomial-based model with memory [91]. Assuming a Volterra model with P^{th}-order nonlinearity and memory order N, the discrete time baseband equivalent PA input output relation reads [117]

$$y(n) = \sum_{\substack{p=1 \\ p \text{ odd}}}^{P} \sum_{m_1=0}^{N} \sum_{m_2=m_1}^{N} \cdots \sum_{m_{(p+1)/2}=m_{(p-1)/2}}^{N} \cdots \sum_{m_{(p+3)/2}=0}^{N} \cdots \sum_{m_p=m_{p-1}}^{N} f_{p,m_1,m_2,\ldots,m_p} \times \prod_{i=1}^{(p+1)/2} x(n-m_i) \prod_{k=(p+3)/2}^{p} x^*(n-m_k), \tag{3.3}$$

where $f_{p,m_1,m_2,\ldots,m_p}$ are the Volterra kernels, where only the odd nonlinearity orders are considered since even order nonlinear products are generally far away from the fundamental zone [70, 133].

However, a major drawback of the full Volterra model in (3.3) is that the number of kernels grows exponentially with the nonlinearity order and memory depth. Therefore, several pruning techniques have been proposed in the literature [41, 46, 74, 96, 137] to reduce the complexity of the full Volterra model. The pruning techniques aim to extract only the most relevant kernels or basis functions, for example based on physical insights of the PA circuits [137]. More details regarding reduced-complexity nonlinear models and associated DPD structures are provided in Section 3.4.

A popular pruned version of the Volterra model is the memory polynomial (MP) or parallel Hammerstein (PH) model, which is widely used for PA modeling and DPD [46, 65, 74, 77, 104, 114, 117]. The discrete time baseband equivalent PH PA output is defined as

$$y(n) = \sum_{\substack{p=1 \\ p \text{ odd}}}^{P} f_{p,n} \star |x(n)|^{p-1} x(n), \tag{3.4}$$

where $f_{p,n}$ denotes the PH branch filter impulse responses of different orders p. The convolution operator ($\star$) in (3.4) is defined as: $f_{p,n} \star x(n) = \sum_{m=0}^{N} f_{p,m} x(n-m)$, where N is the memory order of the filter. This notation will be used throughout the thesis.

The greatest benefit of the basis function representation in all the previously mentioned nonlinear models with memory is that it provides linear-in-parameters models, and therefore the parameter identification can be performed with simple well-known algorithms, such as linear least-squares (LS) fitting, or least-mean-square (LMS) type of adaptive algorithms [21]. The drawback, as the Volterra series model exemplifies, is that a large number of parameters may be required for an accurate fit.

Another popular class of nonlinear models with memory are cascaded or modular structures, which involve different combinations of linear time-invariant filters and (typically) static nonlinearities. The most elementary two-box models are the Wiener model and the Hammerstein model, which are formed by cascading a linear filter and a memoryless nonlinearity, or vice versa, respectively [53, 112]. More elaborate two or three-box models have been proposed for example in [60, 94]. The benefit of such models is, that the constituent blocks can be quite simple, and therefore the overall number of model parameters stays reasonable. The downside is, that the parameter identification procedure inevitably becomes more complex.

3.2 DPD Main Path Processing

In this Section, we shortly describe the two main approaches for DPD main path processing which are the classical behavioral model inversion-based approach, and the injection-based approach, respectively.

3.2.1 PA Behavioral Model Inversion-based Approach

This approach is the most widely used and popular approach for DPD. The fundamental idea is based on applying a nonlinear function at the PA input which approximates the inverse of the PA nonlinear response, such that the combined effect of the two nonlinear subsystems is approximately linear, as shown in Fig. 3.2(a) [53]. Digital predistortion operates in the digital domain, i.e., before the digital-to-analog converter (DAC) in the TX chain, which facilitates the usage of powerful DSP tools for estimating and adapting the DPD coefficients, as will be shown in the next section and in the upcoming chapters. In general, any nonlinear model can be used for DPD, however, in this thesis we mostly focus on the polynomial-based models described shortly in the previous section.

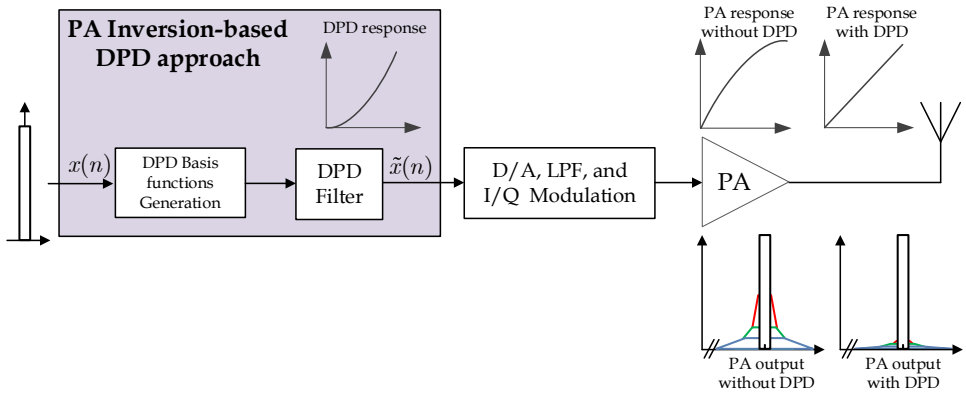

(a) PA inversion-based DPD main path processing approach

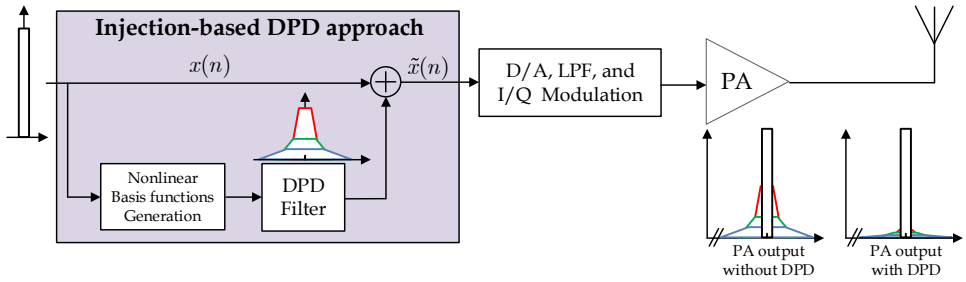

(b) Injection-based DPD main path processing approach

Figure 3.2: DPD main path processing approaches

3.2.2 Injection-based Approach

Another way of looking at DPD, or even predistortion in general, is to consider it as a nonlinear injection operation where a properly filtered version of the nonlinear distortion is injected, at the PA input with opposite phase, such that the nonlinear distortion cancels out at the PA output, as shown in Fig. 3.2(b) [35, 92, 120]. In the classical single carrier and contiguous carrier aggregation scenarios, the difference between the PA inversion-based approach, in Section 3.2.1, and the injection-based approach is almost merely philosophical. However, in noncontiguous carrier aggregation scenarios the difference becomes more obvious. That is because the injection-based approach allows for injecting particular nonlinear distortion components at the most critical sub-band(s) in order to cancel the distortion at the PA output at these sub-band(s) only, with a significantly reduced complexity [34, 75, 109], [P2], [P3]. This kind of flexibility is not directly available when considering the classical inversion-based DPD approach.

The idea of injection-based linearization was initially introduced for RF predistortion in [17, 93]. A combined RF and baseband injection-based linearization was then

introduced in [50]. These techniques required extra RF hardware and required tuning the amplitudes and phases of the injected components in the analog domain, which is not essentially accurate enough. Moreover, including memory effects in the linearization processing becomes quite complicated. Baseband injection-based DPD was thus presented in [35,92,120] as an effective DPD technique, which has the flexibility of applying DSP estimation techniques at baseband. Further discussion regarding injection-based DPD techniques in the more challenging carrier aggregation scenarios will be discussed in Section 3.4.2, and in Chapters 4 and 5.

3.3 DPD Learning Architectures

3.3.1 Direct Learning

The direct learning architecture (DLA) is divided into two steps; first the PA direct model is extracted, then it is used to estimate the DPD coefficients [44,74,80,87,102,131,132], [P4], as shown in Fig. 3.3(a). It can provide very good linearization performance but the DPD parameter or coefficient calculation from the direct model parameters is not always a trivial process since it is, in general, a nonlinear optimization problem [132]. One way of calculating the DPD parameters using the DLA is the P^{th}-order inverse approach [91,111,112]. Closed form solutions can be used to obtain the DPD parameters from the direct PA model parameters, in memoryless direct model and DPD cases, which are usually estimated via linear estimation techniques, e.g., least squares. This procedure becomes more complicated when considering memory effects in the DPD [98].

3.3.2 Indirect Learning

The indirect learning architecture (ILA) is one of the most widely used DPD learning architectures due to its simplicity and good performance [19,20,32,45,46,49,135]. In the ILA approach, a postdistorter is first estimated by minimizing the error between the postdistorter output and the PA input signal as shown in Fig. 3.3(b). This postdistorter is then used as a predistorter assuming that they are equal. This is indeed true in case of the pth-order inverse of Volterra nonlinearities [91,111,112], which is an approximation of the exact inverse. This theory, however, is not always true when considering the exact inverse of a nonlinear system where the pre-inverse and post-inverse are not necessarily equal, provided that they exist [91]. That is one of the reasons why the ILA learning operation is usually iterated a couple of times until a satisfactory performance is obtained. Also, despite its simplicity, ILA-based learning suffers from a well-known bias problem in the DPD parameter estimation due to the noise in the feedback RX [18].

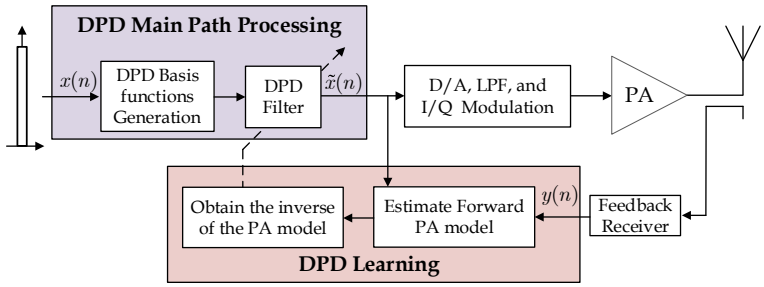

(a) Direct learning architecture (DLA)

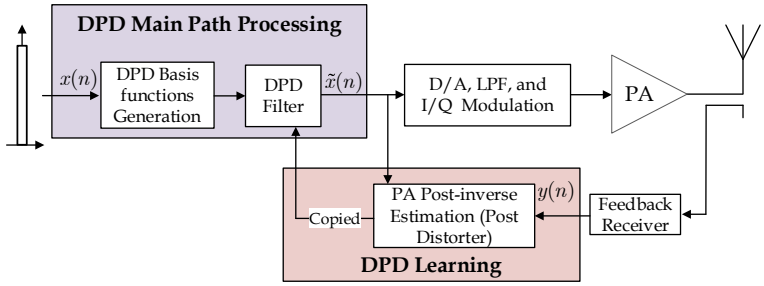

(b) Indirect learning architecture (ILA)

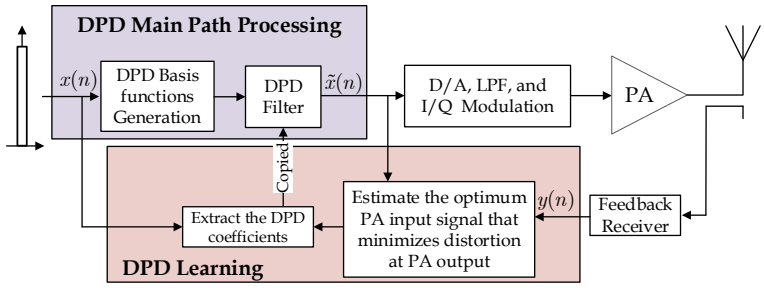

(c) Iterative learning control (ILC)

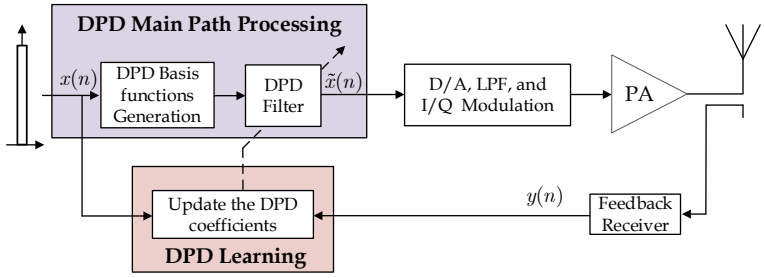

(d) Closed loop architecture

Figure 3.3: DPD learning architectures

This to some extent limits the capability of using low cost components in the feedback RX when high performance linearization is desired.

3.3.3 Iterative Learning Control

Iterative learning control (ILC) is an iterative technique used in control theory to invert the dynamics of linear and nonlinear dynamical systems [90, 95, 121]. ILC has been introduced in [36] as a novel method for DPD learning. Instead of focusing on identifying the DPD coefficients right away, ILC uses an iterative learning algorithm to find the optimal PA input signal that produces the desired linear output response. Once the optimal PA input signal is found, the DPD coefficients can be estimated using standard modeling approaches, e.g., linear least squares (LS), as shown in Fig. 3.3(c).

3.3.4 Closed Loop Learning

The closed loop learning DPD architecture is based on directly updating the DPD coefficients based on the error signal extracted between the PA distorted output and the input signal without distortion [28–31, 68, 69], [P2], [P3], as shown in Fig. 3.3(d). First, the observation at the PA output is divided by the linear gain of the PA which can easily be estimated using linear estimation techniques. Then, the nonlinear distortion at the PA output (error signal) is extracted by subtracting the input signal without distortion from the scaled PA observation signal. This error signal is then used to update the DPD parameters adaptively until the distortion at the PA output is minimized. In the special case when the DPD mitigates the spurious emissions, at the IM sub-bands, in carrier aggregation scenarios, the error signal is directly equal to the observation at the PA output, at the corresponding IM sub-band [P2].

3.4 Reduced-complexity DPD: State-of-the-art

The state-of-the-art of reduced-complexity DPD is shortly summarized in this Section as per the author's knowledge to date. We start with general reduced-complexity techniques that are applicable to any transmit spectrum scenario. Then we move to more specific techniques for reducing the complexity of DPD in the more challenging carrier aggregation scenarios with relatively wide carrier spacing.

3.4.1 General Techniques for Reducing DPD Complexity

In this Section, we shortly summarize some of the main techniques available in the existing literature for DPD complexity reduction which can, in principle, be used in any

carrier allocation scenario. These techniques can also be applied to any of the DPD main path processing architectures explained in Section 3.2, or in any of the DPD learning architectures explained in Section 3.3. Complexity reduction in the DPD processing can, in general, be achieved by two methods: the first is based on reduced-complexity DPD structures using nonlinear models with fewer parameters while not essentially sacrificing the linearization performance. The second method is based on reducing the required sample rates for DPD by filtering the observation at the PA output and the DPD basis functions. Both strategies contribute to complexity reduction in the DPD main path processing and learning. We start with a summary of reduced complexity nonlinear models, then move to shortly discuss reduced-complexity DPD which is based on reducing the required sample rate for DPD processing and learning.

Reduced-complexity Nonlinear Models

Nonlinear models representing the power amplifier nonlinear distortion products are the cornerstone of any DPD system, and various models are used in the literature as explained in Section 3.1. The Volterra model is the most general model which can, in principle, represent any dynamic nonlinear distortion with high accuracy. However, the number of Volterra kernels increases exponentially with the nonlinear order P and memory order N as shown in (3.3), which increases the DPD processing and learning computational complexity. Moreover, a large number of parameters commonly implies a high condition number of the associated data matrix which can introduce stability and numerical problems in the DPD parameter estimation procedure. That is why there has a been a lot of efforts in the literature to reduce the number of these kernels (basis functions) through an operation known as *pruning*.

The simplest pruning method lead to the well-known MP or PH model in (3.4) in which all the off-diagonal elements of the Volterra series are set to zero. In [134, 136], some of the off-diagonal terms were included to improve the modeling accuracy with reasonable number of coefficients, while in [137] the physical behavior of the PA circuit was considered to select the most relevant Volterra kernels. In [39], the modeling accuracy represented by the normalized mean square error (NMSE) was used as a metric to rank the nonlinear basis functions and consequently choose the most relevant. Various effective pruning methods have also been introduced in [39, 122, 123, 130] to reduce the DPD structural complexity in different transmit spectrum scenarios.

More sophisticated signal processing algorithms were used in [15, 55, 57, 119, 128] to reduce the number of basis functions used for PA dynamic nonlinear modeling and/or DPD. In [15, 119], the least absolute shrinkage and selection operator (LASSO) approach was used. LASSO is a well known signal processing algorithm in which a reduced set of basis functions can be obtained by putting a constraint on the L1-norm of the parameter

vector [118]. Ridge regression can also be used to reduce the number of model parameters and resolve ill-conditioning problems [62], and it was applied in [57] in the context of reduced-complexity DPD. In [128], basis functions were adaptively added or removed from the basis function set based on their correlation with the residual distortion at the PA output, and thus only the most important/relevant basis functions were used. Finally, a comparison between some of the above mentioned model order reduction techniques was provided in [55].

Reduced DPD sample rates

The computational complexity, cost, and power consumption of any DPD system are directly related to the required sample rates for DPD processing and learning. That is why there has been some recent research efforts that aim at reducing the required sampling rate of the digital-to-analog converter (DAC) in the DPD main path, and the analog-to-digital converter (ADC) in the feedback receiver path. This can be achieved by filtering the observation at the PA output and/or the basis functions used for predistortion with a filter whose bandwidth is less than Q times the bandwidth of the baseband signal, where Q is the nonlinearity order of the DPD processing [28, 88, 126]. These works assume that the spectral regrowth lying outside the filter bandwidth can be filtered out using the TX analog filter(s) [126], or that it can be extrapolated using some extra signal processing in the DPD learning phase [88].

3.4.2 Reduced-complexity DPD in CA Scenarios

As a rule of thumb, classical DPD requires five to seven times the sample rate of the original baseband signal, which becomes increasingly high and complex when the aggregated bandwidth increases beyond a certain limit, e.g., in LTE-A noncontiguous CA scenarios. There has thus been a lot of active research particularly in the area of developing reduced-complexity DPD in flexible spectrum access scenarios [24, 25, 34, 75, 85, 86, 89, 106, 109, 110, 124, 127]. These developments mainly focus on finding ways to reduce the required sample rates in the DPD main path and feedback path.

Concurrent DPD

There have recently been many works on efficient digital predistortion structures and techniques for CA transmitters that employ only a single PA [24, 34, 86, 106, 110]. When the primary focus of the DPD is to linearize the main CCs, these techniques are called in the literature *concurrent DPD*. In such cases, the main CCs are assumed to be separated by a large distance and the spurious emissions are assumed to be properly filtered out by the transmit RF filter. The advantage of such concurrent DPD techniques is

the reduced sampling rates of both the DAC and ADC in the DPD system compared to conventional full-band DPD which linearizes the whole aggregated spectrum at a significantly higher sampling rate. However, when the number of CCs increases, the concurrent DPD structural complexity also increases thus increasing the number of DPD parameters. Consequently, pruning and other model order reduction techniques explained in Section 3.4.1 become even more relevant and important in such concurrent DPD structures [122, 123, 130]. Moreover, classical concurrent DPD architectures require a number of feedback observation receivers equal to the number of CCs. There have thus been some recent research efforts to reduce the complexity of such concurrent DPD solutions and use only a single feedback receiver for parameter estimation [85, 89, 127], [P3]. Additionally, some works have added more flexibility to such concurrent DPD techniques by allowing the linearization of, for example, only one of the CCs if needed to further reduce the DPD complexity in certain scenarios [124], [P3].

DPD for Spurious Emission Mitigation

Complementary to the DPD methods that seek to linearize the main carriers, there has been some efforts to develop DPD techniques that can suppress the spurious emissions in non-contiguous transmission cases, while not concentrating specifically on the linearization of the main component carriers. This is motivated by fact that in many CA scenarios, the spurious emissions can easily violate the emission limits in the spurious region, and/or desensitize the own RX in FDD transceivers, as explained in more details in Chapter 2.

These spur suppression DPD techniques use the injection-based DPD approach in which a suitable signal is injected at the sub-band(s) where the spurious emissions need to be mitigated. The injected signal is properly filtered such that the level of the emissions at the PA output is reduced. In [75, 109] the estimation of the DPD coefficients was based on the direct learning architecture with P^{th}-order inverse, and memoryless DPD processing. While in [25] a memoryless least-squares fit between the observed intermodulation distortion at the considered sub-band and certain basis functions was performed. The basis functions were generated using a wideband composite carrier baseband equivalent signal, followed by sub-band filtering. The estimated and regenerated IMD was then applied at the PA input, oppositely phased, such that it is canceled at the PA output. Meanwhile in [P2], the estimation was based on the closed loop DPD architecture with decorrelation-based learning, and memory effects were included.

CHAPTER 4

Sub-band DPD for Spurious Emission Mitigation

In this Chapter, the contributions to DPD for spurious emission mitigation in [P1], [P2], [P5] - [P7], and partly in [14, 116] are reviewed. The elementary third-order sub-band DPD for spurious emission mitigation was proposed in [P5] using a novel decorrelation-based closed loop learning algorithm, which was then extended in [P6] to include memory-based processing. A more implementation friendly version of the algorithm was then presented in [14] along with an FPGA implementation of the DPD solution. Higher-order nonlinearity processing with memory was then introduced in [P2] along with comprehensive RF measurements. The sub-band DPD solution was then extended in [116] to enhance its performance when linearizing multiple sub-bands and further reduce the complexity, especially for hardware implementation. In the special case when the spurious emissions overlap with the own RX band in FDD transceivers, the sub-band DPD proposed in [P7] used the main RX for DPD learning without requiring any additional observation RX. Finally, the overview article [P1] highlighted the main principles and advantages of such low complexity sub-band DPD solutions.

This Chapter is organized as follows. Section 4.1 presents the mathematical modeling of the different considered spurious components at different sub-bands, produced by a nonlinear PA with memory. Stemming from this modeling, also the corresponding main path processing of the proposed DPD is formulated. Then, Section 4.2 presents the proposed DPD parameter learning solutions, covering both sample-adaptive and block-adaptive decorrelation-based solutions at different sub-bands. Section 4.3 shortly presents a lower complexity sub-band DPD in the special case when the spurious emissions overlap with the own RX band in FDD transceivers. Section 4.4 then analyzes

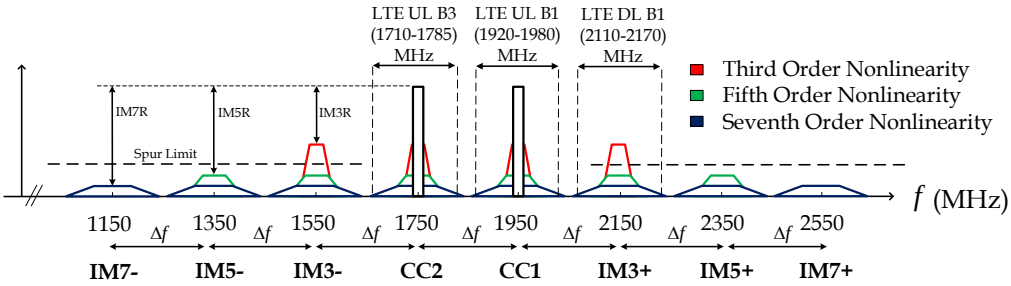

Figure 4.1: Illustration of different distortion components created by a nonlinear PA when excited with a non-contiguous CA signal with two component carriers. Here, nonlinear distortion components up to order 7 are shown.

the computing complexity of the sub-band DPD in terms of the number of floating point operations. Finally, Sections 4.5 and 4.6 report some simulations and RF measurements evidencing excellent spurious emission suppression in different realistic scenarios.

4.1 Nonlinear Distortion Modeling and DPD Main Path Processing

4.1.1 Nonlinear Distortion Modeling

When a noncontiguous dual-carrier signal is applied at the PA input, the PA nonlinearity leads to intermodulation (IM) distortion at different IM sub-bands (i.e., IM3, IM5, etc.), as shown in Fig. 4.1, and as also explained in Section 2.3. In general, each IM sub-band includes nonlinear distortion components of different orders, as shown in Fig. 4.1. For example, in the case of seventh-order PA nonlinearity, the IM3 sub-band contains third, fifth and seventh-order nonlinear components, while the IM5 sub-band contains fifth and seventh-order components, and so on.

In this dual-carrier scenario, the composite baseband equivalent input and output signals of the P^{th}-order Parallel Hammerstein (PH) PA model, with monomial nonlinearities and FIR branch filters, respectively, read

$$x(n) = x_1(n)e^{j2\pi\frac{f_{IF}}{f_s}n} + x_2(n)e^{-j2\pi\frac{f_{IF}}{f_s}n}, \tag{4.1}$$

$$y(n) = \sum_{\substack{p=1 \\ p \text{ odd}}}^{P} f_{p,n} \star |x(n)|^{p-1}x(n), \tag{4.2}$$

where $x_1(n)$ and $x_2(n)$ are the baseband component carrier signals, f_{IF} refers to half the carrier spacing between the CCs, $f_{p,n}$ denotes the PH branch filter impulse responses of order p, and $\star$ is the convolution operator.

Direct substitution of (4.1) in (4.2) allows extracting the baseband equivalent distortion terms at the IM sub-bands (e.g., IM3, IM5, and IM7 sub-bands), which, through straight-forward manipulations, yield

$$y_{IM3_{\pm}}(n) = \sum_{\substack{p=3 \\ p \text{ odd}}}^{P} f_{3\pm,p,n} \star u_{3\pm,p}(n), \tag{4.3}$$

$$y_{IM5_{\pm}}(n) = \sum_{\substack{p=5 \\ p \text{ odd}}}^{P} f_{5\pm,p,n} \star u_{5\pm,p}(n), \tag{4.4}$$

$$y_{IM7_{\pm}}(n) = \sum_{\substack{p=7 \\ p \text{ odd}}}^{P} f_{7\pm,p,n} \star u_{7\pm,p}(n), \tag{4.5}$$

where $f_{3\pm,p,n}$, $f_{5\pm,p,n}$, and $f_{7\pm,p,n}$ denote the baseband equivalent impulse responses corresponding to the wideband PH PA model filters $f_{p,n}$, evaluated at the IM3±, IM5±, and IM7± sub-bands, respectively.

Assuming then a 7^{th} order PA model (i.e., $P = 7$), as a concrete high-order example, the static nonlinear (SNL) basis functions $u_{3\pm,p}(n)$, $u_{5\pm,p}(n)$, and $u_{7\pm,p}(n)$ read

$$u_{3+,3}(n) = x_2^*(n)x_1^2(n), \tag{4.6}$$

$$u_{3+,5}(n) = u_{3+,3}(n)(2|x_1(n)|^2 + 3|x_2(n)|^2), \tag{4.7}$$

$$u_{3+,7}(n) = u_{3+,3}(n)(3|x_1(n)|^4 + 6|x_2(n)|^4 + 12|x_1(n)|^2|x_2(n)|^2), \tag{4.8}$$

$$u_{5+,5}(n) = (x_2(n)^*)^2 x_1(n)^3, \tag{4.9}$$

$$u_{5+,7}(n) = u_{5+,5}(n)(4|x_2(n)|^2 + 3|x_1(n)|^2), \tag{4.10}$$

$$u_{7+,7}(n) = (x_2(n)^*)^3 x_1(n)^4. \tag{4.11}$$

The corresponding basis functions for the negative IM sub-bands can be obtained by simply interchanging $x_1(n)$ and $x_2(n)$ in the above expressions. Next, these behavioral modeling results are utilized to formulate the sub-band DPD concept which was used in [P2], [P5] - [P7] and [14].

4.1.2 Sub-band DPD Main Path Processing

The key idea of the sub-band DPD concept is to inject a proper additional low-power cancellation signal, with structural similarity to (4.3), (4.4), and (4.5) into the PA input

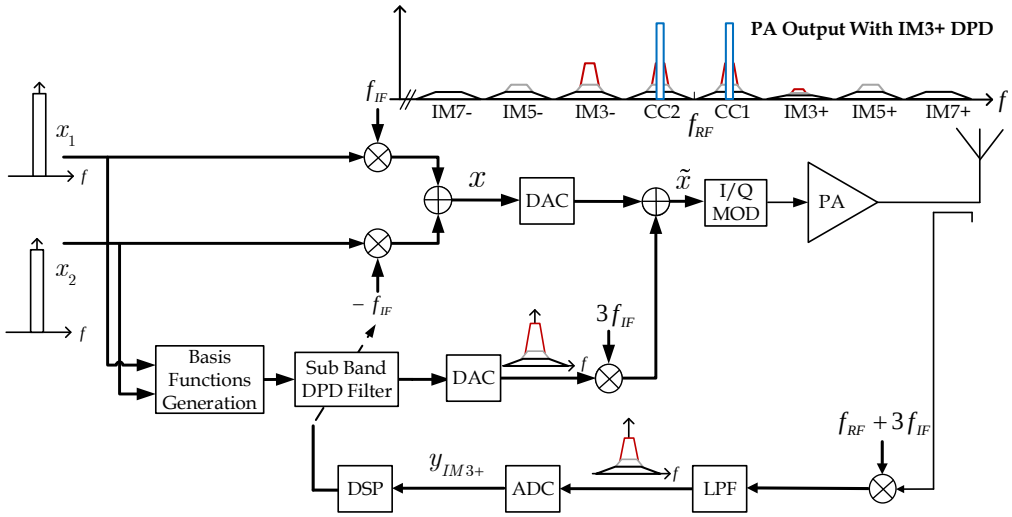

Figure 4.2: The proposed sub-band DPD processing principle focusing on the IM3+ sub-band. Thick lines are used to indicate complex I/Q processing. For presentation simplicity, TX filtering between the feedback coupler and the antenna is not shown.

at the corresponding frequencies, such that the level of the IM distortion at the PA output is reduced. An appropriate digital injection signal can be obtained by adopting the basis functions in (4.6)-(4.11), combined with proper filtering, as shown in Fig. 4.2 for the IM3+ sub-band DPD as an example. The advantage of this injection-based DPD structure is that it allows linearizing each sub-band separately with a lower rate DPD and thus reducing the overall DPD complexity as shown in [P2] and in Section 4.4. On the other hand, the classical DPD philosophy based on inverting the PA model does not provide such flexibility, in general.

4.2 Decorrelation-based DPD Learning

Decorrelation-based learning is a signal processing concept used for separating a particular useful signal from an unwanted interference by decorrelating it from this interference, i.e, minimizing the correlation between the useful signal and the interference. This concept has has been used in the literature in the context of interference cancellation and signal separation, mostly in linear systems [40, 52, 59]. However, in this work, this is the first time that this concept is used in the context of sub-band DPD, while utilizing the injection-based main path processing approach. The unwanted interference here is the nonlinear distortion due to the PA per sub-band. The decorrelation-based DPD learning algorithm is applied in this Chapter, along with the injection-based main path DPD processing, for spurious emission mitigation at the IM sub-bands. It is also applied

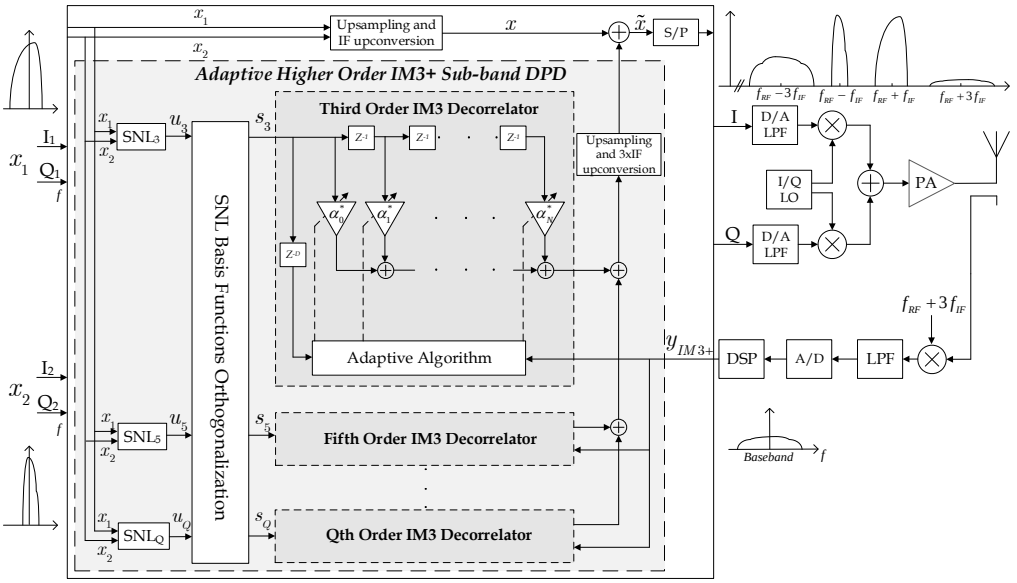

Figure 4.3: Detailed block diagram of the sample-adaptive decorrelation-based IM3+ sub-band DPD with higher-order nonlinearities and memory.

in Chapter 5 in the context of linearization of the main carriers for mitigating in-band and out-of-band distortion due to the PA.

4.2.1 Sample-adaptive Learning

The sample-adaptive decorrelation-based DPD learning algorithm in [P2] is now shortly reviewed, and the reader is referred to the original article for full details. Based on the nonlinear distortion modeling and the sub-band DPD concept explained in the previous section, a computationally feasible and highly efficient closed-loop DPD estimation algorithm with adaptive filtering was developed in [P2]. The DPD parameter optimization task was formulated as minimizing the correlation between the nonlinear distortion at the considered sub-band at the PA output, and the basis functions representing this nonlinear distortion. Those basis functions were orthogonalized for better numerical properties and stability when used in the adaptive filtering and parameter estimation context [105, 107, 108].

For simplicity of presentation, the IM3 sub-band DPD is considered here which can then easily be generalized to include other sub-bands, as shown also in [P2]. The orthogonal version of the IM3 sub-band basis functions $u_{3\pm,q}(n)$ in (4.6)-(4.11) are denoted by $s_{3\pm,q}(n)$. The DPD filter per sub-band has nonlinearity order Q and memory depth N per nonlinearity order (i.e., $N+1$ memory taps). And since the proposed DPD

solution is adaptive, we adopt the adaptive filtering notations. The l^{th} memory tap of the DPD filter applied to the q^{th} order IM3± basis functions, $s_{3\pm,q}(n)$, is denoted by $\alpha_{3\pm,q,l}(n)$, where n is the time index. The DPD adaptive filter coefficients in a vector format can thus be defined as follows:

$$\boldsymbol{\alpha}_{3\pm,q}(n) = [\alpha_{3\pm,q,0}(n)\ \alpha_{3\pm,q,1}(n)\ ...\ \alpha_{3\pm,q,N}(n)]^T, \tag{4.12}$$

$$\bar{\boldsymbol{\alpha}}_{3\pm}(n) = [\boldsymbol{\alpha}_{3\pm,3}(n)^T\ \boldsymbol{\alpha}_{3\pm,5}(n)^T\ ...\ \boldsymbol{\alpha}_{3\pm,Q}(n)^T]^T. \tag{4.13}$$

Similarly, the basis function samples representing the nonlinear distortion at the IM3± sub-bands can also be grouped into a vector form as follows.

$$\mathbf{s}_{3\pm,q}(n) = [s_{3\pm,q}(n)\ \ s_{3\pm,q}(n-1)\ ...\ s_{3\pm,q}(n-N)]^T, \tag{4.14}$$

$$\bar{\mathbf{s}}_{3\pm}(n) = [\mathbf{s}_{3\pm,3}(n)^T\ \ \mathbf{s}_{3\pm,5}(n)^T\ \ ...\ \ \mathbf{s}_{3\pm,Q}(n)^T]^T. \tag{4.15}$$

The instantaneous sample of the composite baseband equivalent PA input signal $\tilde{x}(n)$ with the IM3± sub-band DPD now reads

$$\tilde{x}(n) = x(n) + [\bar{\boldsymbol{\alpha}}_{3+}(n)^H \bar{\mathbf{s}}_{3+}(n)]e^{j2\pi\frac{3f_{IF}}{f_s}n} + [\bar{\boldsymbol{\alpha}}_{3-}(n)^H \bar{\mathbf{s}}_{3-}(n)]e^{-j2\pi\frac{3f_{IF}}{f_s}n} \tag{4.16}$$

Then, in order to adaptively update the filter coefficients $\bar{\boldsymbol{\alpha}}_{3\pm}(n)$, the IM3± sub-bands are observed at the PA output with a feedback receiver, in a sequential manner, as illustrated in Fig. 4.3. The DPD coefficients are updated as follows:

$$\bar{\boldsymbol{\alpha}}_{3\pm}(n+1) = \bar{\boldsymbol{\alpha}}_{3\pm}(n) - \frac{\mu}{||\bar{\mathbf{s}}_{3\pm}(n)||^2 + C}\,\bar{\mathbf{s}}_{3\pm}(n)e^*_{3\pm}(n), \tag{4.17}$$

where $e_{3\pm}(n)$ denotes the baseband equivalent of the residual IM3 spurious emissions at the PA output with the current DPD coefficients. The scaling factor $||\bar{\mathbf{s}}_{3\pm}(n)||^2 + C$ normalizing the learning step-size μ in (4.17) is philosophically similar to that of the Normalized Least Mean Square (NLMS) algorithm, in effect making the learning characteristics more robust against the input data dynamics [61]. The overall processing flow is graphically illustrated in Fig. 4.3.

4.2.2 Block-adaptive Learning

A block-adaptive version of the decorrelation-based learning rule was proposed in [14] and [P2]. In principle, the algorithm is similar to the block-adaptive LMS solution in [61]. Two distinct blocks were defined in the processing, as illustrated in Fig. 4.4. A single update cycle of the learning algorithm will utilize M samples whereas the DPD parameter update interval is L samples, with $M \leq L$. Thus, by proper choice of M and

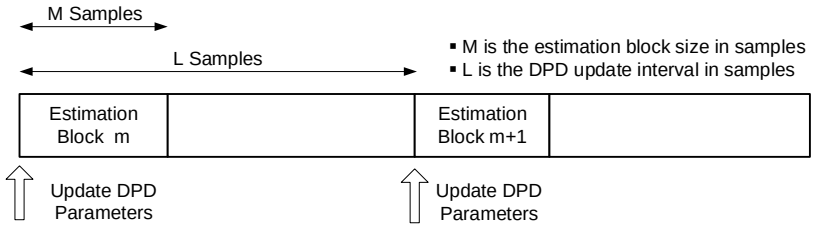

Figure 4.4: Block-adaptive DPD learning concept. The DPD parameters estimated in the current estimation block m are applied in the sub-band DPD main path processing during the next block $m + 1$.

L, arbitrarily long loop delays can in principle be tolerated, facilitating stable operation under various hardware and software processing latency constraints.

The block-adaptive IM3+ sub-band DPD coefficient update, for example, reads

$$\bar{\boldsymbol{\alpha}}_{3+}(m+1) = \bar{\boldsymbol{\alpha}}_{3+}(m) - \mu\, \mathbf{S}_{3+}(m)\mathbf{e}^*_{3+}(m), \tag{4.18}$$

where $\mathbf{e}^*_{3+}(m)$ refers to the element-wise conjugated error signal block of M samples, and $\mathbf{S}_{3+}(m)$ denotes the convolution matrix of the orthogonal basis function samples, all within the processing block m, as defined in [P2]. The obtained new DPD coefficients are then applied on the next block of L samples as illustrated in Fig. 4.4. The reader is referred to [14] and [P2] for more details regarding the algorithm development and performance. An FPGA implementation of this algorithm was also presented in [14].

4.2.3 Further Enhancements

In [116] an iterative version of the block-adaptive sub-band DPD learning was proposed that takes into consideration the mutual effect of, for example, the IM3+ sub-band DPD on the IM3- sub-band, and so on. A mathematical analysis was performed to show the impact of the positive IM3 sub-band DPD on the negative IM3 sub-band when a dual carrier signal is applied to a nonlinear PA, and thus providing a theoretical foundation and motivation for this work. This solution iterated between the different spurious components until a satisfactory performance was achieved for each of them. The iterations have proved to be useful in [116], particularly when operating in a very nonlinear region of the PA. Though even in those cases, usually only one additional iteration has been needed.

Furthermore, in order to add more flexibility and complexity reduction to the proposed DPD, the learning of the higher order nonlinearities in each sub-band was done sequentially one order at a time in [116]. This has the advantage of reducing the hardware complexity by essentially using one learning module for all the nonlinearity

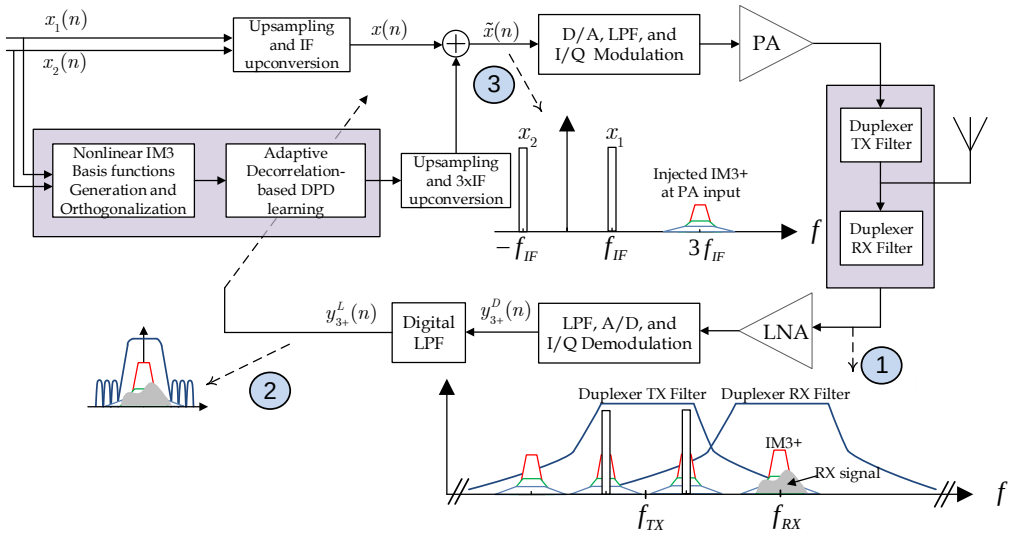

Figure 4.5: Block diagram of the proposed sub-band DPD solution which uses the main RX for learning the DPD coefficients.

orders. An additional flexibility advantage is that we can stop adding higher orders in the learning phase once a sufficient spurious emission suppression is achieved, thus further reducing the DPD complexity. A drawback of this solution is that it takes a longer time to converge. To alleviate this problem, two additional modifications were proposed in [116] in order to enhance the convergence speed of the proposed DPD parameter learning solution. The first used a variable learning rate μ during the DPD parameter learning in order to have a faster convergence at the initial phase of the learning while not sacrificing the steady state error. The second modification was that the DPD coefficients can be stored once they are converged, and act as a starting point for learning once the same carrier configuration is used again. The algorithm descriptions and theoretical foundation as well as supporting simulations and WARPLab results are provided in [116], and the reader is referred to the original article for more details.

4.3 Using the main RX for DPD Learning

In FDD devices, in addition to violating the general spurious emission limits, the generated spurious components can also overlap with the device's own receive band, causing own receiver desensitization [47, 71, 72, 103, 125]. This becomes particularly problematic in CA scenarios, due to limited duplexing distance, as well as finite TX-RX duplexer isolation, which is in the order of 50-60 dB in most commercial UE's. A novel spur-injection sub-band DPD solution was presented in [P7] which aimed at suppressing

these particular emissions at the own RX band. The DPD solution used directly the device's own RX for learning, and thus does not require any extra observation RX, as shown in Fig. 4.5. However, this implies that the DPD processing and parameter learning have to consider the RF duplex filters' frequency responses for proper parameter estimation and predistortion. The DPD learning solution is based on the decorrelation principle used earlier in this Chapter. The reader is referred to [P7] for more details regarding the algorithm development and performance.

4.4 Complexity Perspectives

In many CA transmission scenarios, particularly in mobile terminals, spurious emissions at the IM sub-bands impose strict linearity constraints on the PA which can be relaxed through DPD, as explained in Chapter 2. In such scenarios, the proposed sub-band DPD in this Chapter has a major advantage over the classical full-band DPD in terms of the required computational complexity. This complexity reduction aspect is even more emphasized when the carrier spacing between the CCs is relatively wide, and thus very high speed ADCs and DACs are required in the classical DPD solutions. In many other CA scenarios, the in-band and out-of-band distortion products are critical as well due to their negative impact on the transmit signal quality (EVM) and co-existence with other users (ACLR), respectively. Such aspects are considered in Chapter 5 in which a reduced-complexity concurrent DPD is developed particularly for mitigating the in-band and out-of-band distortion products in CA scenarios. A more complete reduced-complexity DPD solution is also presented in Chapter 5 which can handle all different distortion products, i.e., spurious emissions, in-band emissions, and out-of-band emissions.

In this Section, we provide a comparison between the complexity of the full-band DPD and that of the proposed IM sub-band DPD. The complexity comparison is conducted under the assumption that the spurious emissions are the main limiting factor restricting the PA from operating at higher power efficiency levels. This is indeed a valid assumption in many scenarios, especially for mobile devices, as demonstrated in [8,73,78,99,100,103], and as explained in more details in Chapter 2. In general, the computational complexity of any DPD can be classified into two main parts: the learning complexity and the main path processing complexity. The learning complexity involves the DPD parameter estimation and adaptation, while the real-time main path processing complexity involves the number of computations done per second while the DPD is operating. In this Section, we will focus on the DPD real-time main path processing complexity which is the most critical especially for mobile-type devices. This is due to the fact that the main path processing has to operate in real-time as opposed to the parameter estimation

Table 4.1: Comparison of main path processing complexities of ninth order sub-band and full-band DPDs. Two 1 MHz CCs with 20 MHz carrier spacing is assumed. DPD sample rate is 189 MSPS for the full-band and 9 MSPS for the sub-band DPD.

	Sub-band DPD				**Full-band DPD**
	IM3 +/- Sub-band	IM5 +/- Sub-band	IM7 +/- Sub-band	IM9 +/- Sub-band	Full-band
BF Generation FLOP	37	40	45	48	11
DPD Filtering FLOP	$32(N_1+1)$ - 2	$24(N_1+1)$ - 2	$16(N_1+1)$ - 2	$8(N_1+1)$ - 2	$40(N_2+1)$ - 2
Total Number of FLOP	$32(N_1+1)$ + 35	$24(N_1+1)$ + 38	$16(N_1+1)$ + 43	$8(N_1+1)$ + 46	$40(N_2+1)$ + 9
GFLOP/s ($N_1 = 1$, $N_2 = 3$)	**0.891**	**0.774**	**0.675**	**0.558**	**31.941**

and adaptation processing which can operate on a much slower rate. For a quantitative comparison, we shall use the number of floating point operations per second (FLOP/s) as the main quantitative metric.

Basis function generation followed by the actual predistortion filtering using the basis functions are the two main operations performed in the DPD main path processing [117]. The number of floating point operations required to perform these two operations is shown in Table 4.1 for ninth-order sub-band and full-band DPDs, respectively, where N_1 and N_2 are the corresponding memory depths per adopted basis function. The full-band DPD architecture that we use also in our comparative performance simulations in Section 4.5.2, and which is also widely applied otherwise, is based on the PH architecture with ninth order nonlinearity. Another important factor to be considered when comparing the two DPD architectures is frequency selectivity of the nonlinear PA. This implies that when memory effects of the PA are considered, substantially longer filters are needed for the full-band DPD compared to the sub-band DPD for a given linearization performance. We thus assume a memory depth of 1 (i.e., two memory taps) per basis function for the sub-band DPD, while a memory depth of 3 per basis function is assumed for the full-band DPD.

Considering an LTE-A UL scenario of two 1 MHz CCs with 20 MHz carrier spacing as a concrete example, the required sample rate by the full-band DPD is $9 \times (20 + 1) = 189$ MSPS, while the sub-band DPD sample rate is only $9 \times 1 = 9$ MSPS. Consequently, as shown in Table 4.1, a huge reduction in the number of floating point operations per second (FLOP/s) can be achieved using the sub-band DPD. Moreover, this CA scenario is particularly challenging from the PA nonlinearity perspective due to the narrow allocated bandwidth per CC, which means that the power of the IM spurious

emissions becomes concentrated in a very narrow portion of the spectrum and can thus more easily violate the -30 dBm/1MHz spurious emission limit [2, 7, 78].

4.5 Simulation Results

In this Section, we quantify the IM sub-band DPD performance using Matlab simulations with practical models for mobile-like PAs designed for low-cost devices. The linearization performance and complexity is also quantitatively compared against the classical full-band DPD. The PA model used in the simulations is a ninth-order parallel Hammerstein model, with four memory taps per branch, and the parameters have been identified using measurements with a true mobile PA.

4.5.1 Sub-band DPD Performance

Two simulation examples are presented in this subsection. The first demonstrates the linearization performance at a particular sub-band, e.g., IM3+ sub-band, when adding higher-order basis functions to the DPD processing. The second example demonstrates the effectiveness of the proposed sub-band DPD when linearizing different sub-bands, e.g., IM3, IM5, IM7, etc., while fixing the nonlinearity order of the DPD processing. The sub-band DPD structure used in these simulations contains two taps per basis function (i.e., $N = 1$). The block-adaptive learning principle is adopted, with 200 blocks each containing 1000 samples, at the sub-band DPD sample rate. The transmit waveform is composed of two 1 MHz LTE-A UL SC-FDMA component carriers with QPSK data modulation, and the CC spacing is 12 MHz.

Fig. 4.6 compares the linearization performance of the IM3+ sub-band DPD when using third-order and higher nonlinear processing. The IM3 spurious emissions are suppressed by up to 40 dB when adopting ninth-order processing. Furthermore, to demonstrate the capability of the sub-band DPD to suppress the spurious emissions below the -30 dBm/MHz spurious emission limit, Fig. 4.7 shows how the IM3 spurious emission level changes while varying the TX power and using different sub-band DPD nonlinearity orders. When using a seventh-order, or higher, sub-band DPD, the spurious emissions are clearly below the general spurious emission limit even at high UE TX powers up to +23 dBm.

Fig. 4.8 then demonstrates the linearization performance of the negative IM3, IM5, and IM7 sub-band DPDs with ninth-order nonlinear processing. The achieved spurious emission suppression is 40 dB, 35 dB, and 18 dB at IM3-, IM5-, and IM7- sub-bands, respectively.

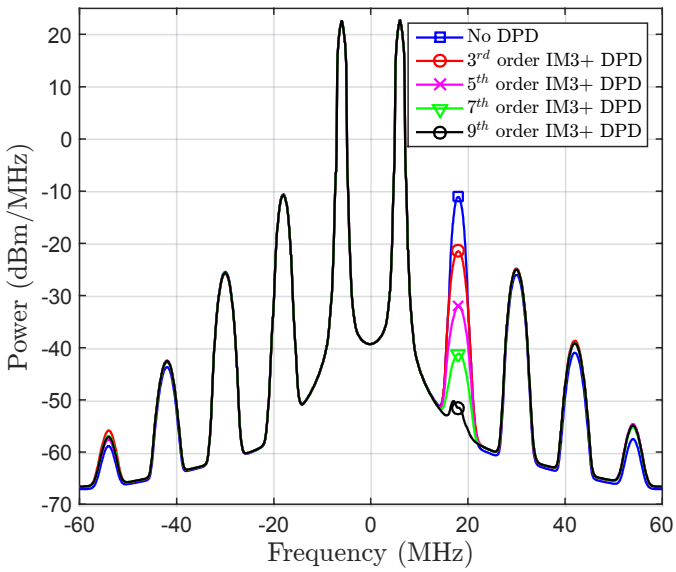

Figure 4.6: Baseband equivalent PA output spectrum at +24 dBm with two 1 MHz LTE-A UL carriers and 12 MHz CC separation using a ninth-order PA with memory. Different orders of the IM3+ sub-band DPD are compared, with memory depth equal to 1 per DPD SNL basis function.

Table 4.2: Comparison of main path processing complexity and linearization performance of full-band versus sub-band DPD. Two 1 MHz LTE-A UL carriers with QPSK data modulation and 20 MHz carrier spacing are used.

	DPD Running Complexity			**Transmitter Performance**			
	Coeffs	Fs (MSPS)	GFLOP/s	EVM (%)	Positive IM3R (dBc)	Positive IM5R (dBc)	TX Power (dBm)
No DPD	N/A	N/A	N/A	1.2527	35.5744	56.4272	+20
Full-Band ILA DPD	20	189	31.941	0.1058	61.9428	63.9842	+19
IM3+ Sub-Band DPD	8	9	**0.891**	1.2489	**68.3291**	N/A	+20
IM5+ Sub-Band DPD	6	9	**0.774**	1.2529	N/A	**71.9823**	+20

4.5.2 Full-band versus Sub-band DPD Complexity and Performance Comparison

The linearization performance and complexity of the sub-band DPD is compared against the full-band DPD in this subsection. The assumption made in this particular example

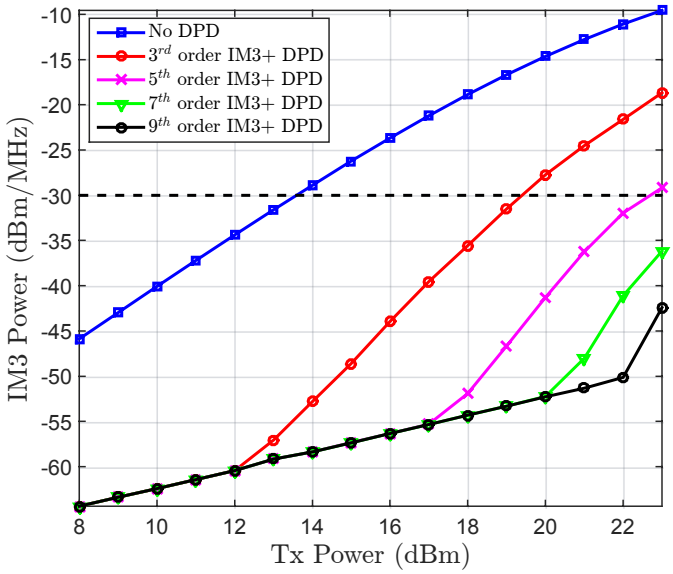

Figure 4.7: IM3 spurious emissions vs. TX power using different orders of the IM3+ sub-band DPD processing, with memory depth equal to 1 per DPD SNL basis function. A ninth-order PA with memory is used, and 2 dB TX filter insertion loss is assumed.

is that the IM3 and IM5 spurious emissions can violate the emission limits, while other emissions, including the in-band and out-of-band emissions, are already below the emission limits. The proposed sub-band DPD thus has the capability to tune its linearization to only the problematic sub-bands, while the full-band DPD does not have this flexibility, thus inevitably becoming much more complex. The sub-band DPD structure has ninth-order nonlinearity and two memory taps per SNL basis function. The sub-band DPD block-adaptive decorrelation-based learning uses 200 blocks with block size $M = 1000$ each. The full-band DPD, in turn, adopts the PH structure with ninth-order nonlinearity and four memory taps per PH branch. The full-band DPD learning is based on the ILA approach with two 2 ILA iterations utilizing 100k samples each.

Table 4.2 shows that the sub-band DPD achieves better linearization performance, in terms of suppression of spurious IM emissions at the IM3 and IM5 sub-bands, despite its significantly lower complexity measured by the number of GFLOP/s. Moreover, the full-band DPD, which is based on the ILA structure, requires an additional 1-2 dB back off to guarantee stable operation, which is not required in the sub-band DPD. Consequently, the transmitter becomes more power efficient when using the sub-band DPD.

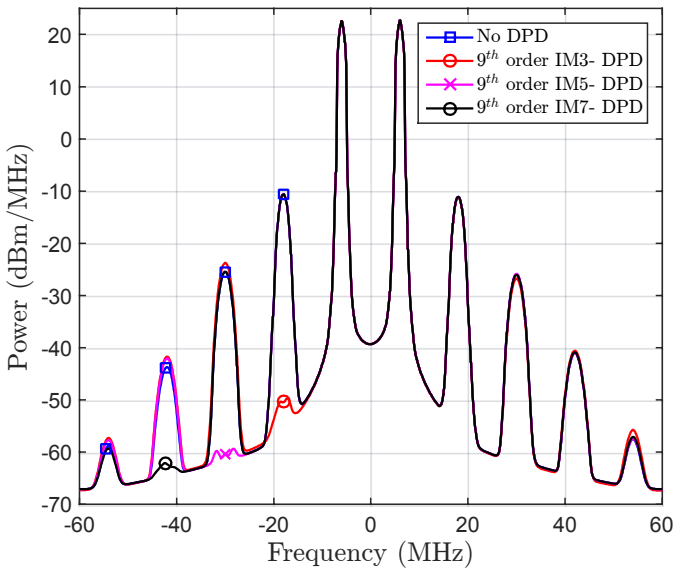

Figure 4.8: Baseband equivalent of two 1 MHz LTE-A UL carriers with 12 MHz separation using a ninth order PH PA extracted from a real mobile PA at +24 dBm. Ninth order negative IM3, IM5, and IM7 sub-band DPD solutions are shown, with memory depth equal to 1 per DPD SNL basis function.

On the other hand, the full-band DPD outperforms the sub-band DPD in terms of the in-band distortion mitigation (i.e., EVM). This is expected, since the full-band DPD linearizes the whole transmit band, including the main CCs and the spurious IM emissions. In this context, it is worth mentioning that a reduced-complexity concurrent DPD, developed particularly for linearizing the main carriers is also developed in this thesis with significantly lower complexity than the full-band DPD. The developed concurrent DPD is highly compatible with the decorrelation-based sub-band DPD in this Chapter since its learning is also based on the simple decorrelation principle. It can thus be easily complemented with the sub-band DPD for IM spurious emissions in order to enhance the EVM and ACLR as well, as will be shown in Chapter 5.

4.6 RF Measurement Results

In this Section, RF measurements are presented to demonstrate the effectiveness of the sub-band DPD solution in real RF environments. Two different intra-band LTE-A CA RF measurement examples are demonstrated. The first experiment demonstrates the violation of the spurious emission limit due to the emission of the IM3+ spur inside

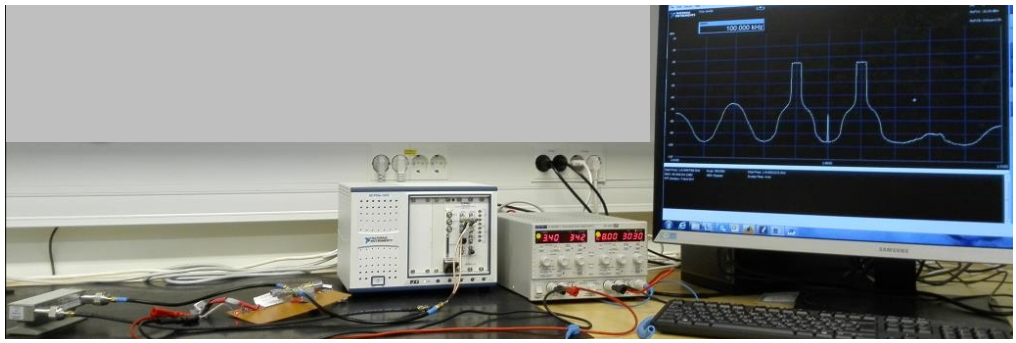

(a) Photo of the RF measurement setup

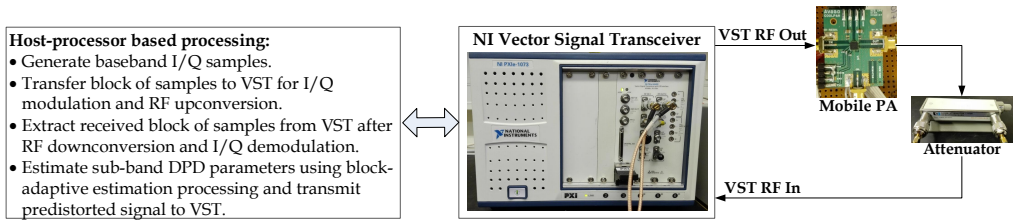

(b) Block diagram of the RF measurement setup

Figure 4.9: Hardware setup used in the RF measurements for testing and evaluating the proposed sub-band DPD.

the TX band, thus not being attenuated by the TX filter. The second experiment demonstrates an own RX desensitization example, in FDD transceiver context, where the IM3+ spur is located at the own RX band and is not sufficiently attenuated by the duplexer TX filter.

4.6.1 RF Measurement Setup

The National Instruments (NI) PXIe-5645R VST used in the RF measurements includes both a vector signal generator (VSG), and a vector signal analyzer (VSA) with 80 MHz instantaneous bandwidth. The I/Q samples are first generated locally on the host processor, and then transferred to the VSG to perform RF I/Q modulation at the desired power level at the PA input. The VST RF output is then connected to the input port of the external PA, whose output port is connected to the VST RF input through a 40 dB attenuator, implementing the observation receiver, as illustrated in Fig. 4.9. The VSA performs RF I/Q demodulation to bring the signal back to baseband. The baseband I/Q observation block is then filtered to select the IM3 sub-band which is used for block-based adaptive sub-band DPD learning, after proper alignment with the locally generated basis functions. The number of blocks used by the sub-band DPD is 20 with

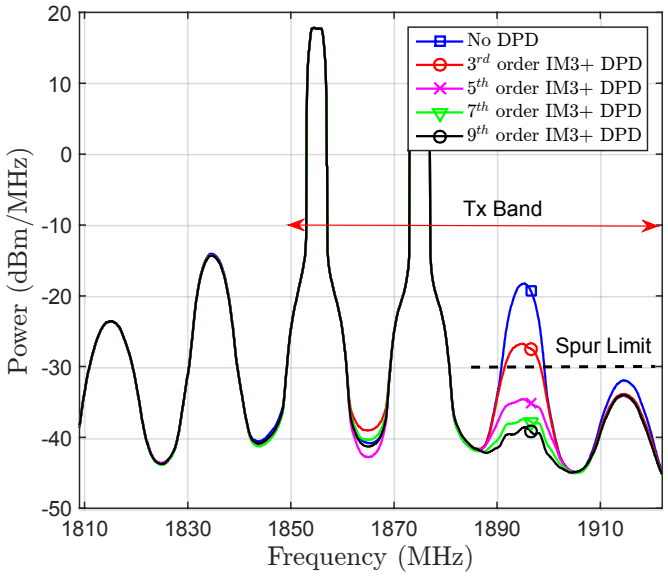

Figure 4.10: An LTE-A band 25 RF measurement example at the UE PA output showing the gain from using an IM3+ sub-band DPD. IM3 spur reduction with third, fifth, seventh, and ninth-order sub-band DPDs are demonstrated, using a real commercial mobile PA operating at +25 dBm. An LTE-A UL CA signal with two 3 MHz CCs and 20 MHz carrier spacing is used.

block size $M = 10k$ each, and the DPD memory depth $N = 1$. The ACPM-5002-TR1 mobile terminal power amplifier used in these measurements is designed for LTE-A UL band 25 (1850-1915 MHz), with 29 dB gain and +31 dBm 1-dB compression point..

4.6.2 Spurious Emission Limit Violation Example

In this intraband CA example, two 3 MHz CCs are transmitted with 20 MHz carrier spacing at +25 dBm TX power, as shown in Fig. 4.10. The intermodulation distortion at the IM3+ sub-band is emitted inside the TX band (1850-1915 MHz), and is clearly violating the spurious emission limit (-30 dBm/MHz) when no DPD is used. When using the sub-band DPD, the spurious emission level is well below the emission limit, given that at least fifth-order processing is deployed. In general, more than 20 dB of measured spurious emission suppression is achieved with the ninth order IM3 sub-band DPD, thus giving more than 10 dB additional gain compared to the basic third-order sub-band DPD as shown in Fig. 4.10. Notice that there is no need for predistorting the negative IM3 sub-band in this example, since those emissions will be filtered out by the TX filter.

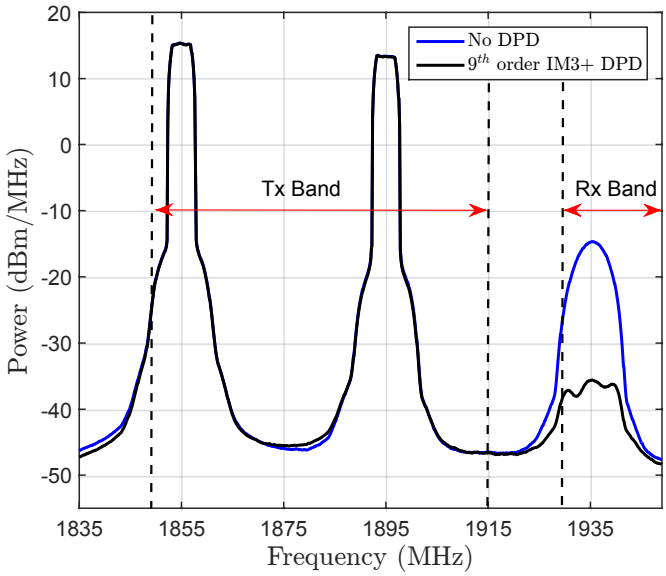

Figure 4.11: An LTE-A band 25 RF measurement example at the UE PA output showing the gain from using a ninth-order IM3+ sub-band DPD when the IM3+ is falling at own RX band. An LTE-A UL CA signal with two 5 MHz CCs and 40 MHz carrier spacing is used with a real commercial mobile PA operating at +25 dBm.

4.6.3 Own Receiver Desensitization Example

In this intraband CA example, two 5 MHz CCs are transmitted with 40 MHz carrier spacing at +25 dBm TX power, as shown in Fig. 4.11. The spurious emission at the IM3+ sub-band falls on top of the own RX band, and therefore potentially desensitizing the own receiver when no DPD is used. More than 20 dB of spurious emission suppression is achieved when adopting the IM3+ sub-band DPD with ninth-order nonlinear processing. Fig. 4.12 shows the real-time convergence of the block-adaptive sub-band DPD coefficients demonstrating stable operation in a real RF environment.

To further demonstrate the problem, a UE duplexer TX filter with 65 dB attenuation at the own RX band is assumed [1] in this example. The integrated power of the IM3+ spur at the RX band without DPD will then be approximately -73 dBm/5MHz, which is 25 dB above the effective RX noise floor when assuming 9 dB UE RX noise figure (NF) [7]. On the other hand, when the proposed IM3+ sub-band DPD is deployed, the integrated power of the IM3+ spur at the RX band will be approximately -95 dBm/5MHz, which is only 3 dB above the effective RX noise floor.While the residual

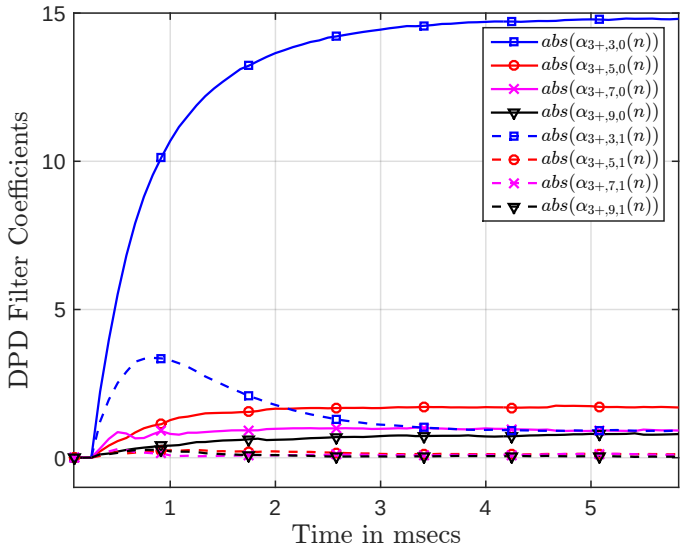

Figure 4.12: Convergence of the ninth-order sub-band DPD coefficients, with memory depth $N = 1$ per basis function, when the positive IM3 sub-band is considered and block-adaptive learning is deployed. An RF measurement example with two 5 MHz LTE-A UL CCs and 40 MHz carrier spacing is used with a real commercial mobile PA operating at +25 dBm.

spur is still slightly above the effective RX noise floor, the sensitivity degradation is substantially smaller despite operating at a maximum PA output power of +25 dBm.

CHAPTER 5

Reduced-complexity Concurrent DPD

In this Chapter, the contributions to concurrent DPD in [P3] are reviewed. The term *concurrent DPD* is used in the literature when concurrently linearizing two or more of the main CCs with the sub-band DPD concept. The term *sub-band*, in this thesis, refers to any main CC or spurious IM band, as explained in Chapter 2. Consequently, the term *sub-band DPD* refers to the general structure where the DPD can linearize any of the sub-bands whether being the main carriers or the spurious IM components. Thus, the concurrent DPD is considered a subset of the sub-band DPD. On the other hand, the term *full-band DPD* refers to the classical DPD concept where the overall aggregated signal is treated as one wideband signal using a single DPD.

The proposed reduced-complexity concurrent DPD solution is compared against state-of-the-art concurrent DPD solutions and shown to have significantly lower complexity despite its excellent linearization performance. It can also be complemented with the IM sub-band DPD in Chapter 4 to provide a more complete DPD solution that can flexibly linearize any sub-band of choice, based on the targeted linearization performance, with reduced-complexity DPD main path processing and learning when compared to state-of-the-art DPD solutions.

This Chapter is organized as follows. Section 5.1 presents the mathematical modeling of the nonlinear distortion produced by a nonlinear PA with memory at and around the main carriers in a dual-carrier CA scenario. Stemming from this modeling, the corresponding main path processing of the proposed concurrent DPD is formulated. Then, Section 5.2 presents the DPD parameter learning solution. Section 5.3 integrates the concurrent DPD in this Chapter with the IM sub-band DPD in Chapter 4 to provide

a more complete DPD solution. A full-band DPD version of the proposed concurrent DPD is then introduced in Section 5.4. Section 5.5 then analyzes the complexity of the concurrent DPD in terms of the number of floating point operations and compares it against state-of-the-art concurrent DPD solutions. Finally, Sections 5.6 and 5.7 report some simulations and RF measurements, evidencing excellent linearization performance in different realistic scenarios.

5.1 Nonlinear Distortion Modeling and Concurrent DPD Main Path Processing

In this Section, the mathematical modeling of the nonlinear distortion produced by a nonlinear PA with memory, at and around the main carriers in a dual-carrier CA scenario, is presented. Stemming from this modeling, the corresponding main path processing of the proposed concurrent DPD is formulated.

5.1.1 Nonlinear Distortion Modeling

For convenience we reintroduce in this Chapter the composite baseband equivalent input and output signals of the P^{th} order Parallel Hammerstein (PH) PA model, with monomial nonlinearities and FIR branch filters, respectively, which read

$$x(n) = x_1(n)e^{j2\pi\frac{f_{IF}}{f_s}n} + x_2(n)e^{-j2\pi\frac{f_{IF}}{f_s}n}, \tag{5.1}$$

$$y(n) = \sum_{\substack{p=1 \\ p \text{ odd}}}^{P} f_{p,n} \star |x(n)|^{p-1}x(n), \tag{5.2}$$

where $x_1(n)$ and $x_2(n)$ are the baseband component carrier signals, f_{IF} refers to half the carrier spacing between the CCs, $f_{p,n}$ denotes the PH branch filter impulse responses of order p, and $\star$ is the convolution operator.

Direct substitution of (5.1) in (5.2) allows extracting the baseband equivalent distortion terms at and around the main CCs, which, through straight-forward manipulations, yield

$$y_{\pm}(n) = \sum_{\substack{p=1 \\ p \text{ odd}}}^{P} f_{\pm,p,n} \star u_{\pm,p}(n), \tag{5.3}$$

where $f_{\pm,p,n}$ denote the baseband equivalent impulse responses corresponding to the wideband PH PA model filters $f_{p,n}$, evaluated around $x_1(n)$ and $x_2(n)$ respectively.

Assuming then a 7^{th} order PA model (i.e., $P = 7$), as a concrete high-order example, the basis functions representing the nonlinear distortion around the first CC $x_1(n)$, for example, read

$$u_{+,1}(n) = x_1(n), \tag{5.4}$$

$$u_{+,3}(n) = x_1(n)|x_1(n)|^2 + 2x_1(n)|x_2(n)|^2, \tag{5.5}$$

$$u_{+,5}(n) = x_1(n)|x_1(n)|^4 + 3x_1(n)|x_2(n)|^4 + 6x_1(n)|x_1(n)|^2|x_2(n)|^2, \tag{5.6}$$

$$u_{+,7}(n) = x_1(n)|x_1(n)|^6 + 4x_1(n)|x_2(n)|^6 + 12x_1(n)|x_1(n)|^4|x_2(n)|^2 + 18x_1(n)|x_1(n)|^2|x_2(n)|^4. \tag{5.7}$$

Similarly, the corresponding basis functions for the second CC $x_2(n)$ (i.e., $u_{-,p}(n)$) can be obtained by interchanging $x_1(n)$ and $x_2(n)$ in the above expressions. Next, the behavioral model in (5.3)-(5.7) is utilized to formulate the proposed injection based concurrent DPD concept, specifically tailored to suppress the distortion at and around the main carriers.

5.1.2 Concurrent DPD Main Path Processing

Since we are mostly concerned about the nonlinear distortion at and around the main carriers, we first rewrite equation (5.3) to separate the linear part from the nonlinear terms as

$$y_{\pm}(n) = f_{\pm,1,n} \star u_{\pm,1}(n) + \sum_{\substack{p=3 \\ p \text{ odd}}}^{P} f_{\pm,p,n} \star u_{\pm,p}(n). \tag{5.8}$$

The key idea of the proposed concurrent DPD concept is to inject a proper additional low-power cancellation signal, with structural similarity to the nonlinear terms in (5.8), into the PA input, such that the level of these nonlinearities at the PA output is reduced. Therefore, an appropriate digital injection signal, to mitigate the nonlinear distortion terms around $x_1(n)$, can be obtained by adopting the SNL basis functions $u_{+,p}(n)$ in (5.5)-(5.7), combined with proper filtering. Similarly, an additional digital injection signal can be applied at the PA input to mitigate the nonlinear distortion around $x_2(n)$ by applying another bank of DPD filters onto the SNL basis functions $u_{-,p}(n)$. This flexibility in operation is an advantage of the proposed DPD principle, since it might not be required in all scenarios to mitigate the distortion around both CCs. For example, the EVM and/or ACLR requirements can be, in general, different between the two CCs, and thus only one of the two CCs might need predistortion.

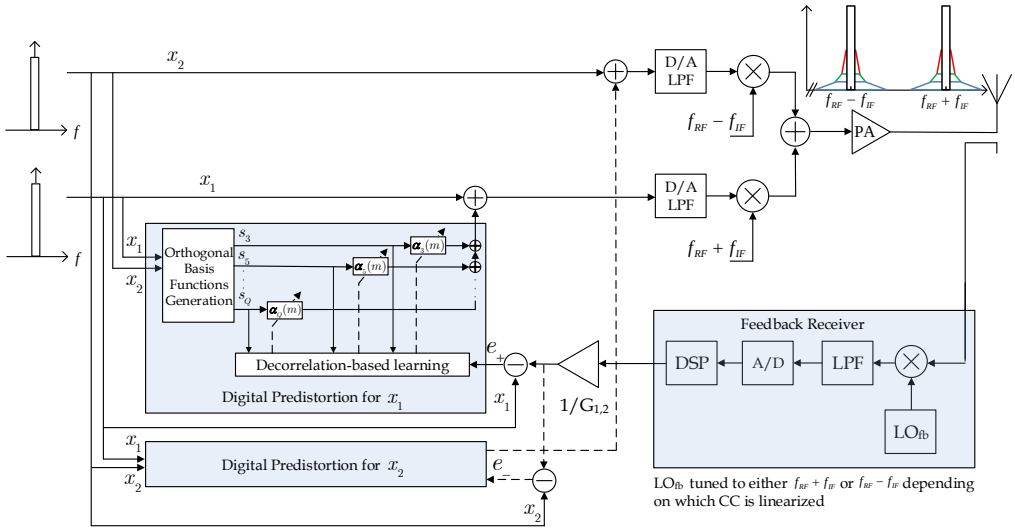

Figure 5.1: Block diagram of the adaptive decorrelation-based concurrent DPD adopting closed-loop learning with a single feedback observation receiver. The PA distortion is observed in a per-CC manner and the DPD coefficients of a given CC are adaptively estimated using the decorrelation-based learning rule.

5.2 Decorrelation-based Concurrent DPD

The decorrelation-based concurrent DPD learning algorithm in [P3] is now shortly reviewed, and the reader is referred to the original article for more details. Based on the nonlinear distortion modeling and the concurrent DPD concept explained in the previous section, a computationally feasible and highly efficient closed-loop DPD estimation algorithm with adaptive filtering was developed in [P3]. The DPD parameter optimization task was formulated as minimizing the correlation between the nonlinear distortion at and around the considered main carrier at the PA output, and the basis functions representing this nonlinear distortion. Those basis functions were also orthogonalized for better numerical properties and stability when used in the adaptive filtering and parameter estimation context [105, 107, 108].

The baseband equivalent nonlinear distortion terms, denoted by $e_{\pm}(n)$ at the PA output around $x_1(n)$ and $x_2(n)$ respectively, can then be calculated as follows

$$e_+(n) = h_{Q,n}^{LPF} \star \{y(n)e^{-j2\pi \frac{f_{IF}}{f_s} n}\}/G_1 - x_1(n) \tag{5.9}$$

$$e_-(n) = h_{Q,n}^{LPF} \star \{y(n)e^{j2\pi \frac{f_{IF}}{f_s} n}\}/G_2 - x_2(n), \tag{5.10}$$

where $h_{Q,n}^{LPF}$ denotes an ideal low pass filter with passband width Q times the bandwidth of the wider component carrier, G_1 and G_2 are the estimated complex linear gains of

the PA at $x_1(n)$ and $x_2(n)$ respectively. Adopting the adaptive filtering notations in a similar manner to Chapter 4, the adaptive filter coefficients in vector form read

$$\boldsymbol{\alpha}_{\pm,q}(n) = [\alpha_{\pm,q,0}(n)\ \alpha_{\pm,q,1}(n)\ ...\ \alpha_{\pm,q,N}(n)]^T, \tag{5.11}$$

$$\bar{\boldsymbol{\alpha}}_{\pm}(n) = [\boldsymbol{\alpha}_{\pm,3}(n)^T\ \boldsymbol{\alpha}_{\pm,5}(n)^T\ ...\ \boldsymbol{\alpha}_{\pm,Q}(n)^T]^T. \tag{5.12}$$

Similarly, the orthogonalized basis function samples in vector form read

$$\mathbf{s}_{\pm,q}(n) = [s_{\pm,q}(n)\ \ s_{\pm,q}(n-1)\ ...\ s_{\pm,q}(n-N)]^T, \tag{5.13}$$

$$\bar{\mathbf{s}}_{\pm}(n) = [\mathbf{s}_{\pm,3}(n)^T\ \ \mathbf{s}_{\pm,5}(n)^T\ \ ...\ \ \mathbf{s}_{\pm,Q}(n)^T]^T. \tag{5.14}$$

The instantaneous sample of the composite baseband equivalent PA input signal $\tilde{x}(n)$ with the concurrent DPD for both CCs now reads

$$\tilde{x}(n) = x(n) + [\bar{\boldsymbol{\alpha}}_{+}(n)^H \bar{\mathbf{s}}_{+}(n)]e^{j2\pi\frac{f_{IF}}{f_s}n} + [\bar{\boldsymbol{\alpha}}_{-}(n)^H \bar{\mathbf{s}}_{-}(n)]e^{-j2\pi\frac{f_{IF}}{f_s}n} \tag{5.15}$$

Then, in order to adaptively update the filter coefficients $\bar{\boldsymbol{\alpha}}_{\pm}(n)$, the main carriers' sub-bands are observed at the PA output with a single feedback receiver, in a sequential manner, and the coefficients are then updated as

$$\bar{\boldsymbol{\alpha}}_{\pm}(n+1) = \bar{\boldsymbol{\alpha}}_{\pm}(n) - \frac{\mu}{||\bar{\mathbf{s}}_{\pm}(n)||^2 + C}\,\bar{\mathbf{s}}_{\pm}(n)e^*_{\pm}(n). \tag{5.16}$$

The overall processing flow is graphically illustrated in Fig. 5.1. Similar to the DPD for spurious emissions mitigation, a block-adaptive version of this decorrelation-based sample-adaptive algorithm was also derived and adopted. The reader is referred to [P3] for more details.

It is worth mentioning that the fact that the learning of the DPD coefficients for the two CCs is done sequentially, can in principle cause, in particular if the PA is very deep in saturation, some inter-dependence between the optimal coefficients of the DPD stages of CC1 and CC2. Specifically, in very deep saturation, and assuming that the DPD coefficients of CC1 are learned first, then activating the DPD unit of CC2 may cause slight degradation of the linearization of CC1. We hypothesize that then iterating shortly the learning between the CCs can reduce this mutual effect while reaching an improved linearization performance for the CCs. On the other hand, this may require somewhat more learning samples in the overall learning procedure. It is also possible to perform the learning for the two CCs in parallel, instead of sequentially, while still using only a single narrowband observation receiver. However, this will require storing the PA observation samples and basis function samples of one of the two CCs in memory in order to allow learning the DPD coefficients for CC1 and CC2 simultaneously. Such

methods can be an interesting topic for future work. Another interesting point for future work is extending the proposed concurrent DPD to support transmitting more than two component carriers. The decorrelation-based learning, as such, can support any number of bands or CCs, but the basis functions for scenarios with more than two CCs will be different [123].

5.3 Complete Sub-band DPD Solution

An extended decorrelation-based sub-band DPD solution was presented in [P3] which complements the DPD for spurious emissions mitigation in [P2] with the concurrent DPD discussed earlier in this Chapter. This sub-band DPD has the capability to tune its linearization to whichever sub-band needs linearization, using the decorrelation-based learning rule and a single feedback receiver operating at the lower sample rate. The idea, as also explained earlier, is to minimize the correlation between the nonlinear distortion at the main CCs, and/or at the IM3, IM5, etc., sub-bands, and specific low-rate baseband basis functions representing the nonlinearity at each corresponding sub-band, defined earlier in (5.5)-(5.7) and in (4.6)-(4.11).

The instantaneous sample of the composite baseband equivalent PA input signal $\tilde{x}(n)$ with the complete sub-band DPD adopted now reads

$$\begin{aligned}\tilde{x}(n) = x(n) &+ [\bar{\boldsymbol{\alpha}}_{+}(n)^H \bar{\mathbf{s}}_{+}(n)] e^{j2\pi \frac{f_{IF}}{f_s} n} + [\bar{\boldsymbol{\alpha}}_{-}(n)^H \bar{\mathbf{s}}_{-}(n)] e^{-j2\pi \frac{f_{IF}}{f_s} n} \\ &+ \sum_{\substack{b=3 \\ b \text{ odd}}}^{B} \Big[[\bar{\boldsymbol{\alpha}}_{b+}(n)^H \bar{\mathbf{s}}_{b+}(n)] e^{j2\pi \frac{b f_{IF}}{f_s} n} + [\bar{\boldsymbol{\alpha}}_{b-}(n)^H \bar{\mathbf{s}}_{b-}(n)] e^{-j2\pi \frac{b f_{IF}}{f_s} n} \Big], \end{aligned} \tag{5.17}$$

where $b = 3, 5, ..., B$ is the sub-band index (i.e., $b = 3$ for the IM3 sub-bands, $b = 5$ for the IM5 sub-bands, etc.), and $\bar{\boldsymbol{\alpha}}_{b\pm}(n)$ and $\bar{\mathbf{s}}_{b\pm}(n)$ are defined as in (4.13) and (4.15) using the orthogonalized basis function samples corresponding to the b^{th} sub-band.

Adopting the block-adaptive DPD learning notations as in [P3], the orthogonalized basis function blocks of M samples, used for DPD learning, in matrix form then read

$$\mathbf{s}_{b\pm,q}(n_m) = [s_{b\pm,q}(n_m)\ s_{b\pm,q}(n_m - 1) \ldots s_{b\pm,q}(n_m - N)], \tag{5.18}$$

$$\mathbf{S}_{b\pm,q}(m) = [\mathbf{s}_{b\pm,q}(n_m)^T\ \mathbf{s}_{b\pm,q}(n_m + 1)^T \ldots \mathbf{s}_{b\pm,q}(n_m + M - 1)^T]^T, \tag{5.19}$$

$$\mathbf{S}_{b\pm}(m) = [\mathbf{S}_{b\pm,b}(m)\ \mathbf{S}_{b\pm,b+2}(m) \ldots \mathbf{S}_{b\pm,Q}(m)]^T, \tag{5.20}$$

where n_m denotes the index of the first sample of block m, and $Q \geq B$. For the main carriers' sub-bands, i.e., $b = 1$, the linear basis functions are not included in the DPD learning or filtering, only the nonlinear basis functions are used.

The block-adaptive decorrelation-based DPD coefficient update for the b^{th} sub-band then reads

$$\bar{\boldsymbol{\alpha}}_{b\pm}(m+1) = \bar{\boldsymbol{\alpha}}_{b\pm}(m) - \mu\, \mathbf{S}_{b\pm}(m)\mathbf{e}^*_{b\pm}(m), \tag{5.21}$$

where $\mathbf{e}^*_{b\pm}(m)$ refers to the element-wise conjugated error signal block of M samples at the b^{th} sub-band. For $b = 1$, $e_{\pm}(n)$ are defined in (5.9) and (5.10), while for the IM sub-bands $b = 3, 5, ..., B$, $e_{b\pm}(n)$ denotes the baseband equivalents of the PA output at the b^{th} sub-bands, with the corresponding sub-band DPDs included adopting the current coefficients, $\bar{\boldsymbol{\alpha}}_{b\pm}(n)$.

Thus, as we can see from (5.21), the DPD learning for all the sub-bands including the main carriers is using the simple decorrelation principle. Since the learning is done one sub-band at a time, one and the same computing engine or correlator can be reused in the actual hardware implementation for the different sub-bands, thus providing a very simple, cost-effective, and high performance solution, which was also demonstrated through comprehensive simulations and RF measurements in [P2] and [P3].

5.4 Decorrelation-based Full-band DPD

The decorrelation-based DPD learning algorithm described earlier can be used in the more classical single carrier/band transmission scenarios as well. In these scenarios, $x_1(n)$ becomes the main/only carrier of interest while $x_2(n)$ can simply be set to zero in (5.5)-(5.7). The decorrelation-based learning can then minimize the correlation between these single carrier -based basis functions and the nonlinear distortion around the main carrier $x_1(n)$ using the same learning rule as explained earlier, while setting $f_{IF} = 0$. This single carrier mode of operation can also be used when the carrier spacing between the two CCs gets narrower, by interpreting the composite baseband signal as one arbitrary baseband waveform centered at zero frequency. This approach naturally assumes that the sample rate for processing the composite signal as a whole is still feasible, implying then also that all sub-bands are processed and linearized simultaneously.

5.5 Complexity Analysis and Comparison against State-of-the-art

In this Section, a quantitative comparison between the complexities of the single feedback concurrent DPD in this work, and the existing state-of-the-art single feedback concurrent DPDs in [85, 89, 127] is presented. The complexities of the classical full-band DPD and the dual feedback concurrent DPD, as in [24], are also presented for reference. The

Table 5.1: DPD main path processing computational complexity comparison. The oversampling factor $R = Q$ without filtered basis functions, and $R < Q$ with filtered basis functions.

	BF generation (FLOP/sample)	BF extra filtering if $R < Q$ (FLOP/sample)	DPD main path processing (FLOP/sample)	Minimum processing sample rate (MSPS)
1-Full-band ILA DPD	$Q+2$	$\sum_{q=3}^{Q}[4N_b+2]R/q$	$(Q+1)(4N+3)$	$R(W_1+W_2+\Delta f)$
2-Concurrent DPD 1 in [24]	$6+4\sum_{q=3}^{Q} q$	$2\sum_{q=3}^{Q}[4N_b+2]R/q$	$2(Q+1)(4N+3)$	$R \times max(W_1, W_2)$
3-Concurrent DPD 2 in [85, 89]	$6+4\sum_{q=3}^{Q} q$	$2\sum_{q=3}^{Q}[4N_b+2]R/q$	$2(Q+1)(4N+3)$	$R \times max(W_1, W_2)$
4-Concurrent DPD 3 in [127]	$Q+2$	$2\sum_{q=3}^{Q}[4N_b+2]R/q$	$(Q+1)(4N+3)$ $+2(5N_s+6)$	$R(W_1+W_2)$
5-Concurrent DPD in this work	$6+4\sum_{q=3}^{Q} q$	$2\sum_{q=3}^{Q}[4N_b+2]R/q$	$2(Q-1)(4N+3)$	$R \times max(W_1, W_2)$

Table 5.2: DPD learning complexity comparison.

	PA estimation (FLOP/M samples)	BF generation (FLOP/KM samples)	DPD estimation (FLOP/KM samples)
1-Full-band ILA DPD	0	$KM[Q+2]$	$4K[(M+(Q+1)(N+1)/6)$ $\times(Q+1)^2(N+1)^2/4]$
2-Concurrent DPD 1 in [24]	0	$KM[6+4\sum_{q=3}^{Q} q]$	$4K[(M+(Q+1)(N+1)/3)$ $\times(Q+1)^2(N+1)^2]$
3-Concurrent DPD 2 in [85, 89]	$4[(M+(Q+1)(N+1)/3)$ $\times(Q+1)^2(N+1)^2]+$ $8M(Q+1)(N+1)-2M$	$KM[6+4\sum_{q=3}^{Q} q]$	$4K[(M+(Q+1)(N+1)/3)$ $\times(Q+1)^2(N+1)^2]$
4-Concurrent DPD 3 in [127]	$4[(M+(Q+1)(N+1)/6)$ $\times(Q+1)^2(N+1)^2/4]+$ $4M(Q+1)(N+1)-2M$	$KM[Q+2]$	$4K[(M+(Q+1)(N+1)/6)$ $\times(Q+1)^2(N+1)^2/4]$
5-Concurrent DPD in this work	$16M-4$	0	$4K[(2M+1)(Q-1)(N+1)$ $-M]$

number of FLOP is the main quantification metric used in this analysis. Both the DPD main path processing complexity and the learning complexity are included in the complexity comparisons, as shown in Tables 5.1 and 5.2, respectively. Moreover, in order to ensure a fair comparison among the considered DPD methods, a set of practical and reasonable assumptions were made, and the reader is referred to [P3] for more details regarding these assumptions.

The notations used in the complexity analysis are consistent with the notations throughout the thesis, along with some additional symbols that are all summarized here: Q denotes the DPD nonlinearity order; N denotes the DPD filter memory order, where it is assumed that each q^{th} order DPD filter $\alpha_{\pm,q,l}$ has $N+1$ memory taps, for simplicity; M denotes the estimation block size in both the block-adaptive filtering used in this work, as well as the block LS estimation; K denotes the number of block-adaptive

iterations in this work, as well as the number of ILA iterations in ILA-based DPD learning; W_1, W_2, denote the bandwidths of the first and second CCs respectively, while the carrier spacing is denoted with Δf; Finally, N_s denotes the memory depth of the filters used in [127] for carrier separation and relocation before transmitting each CC on separate TX chains. These filters are assumed to be FIR filters with symmetrical coefficients.

In case of applying additional filtering to the basis functions (BFs) to reduce the DPD processing sample rate, the symbol R denotes the amount of oversampling applied in the basis functions generation compared to the original CC bandwidths W_1 and W_2. In the normal scenario without filtered BFs, this oversampling factor $R = Q$, otherwise $R < Q$. N_b denotes the memory depth of the BF band-limitation filter used for filtering the basis functions, which is assumed to be a computationally efficient polyphase FIR decimation filter [101].

The main findings of the complexity comparison in Tables 5.1 and 5.2 can be summarized as follows. Regarding the DPD main path processing, the concurrent DPD developed in this work has lower complexity than any of the other considered techniques because it does not require processing the linear basis function, as opposed to the other methods. The reason for not including the linear term is that the primary objective of the DPD is to mitigate the nonlinear distortion only, while the linear distortion can be considered part of the overall communications channel, which is always equalized at the receiver side. Meanwhile, the concurrent DPD solutions in [24,85,89,127] utilize the ILA-based learning concept, which requires using the linear term for a correct post-inverse estimation. Moreover, when comparing to the single feedback concurrent DPD in [127], the concurrent DPD in this work has significantly lower main path complexity, despite having greater basis function generation complexity. This is because in [127], a single DPD is used for both CCs, resulting in a higher DPD sample rate. Additionally, two carrier separation and relocation filters are required in [127] to transmit the aggregated carriers on separate TX chains, thus adding to the overall DPD running complexity.

Regarding the DPD learning complexity, a direct PA model estimation is required in [85, 89, 127] which significantly adds to the DPD learning complexity. On the other hand, in this work only the linear gain of the PA is required, implying substantially lower complexity. Moreover, in this work, the same basis function samples used in the DPD main path processing can be reused in the decorrelation-based DPD learning, as illustrated in Fig. 5.1. This is not possible in the other DPD solutions due to the nature of the ILA-based learning which requires a post-inverse estimation whose basis functions are generated from the PA output samples.

Concrete numerical examples of the overall main path processing complexity, in terms of FLOP per second, as well as the learning complexity in terms of FLOP per

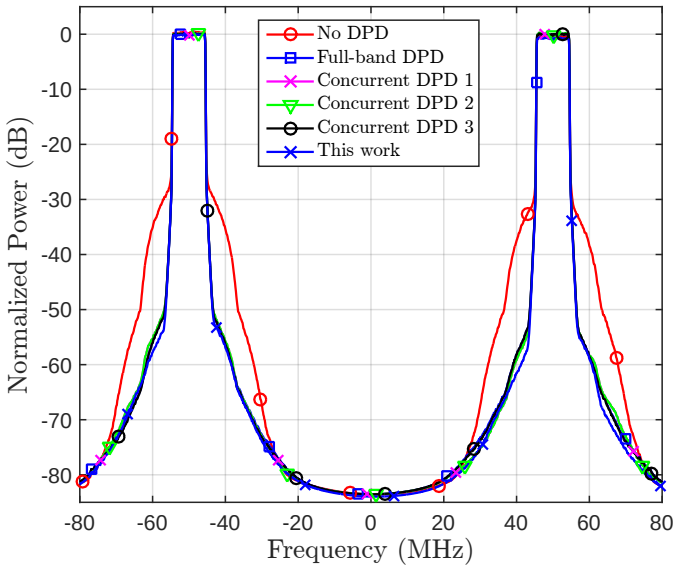

Figure 5.2: Normalized PA output spectra of a concurrent noncontiguous intraband CA transmitter with two 10 MHz OFDM carriers with 100 MHz spacing, and 16-QAM subcarrier modulation. The peak-to-average power ratio (PAPR) is 12.5 dB. A ninth-order PH model is used. The PA parameters have been identified using RF measurements with a true mobile PA transmitting at +22 dBm.

learning procedure, will be provided in Section 5.6, together with the corresponding linearization performance results.

5.6 Simulation Results

In this Section, the linearization performance and complexity of the concurrent DPD in this work is compared against state-of-the-art concurrent DPD methods using practical carrier aggregation-based simulation studies. The PA model used in the simulations is a ninth-order parallel Hammerstein model, with four memory taps per branch, and the parameters have been identified using measurements with a true mobile PA. Both the in-band waveform purity and the adjacent channel leakage due to spectral regrowth are quantified using the well-known EVM and ACLR metrics [8, 42].

In the considered CA example, two 10 MHz OFDM CCs are transmitted with 100 MHz CC spacing, as shown in Fig. 5.2. The PA model used is a ninth-order PH model whose parameters have been identified using RF measurements with a true mobile PA transmitting at +22 dBm. This mobile PA has 29 dB gain, and +31 dBm 1-dB

Table 5.3: Complexity and performance comparison with state-of-the-art concurrent DPD methods

	DPD main path processing and learning complexities				**DPD performance of CC1**	
	Main path processing (GFLOP/s)	Overall learning (MFLOP)	DPD sample rate (MSPS)	Number of estimation samples	EVM (%)	ACLR L / R (dBc)
Without DPD	0	0	N/A	N/A	4.0063	35.5208 / 36.1878
1-Full-band ILA DPD	238.59	108.6	990	30k	0.5162	53.9113 / 51.8576
2-Concurrent DPD 1 in [24]	28.98	114	90	30k (per CC)	0.5315	53.4451 / 51.5275
3-Concurrent DPD 2 in [85, 89]	28.98	152.4	90	40k (per CC)	0.5311	53.4453 / 51.5273
4-Concurrent DPD 3 in [127]	113.94	146.4	180	40k (per CC)	0.5163	53.0010 / 51.5543
5-Concurrent DPD in this work	25.02	18.96	90	100k (per CC)	0.5250	53.8733 / 51.6361

compression point. The adopted parametrizations of the different DPD solutions are as follows: The estimation block size $M = 10k$ samples, and the DPD nonlinearity order $Q = 9$ in all the considered DPD methods. The number of block-adaptive iterations $K = 10$ in the concurrent DPD in this work, while the number of ILA iterations $K = 3$ in all the other considered DPD methods. In [24, 85, 89] and in this work, the DPD memory order $N = 2$ per CC. Meanwhile, in [127] and in the full-band DPD the two CCs are predistorted with a single DPD, and thus a higher DPD memory order $N = 5$ is used. No filtering of the basis functions is performed in this comparison (i.e., $N_b = 0$). Additionally, in [127], $N_s = 50$.

The linearization performance is more or less the same in all the considered DPD methods, as demonstrated in Fig. 5.2 and in Table 5.3. However, the complexity is clearly in favor of the concurrent DPD solution in this work, showing a notable advantage in both the DPD main path processing complexity and learning complexity. The main path complexity is measured in GFLOP per second (GFLOP/s), while the learning complexity is measured in terms of the overall number of FLOP used in the learning process.

5.7 RF Measurement Results

In this Section, RF measurements using three commercially available power amplifiers are presented to demonstrate the effectiveness of the proposed concurrent DPD solution in real RF environments. The first PA is an LTE-A band 1 base station (BS) PA, and the second is a general purpose wideband PA, suitable for interband CA. The third PA is

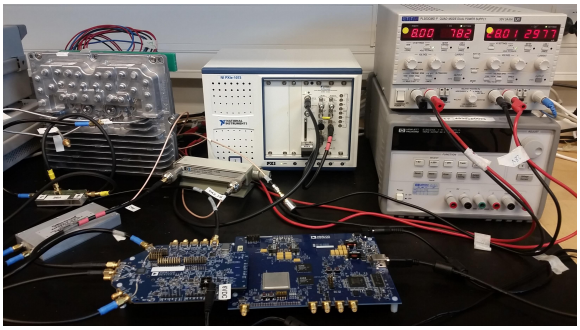

(a) Photo of the RF measurement setup

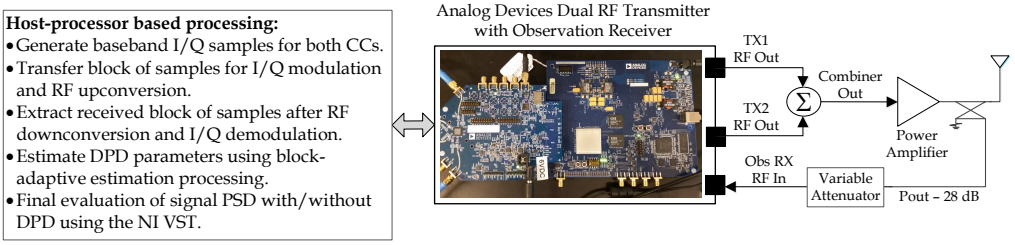

(b) Block diagram of the RF measurement setup

Figure 5.3: Hardware setup used in the RF measurements for testing and evaluating the proposed decorrelation-based concurrent DPD.

an LTE-A band 25 user equipment (UE) PA. In addition to quantifying the performance of the proposed decorrelation-based DPD solution, other state-of-the-art DPD methods, which are based on the ILA principle for learning, are also implemented for reference. A photo of the RF measurement setup is shown in Fig. 5.3(a).

5.7.1 RF Measurement Setup

The Analog Devices AD9368-2 evaluation board used in the RF measurements has two RF transmitters, each with 250 MHz instantaneous bandwidth, that are used for implementing CA transmission scenarios. The board is also equipped with an observation receiver, with 200 MHz instantaneous bandwidth, which is used as the DPD feedback receiver, as shown in Fig 5.3(b). The I/Q samples are first generated locally on the host processor, and then transferred to the evaluation board to perform RF I/Q modulation at the desired power level at the PA input. In the noncontiguous CA scenarios, the RF outputs of the two TX chains are combined using an RF combiner, and then connected to the input port of the external power amplifier. The PA output is then attenuated

and fed into the observation receiver input. The observation receiver performs RF I/Q demodulation to bring the signal back to baseband, which is then used for the DPD learning.

In the RF measurements, the following DPD parameters are used: the estimation block size $M = 10k$ samples, and the DPD nonlinearity order $Q = 9$ in all the considered DPD methods. The number of block-adaptive iterations $K = 10$ in the proposed DPD solution, while the number of ILA iterations is $K = 3$ in all the other considered ILA-based reference DPD methods. In [24, 85, 89] and in the proposed DPD, the DPD memory order $N = 1$ per CC. In case a full-band DPD is used to linearize the two aggregated CCs, the DPD memory order $N = 3$.

5.7.2 Base Station Measurement Examples

In this subsection, three different LTE-A RF measurement scenarios are demonstrated: a contiguous intraband CA scenario, a noncontiguous intraband CA scenario, and a noncontiguous interband CA scenario. A commercial LTE-A Band 1 (2110-2170 MHz) BS PA is used in the first two scenarios. The freescale BS PA (model no. MD7IC2250GN) is a Doherty PA with 31 dB gain, and +47 dBm 1-dB compression point. A driver amplifier is used before the Doherty PA with 14 dB gain and +25 dBm 1-dB compression point. In the third interband CA scenario, a general-purpose wideband PA (model no. ZHL-4240) with 40 dB gain, and +28 dBm 1-dB compression point is used.

Contiguous Intraband CA Scenario

In this LTE-A Band 1 contiguous intraband CA scenario, two adjacent 20 MHz CCs are transmitted. The two CCs are interpreted as one CC (i.e, CC1), which is transmitted via one RF transmit chain of the evaluation board. The classical ILA-based DPD is also implemented for reference, and compared to the decorrelation-based DPD in this work in Fig. 5.4. Table 5.4 shows the corresponding ACLR and EVM results. The proposed DPD solution and the existing ILA-based DPD are shown to provide very similar performance, despite the complexity reduction achieved from using the proposed solution.

Noncontiguous Intraband CA Scenario

In this LTE-A Band 1 noncontiguous intraband CA scenario, two 10 MHz CCs are transmitted with 30 MHz CC spacing. An RF combiner combines the RF signals of the two CCs which are transmitted via separate RF TX chains of the evaluation board, as also illustrated in Fig. 5.3. The DPD learning is done sequentially where 30 MHz observation BW is used per CC. Iterative clipping and filtering -based PAPR reduction

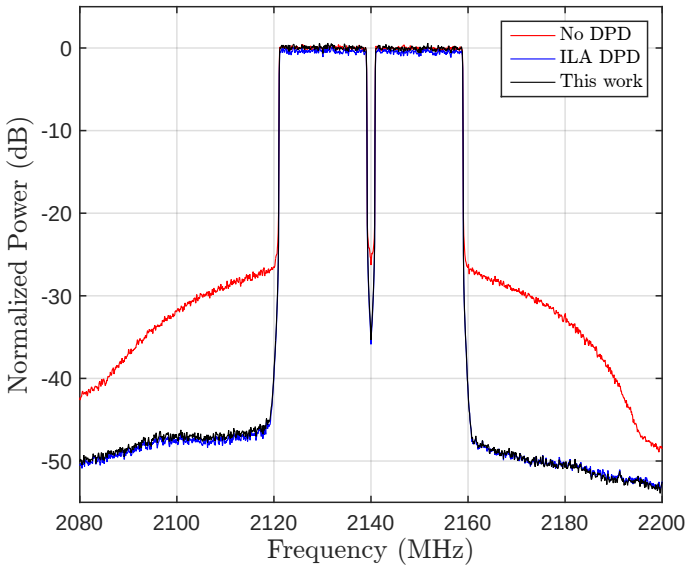

Figure 5.4: An RF measurement example at LTE DL Band 1 (2110-2170 MHz) showing the normalized PA output spectra of a contiguous intraband CA transmitter with two 20 MHz OFDM carriers. 16-QAM subcarrier modulation is used per CC. Spectral regrowth and EVM are reduced when using the proposed decorrelation-based DPD with a real commercial base station PA operating at +36 dBm output power.

Table 5.4: BS RF Measurement Scenarios and Obtained Results

Scenario	DPD Type	EVM [%]	ACLR L / R of CC1 (dBc)	ACLR L / R of CC2 (dBc)	TX Power (dBm)	PAPR (dB)
Cont. Intraband CA	No DPD	5.65	30.89 / 31.56	N/A	+36	8.8
	ILA DPD	1.97	46.87 / 49.66	N/A	+36	8.8
	This work	2.04	46.95 / 50.12	N/A	+36	8.8
Noncont. Intraband CA	No DPD	5.54	36.60 / 36.63	36.41 / 36.36	+34	9.87
	ILA DPD	1.85	49.85 / 48.72	49.99 / 49.85	+34	9.87
	This work	1.93	49.89 / 49.33	49.98 / 49.87	+34	9.87
Noncont. Interband CA	No DPD	3.92	35.47 / 36.08	36.36 / 35.95	+23	9.94
	Conc. DPD 1	1.24	48.05 / 48.10	48.16 / 48.12	+22	9.94
	Conc. DPD 2	1.25	48.05 / 48.09	48.15 / 48.12	+22	9.94
	This work	1.28	50.07 / 49.95	49.13 / 49.08	+23	9.94

is applied to each CC separately in this scenario. The classical full-band ILA-based DPD is also implemented for reference, with block LS based parameter learning per ILA iteration, and compared to the proposed concurrent DPD in Fig. 5.5. Table 5.4 shows the corresponding ACLR and EVM results. The linearization performance numbers are

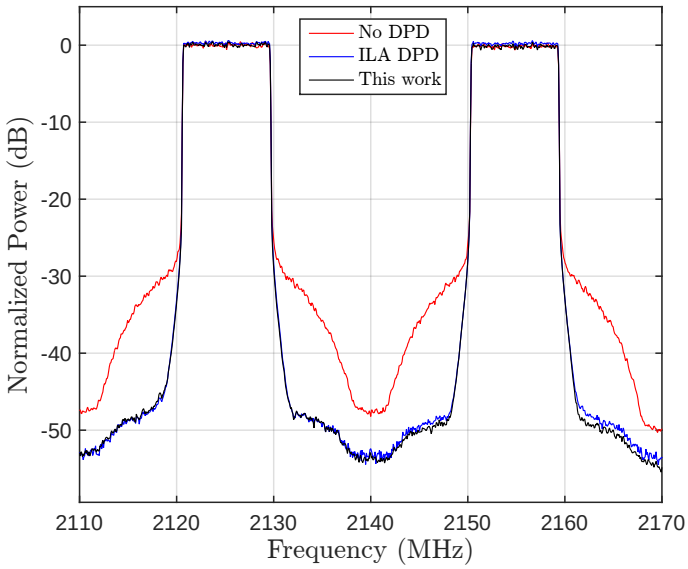

Figure 5.5: An RF measurement example at LTE DL Band 1 (2110-2170 MHz) showing the normalized PA output spectra of a concurrent noncontiguous intraband CA transmitter with two 10 MHz OFDM carriers. The CC spacing is 30 MHz, and 16-QAM subcarrier modulation is used. Spectral regrowth and EVM are reduced when using the proposed decorrelation-based concurrent DPD with a real commercial base station PA operating at +34 dBm output power.

again very similar despite the proposed concurrent DPD being significantly less complex than the full-band ILA-based DPD.

Noncontiguous Interband CA Scenario

In this LTE-A noncontiguous interband CA scenario, the two aggregated CCs are located at Band 2 (1930-1990 MHz), and Band 4 (2110-2155 MHz) respectively, which is a practical DL LTE-A interband CA scenario [6]. Iterative clipping and filtering -based PAPR reduction is again applied to each CC separately. The performance of the single feedback concurrent DPD in this work is compared against two different concurrent DPD techniques: the classical concurrent DPD reported in [24] with two feedback receivers, and the single feedback concurrent DPD developed in [85, 89].

The normalized PA output spectra without DPD and with the three considered concurrent DPD techniques are shown in Fig. 5.6. An extra 1 dB backoff is applied in the concurrent DPDs in [24, 85, 89] for proper operation, however, this is not required for the concurrent DPD in this work because it does not use the ILA principle for learning. The results in Fig. 5.6 and Table 5.4 again demonstrate very good linearization

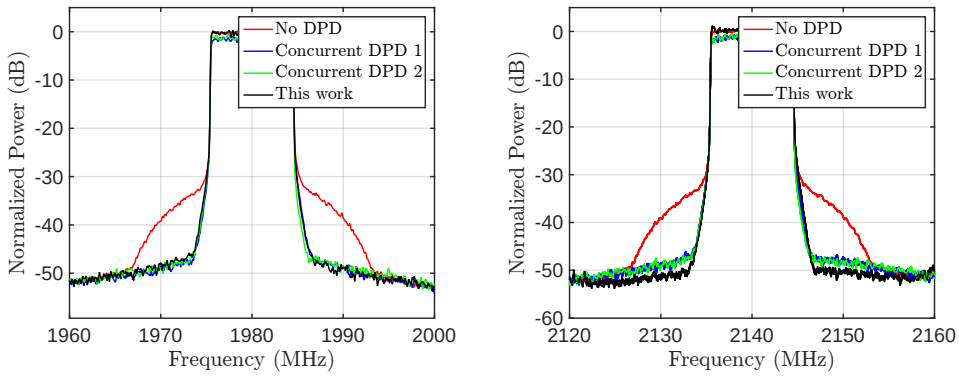

Figure 5.6: A practical LTE-A DL interband CA RF measurement example showing the normalized PA output spectra with and without DPD using a real commercial wideband PA operating at +23 dBm output power. The OFDM CCs are 10 MHz each and transmitted at LTE-A DL bands 2 (1930-1990 MHz) and 4 (2110-2155 MHz) respectively, with 160 MHz CC spacing. 16-QAM subcarrier modulation is used per CC. Spectral regrowth and EVM are reduced when using the proposed decorrelation-based concurrent DPD, which slightly outperforms the concurrent DPDs in [24, 85, 89].

performance of the concurrent DPD in this work, which is even slightly better than the other concurrent DPDs despite its reduced complexity, as explained in Section 5.5.

5.7.3 UE Measurement Example

An LTE-A UE RF measurement scenario demonstrating the flexibility of the proposed DPD is presented next. The LTE-A UL Band 25 (1850-1915 MHz) power amplifier adopted in this measurement example has 29 dB gain, and +31 dBm 1-dB compression point. In this scenario, the spur at the negative IM3 sub-band is emitted within the TX band and is thus not suppressed by the TX/antenna filter. On the other hand, the spur at the positive IM3 sub-band is emitted outside the TX band and can thus be filtered out by the TX filter. The two SC-FDMA component carriers in this example have 10 MHz and 5 MHz bandwidths, respectively. The 10 MHz CC uses QPSK data modulation, while the 5 MHz CC uses 64QAM data modulation, and is thus much more sensitive to EVM degradation. The DPD is therefore deliberately configured, in this example, to linearize only the 5 MHz component carrier (i.e., CC2) and the negative IM3 sub-band to demonstrate the great processing and linearization flexibility, as shown in Fig. 5.7. The DPD learning is done sequentially for CC2 and for the negative IM3 sub-band, where 25 MHz observation BW is used per sub-band. Table 5.5 shows the

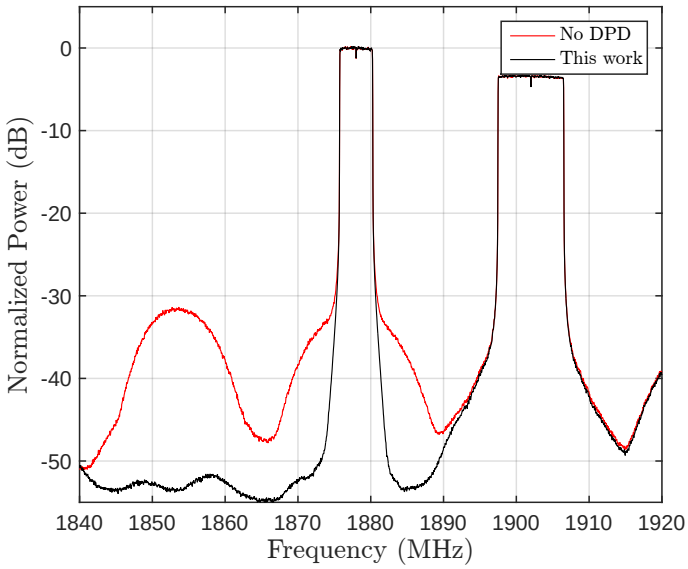

Figure 5.7: An RF measurement example at LTE UL band 25 showing the normalized PA output spectra of a concurrent noncontiguous intraband CA transmitter with 10 MHz and 5 MHz SC-FDMA CCs, using QPSK and 64-QAM data modulation, respectively. Nonlinear distortion at and around the 5 MHz CC as well as at the IM3- sub-band are reduced when using the proposed DPD with a commercial mobile PA operating at +24 dBm output power.

Table 5.5: UE RF Measurement Scenario and Obtained Results

TX Power = +24 dBm	DPD Type	CC2 EVM (%)	CC2 ACLR L / R (dBc)	Negative IM3R (dBc)	PAPR (dB)
Noncontiguous Intraband	No DPD	3.68	33.43 / 33.95	32.04	8.18
CA Scenario	This work	0.73	50.26 / 50.47	53.21	8.18

ACLR, EVM and IM3 spur suppression results in this scenario, evidencing again very high-performance linearization. Notice that the IM spur at the negative IM3 sub-band is suppressed by more than 20 dB through the DPD processing.

CHAPTER 6

Frequency-optimized DPD

In this Chapter, the contributions to frequency-optimized DPD in [P4] are reviewed. A novel approach for reducing the full-band DPD complexity was introduced in [P4] which is different from the sub-band DPD approach in Chapters 4 and 5. Conventional full-band DPD methods typically seek to linearize the entire transmit spectrum, without specifically tailoring the linearization capabilities to any particular regions of the spectrum. On the other hand, the frequency-optimized DPD method optimizes the suppression of unwanted emissions around arbitrary pre-specified frequencies at the PA output. Thus, the DPD is capable of providing better performance at the more critical spectral regions (e.g., own RX band) while using the same running complexity as the classical DPD, or in other words, achieving the same performance at those critical regions with a lower complexity DPD (i.e., lower nonlinearity order and/or memory depth).

This Chapter is organized as follows. Section 6.1 summarizes the mathematical formulation of the problem along with the corresponding main path processing of the proposed frequency-optimized DPD. Then, Section 6.2 presents the actual DPD parameter learning and optimization utilizing the Newton-Raphson algorithm. Section 6.3 then analyzes the complexity of the DPD solution in terms of the number of floating point operations (FLOP), including both the DPD main path processing complexity and the DPD parameter estimation and optimization complexity. Finally, Sections 6.4 and 6.5 report some simulations and RF measurements, evidencing excellent linearization performance when using the proposed frequency-optimized DPD solution in both contiguous and noncontiguous carrier allocation scenarios.

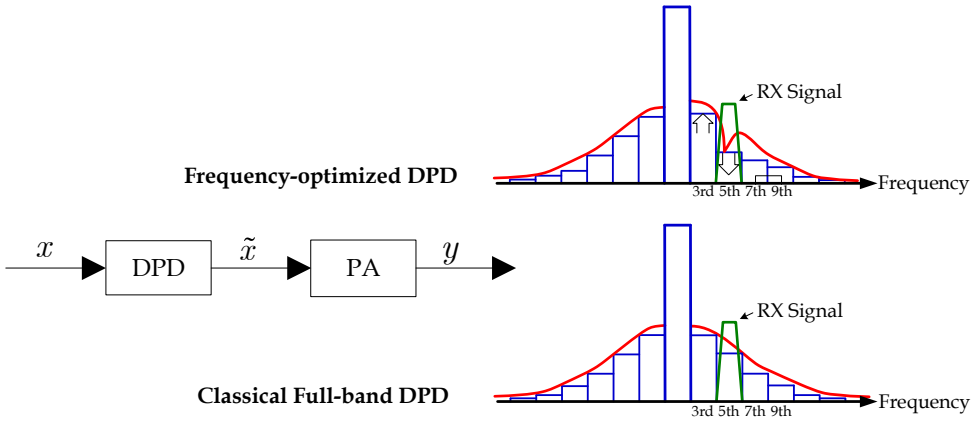

Figure 6.1: DPD and PA input and output signals along with a high level description of the frequency-optimized DPD concept.

6.1 Mathematical Formulation and DPD Main Path Processing

Assuming a P^{th}-order PH PA model, and a Q^{th}-order memoryless polynomial DPD, the composite baseband equivalent input and output signals of the two cascaded modules shown in Fig. 6.1 read

$$\tilde{x}(n) = \sum_{\substack{q=1 \\ q \text{ odd}}}^{Q} \alpha_q |x(n)|^{q-1} x(n), \tag{6.1}$$

$$y(n) = \sum_{\substack{p=1 \\ p \text{ odd}}}^{P} f_{p,n} \star |\tilde{x}(n)|^{p-1} \tilde{x}(n), \tag{6.2}$$

where $x(n)$, $\tilde{x}(n)$, and $y(n)$ are the baseband equivalents of the DPD input, DPD output and PA output respectively, α_q is the memoryless polynomial DPD coefficient of order q, $f_{p,n}$ denotes the PH branch filter impulse response of order p, and $\star$ is the convolution operator. In [P4] it was shown that the cascaded response of the DPD and PA can be written as

$$y(n) = \sum_{\substack{r=1 \\ r \text{ odd}}}^{R} c_{r,n} \star |x(n)|^{r-1} x(n), \tag{6.3}$$

where $R = (P+1)(Q+1) - 1$, and the filters (impulse responses) $c_{r,n}$ consist of the PA model filters $f_{p,n}$ and the DPD coefficients α_q. A truncated version of $y(n)$, namely

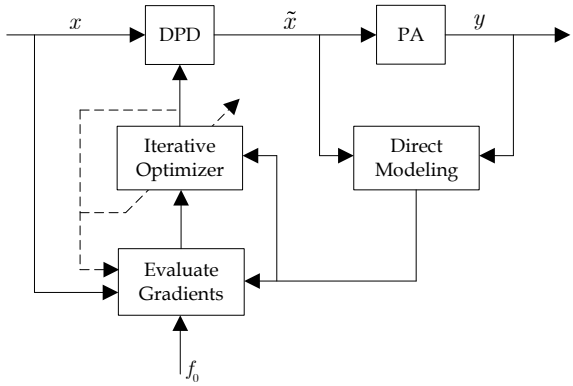

Figure 6.2: The proposed overall block-diagram of the predistortion processing including direct PA modeling/learning, evaluation of PSD derivatives and carrying out iterative DPD parameter optimization.

$y_{tr}(n)$, was used in [P4] in order to reduce the complexity. The effective nonlinear basis functions of $y_{tr}(n)$ were selected from the original ones ($|x(n)|^{r-1}x(n)$) based on which particular band of frequencies was optimized, and based on the most relevant terms (e.g., ignoring the significantly higher order terms).

Invoking the Wiener-Khinchin theorem [37], which states that the autocorrelation function, $R(\tau)$, and the PSD, $S(f)$, form a Fourier transform pair, the PSD of the PA output signal $y(n)$ in (6.3) can be evaluated as shown in [P4]. The suppression of the unwanted emission power at a certain frequency, say $f = f_0$, can be achieved by properly manipulating and optimizing the coefficients $c_{r,n}$ to minimize the PSD evaluated at $f = f_0$. Assuming a known or already estimated PA model coefficients $f_{p,n}$, as well as knowledge of the spectral characteristics of the DPD input signal $x(n)$, this is equivalent to optimizing the DPD coefficients α_q accordingly, and hence the name frequency-optimized DPD. This will be elaborated further in the next section, where the frequency-optimized DPD learning algorithm is shortly reviewed, and the reader is referred to [P4] for more details.

6.2 DPD Learning and Parameter Optimization

The aim of the DPD learning and parameter optimization in [P4], as explained earlier, was to minimize the PSD of the PA output signal around the pre-specified frequency f_0. The first stage in this process is the PA direct modeling in which a memoryless or PH direct-model is extracted from the PA. This model is used, along with the signal statistics of the DPD input signal $x(n)$, to evaluate the PSD at the target frequency as a function of the DPD coefficients, namely $S_{tr}(f = f_0, \boldsymbol{\alpha})$ or simply $S_{tr}(\boldsymbol{\alpha})$, where

$\boldsymbol{\alpha} = [\alpha_1\ \alpha_3\ ...\ \alpha_Q]^T$. The subscript in the PSD $S_{tr}(\boldsymbol{\alpha})$ refers to using the truncated version of the PA output signal $y(n)$ in (6.3), as shown in [P4]. The estimated PA model is also used to extract an initial estimate of the DPD coefficients $\boldsymbol{\alpha}$, after which additional iterative processing at digital baseband is applied to optimize those coefficients for unwanted emission suppression at the target frequency f_0. A block-diagram of the overall processing stages is illustrated in Fig. 6.2. For presentation purposes, the actual DAC and ADC as well as up- and down-conversion stages are not shown in order to focus on the fundamental elements of the transceiver system from a DPD processing perspective.

The final step is to optimize the parameter vector $\boldsymbol{\alpha}$ of the predistorter in order to find $min(S_{tr}(\boldsymbol{\alpha}))$. This is a general optimization problem that aims to seek values for certain design or control variables in order to minimize an objective function. In [P4], the *Newton-Raphson* method was employed due to its fast and reliable performance compared to the gradient decent algorithms [27]. The Newton-Raphson algorithm seeks the minimum of a function $F(\alpha)$ using both first and second derivatives [22, 27].

In its simplest form, with a single variable α to be optimized, and assuming $F(\alpha)$ holomorphic, it can be described as

$$\alpha(n+1) = \alpha(n) - \frac{F'(\alpha(n))}{F''(\alpha(n))}, \tag{6.4}$$

where $\alpha(0)$ is an initial estimate of the minimum point of $F(\alpha)$, and (6.4) is executed in a loop until $|F'(\alpha(n))|$ is sufficiently small [22]. In our problem, a parameter vector $\boldsymbol{\alpha}$ is optimized instead of a scalar. Furthermore, since the objective function in our application is real-valued which is a function of complex valued coefficients α_q (and therefore strictly-speaking non-holomorphic), the differentiation rules of Wirtinger calculus [113] were used. Thus, the DPD coefficients are updated as follows

$$\begin{aligned}\boldsymbol{\alpha}(n+1) = \boldsymbol{\alpha}(n) + &\left(\mathbf{H}_{\boldsymbol{\alpha}\boldsymbol{\alpha}} - \mathbf{H}_{\boldsymbol{\alpha}^*\boldsymbol{\alpha}}\mathbf{H}^{-1}_{\boldsymbol{\alpha}^*\boldsymbol{\alpha}^*}\mathbf{H}_{\boldsymbol{\alpha}\boldsymbol{\alpha}^*}\right)^{-1} \\ &\times \left[\mathbf{H}_{\boldsymbol{\alpha}^*\boldsymbol{\alpha}}\mathbf{H}^{-1}_{\boldsymbol{\alpha}^*\boldsymbol{\alpha}^*}\nabla_{\boldsymbol{\alpha}^*}(S_{tr}(\boldsymbol{\alpha}(n)))^H - \nabla_{\boldsymbol{\alpha}}(S_{tr}(\boldsymbol{\alpha}(n)))^H\right]\end{aligned} \tag{6.5}$$

where the gradients are defined as

$$\nabla_{\boldsymbol{\alpha}}(S_{tr}(\boldsymbol{\alpha})) = \frac{\partial\, S_{tr}(\boldsymbol{\alpha})}{\partial\, \boldsymbol{\alpha}} \qquad \nabla_{\boldsymbol{\alpha}^*}(S_{tr}(\boldsymbol{\alpha})) = \frac{\partial\, S_{tr}(\boldsymbol{\alpha})}{\partial\, \boldsymbol{\alpha}^*} \tag{6.6}$$

and the Hessian matrices as

$$\begin{aligned}\mathbf{H}_{\boldsymbol{\alpha}\boldsymbol{\alpha}} &= \frac{\partial}{\partial\, \boldsymbol{\alpha}}\left(\frac{\partial\, S_{tr}(\boldsymbol{\alpha})}{\partial\, \boldsymbol{\alpha}}\right)^H \qquad \mathbf{H}_{\boldsymbol{\alpha}^*\boldsymbol{\alpha}} = \frac{\partial}{\partial\, \boldsymbol{\alpha}^*}\left(\frac{\partial\, S_{tr}(\boldsymbol{\alpha})}{\partial\, \boldsymbol{\alpha}}\right)^H \\ \mathbf{H}_{\boldsymbol{\alpha}\boldsymbol{\alpha}^*} &= \frac{\partial}{\partial\, \boldsymbol{\alpha}}\left(\frac{\partial\, S_{tr}(\boldsymbol{\alpha})}{\partial\, \boldsymbol{\alpha}^*}\right)^H \qquad \mathbf{H}_{\boldsymbol{\alpha}^*\boldsymbol{\alpha}^*} = \frac{\partial}{\partial\, \boldsymbol{\alpha}^*}\left(\frac{\partial\, S_{tr}(\boldsymbol{\alpha})}{\partial\, \boldsymbol{\alpha}^*}\right)^H\end{aligned} \tag{6.7}$$

Table 6.1: Approximate number of FLOP required for DPD parameter estimation and optimization assuming 5^{th} order non-linearity and 3 memory taps for the power amplifier, and 7^{th} order non-linearity for the DPD

	Number of FLOP per M samples
Initial Parameter Estimation	$(81 \times M + 243)$
DPD Parameter Optimization	
Basis Functions Generation	$(4 \times M)$
PSD Evaluation	$(40 \times M + 178)$
Newton-Raphson Update	$1.4k$
Total Number of FLOP	$(44 \times M + 1.6k)$

Notice that for any given DPD order and PA model type (memoryless or PH), the needed derivatives can be pre-calculated analytically, and then simply evaluated with the PA model parameters at hand and the current DPD coefficient values [P4].

6.3 Complexity Perspectives

In this Section, a quantitative computational complexity analysis of the frequency-optimized DPD solution is presented. The primary metric used to quantify the complexity is the number of floating point operations (FLOP) [117]. The overall DPD processing can be divided into three computational stages: the initial parameter estimation stage, the parameter optimization and adaptation stage, and the real-time DPD main path processing stage. In the following analysis, the non-linearity orders of the power amplifier and the DPD are assumed to be five and seven, respectively.

The initial DPD parameters are computed using the direct learning approach. A direct least-squares memoryless polynomial identification of the PA is computed, followed by calculating the Pth-order inverse DPD coefficients. A parallel Hammerstein (PH) model of the PA is also identified in order to be used in the DPD parameter optimization stage. Assuming fifth order non-linearity with three memory taps per non-linearity order, as a practical example, the number of FLOP required by this stage is approximately $(81 \times M + 243)$, where M is the estimation block size [56], as shown in Table 6.1.

The computations associated with the parameter optimization and adaptation stage can be divided into three main parts. The first part is the *Basis Functions Generation*, which is then used for the *PSD Evaluation* part. Finally, the last part is the *Newton-Raphson Update*, where the Newton optimization coefficient update is performed. Table 6.1 summarizes the number of FLOP required by each of these parts for a block of M samples, and more details are provided in [P4].

The DPD real-time running stage is the most critical from the point of view of timing, hardware resources, and power consumption, especially in mobile devices, and

it is identical to classical DPD solutions. The total number of FLOP required for this stage is 28 FLOP per processed sample [P4]. Taking into consideration the performance gain when using the optimized coefficients, this yields a performance advantage over existing methods for any given run-time complexity, or alternatively, run-time complexity reduction for a given linearization performance.

Using $M = 100k$ as an example block size, the approximate number of FLOP required in the parameter estimation stage is 8.1 MFLOP, and in the parameter optimization the corresponding number is 4.5 MFLOP. These FLOP are not computed on a frequent basis (only in the order of msecs) compared to the system sampling time which is in the order of μsecs. On the other hand, the main path processing of the DPD requires 28 FLOP per sample. With an example real-time DPD processing rate of 100 MHz, this is equivalent to 2.8 GFLOP/s. While this is already a substantial amount of processing, it is still clearly within the processing power of state-of-the-art computing platforms even in mobile devices [48].

6.4 Simulation Results

In this Section, two kinds of communication waveforms are used to test and demonstrate the frequency-optimized DPD concept through simulations. The first example uses a 16-QAM single-carrier signal with root-raised cosine pulse, 22% roll-off. The second example is an LTE-Advanced UL non-contiguous multi-cluster scenario with two 2 MHz clusters at the edge of a 10 MHz LTE carrier. The PA model used is a 5th-order Parallel Hammerstein memory-based PA model, and a 7th-order memoryless DPD is deployed. A conventional 7th-order inverse solution is used as the starting point for the optimization algorithm in which initial values of the DPD coefficients α_3, α_5, and α_7 are obtained, while the linear coefficient α_1 is set to one. In these simulations, the proposed frequency-optimized method is deployed to reduce the emissions that fall within either the 3rd- or 5th-order regrowth or intermodulation regions.

6.4.1 Contiguous Carrier Allocation Example

In the first optimization scenario, the DPD target frequency f_0 is set to the center of the right adjacent channel (AC), and then in the second optimization scenario to the center of the second right adjacent channel which is at the spurious region. In both scenarios, the 5th-order and 7th-order DPD coefficients α_5 and α_7 are jointly optimized, while α_3 is fixed. Fig. 6.3 shows example PA output spectra, of a 10 MHz 16-QAM single-carrier waveform, with different optimization target frequencies. It can be clearly seen that the proposed DPD approach indeed tunes most of the available unwanted emission suppression to the defined target frequency, in different scenarios. For a more

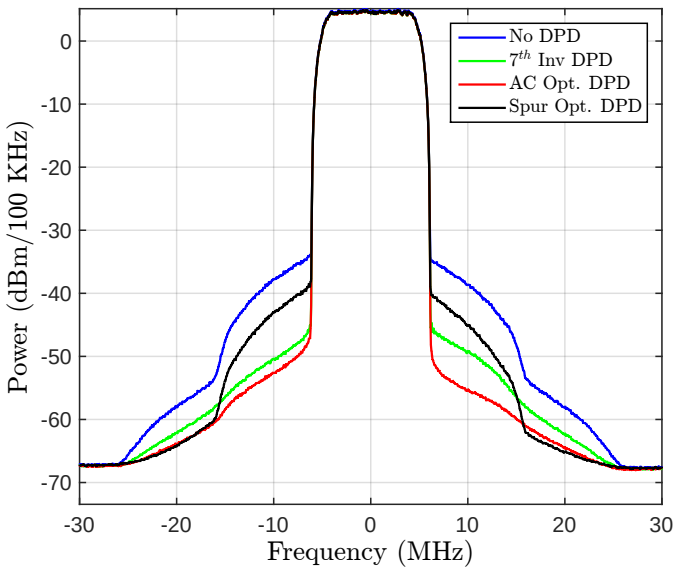

Figure 6.3: Baseband equivalent power spectra of 10 MHz 16-QAM single-carrier signals with root-raised cosine pulse and 22% roll-off, with different DPD solutions and PH PA model. Four cases are shown: Without DPD, using a conventional 7-th order inverse DPD, right adjacent channel (AC) optimized DPD and second right adjacent channel (Spur) optimized DPD.

Table 6.2: Values of ACLR, SRR, and EVM using parallel Hammerstein PA Model and Quasi-memoryless DPD Model in the contiguous carrier allocation scenario.

	ACLR L / R (dBc)	SRR L / R (dBc)	EVM (%)
Without DPD	43.8566 / 44.5309	63.8390 / 63.9644	6.4619
Conventional DPD	56.0416 / 55.0876	67.7376 / 67.9649	2.3556
AC Optimized DPD	58.1250 / 60.9337	69.6208 / 70.2154	2.3484
Spur Optimized DPD	48.8356 / 50.5666	69.7659 / 71.0010	2.3783

quantitative analysis and elaboration, Table 6.2 shows the obtained ACLR and spurious emission rejection ratio (SRR) values in different predistortion scenarios. The ACLR is evaluated over the adjacent channel(s) as defined in Section 2.3, while the SRR is evaluated over the second adjacent channel(s) in a similar fashion, and is defined as the ratio between the wanted signal power and the power in the spurious domain (P_{spur}), which reads

$$SRR_{dB} = 10 \log_{10} \frac{P_{wanted}}{P_{spur}} \tag{6.8}$$

The measurement bandwidths are equal to the wanted channel bandwidth in both the ACLR and SRR calculations.

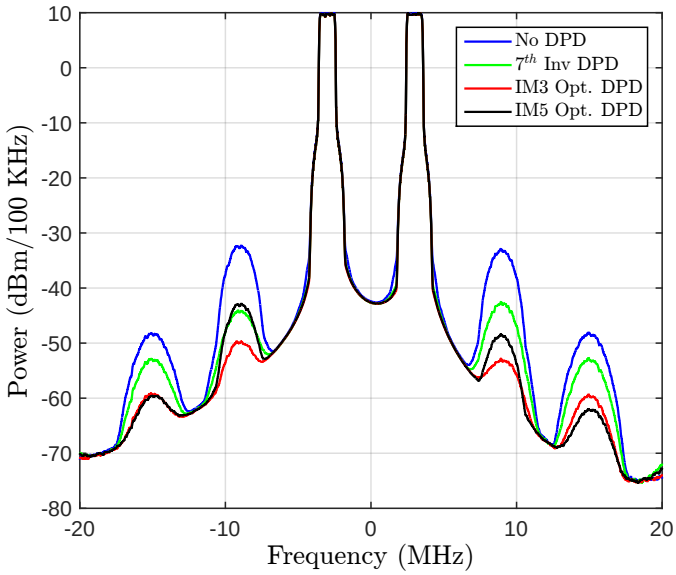

Figure 6.4: Baseband equivalent power spectra of LTE-A UL signals with different DPD solutions, using multi-cluster SC-FDMA transmission, QPSK data modulation, and PH PA model. Four cases are compared: Without DPD, using a conventional DPD, and proposed IM3 and IM5 optimized DPDs.

Table 6.3: Values of IM3R, IM5R, and EVM using parallel Hammerstein PA Model and Quasi-memoryless DPD Model in the noncontiguous carrier allocation scenario.

	IM3R L / R (dBc)	IM5R L / R (dBc)	EVM (%)
Without DPD	40.4529 / 41.1885	55.0491 / 54.9336	3.3245
Conventional DPD	51.1442 / 49.8385	58.6405 / 58.3671	1.0450
IM3 Optimized DPD	56.0137 / 56.7854	62.1339 / 61.6174	1.0054
IM5 Optimized DPD	50.5793 / 54.7730	62.2519 / 62.2458	1.0284

6.4.2 Noncontiguous Carrier Allocation Example

In this example, we seek to optimize the DPD coefficients to minimize the emissions either at the third-order or fifth-order intermodulation frequencies, i.e., IM3 and IM5 sub-bands. The emission reduction is quantified using the IM3R and IM5R reduction ratios as explained in Section 2.3. To be exact, the optimization/target frequency is set to the center of the right-hand-side IM3 or IM5 sub-band (i.e., IM3+ or IM5+ sub-band).

Fig. 6.4 shows the power spectra of the considered noncontiguous carrier allocation scenario which resembles an LTE-A UL multi-cluster scenario with two 2 MHz clusters at the edge of a 10 MHz carrier. Table 6.3 shows the corresponding EVM, IM3R, and IM5R values. It can clearly be seen that the reduction in the unwanted emissions

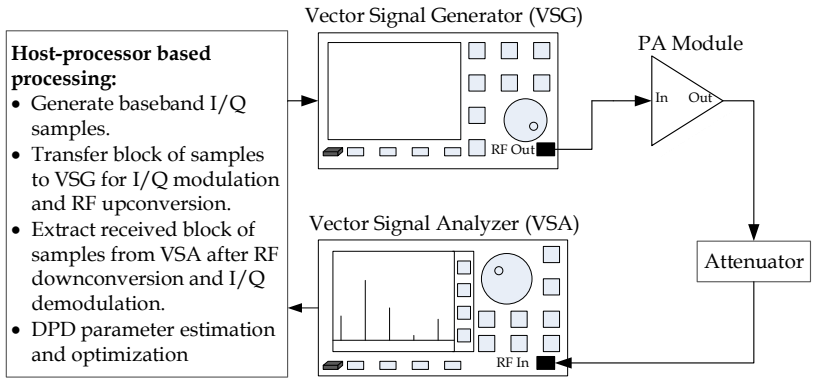

Figure 6.5: Measurement Setup used in the Lab to test the frequency-optimized DPD solution against the conventional 7th-order inverse DPD solution. Digital signal processing is done in Matlab, while the vector signal generator (VSG) and the vector signal analyzer (VSA) perform the RF processing to and from the PA.

at the IM3+ sub-band is better in case of the IM3 optimized DPD compared to the conventional DPD, and the same applies for the IM5+ sub-band. The extra gains from the optimization are in the order of 4-7 dB.

6.5 RF Measurement Results

In order to further elaborate and demonstrate the operation of the frequency-optimized DPD solution, actual RF measurements have been performed using a commercial LTE-A UE power amplifier. The overall measurement setup is shown in Fig. 6.5. The I/Q samples are first generated locally on the computer, then transferred to the vector signal generator (VSG) to perform I/Q modulation. The RF center-frequency used in these measurements is 1.89 GHz corresponding to LTE band 25. The VSG output is then connected to the input port of the PA whose output port is thereon connected to the vector signal analyzer (VSA) via an attenuator. The VSA implements the observation receiver for direct model identification as well as for measuring the actual PA output spectrum, with and without DPD processing.

In the following two measurement examples, the 7th-order inverse DPD solution is used as the starting point for the DPD optimization routine. A direct PA model is thus first extracted for this purpose using 100k I/Q samples and least squares model fitting. Next, the necessary PSD derivatives are evaluated, using a memoryless or a PH memory-based identified PA model as well as the original baseband data samples. The iterative Newton-Raphson DPD optimization is then performed as explained in [P4].

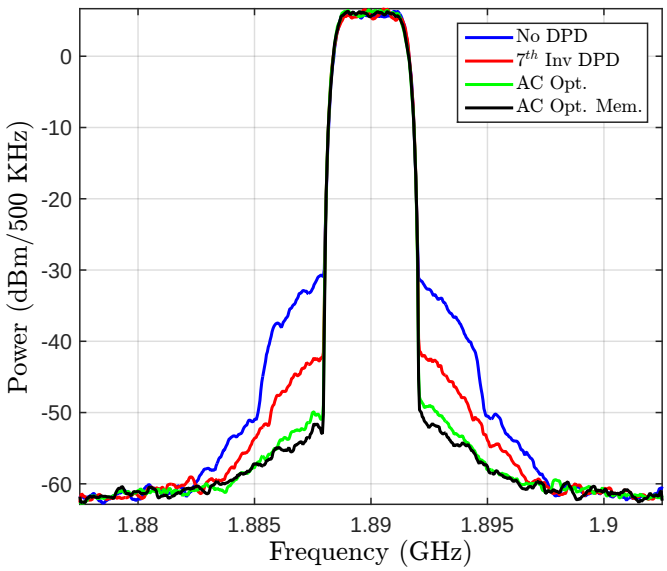

Figure 6.6: RF power spectra of a 16-QAM single-carrier signal with root-raised cosine pulse, 22% roll-off at the output of a commercial mobile PA in the Lab. Four cases are compared; without any DPD, using a conventional 7-th order inverse DPD, and ACLR-optimized proposed DPD with both memoryless PA identification and PH-memory based PA identification in the optimization. TX power is 16.5 dBm.

The first example uses a 16-QAM single-carrier signal with 3 MHz BW, and the optimization frequency is set to the center of the right adjacent channel (AC). The resulting spectra are shown in Fig. 6.6, including DPD optimization both with memoryless and with memory-based identified direct PA models. Clearly the proposed optimization solution can provide around 5 dB gain at the target frequency, already with purely memoryless optimization, while then incorporating the identified PA model with memory brings in this example an additional 1-2 dB gain.

In the second example, we deploy a multi-cluster SC-FDMA signal with QPSK data modulation, 0.5 MHz cluster bandwidth allocation and 3 MHz separation between the clusters. The target optimization frequency is set to the center of the IM3+ sub-band, and the resulting spectra are shown in Fig. 6.7, including DPD optimization both with memoryless and with memory-based identified direct PA models. The proposed optimization solution provides around 8 dB gain at the target frequency with purely memoryless optimization. An additional 3-4 dB gain is achieved when incorporating the identified PA model with memory.

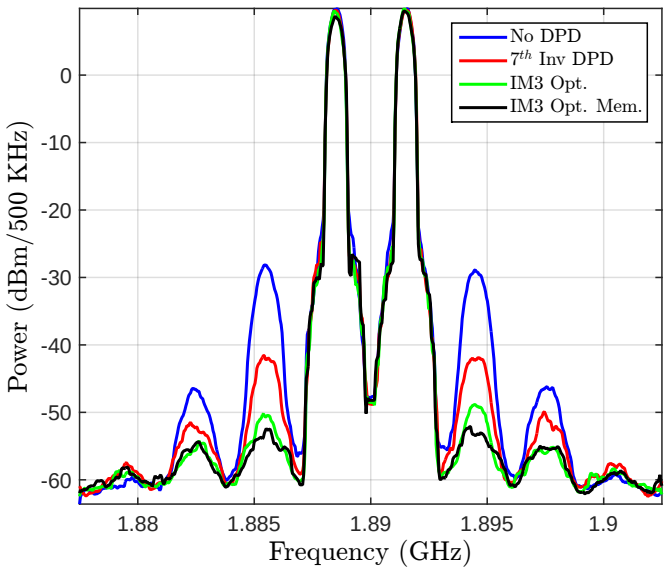

Figure 6.7: RF power spectra of measured LTE-A UL signals with multi-cluster SC-FDMA transmission and QPSK data modulation at the output of a commercial mobile PA in the lab. Four cases are compared; without any DPD, using a conventional 7-th order inverse DPD, and IM3-optimized proposed DPD with both memoryless and PH-memory based PA identification in the optimization. TX power is 15.5 dBm.

CHAPTER 7

Thesis Summary and Future Work

7.1 Thesis Summary

The target of this thesis was to develop advanced, low-complexity, DPD techniques for mitigating nonlinear distortion due to the power amplifier of the RF transmitter. The main focus was on the more challenging flexible spectrum access scenarios, while acknowledging the applicability of some of the developed algorithms in the classical transmission scenarios as well. Detailed modeling of the PA nonlinear distortion in carrier aggregation-like scenarios was performed, and mathematical expressions of the distortion components at different sub-bands were derived, which acted as the starting point of the DPD developments in this work. Since PA memory effects are almost unavoidable in the considered wideband and flexible scenarios, practical nonlinear models with memory were assumed in all the modeling and developments. Moreover, all the developed DPD solutions have been extensively tested using realistic simulations and practical RF measurements with commercial off-the-shelf power amplifiers and state-of-the-art RF measurement equipment.

The main findings and results of this thesis are summarized in the following. In [P5], a novel spur-injection based sub-band DPD structure, for spurious emission mitigation in noncontiguous transmission scenarios, was introduced. An efficient decorrelation-based

closed-loop learning algorithm was also developed for this sub-band DPD, particularly for mitigating the spurious emissions at the third-order IM sub-bands. Memory effects and higher-order nonlinear processing were then included in [P6] and [P2], respectively. A detailed complexity analysis of the proposed sub-band DPD was performed in [P2] along with extensive RF measurement examples evidencing excellent linearization performance. In the special case when the spurious emissions overlap with the own RX band in FDD transceivers, the work in [P7] proposed a novel sub-band DPD solution that used the main RX for DPD learning without requiring any additional observation RX, thus further reducing the DPD complexity. The main principles and advantages of such low complexity sub-band DPD solutions were highlighted in [P1] to spark discussions and further developments in this important research topic. These findings were all summarized in Chapter 4 of this thesis.

In [P3], a novel concurrent DPD utilizing the decorrelation-based learning concept and a single-feedback receiver path was developed. The developed DPD focused on linearizing the main carriers. Its complexity was analyzed in a detailed and quantitative manner against state-of-the-art concurrent DPD solutions evidencing a significantly reduced complexity in both the DPD main path processing and parameter learning computational requirements, despite having even slightly better linearization performance. Moreover, the proposed concurrent DPD was complemented with the sub-band DPD for IM spurious emission mitigation in [P2] in order to flexibly linearize any sub-band of choice based on the targeted linearization performance, while still using fewer and simpler hardware components when compared to all state-of-the-art DPD techniques in the literature. Extensive RF measurements were performed evidencing excellent linearization performance in various challenging scenarios while using commercial off-the-shelf RF power amplifiers used in advanced base station equipment and mobile terminals. These findings were all summarized in Chapter 5 of this thesis.

In [P4], a novel frequency-optimized DPD was developed which can tailor its linearization capabilities to any particular regions of the spectrum. Starting from a detailed mathematical modeling of the power spectrum at the PA output as a function of the DPD coefficients, a Newton-Raphson optimization routine was utilized to optimize the suppression of unwanted emissions at arbitrary pre-specified frequencies at the PA output. A complexity analysis was performed showing the number of floating point operations required in both the DPD main processing and the parameter optimization routine. The proposed DPD was shown, through practical simulations and RF measurements, to provide better performance at the more critical spectral regions (e.g., adjacent channels or own RX band) while using the same running complexity as the classical DPD, or in other words, it can achieve the same performance at those critical regions with a lower complexity DPD. These findings were all summarized in Chapter 6 of this thesis.

7.2 Future Work

There are some interesting research points that can act as a continuation to the work done in this thesis, which are hereby summarized. The developed decorrelation-based DPD learning algorithm along with the proposed DPD structures in this thesis can be modified and extended to consider scenarios with multiple antennas at the transmitter. In the even more challenging case of massive MIMO, 10's or 100's of antennas can be used, and thus the complexity per RF chain becomes particularly more critical. Consequently, low cost, size, and highly nonlinear power amplifiers are expected to be adopted. This is an area where reduced-complexity DPD solutions can fit very well. Moreover, combining such DPD solutions with novel PAPR reduction techniques for further energy efficiency enhancement in MIMO transmitters is an interesting point for future research.

Further reduction in the DPD complexity can be achieved through limiting the linearization to a specified bandwidth even when considering higher-order basis functions. This can be achieved by filtering the basis functions used for DPD in the main path as well the observation at the PA output in the feedback receiver path. Although the idea has already been developed in other works, a detailed complexity analysis has not been performed yet. Additionally, the band-limiting filter design opens some research questions, like for example, how much aliasing can be allowed from the higher-order nonlinear basis functions, and to what extent is the linearization performance impacted when simpler filter structures are used. Such research questions have not been answered in the literature yet.

There is room for future developments in the frequency-optimized DPD as well. So far, despite considering memory effects in the PA, only memoryless DPD structures were assumed. Adding memory to the DPD is certainly an interesting and natural continuation of the study in [P4]. However, this implies more DPD parameters, and thus the optimization routine and PSD evaluation procedure will become more challenging which opens the door for new ideas. Moreover, extending the frequency-optimized DPD to include more than one optimization frequency is also an interesting point for future study.

References

[1] *Avago Band 25 LTE-Advanced UE Duplexer, ACMD-6125. Available at: http://docs.avagotech.com/docs/AV02-4214EN.*

[2] *International Telecommunication Union Radio Communication Sector, Recommendation ITU-R SM.329-12 Unwanted emissions in the spurious domain. Available at: https://www.itu.int/.*

[3] "IEEE Standard for Information technology–Telecommunications and information exchange between systems–Local and metropolitan area networks–Specific requirements–Part 11: Wireless LAN Medium Access Control (MAC) and Physical Layer (PHY) Specifications–Amendment 4: Enhancements for Very High Throughput for Operation in Bands below 6 GHz." *IEEE Std 802.11ac(TM)-2013*, pp. 1–425, Dec 2013.

[4] "ISO/IEC/IEEE International Standard – Information technology – Telecommunications and information exchange between systems – Local and metropolitan area networks– Specific requirements – Part 22: Cognitive Wireless RAN Medium Access Control (MAC) and Physical Layer (PHY) specifications: Policies and procedures for operation in the TV Band," *ISO/IEC/IEEE 8802-22:2015*, pp. 1–678, May 2015.

[5] *LTE Evolved Universal Terrestrial Radio Access (E-UTRA) Base Station (BS) conformance testing, 3GPP TS 36.141 V13.6.0 (Release 13)*, Dec. 2016.

[6] *LTE Evolved Universal Terrestrial Radio Access (E-UTRA) Base Station (BS) radio transmission and reception, 3GPP TS 36.104 V13.6.0 (Release 13)*, Dec. 2016.

[7] *LTE Evolved Universal Terrestrial Radio Access (E-UTRA) RF system scenarios, 3GPP TR 36.942 V13.0.0 (Release 13)*, Jan. 2016.

[8] *LTE Evolved Universal Terrestrial Radio Access (E-UTRA) User Equipment (UE) radio transmission and reception, 3GPP TS 36.101 V13.6.1 (Release 13)*, Jan. 2017.

[9] *LTE Evolved Universal Terrestrial Radio Access (E-UTRA) User Equipment (UE) conformance specification Radio transmission and reception, 3GPP TS 36.521 V13.3.0 (Release 13)*, Sept. 2016.

[10] M. Abdelaziz, L. Anttila, S. Dikmese, M. Renfors, A. M. Wyglinski, and M. Valkama, "Flexible Digital Predistortion for Future Spectrally-Agile Waveforms and 5G Radio Systems," in *Vehicular Technology Conference (VTC Fall), 2015 IEEE 82nd*, Sept 2015, pp. 1–7.

[11] M. Abdelaziz, L. Anttila, M. Renfors, and M. Valkama, "PAPR reduction and digital predistortion for non-contiguous waveforms with well-localized spectrum." in *13th International Symposium on Wireless Communication Systems*, Sept. 2016.

[12] M. Abdelaziz, L. Anttila, and M. Valkama, "Reduced-complexity digital predistortion for massive MIMO," in *2017 IEEE International Conference on Acoustics, Speech and Signal Processing (ICASSP)*, March 2017.

[13] M. Abdelaziz, A. Ghazi, L. Anttila, J. Boutellier, T. Lähteensuo, X. Lu, J. Cavallaro, S. Bhattacharyya, M. Juntti, and M. Valkama, "Mobile transmitter digital predistortion: Feasibility analysis, algorithms and design exploration," in *47th Asilomar Conf. Signals Systems Computers, Pacific, Grove, CA, USA*, Nov. 2013.

[14] M. Abdelaziz, C. Tarver, K. Li, L. Anttila, M. Valkama, and J. Cavallaro, "Subband digital predistortion for noncontiguous transmissions: Algorithm development and real-time prototype implementation," in *49th Asilomar Conf. Signals, Systems, and Computers, Pacific, Grove, CA, USA.*, Nov. 2015.

[15] A. Abdelhafiz, A. Kwan, O. Hammi, and F. M. Ghannouchi, "Digital Predistortion of LTE-A Power Amplifiers Using Compressed-Sampling-Based Unstructured Pruning of Volterra Series," *IEEE Transactions on Microwave Theory and Techniques*, vol. 62, no. 11, pp. 2583–2593, Nov 2014.

[16] M. Agiwal, A. Roy, and N. Saxena, "Next Generation 5G Wireless Networks: A Comprehensive Survey," *IEEE Communications Surveys Tutorials*, vol. 18, no. 3, pp. 1617–1655, thirdquarter 2016.

[17] C. S. Aitchison, M. Mbabele, M. R. Moazzam, D. Budimir, and F. Ali, "Improvement of third-order intermodulation product of RF and microwave amplifiers by injection," *IEEE Transactions on Microwave Theory and Techniques*, vol. 49, no. 6, pp. 1148–1154, Jun 2001.

[18] S. Amin, E. Zenteno, P. N. Landin, D. Rönnow, M. Isaksson, and P. Händel, "Noise impact on the identification of digital predistorter parameters in the indirect learning architecture," in *2012 Swedish Communication Technologies Workshop (Swe-CTW)*, Oct 2012, pp. 36–39.

[19] L. Anttila, P. Händel, O. Mylläri, and M. Valkama, "Recursive learning-based joint digital predistorter for power amplifier and I/Q modulator impairments," *International Journal of Microwave and Wireless Technologies*, vol. 2, no. 02, pp. 173–182, April 2010.

[20] L. Anttila, P. Händel, and M. Valkama, "Joint mitigation of power amplifier and I/Q modulator impairments in broadband direct-conversion transmitters," *IEEE Transactions on Microwave Theory and Techniques*, vol. 58, pp. 730–739, April 2010.

[21] E. Aschbacher, "Digital Pre-distortion of Microwave Power Amplifiers," Ph.D. dissertation, Vienna University of Technology, 2005.

[22] M. Bartholomew-Biggs, *Nonlinear Optimization with Engineering Applications*. Springer, 2008.

[23] S. Bassam, W. Chen, M. Helaoui, and F. Ghannouchi, "Transmitter architecture for CA: Carrier Aggregation in LTE-Advanced systems," *IEEE Microwave Magazine*, vol. 14, 2013.

[24] S. Bassam, F. Ghannouchi, and M. Helaoui, "2-D Digital Predistortion (2-D-DPD) architecture for concurrent dual-band transmitters," *IEEE Transactions on Microwave Theory and Techniques*, vol. 59, pp. 2547–2553, Oct. 2011.

[25] S. Bassam, M. Helaoui, and F. Ghannouchi, "Channel-selective multi-cell digital predistorter for multi-carrier transmitters," *IEEE Transactions on Microwave Theory and Techniques*, vol. 60, pp. 2344–2352, Aug. 2012.

[26] H. Bogucka, P. Kryszkiewicz, and A. Kliks, "Dynamic spectrum aggregation for future 5G communications," *IEEE Communications Magazine*, vol. 53, no. 5, pp. 35–43, May 2015.

[27] S. Boyd and L. Vandenberghe, *Convex Optimization*. Cambridge University Press, 2004.

[28] R. Braithwaite, "Closed-Loop Digital Predistortion (DPD) Using an Observation Path With Limited Bandwidth," *IEEE Transactions on Microwave Theory and Techniques*, vol. 63, no. 2, pp. 726–736, Feb. 2015.

[29] R. N. Braithwaite, "Wide bandwidth adaptive digital predistortion of power amplifiers using reduced order memory correction," in *Microwave Symposium Digest, 2008 IEEE MTT-S International*, June 2008, pp. 1517–1520.

[30] R. N. Braithwaite, "A comparison of indirect learning and closed loop estimators used in digital predistortion of power amplifiers," in *2015 IEEE MTT-S International Microwave Symposium*, May 2015, pp. 1–4.

[31] R. N. Braithwaite, "Computationally efficient coefficient estimator used in memory-based digital predistortion (DPD) models," in *2016 87th ARFTG Microwave Measurement Conference (ARFTG)*, May 2016, pp. 1–4.

[32] R. Braithwaite, *General principles and design overview of digital predistortion; Chapter 6 in Digital Front-End in Wireless Communications and Broadcasting.* Cambridge: Cambridge University Press, 2011.

[33] K. Bulusu, H. Shaiek, D. Roviras, R. Zayani, M. Renfors, L. Anttila, and M. Abdelaziz, "Power amplifier effects and peak-to-average power mitigation," in *Orthogonal waveforms and filter banks for future communication systems.* Elsevier, 2017, ch. 18.

[34] M. Cabarkapa, N. Neskovic, and D. Budimir, "A Generalized 2-D Linearity Enhancement Architecture for Concurrent Dual-Band Wireless Transmitters," *IEEE Transactions on Microwave Theory and Techniques*, vol. 61, no. 12, pp. 4579–4590, Dec 2013.

[35] M. Cabarkapa, N. Neskovic, A. Neskovic, and D. Budimir, "Adaptive nonlinearity compensation technique for 4G wireless transmitters," *Electronics Letters*, vol. 48, no. 20, pp. 1308–1309, September 2012.

[36] J. Chani-Cahuana, P. N. Landin, C. Fager, and T. Eriksson, "Iterative Learning Control for RF Power Amplifier Linearization," *IEEE Transactions on Microwave Theory and Techniques*, vol. 64, no. 9, pp. 2778–2789, Sept 2016.

[37] C. Chatfield, *The Analysis of Time Series: An Introduction, Sixth Edition.* CRC Press, 2003.

[38] S. Chen and J. Zhao, "The requirements, challenges, and technologies for 5G of terrestrial mobile telecommunication," *IEEE Communications Magazine*, vol. 52, no. 5, pp. 36–43, May 2014.

[39] W. Chen, S. Zhang, Y. J. Liu, F. M. Ghannouchi, Z. Feng, and Y. Liu, "Efficient Pruning Technique of Memory Polynomial Models Suitable for PA Behavioral Modeling and Digital Predistortion," *IEEE Transactions on Microwave Theory and Techniques*, vol. 62, no. 10, pp. 2290–2299, Oct 2014.

[40] D. V. Compernolle and S. van Gerven, "Signal separation in a symmetric adaptive noise canceler by output decorrelation," in *1992 IEEE International Conference on Acoustics, Speech and Signal Processing (ICASSP)*, vol. 4, Mar 1992, pp. 221–224 vol.4.

[41] C. Crespo-Cadenas, J. Reina-Tosina, M. Madero-Ayora, and J. Munoz-Cruzado, "A New Approach to Pruning Volterra Models for Power Amplifiers," *IEEE Transactions on Signal Processing*, vol. 58, no. 4, pp. 2113–2120, April 2010.

[42] E. Dahlman, S. Parkvall, and J. Skold, *4G LTE/LTE-Advanced for Mobile Broadband.* Elsevier Ltd., 2011.

[43] S. Dikmese, M. Abdelaziz, L. Anttila, M. Renfors, and M. Valkama, "Dynamic and flexible spectrum use with frequency localized waveforms under transmitter nonidealities," in *Vehicular Technology Conference (VTC Fall), 2015 IEEE 82nd*, Sept 2015, pp. 1–6.

[44] L. Ding, F. Mujica, and Z. Yang, "Digital predistortion using direct learning with reduced bandwidth feedback," in *Microwave Symposium Digest (IMS), 2013 IEEE MTT-S International*, June 2013, pp. 1–3.

[45] L. Ding, R. Raich, and G. Zhou, "A Hammerstein predistortion linearization design based on the indirect learning architecture," in *2002 IEEE International Conference on Acoustics, Speech and Signal Processing (ICASSP)*, November 2002, pp. 2689–2692.

[46] L. Ding, G. Zhou, D. Morgan, Z. Ma, J. Kenney, J. Kim, and C. Giardina, "A robust digital baseband predistorter constructed using memory polynomials," *IEEE Transactions on Communications*, vol. 52, no. 1, pp. 159–165, January 2004.

[47] Ericsson and ST-Ericsson, "R4-123797, UE reference sensitivity requirements with two UL carriers. Available at: http://www.3gpp.org/," 3GPP, Tech. Rep., Feb. 2013.

[48] M. S.-L. et al., "A 28 nm DSP powered by an on-chip LDO for high-performance and energy-efficient mobile applications," *IEEE Journal of Solid-State Circuits*, vol. 50, no. 1, pp. 81–91, Jan 2015.

[49] C. Eun and E. Powers, "A new Volterra predistorter based on the indirect learning architecture," *IEEE Transactions on Signal Processing*, vol. 45, no. 1, pp. 223–227, January 1997.

[50] C.-W. Fan and K. K. M. Cheng, "Theoretical and experimental study of amplifier linearization based on harmonic and baseband signal injection technique," *IEEE Transactions on Microwave Theory and Techniques*, vol. 50, no. 7, pp. 1801–1806, Jul 2002.

[51] A. Georgakopoulos, A. Margaris, K. Tsagkaris, and P. Demestichas, "Resource Sharing in 5G Contexts: Achieving Sustainability with Energy and Resource Efficiency," *IEEE Vehicular Technology Magazine*, vol. 11, no. 1, pp. 40–49, March 2016.

[52] S. V. Gerven and D. V. Compernolle, "Signal separation by symmetric adaptive decorrelation: stability, convergence, and uniqueness," *IEEE Transactions on Signal Processing*, vol. 43, no. 7, pp. 1602–1612, Jul 1995.

[53] F. M. Ghannouchi and O. Hammi, "Behavioral modeling and predistortion," *IEEE Microwave Magazine*, pp. 52–64, Dec. 2009.

[54] A. Ghazi, J. Boutellier, M. Abdelaziz, X. Lu, L. Anttila, J. R. Cavallaro, S. S. Bhattacharyya, M. Valkama, and M. Juntti, "Low power implementation of digital predistortion filter on a heterogeneous application specific multiprocessor," in *2014 IEEE International Conference on Acoustics, Speech and Signal Processing (ICASSP)*, May 2014, pp. 8336–8340.

[55] P. L. Gilabert, G. Montoro, T. Wang, M. N. Ruiz, and J. A. Garcia, "Comparison of model order reduction techniques for digital predistortion of power amplifiers," in *2016 46th European Microwave Conference (EuMC)*, Oct 2016, pp. 182–185.

[56] G. H. Golub and C. F. Loan, *Matrix Computations, Third Edition*. Johns Hopkins University Press, 1996.

[57] L. Guan and A. Zhu, "Optimized Low-Complexity Implementation of Least Squares Based Model Extraction for Digital Predistortion of RF Power Amplifiers," *IEEE Transactions on Microwave Theory and Techniques*, vol. 60, no. 3, pp. 594–603, March 2012.

[58] L. Guan and A. Zhu, "Green communications: Digital predistortion for wideband RF power amplifiers," *IEEE Microwave Magazine*, vol. 15, no. 7, pp. 84–89, Dec. 2014.

[59] A. Haimovich, Y. Bar-Ness, and R. Manzo, "A stochastic gradient-based decorrelation algorithm with applications to multicarrier CDMA," in *Vehicular Technology Conference, 1995 IEEE 45th*, vol. 1, Jul 1995, pp. 464–468 vol.1.

[60] O. Hammi and F. Ghannouchi, "Twin nonlinear two-box models for power amplifiers and transmitters exhibiting memory effects with application to digital predistortion," *IEEE Microwave and Wireless Components Letters*, vol. 19, no. 8, pp. 530–532, August 2009.

[61] S. Haykin, *Adaptive Filter Theory, Fifth Edition*. Pearson, 2014.

[62] A. Hoerl and R. Kennard, "Ridge regression biased estimation for nonorthogonal problems," *Technometrics*, vol. 12, no. 3, pp. 55–67, Aug 1970.

[63] X. Hong, J. Wang, C. X. Wang, and J. Shi, "Cognitive radio in 5G: a perspective on energy-spectral efficiency trade-off," *IEEE Communications Magazine*, vol. 52, no. 7, pp. 46–53, July 2014.

[64] C. Hoymann, D. Astely, M. Stattin, G. Wikström, J. F. Cheng, A. Höglund, M. Frenne, R. Blasco, J. Huschke, and F. Gunnarsson, "LTE release 14 outlook," *IEEE Communications Magazine*, vol. 54, no. 6, pp. 44–49, June 2016.

[65] M. Isaksson, D. Wisell, and D. Ronnow, "A comparative analysis of behavioral models for RF power amplifiers," *IEEE Transactions on Microwave Theory and Techniques*, vol. 54, no. 1, pp. 348–359, Jan 2006.

[66] J. Joung, C. K. Ho, K. Adachi, and S. Sun, "A Survey on Power-Amplifier-Centric Techniques for Spectrum- and Energy-Efficient Wireless Communications," *IEEE Communications Surveys Tutorials*, vol. 17, no. 1, pp. 315–333, Firstquarter 2015.

[67] A. Katz, J. Wood, and D. Chokola, "The Evolution of PA Linearization: From Classic Feedforward and Feedback Through Analog and Digital Predistortion," *IEEE Microwave Magazine*, vol. 17, no. 2, pp. 32–40, Feb 2016.

[68] N. Kelly and A. Zhu, "A modified simultaneous perturbation stochastic optimization algorithm for digital predistortion model extraction," in *Integrated Nonlinear Microwave and Millimetre-wave Circuits Workshop (INMMiC), 2015*, Oct 2015, pp. 1–3.

[69] N. Kelly and A. Zhu, "Low-Complexity Stochastic Optimization-Based Model Extraction for Digital Predistortion of RF Power Amplifiers," *IEEE Transactions on Microwave Theory and Techniques*, vol. 64, no. 5, pp. 1373–1382, May 2016.

[70] P. Kenington, *High-Linearity* RF *Amplifier Design*. Boston: Artech House, 2000.

[71] A. Kiayani, M. Abdelaziz, L. Anttila, V. Lehtinen, and M. Valkama, "DSP-based suppression of spurious emissions at RX band in carrier aggregation FDD transceivers," in *2014 22nd European Signal Processing Conference (EUSIPCO)*, Sept 2014, pp. 591–595.

[72] A. Kiayani, M. Abdelaziz, L. Anttila, V. Lehtinen, and M. Valkama, "Digital Mitigation of Transmitter-Induced Receiver Desensitization in Carrier Aggregation FDD Transceivers," *IEEE Transactions on Microwave Theory and Techniques*, vol. 63, no. 11, pp. 3608–3623, Nov 2015.

[73] A. Kiayani, V. Lehtinen, L. Anttila, T. Lahteensuo, and M. Valkama, "Linearity Challenges of LTE-Advanced Mobile Transmitters: Requirements and Potential Solutions," *IEEE Communications Magazine*, vol. 55, no. 6, pp. 170–179, June 2017.

[74] J. Kim and K. Konstantinou, "Digital predistortion of wideband signals based on power amplifier model with memory," *Electronics Letters*, vol. 37, no. 23, pp. 1417–1418, November 2001.

[75] J. Kim, P. Roblin, D. Chaillot, and Z. Xie, "A generalized architecture for the frequency-selective digital predistortion linearization technique," *IEEE Transactions on Microwave Theory and Techniques*, vol. 61, pp. 596–605, Jan. 2013.

[76] W.-J. Kim, S. P. Stapleton, J. H. Kim, and C. Edelman, "Digital predistortion linearizes wireless power amplifiers," *IEEE Microwave Magazine*, vol. 6, no. 3, pp. 54–61, Sept 2005.

[77] H. Ku and J. S. Kenney, "Behavioral modeling of nonlinear RF power amplifiers considering memory effects," *IEEE Transactions on Microwave Theory and Techniques*, vol. 51, no. 12, pp. 2495–2504, Dec 2003.

[78] T. Lähteensuo, "Linearity Requirements in LTE Advanced Mobile Transmitter." Master's thesis, Tampere University of Technology, Tampere, Finland., May 2013.

[79] P. Landin, "Digital baseband modeling and correction of radio frequency power amplifiers," Ph.D. dissertation, Royal Institute of Technology (KTH), 2012.

[80] N. Lashkarian, J. Shi, and M. Forbes, "A direct learning adaptive scheme for power-amplifier linearization based on wirtinger calculus," *IEEE Transactions on Circuits and Systems I: Regular Papers*, vol. 61, no. 12, pp. 3496–3505, Dec 2014.

[81] P. M. Lavrador, T. R. Cunha, P. M. Cabral, and J. C. Pedro, "The Linearity-Efficiency Compromise," *IEEE Microwave Magazine*, vol. 11, no. 5, pp. 44–58, Aug 2010.

[82] J. Lee, Y. Kim, Y. Kwak, J. Zhang, A. Papasakellariou, T. Novlan, C. Sun, and Y. Li, "LTE-advanced in 3GPP Rel -13/14: an evolution toward 5G," *IEEE Communications Magazine*, vol. 54, no. 3, pp. 36–42, March 2016.

[83] K. Li, A. Ghazi, J. Boutellier, M. Abdelaziz, L. Anttila, M. Juntti, M. Valkama, and J. R. Cavallaro, "Mobile GPU accelerated digital predistortion on a software-defined mobile transmitter," in *2015 IEEE Global Conference on Signal and Information Processing (GlobalSIP)*, Dec 2015, pp. 756–760.

[84] J. Liu and W. Xiao, "Advanced carrier aggregation techniques for multi-carrier ultra-dense networks," *IEEE Communications Magazine*, vol. 54, no. 7, pp. 61–67, July 2016.

[85] Y. Liu, J. Yan, and P. Asbeck, "Concurrent dual-band digital predistortion with a single feedback loop," *IEEE Transactions on Microwave Theory and Techniques*, vol. 63, no. 5, pp. 1556–1568, May 2015.

[86] Y. J. Liu, W. Chen, J. Zhou, B. H. Zhou, and F. M. Ghannouchi, "Digital Predistortion for Concurrent Dual-Band Transmitters Using 2-D Modified Memory Polynomials," *IEEE Transactions on Microwave Theory and Techniques*, vol. 61, no. 1, pp. 281–290, Jan 2013.

[87] Y. Liu, X. Quan, W. Pan, S. Shao, and Y. Tang, "An accurate digital predistortion for wideband power amplifiers based on directly solving the inverse model function," *Circuits, Systems, and Signal Processing*, vol. 35, no. 8, pp. 2704–2722, 2016.

[88] Y. Ma, Y. Yamao, Y. Akaiwa, and K. Ishibashi, "Wideband digital predistortion using spectral extrapolation of band-limited feedback signal," *IEEE Transactions on Circuits and Systems*, 2014.

[89] Y. Ma and Y. Yamao, "Spectra-Folding Feedback Architecture for Concurrent Dual-Band Power Amplifier Predistortion," *IEEE Transactions on Microwave Theory and Techniques*, vol. 63, no. 10, pp. 3164–3174, Oct 2015.

[90] O. Markusson, H. Hjalmarsson, and M. Norrlof, "Iterative learning control of nonlinear non-minimum phase systems and its application to system and model inversion," in *Decision and Control, 2001. Proceedings of the 40th IEEE Conference on*, vol. 5, 2001, pp. 4481–4482 vol.5.

[91] V. J. Mathews and G. L. Sicuranza, *Polynomial Signal Processing*. Wiley, 2000.

[92] N. Mizusawa and S. Kusunoki, "Third- and fifth-order baseband component injection for linearization of the power amplifier in a cellular phone," *IEEE Transactions on Microwave Theory and Techniques*, vol. 53, no. 11, pp. 3327–3334, Nov 2005.

[93] M. Modeste, D. Budimir, M. R. Moazzam, and C. S. Aitchison, "Analysis and practical performance of a difference frequency technique for improving the multicarrier IMD performance of RF amplifiers," in *Technologies for Wireless Applications, 1999. Digest. 1999 IEEE MTT-S Symposium on*, Feb 1999, pp. 53–56.

[94] J. Moon and B. Kim, "Enhanced Hammerstein Behavioral Model for Broadband Wireless Transmitters," *IEEE Transactions on Microwave Theory and Techniques*, vol. 59, no. 4, pp. 924–933, April 2011.

[95] K. Moore, *Iterative Learning Control*. Artech House, 2006.

[96] D. Morgan, Z. Ma, J. Kim, M. Zierdt, and J. Pastalan, "A Generalized Memory Polynomial Model for Digital Predistortion of RF Power Amplifiers," *IEEE Transactions on Signal Processing*, vol. 54, no. 10, pp. 3852–3860, October 2006.

[97] A. Mukherjee, J. F. Cheng, S. Falahati, H. Koorapaty, D. H. Kang, R. Karaki, L. Falconetti, and D. Larsson, "Licensed-Assisted Access LTE: coexistence with IEEE 802.11 and the evolution toward 5G," *IEEE Communications Magazine*, vol. 54, no. 6, pp. 50–57, June 2016.

[98] S. W. Nam and E. J. Powers, "On the linearization of Volterra nonlinear systems using third-order inverses in the digital frequency-domain," in *IEEE International Symposium on Circuits and Systems*, May 1990, pp. 407–410 vol.1.

[99] Nokia, "R4-121205 Way forward for non-contiguous intraband transmitter aspects. Available at: http://www.3gpp.org/," 3GPP, Tech. Rep., Feb. 2013.

[100] Nokia, "R4-124353, Non-contiguous intraband unwanted emission. Available at: http://www.3gpp.org/," 3GPP, Tech. Rep., Feb. 2013.

[101] A. V. Oppenheim and R. W. Schafer, *Discrete-Time Signal Processing, 3rd Edition*. Prentice Hall, 1999.

[102] W. Pan, Y. Liu, and Y. Tang, "A predistortion algorithm based on accurately solving the reverse function of memory polynomial model," *IEEE Wireless Communications Letters*, vol. 1, no. 4, pp. 384–387, August 2012.

[103] C. Park, L. Sundström, A. Wallen, and A. Khayrallah, "Carrier aggregation for LTE-advanced: Design challenges of terminals," *IEEE Communications Magazine*, pp. 76–84, Dec. 2013.

[104] J. C. Pedro and S. A. Maas, "A comparative overview of microwave and wireless power-amplifier behavioral modeling approaches," *IEEE Transactions on Microwave Theory and Techniques*, vol. 53, no. 4, pp. 1150–1163, April 2005.

[105] H. Qian, S. Yao, H. Huang, and W. Feng, "A low-complexity digital predistortion algorithm for power amplifier linearization," *IEEE Transactions on Broadcasting*, vol. 60, no. 4, pp. 670–678, Dec. 2014.

[106] H. Qian, S. Yao, H. Huang, X. Yang, and W. Feng, "Low complexity coefficient estimation for concurrent dual-band digital predistortion," *IEEE Transactions on Microwave Theory and Techniques*, vol. 63, no. 10, pp. 3153–3163, Oct 2015.

[107] R. Raich, H. Qian, and G. T. Zhou, "Orthogonal polynomials for power amplifier modeling and predistorter design," *IEEE Transactions on Vehicular Technology*, vol. 53, no. 5, pp. 1468–1479, Sept 2004.

[108] R. Raich and G. T. Zhou, "Orthogonal polynomials for complex gaussian processes," *IEEE Transactions on Signal Processing*, vol. 52, no. 10, pp. 2788–2797, Oct 2004.

[109] P. Roblin, S. K. Myoung, D. Chaillot, Y. G. Kim, A. Fathimulla, J. Strahler, and S. Bibyk, "Frequency-selective predistortion linearization of RF power amplifiers," *IEEE Transactions on Microwave Theory and Techniques*, vol. 56, pp. 65–76, Jan. 2008.

[110] P. Roblin, C. Quindroit, N. Naraharisetti, S. Gheitanchi, and M. Fitton, "Concurrent linearization," *IEEE Microwave Magazine*, pp. 75–91, Nov. 2013.

[111] M. Schetzen, "Theory of pth-order inverses of nonlinear systems," *IEEE Transactions on Circuits and Systems*, vol. 23, no. 5, pp. 285–291, May 1976.

[112] M. Schetzen, *The Volterra and Wiener Theories of Nonlinear Systems*. New York: Wiley, 1980.

[113] P. Schreier and L. Scharf, *Statistical Signal Processing of Complex-Valued Data*. Cambridge University Press, 2010.

[114] D. Schreurs, M. O'Droma, A. A. Goacher, and M. Gadringer, *RF power amplifier behavioral modeling*. Cambridge University Press New York, NY, USA, 2008.

[115] Z. Shen, A. Papasakellariou, J. Montojo, D. Gerstenberger, and F. Xu, "Overview of 3GPP LTE-advanced carrier aggregation for 4G wireless communications," *IEEE Communications Magazine*, vol. 50, no. 2, pp. 122–130, February 2012.

[116] C. Tarver, M. Abdelaziz, L. Anttila, M. Valkama, and J. Cavallaro, "Low-complexity, sub-band DPD with sequential learning: Novel algorithms and WARPLab implementation," in *IEEE International Workshop on Signal Processing Systems (SiPS 2016)*, Oct. 2016.

[117] A. Tehrani, H. Cao, S. Afsardoost, T. Eriksson, M. Isaksson, and C. Fager, "A comparative analysis of the complexity/accuracy tradeoff in power amplifier behavioral models," *IEEE Transactions on Microwave Theory and Techniques*, vol. 58, pp. 1510–1520, June 2010.

[118] R. Tibshirani, "Regression Shrinkage and Selection via the LASSO," *Journal of the Royal Statistical Society*, vol. 58, pp. 267–288, 1996.

[119] D. Wisell, J. Jalden, and P. Händel, "Behavioral Power Amplifier Modeling Using the LASSO," in *2008 IEEE Instrumentation and Measurement Technology Conference*, May 2008, pp. 1864–1867.

[120] M. Xiao and P. Gardner, "Digital baseband injection techniques to reduce spectral regrowth in power amplifier," in *Microwave Symposium Digest, 2008 IEEE MTT-S International*, June 2008, pp. 1513–1516.

[121] J. Xu and Y. Tan, *Linear and Nonlinear Iterative Learning Control*. Springer-Verlag, 2003.

[122] M. Younes and F. M. Ghannouchi, "Behavioral Modeling of Concurrent Dual-Band Transmitters Based on Radially-Pruned Volterra Model," *IEEE Communications Letters*, vol. 19, no. 5, pp. 751–754, May 2015.

[123] M. Younes, A. Kwan, M. Rawat, and F. M. Ghannouchi, "Linearization of Concurrent Tri-Band Transmitters Using 3-D Phase-Aligned Pruned Volterra Model," *IEEE Transactions on Microwave Theory and Techniques*, vol. 61, no. 12, pp. 4569–4578, Dec 2013.

[124] C. Yu, M. Allegue-Martinez, Y. Guo, and A. Zhu, "Output-Controllable Partial Inverse Digital Predistortion for RF Power Amplifiers," *IEEE Transactions on Microwave Theory and Techniques*, vol. 62, no. 11, pp. 2499–2510, Nov 2014.

[125] C. Yu, W. Cao, Y. Guo, and A. Zhu, "Digital Compensation for Transmitter Leakage in Non-Contiguous Carrier Aggregation Applications With FPGA Implementation," *IEEE Transactions on Microwave Theory and Techniques*, vol. 63, no. 12, pp. 4306–4318, Dec 2015.

[126] C. Yu, L. Guan, E. Zhu, and A. Zhu, "Band-Limited Volterra Series-Based Digital Predistortion for Wideband RF Power Amplifiers," *IEEE Transactions on Microwave Theory and Techniques*, vol. 60, no. 12, pp. 4198–4208, Dec 2012.

[127] C. Yu, J. Xia, X. Zhu, and A. Zhu, "Single-Model Single-Feedback Digital Predistortion for Concurrent Multi-Band Wireless Transmitters," *IEEE Transactions on Microwave Theory and Techniques*, vol. 63, no. 7, pp. 2211–2224, July 2015.

[128] X. Yu and H. Jiang, "Digital Predistortion Using Adaptive Basis Functions," *IEEE Transactions on Circuits and Systems I: Regular Papers*, vol. 60, no. 12, pp. 3317–3327, Dec 2013.

[129] G. Yuan, X. Zhang, W. Wang, and Y. Yang, "Carrier aggregation for LTE-advanced mobile communication systems," *IEEE Communications Magazine*, vol. 48, no. 2, pp. 88–93, February 2010.

[130] S. Zhang, W. Chen, F. M. Ghannouchi, and Y. Chen, "An iterative pruning of 2-D digital predistortion model based on normalized polynomial terms," in *2013 IEEE MTT-S International Microwave Symposium Digest (MTT)*, June 2013, pp. 1–4.

[131] D. Zhou and V. Debrunner, "A simplified adaptive nonlinear predistorter for high power amplifiers based on the direct learning algorithm," in *2004 IEEE International Conference on Acoustics, Speech and Signal Processing (ICASSP)*, vol. 4, May 2004, pp. iv–1037–40 vol.4.

[132] D. Zhou and V. DeBrunner, "A novel adaptive nonlinear predistorter based on the direct learning algorithm," in *2004 IEEE International Conference on Communications (ICC)*, vol. 4, June 2004, pp. 2362–2366 Vol.4.

[133] G. T. Zhou, H. Qian, L. Ding, and R. Raich, "On the baseband representation of a bandpass nonlinearity," *IEEE Transactions on Signal Processing*, vol. 53, no. 8, pp. 2953–2957, Aug 2005.

[134] A. Zhu and T. J. Brazil, "Behavioral modeling of RF power amplifiers based on pruned Volterra series," *IEEE Microwave and Wireless Components Letters*, vol. 14, no. 12, pp. 563–565, Dec 2004.

[135] A. Zhu and T. Brazil, "An adaptive Volterra predistorter for the linearization of RF high power amplifiers," in *IEEE MTT-S*, June 2002, pp. 461–464.

[136] A. Zhu, J. C. Pedro, and T. J. Brazil, "Dynamic Deviation Reduction-Based Volterra Behavioral Modeling of RF Power Amplifiers," *IEEE Transactions on Microwave Theory and Techniques*, vol. 54, no. 12, pp. 4323–4332, Dec 2006.

[137] A. Zhu, J. C. Pedro, and T. R. Cunha, "Pruning the Volterra Series for Behavioral Modeling of Power Amplifiers Using Physical Knowledge," *IEEE Transactions on Microwave Theory and Techniques*, vol. 55, no. 5, pp. 813–821, May 2007.

[138] R. Zi, X. Ge, J. Thompson, C. X. Wang, H. Wang, and T. Han, "Energy Efficiency Optimization of 5G Radio Frequency Chain Systems," *IEEE Journal on Selected Areas in Communications*, vol. 34, no. 4, pp. 758–771, April 2016.

Publications

Publication 1

M. Abdelaziz, Z. Fu, L. Anttila, A. M. Wyglinski, and M. Valkama, "Digital predistortion for mitigating spurious emissions in spectrally agile radios," *IEEE Communications Magazine*, vol. 54, no. 3, pp. 60-69, March 2016.

Digital Predistortion for Mitigating Spurious Emissions in Spectrally Agile Radios

Mahmoud Abdelaziz, *Student Member, IEEE,* Zhu Fu, *Member, IEEE,*
Lauri Anttila, *Member, IEEE,* Alexander M. Wyglinski, *Senior Member, IEEE*
Mikko Valkama, *Senior Member, IEEE,*

Abstract

Spectrally non-contiguous transmissions pose serious transceiver design challenges due to the nonlinear power amplifier (PA). When two or more non-contiguous carriers with close proximity are amplified by the same PA, spurious emissions inside or in the vicinity of the transmitter RF band are created. These spurious emissions may violate emission limits or otherwise compromise network coverage and reliability. Lowering the transmit power is a straightforward remedy, but it will reduce throughput, coverage, and power efficiency of the device. To improve linearity without sacrificing performance, several digital predistortion (DPD) techniques have recently been proposed to target the spurious emissions *explicitly*. These techniques are designed to minimize the computational and hardware complexity of DPD, thus making them better suited for mobile terminals and other low cost devices. In this article, these recent advances in DPD for non-contiguous transmission scenarios are discussed, with a focus on mitigating the spurious emissions in the concrete example case of non-contiguous dual-carrier transmission. The techniques are compared with more traditional DPD approaches in terms of their computational and hardware complexities, as well as linearization performance.

Index Terms

Carrier aggregation, cognitive radio (CR), digital predistortion (DPD), dynamic spectrum access (DSA), IEEE 802.22, software-defined radio (SDR), spectrally agile multicarrier transmission, spurious emission, TV white space, 3GPP LTE-Advanced.

Mahmoud Abdelaziz, Lauri Anttila, and Mikko Valkama are with the Department of Electronics and Communications Engineering, Tampere University of Technology, Tampere, Finland.

Alexander M Wyglinski is with the Wireless Innovation laboratory, Department of Electrical and Computer Engineering, Worcester Polytechnic Institute, Worcester, MA 01609, USA, URL: (see http://www.wireless.wpi.edu/).

Zhu Fu was with the Wireless Innovation laboratory. She is now with Qualcomm Inc., San Jose, CA, USA.

This work was partially supported by the Finnish Funding Agency for Innovation (Tekes) and the National Science Foundation (NSF) under the projects "Cross-Layer Modeling and Design of Energy-Aware Cognitive Radio Networks" and "Future Uncoordinated Small-Cell Networks Using Reconfigurable Antennas". The work was also supported by the Academy of Finland under grant 284694.

I. Introduction

3GPP LTE-Advanced (LTE-A) and cognitive radio (CR) type developments are recent examples of wireless communication systems that seek to utilize spectrally non-contiguous carriers in order to increase data rates and spectral flexibility. In LTE-A, carrier aggregation (CA) enables bandwidth expansion up to 100 MHz by aggregating five 20 MHz LTE carriers [1]. In the TV white space (TVWS) standard IEEE 802.22, known as the first cognitive radio standard, the aggregation of several carriers is called channel bonding [2]. In this article, we refer to all such transmission schemes simply as carrier aggregation or CA, and use the attributes contiguous and non-contiguous to separate spectrally contiguous and non-contiguous allocations.

One of the most challenging engineering concerns in the RF part of a transmitter is the power amplifier (PA), particularly due to its nonlinearity. Multicarrier transmissions exhibit very large peak-to-average power ratios (PAPRs), and when they are combined with the nonlinear behavior of the PA, can generate severe unwanted spectral emissions in the adjacent channels or in more distant portions of the spectrum. The levels of these emissions are mandated and enforced by federal regulators, such as the US Federal Communications Commission (FCC; see, e.g., [4]). Recently, it has been demonstrated in LTE-Advanced mobile transmitters with non-contiguous CA or multicluster type transmissions, that PA nonlinearities lead to spurious emissions that can violate the given spectrum emission limits [1], [3], or lead to own receiver desensitization in frequency-division duplexing (FDD) systems [3]. Within the CR context, the spurious emissions can also interfere with primary user (PU) transmissions or other secondary users (SU).

One obvious solution to decrease nonlinear distortion is to back off the transmit power. In 3GPP terminology, this is known as Maximum Power Reduction (MPR), and MPR values up to 16 dB are allowed in some CA use cases for mobile terminals [1]. However, this approach yields a significantly lower PA efficiency as well as a substantial reduction in the uplink coverage and throughput. For example, if we assume the well-known COST Hata propagation model for urban areas[1], along with a base station antenna height of 50 m, a 10 dB reduction in transmit power will result in halving of the coverage[2]. Thus, there is a clear need for alternative linearization solutions that do not possess such drastic adverse effects. This article focuses on one linearization solution in particular: digital predistortion (DPD).

Most of the current DPD literature is focused on base stations and other infrastructure nodes where DPD is the *de facto* solution for linearization. However, only few published works consider DPD for mobile terminals and other low cost devices. One of the main reasons is that usually the cost of implementing a DPD solution, in terms of hardware and needed computations, is relatively high. Furthermore, with traditional contiguous transmit spectrum, linearization of mobile transmitters is usually not needed since transmit power levels are generally smaller and emission limits looser relative to base

[1] *Digital Mobile Radio Towards Future Generation Systems*, COST 231 Final Report. Available at http://146.193.65.101/cost231/

[2] Coverage is defined here as the distance over which a certain received signal-to-noise ratio is obtained.

stations or infrastructure nodes. However, this is about to change as non-contiguous CA waveforms are being deployed across a variety of systems.

This article addresses the nonlinearities of terminals that transmit non-contiguous CA waveforms, the resulting spurious emissions, as well as their suppression with DPD. The primary focus is on LTE-Advanced mobile terminals while we also acknowledge that another potential application area is in TVWS devices. The objectives of this article are generally three-fold: (i) To highlight the problem of PA-induced spurious emissions with non-contiguous transmissions, and the potential problems it may create in different systems; (ii) To demonstrate that back-off is not the only feasible solution to decreasing the unwanted emissions, but DPD is a potential solution that does not sacrifice the power efficiency, coverage, or throughput of the mobile user; (iii) To increase the awareness of the readership of this magazine with respect to recent advances in DPD for non-contiguous transmission schemes. We consider this to be one key element in enhancing the flexibility of radio spectrum usage in emerging radio communication systems.

The rest of this article is organized as follows. Section II gives an overview of the linearity challenges with spectrally non-contiguous transmissions, and presents the relevant emission regulations of 3GPP LTE-Advanced. Recent advances of DPD techniques for spurious emission suppression are discussed in Section III. Section IV discusses the implementation complexity of the methods presented in Section III. Simulation and RF measurement results are provided in Section V. Finally, several concluding remarks are made in Section VI.

II. Linearity Challenges in Employing Non-Contiguous Transmissions

A. 3GPP LTE-Advanced and Unwanted Emissions

In order to meet the requirements of the International Mobile Telecommunications-Advanced (IMT-A) specifications, 3GPP began introducing carrier aggregation (CA) from Release 10 onwards. Release 10 is also the first release where the technology is called LTE-Advanced (LTE-A). For the uplink, Release 10 introduced contiguous CA, allowing only contiguous UE resource allocation per individual carrier. Uplink specifications were again updated with Release 11, which introduced the so-called multicluster transmission, which means that non-contiguous resource allocation can be performed within a single uplink carrier. Release 12 yielded two additional major updates, as non-contiguous intraband CA and interband CA were introduced, where the LTE-A UE can be allocated UL resources across aggregated spectrum consisting of two or more component carriers (CCs). The CCs may possess a bandwidth of any single carrier bandwidth defined within the LTE specifications and a maximum of five component carriers can be aggregated, with a theoretical maximum aggregated bandwidth equal to 100 MHz.

In general, the transmitter unwanted emissions can be divided into three parts: (i) The emissions within the carrier bandwidth, (ii) the out-of-band (OOB) emissions, and (iii) the spurious emissions. The OOB emissions are unwanted emissions immediately outside the assigned channel bandwidth resulting from the modulated waveform characteristics and nonlinearity of the transmitter, but excluding the spurious

emissions, and are specified in terms of the spectrum emission mask and adjacent channel leakage ratio (ACLR). Spurious emissions, in turn, are unwanted emissions that are caused by the transmitter nonlinear effects such as harmonic and intermodulation products, parasitic emissions, and frequency conversion products, with the OOB emissions excluded. The exact requirements for spectral emissions are specified in [1]. In this article, we are mainly interested in the spurious emission limits. For carrier frequencies above 1 GHz, where most LTE-A bands are located, the spurious emission limit is -30 dBm over a 1 MHz measurement bandwidth. This is a general guideline defined by ITU-R [4], which means that it applies to all land mobile services, not just LTE-A.

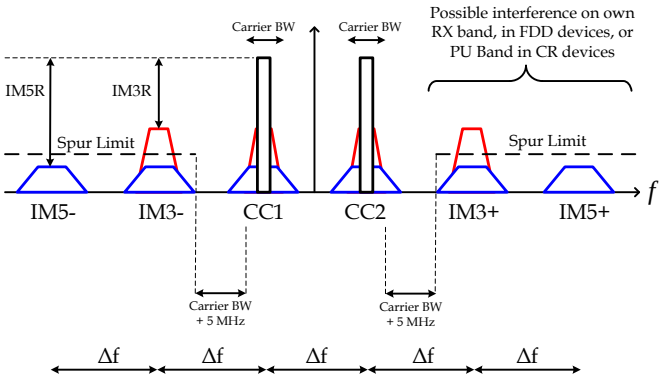

Fig. 1. Example transmit spectrum with non-contiguous carrier aggregation under a nonlinear PA. In this illustration, nonlinear distortion products up to order five are shown, including nonlinear distortion around the main carriers as well as at the IM3 and IM5 sub-bands.

B. Linearity Challenges with Non-contiguous Dual-carrier Transmissions

When a non-contiguous dual-carrier signal is applied to the PA input, the PA nonlinearity leads to intermodulation and cross modulation products affecting many different frequencies, as shown in Fig. 1. Assuming a CC separation of Δf, in addition to the spectral regrowth around the main carriers, intermodulation distortion appears at integer multiples of Δf away from the main CCs. The third-order intermodulation (IM3) sub-bands are centered at Δf from the main CCs, the fifth-order intermodulation (IM5) sub-bands are located at $2\Delta f$ from the main CCs, and so on. These intermodulation distortion (IMD) components may affect the system in two different ways, depending on the CC locations and their separation, as well as on the bandwidth of the transmit filter.

First, the intermodulation spurs created by the nonlinear PA will likely be in the spurious domain, and therefore should obey the more strict spurious emission limits, as opposed to the spectral emission limits which are defined in the vicinity of the carriers [1], [4]. In the context of interband CA, where the component carriers are located at different RF bands, the spurs will likely be filtered out by the transmitter RF filter. However, in the case of intraband CA, where the component carriers are inside the

same RF band, some of the spurious IM sub-bands may be located in-band, and therefore will not be mitigated by the transmit RF filter. Narrower bandwidth allocations per CC are more problematic, since the energy of the spurs is more concentrated, therefore more easily violating the spur limit [3]. To avoid spur limit violations, the mobile device should therefore back off its output power to operate within the linear range of the PA. However, this back off will lead to a reduction in the UL coverage range, as well as to inefficient operation of the PA. In Section III, DPD processing is introduced as a solution to allow a mobile device to meet the spurious emission limit while considerably reducing the amount of required back off.

Secondly, in FDD terminals employing non-contiguous intraband transmissions, the spurious components may potentially overlap with the receive band of the device, causing *own receiver desensitization* [3]. Carrier aggregation reduces the duplexing distance between own TX and RX, and therefore reaching sufficient isolation between own TX and RX using RF duplexers is increasingly difficult[3]. Own receiver desensitization can also be alleviated with digital predistortion, as will be described in the following.

III. Low-Complexity Sub-band Digital Predistortion for Non-Contiguous Transmission Schemes

In order to meet linearity requirements without sacrificing performance, digital pre-distortion has been proposed and recognized as a promising PA linearization technique due to its accuracy and cost-effectiveness, particularly for high-power high-end base station devices. There have been substantial research efforts over the past 20 years with respect to developing efficient and elaborate DPD techniques for various single-band transmission schemes where linearization for the whole transmit band is essentially pursued. These conventional DPD approaches take as their inputs the full composite transmit band, and we thus refer to these DPD approaches as *full-band DPD*. The tutorial paper in [5] provides an overview of these techniques, while this paper only addresses these techniques from the DPD complexity perspective. There have also been a handful of recent works on efficient linearization techniques for multi-band transmitters that employ only a single PA, where it has been assumed that the component carriers are separated by enough distance such that the spurious emissions are filtered out by the transmit filter. This approach, referred to as *concurrent linearization*, is treated in a recent overview paper [6]. Such techniques are also out of the scope of this paper.

The scope of this paper is to introduce efficient low complexity DPD techniques for mitigating the spurious emissions of non-contiguous transmissions, while not concentrating specifically on the linearization of the component carriers. This approach is motivated by two main factors. First, the emission limits in the spurious region are stricter than in the spectral regrowth region around the component carriers, and are therefore more easily violated in the context of intraband non-contiguous CA. Second, by concentrating linearization efforts to certain spurious emissions only, the processing and

[3]This problem has been acknowledged by 3GPP, e.g., in R4-123797, *"UE reference sensitivity requirements with two UL carriers"*, Ericsson and ST-Ericsson, available at http://www.3gpp.org

hardware complexity of a device can be significantly reduced, thus facilitating the implementation of DPD linearization in lower-cost devices and potentially even mobile terminals. The main target application for these techniques is thus the mobile terminal transmitter, where computational and hardware complexity are critical, although there are no technical limitations to applying these techniques in base stations or infrastructure nodes as well.

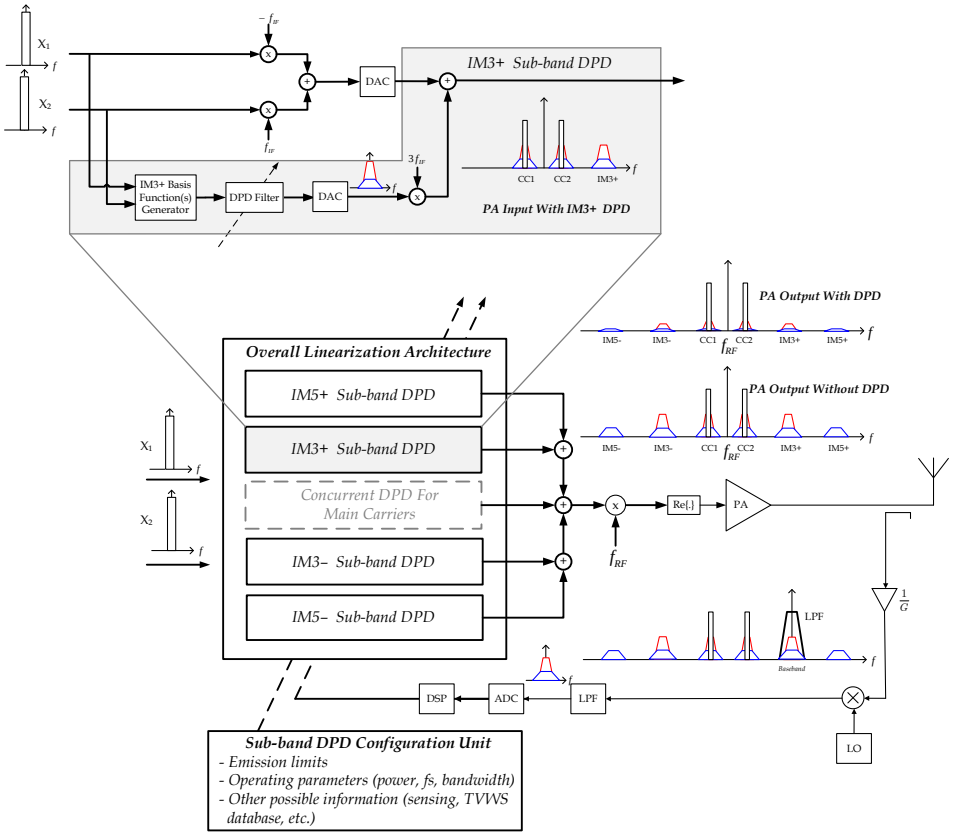

Fig. 2. Top: A detailed block diagram showing the spur injection based sub-band DPD operating principle for the positive IM3 sub-band. Bottom: Complete linearization architecture with multiple sub-band DPD stages, that can be flexibly activated based on prevailing emission limits and spectrum access scenario. The architecture can also be complemented with the concurrent DPD block, shown in gray, if main carrier linearization is pursued.

There have been some recent studies in the literature that consider the mitigation of the spurious emissions explicitly. In [7], [8], such processing was added to complement a concurrent linearization system, while assuming frequency-flat PA responses within the processed spurious sub-bands. In [7], the DPD parameter estimation was done offline, based on extracting the quasi-memoryless PA parameters using a large-signal network analyzer (LSNA). In [8], a memoryless least-squares fit between the observed IMD at the considered sub-band and certain basis functions was performed. The estimated

and regenerated IMD was then injected to the PA input, oppositely phased, such that it cancels the IMD at the PA output. In [9], on the other hand, the IM3 spurious sub-bands were specifically targeted, and component carrier linearization was not pursued. Furthermore, the DPD parameter identification was based on closed-loop feedback with a decorrelation-based learning rule. A block-adaptive version of this DPD solution was developed and tested in a real-time FPGA implementation in [10], demonstrating a stable response with good linearization performance. All of the above works assume a special DPD structure for the spurious emissions, which we here refer to as *sub-band DPD*. In such processing, the spurious components that we wish to remove from the PA output are modeled explicitly at the digital baseband, and injected into the PA input with proper amplitude and phase such that at the PA output the spurs are suppressed. Such spur injection based sub-band DPD is depicted in Fig. 2, which illustrates in more details the mitigation of the positive IM3 sub-band. The overall linearization architecture with multiple sub-band DPD blocks is illustrated in the same figure. This architecture is also called frequency-selective DPD in [7]. For more technical details, refer to [7]–[10].

In addition to the sub-band DPD concept, several full-band DPD solutions towards mobile terminals are worth mentioning. These solutions have the capability to tune their linearization efforts to certain sub-bands/frequencies, based on the current spectrum allocations and emission limits, to reduce the complexity of the DPD, or both [11]–[13]. These solutions, however, entail a similar complexity disadvantage, compared to the sub-band DPD, as any full-band DPD technique. The complexity perspectives are reviewed in more details in the next section.

IV. Computational and Hardware Complexity Perspectives

A. General Aspects

The relative computational requirements of the sub-band DPD approach when compared to traditional full-band DPD processing are generally reduced, especially when the LTE-A CCs are significantly separated. In this section, we provide a more thorough analysis of the computing and hardware complexity in these two DPD architectures. As an illustrative example, a full-band DPD with fifth order nonlinearity needs to run at a sample rate that is five times the composite dual-carrier signal bandwidth, which quickly becomes impossible when the carrier separation increases. With the sub-band technique, on the other hand, the minimum sample rate is less than or equal to five times the bandwidth of the wider component carrier. To give a numerical example, let us assume a CA scenario with two 1 MHz carriers separated by 30 MHz. The minimum sample rate with a traditional fifth order full-band DPD would be 155 MHz, whereas with the sub-band DPD, it is only 5 MHz. In addition, the required filter lengths in the full-band DPD are likely to be substantially longer than with sub-band DPD, since the former is predistorting a signal band which is an order of magnitude larger. The overall complexity difference therefore grows when the component carrier spacing is increased and/or higher order DPDs are considered.

B. Full-band and Sub-band DPD Running Complexities

We shall focus here on the running complexity of the DPD (see [14]), which is most critical for mobile-type devices. It involves the number of computations performed per second when the DPD is operating and the device is transmitting. To quantify the computational complexity differences between the full-band and sub-band DPD architectures, we shall use the number of floating point operations (FLOPs) per sample and the required sample rate in the predistortion path. The running complexity is further divided into two parts: basis function generation, and predistortion using the basis functions [14].

The full-band DPD architecture that we use as a reference is based on the parallel Hammerstein (PH) nonlinear model. The overall running complexity for a seventh order PH model with memory order six, used as the reference solution in Section V, is 201 FLOPs per output sample [14].

In the sub-band architecture, on the other hand, the third and fifth order basis functions read $x_2^*(n)x_1^2(n)$ and $2|x_1(n)|^2x_2^*(n)x_1^2(n) + 3|x_2(n)|^2x_2^*(n)x_1^2(n)$, respectively, when the positive IM3 sub-band is considered[4]. Consequently, the number of FLOPs required for basis function generation in the sub-band DPD is 22 FLOPs per sample per sub-band. In the sub-band architecture, we can assume a smaller filter length, due to the significantly smaller bandwidth of the predistorted signal. Additionally, the main carriers are not predistorted. Altogether in the filtering stage, assuming filter length of 3, 48 FLOPs per sample are required per sub-band. Thus, the total number of FLOPs required by the sub-band DPD in our example is 70 FLOPs per sample per processed sub-band.

The required sample rates in the example scenario of two 1 MHz CCs with 30 MHz carrier spacing, are 217 MHz and 5 MHz for the full-band and the sub-band DPD's, respectively. Based on these numbers and the above FLOP analysis, the number of FLOPs per second (FLOPS) becomes 43.617 GFLOPS for the full-band DPD, and 0.35 GFLOPS per sub-band for the sub-band DPD. These numbers are also summarized in Table I.

C. System Power Efficiency Perspectives

When a DPD is adopted, a less linear but more efficient PA, that can operate near its saturation region, can generally be used. However, the overall power efficiency of the device is only improved if the extra power consumed by the DPD stage is less than the power savings due to increased PA efficiency. Here, we address this aspect from a mobile device perspective.

We consider a practical scenario where the transmit power at the output of the mobile PA is +26 dBm (i.e. 400 mW), stemming from 3GPP LTE-Advanced requirements [2], [5], and assume that the TX duplexer filter and connector insertion losses are 3 dB. Then, practical example figures of PA power efficiency, when operating in non-linear or linear modes, are around 30% and 20% (or even less), respectively. This means that the power consumed by the nonlinear PA is roughly 1300 mW, while the

[4]This is based on an extension of the analysis done in [9], with higher order nonlinearities considered instead of only third order nonlinearity. Here, $x_1(n)$ and $x_2(n)$ denote the digital baseband waveforms of the two CC's.

corresponding linear PA consumes roughly 2000 mW. In other words, adopting a more power-efficient nonlinear PA saves 700 mW of power in this particular example.

On the other hand, in the CA scenario assumed in the previous subsection, the sub-band DPD requires 350 MFLOPS per sub-band. If we focus our linearization on the two IM3 sub-bands, 700 MFLOPS are required for the sub-band DPD processing. As a practical example, the state-of-the-art 28nm DSP implementation in [15] has a processing power consumption of 23.4 mW at 230 MHz. Assuming 4 FLOPs per clock cycle, this DSP can support 920 MFLOPS, which is clearly sufficient in this example case. Thus, since the DPD already saves 700 mW of power in the PA interface, while consuming only 23.4 mW in the processing, the power budget is clearly in favor of using the sub-band DPD in this example. If the DPD processing is implemented using hardware, an even more power efficient solution can be realized.

D. Flexibility and Feedback Receiver Perspectives

Another clear advantage of the sub-band architecture is that each sub-band DPD block can be switched on or off according to the induced emission levels at these sub-bands, as well as possible band or area specific emission limitations. The overall DPD architecture in Fig. 2 has a configuration unit that can activate/deactivate the sub-band DPD blocks according to the input coming from two different sources. The first is the anticipated/measured spurious emissions relative to the emission limits. The second source is the operating system parameters (power, bandwidth, carrier frequencies, etc.) that are used to decide whether DPD is needed in the current system configuration. In TVWS applications, additional information from spectrum sensing and/or TVWS database can also be employed. In general, this kind of flexibility in the sub-band DPD architecture can lead to substantial power savings, as the linearization can be tailored and directed only to those frequencies where intermodulation suppression is really needed. Such flexibility is not available in the traditional full-band DPD solutions since, by design, the predistorter tries to linearize the full composite transmit band.

In addition to the complexity reduction and flexibility of the DPD main path, the feedback path complexity used for DPD parameter estimation is also greatly reduced. In order to estimate the parameters of the positive IM3 DPD, as an example, we only need to observe the positive IM3 sub-band at the PA output instead of observing the whole signal band (including the IM sub-bands), which is the case with full-band DPD. This reduction in the observation bandwidth reduces the cost, complexity, and power consumption in the feedback path, thus allowing the use of simpler instrumentation and making the approach suitable for mobile-type devices.

V. Simulation and RF Measurement Examples

In order to demonstrate and quantify the performance/complexity trade-offs between full-band and sub-band DPD architectures, both MATLAB simulation and RF measurement results are presented in this section. We quantify the linearization performance primarily through the obtained suppression of the spurious energy at the considered sub-band, while also passband Error Vector Magnitude (EVM)

values are reported. Measurement examples with a commercial LTE-A mobile PA and a small-cell base station PA are also provided as a strong proof-of-concept of the sub-band DPD architecture.

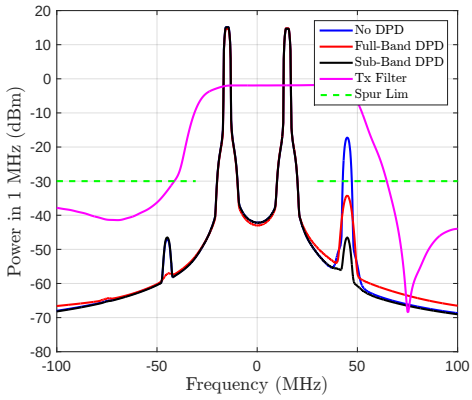

(a)

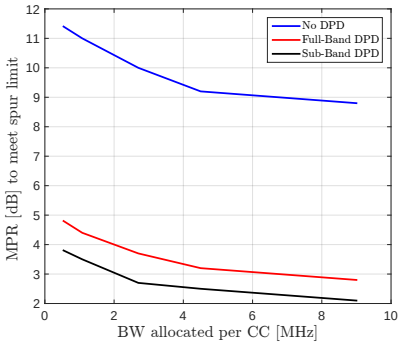

(b)

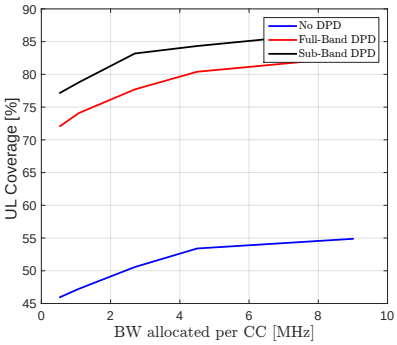

(c)

Fig. 3. Dual-carrier mobile transmitter baseband equivalent power spectra, required MPRs and UL coverage. The full-band and sub-band DPDs are compared to not using DPD. Full-band DPD is 7^{th} order Parallel Hammerstein, while the sub-band DPD builds on 3^{rd} and 5^{th} order basis functions. In (a), two 1 MHz CCs are transmitted with Tx power of +18 dBm. In (b), the required MPRs to meet the TX spurious emission limits are shown, without and with DPD, and with different allocated bandwidths per CC. In (c), UL network coverages after applying the needed backoff (MPR) to meet the emission limits are shown, in percentage of the full coverage at +23 dBm TX power and linear PA. COST Hata propagation model is assumed for radio propagation between the mobile and the basestation, assuming basestation antenna height of 50m.

A. Simulation Scenarios and Results

Now we illustrate two possible applications of the proposed sub-band DPD solution. The first example shows the suppression of spurious IMD components in order to meet the transmitter spurious emission limits without applying a large backoff. In the second example, the sub-band DPD approach is used to

suppress spurious IMD components falling onto the own RX band in an FDD transceiver, thus preventing own RX desensitization.

1) Meeting Spurious Emission Limits: In this example, a carrier aggregated LTE-A uplink signal with QPSK subcarrier modulation is applied to a wide-band parallel Hammerstein PA model of nonlinearity order 5, which is based on measurements of a real mobile PA. The carrier separation between the two CCs is 30 MHz. A transmit filter model based on a real measured mobile duplexer is also used in the simulations. The response of the transmit filter is shown in Fig. 3(a). The occupied bandwidth within each CC is 1 MHz and the carriers are allocated such that the positive IM3 sub-band lies inside the transmit filter passband.

The sub-band DPD is tuned to predistort only the positive IM3 sub-band, since the negative one is already filtered by the transmit filter, as shown in Fig. 3(a). The employed fifth-order sub-band DPD is utilizing two basis functions based on an extended architecture of the one presented in [9], and each basis function is filtered by a three-tap filter.

In the full-band DPD case, implemented for reference, a seventh order parallel Hammerstein DPD based on the indirect learning architecture (ILA) in [5] is used. Altogether four filters, all with 6 taps, are used in the full-band DPD. Three ILA iterations are used. In the full-band DPD, an inherent 1.5 dB backoff needs to be applied to the transmit path in order to account for the slight increase in the PAPR due to the predistortion, something which is not needed in the sub-band DPD. Therefore, for a fair comparison, the transmitter power levels are adjusted such that the output power after the PA is the same for both DPDs.

In Fig. 3(a), the Tx power level is +18 dBm, and it can be seen that without applying any DPD processing, the transmitter clearly violates the spurious emission limit of -30 dBm/MHz. After adopting the DPD processing, the spur levels are below the limit with both DPD architectures.

Table I shows a quantitative comparison of the complexity and performance of the full-band and sub-band DPDs. The complexity is clearly in favor of the sub-band DPD, where the required number of FLOPs per second (FLOPS) is substantially lower than in the full-band DPD, as discussed already in Section IV. As for the actual linearization performance, both DPDs give good suppression for the IM3 distortion. We quantify the suppression of intermodulation power at the IM3 sub-bands through the power ratios relative to the component carrier wanted signal power as shown in Fig. 1, and defined as $IM3R_{dB} = 10\log_{10}(P_{wanted,cc}/P_{IM3})$. The IM3R at the positive IM3 sub-band is shown in Table I for the CC allocations in Fig. 3(a). The sub-band DPD provides better performance in terms of the positive IM3R compared to the full-band DPD in this particular scenario. The inband distortion (i.e., EVM) is also measured, where the full-band DPD outperforms the sub-band DPD. This is expected, since the full-band DPD linearizes the whole transmit band, including the main component carriers. However, the EVM with the sub-band DPD is only around 2.3% which is clearly enough for modulations at least up to 64-QAM. Additionally, the EVM degradation due to the sub-band DPD, as compared to without DPD, is only around 0.06%.

TABLE I

QUANTITATIVE RUNNING COMPLEXITY AND LINEARIZATION PERFORMANCE COMPARISON OF FULL-BAND VERSUS SUB-BAND DPD. TWO 1 MHZ COMPONENT CARRIERS SEPARATED BY 30 MHZ. SC-FDMA COMPONENT CARRIER WAVEFORMS WITH QPSK DATA MODULATION.

	Running Complexity			**Performance**	
	Coeffs	Fs [MSPS]	GFLOPS	EVM [%]	Positive IM3R [dBc]
No DPD	N/A	N/A	N/A	2.23	30.94
Full-Band DPD	24	217	43.6	0.25	46.65
Sub-Band DPD	6	5	0.35	2.29	59.30

Fig. 3(b) shows the required MPR for different transmission scenarios, relative to maximum transmit power of +23 dBm, assuming duplexer and other connector losses of 3 dB. Both full-band and sub-band DPDs are compared versus no DPD, and with the allocation bandwidth per CC varied. A reduction of almost 8 dB in the required MPR can be achieved when the sub-band DPD is used. This directly impacts the uplink coverage of the mobile network as shown in Fig. 3(c), where the percentage of the UL coverage relative to the maximum coverage at +23 dBm is shown with and without DPD, assuming the COST Hata propagation model. As can be seen, coverage extensions in the order of several tens of percentages can be achieved by adopting the sub-band DPD processing.

2) Suppressing Spurious Components at Own RX Band: In FDD transceivers, the TX spurious components may also overlap with the own RX band and thus desensitize the own RX [3]. The proposed IM3 sub-band DPD solution can be effectively applied to relax this problem. In this example, the transmit signal is again a carrier aggregated LTE-A uplink signal with QPSK subcarrier modulation. Each CC is allocated 50 LTE resource blocks (RBs, 10 MHz CC bandwidth), and the CCs are separated in frequency by 50 MHz. The PA is modeled with a fifth-order Wiener nonlinearity, i.e., a linear time-invariant (LTI) filter followed by static nonlinearity. Following typical commercial duplexer stopband responses, the duplexer filter is modeled to have frequency-selective stopband attenuation of around 50 dB at the RX band. The desired RX signal is an LTE-A downlink OFDM(A) signal with 50 RBs and QPSK subcarrier modulation. The spurious IMD at the positive IM3 sub-band due to PA nonlinearity now overlaps with the RX band, thus interfering the desired RX signal. The reference thermal noise power level at RX input is -104 dBm/10 MHz, RX noise figure is 9 dB, and the reference sensitivity level is -93.5 dBm [1], [3].

Fig. 4(a) shows the spectra of different signal components at the RX band at +20 dBm TX power, with and without using the proposed IM3 sub-band DPD. The spectra are normalized relative to the thermal noise level. It can be observed that strong spurious IMD interference leaks through the duplexer filter and appears at the RX band, hence corrupting the reception. The proposed sub-band DPD is able to reduce the unwanted emissions and push the interference below the noise floor.

To further quantify the performance, the own receiver signal-to-interference plus noise ratio (SINR) is evaluated against different TX power levels. The obtained SINR curves with different TX power levels

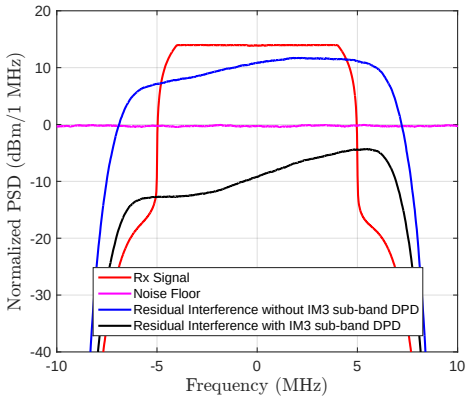

(a)

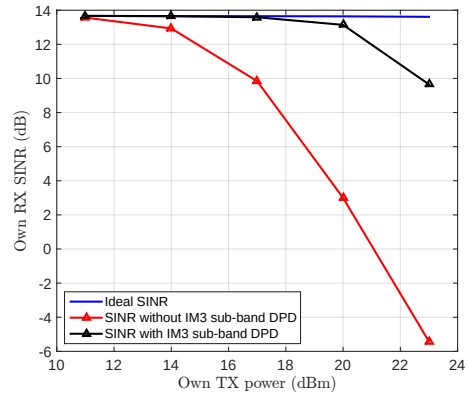

(b)

Fig. 4. Using DPD to relieve own RX desensitization, in the case that own TX IM3 subband overlaps with the own RX band. A fifth order Wiener PA model is used, with PA gain, IIP3, and 1-dB compression point equal to 20 dB, +17 dBm, and +27 dBm, respectively. The transmit signal is a CA LTE-A uplink signal with QPSK subcarrier modulation, 10 MHz allocation per CC, and 50 MHz CC spacing. A duplexer filter model with frequency selective stop band attenuation of 50 dB at the RX band is assumed. The desired RX signal is a 10 MHz LTE-A downlink OFDM(A) signal with QPSK subcarrier modulation. (a) Spectra of different signal components at own RX band at +20 dBm TX power. (b) Illustration of own RX SINR for different TX powers, with and without sub-band DPD.

are shown in Fig. 4(b). The impact of spurious IMD interference on the own receiver performance can now be seen more clearly, indicating that when TX power level increases above +14 dBm, the spurious IM3 starts to deteriorate the RX SINR. The sub-band DPD solution can enhance the SINR at the own RX band by up to 15 dB, and thus substantially extend the usable TX power range.

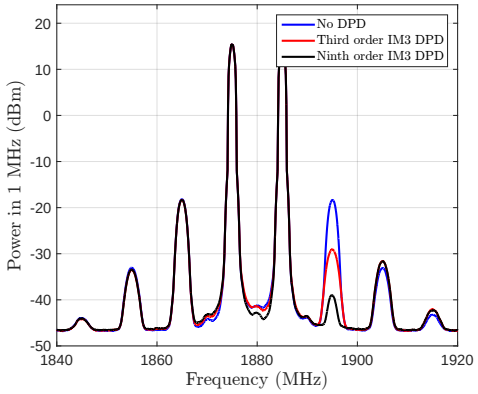

(a)

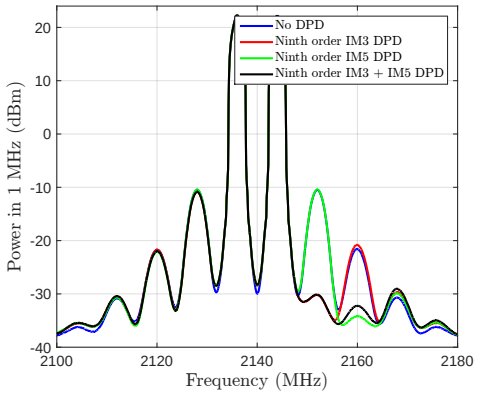

(b)

Fig. 5. Two RF measurement examples showing the gain from using a sub-band DPD focused on the positive IM3 and/or IM5 sub-bands. In (a), IM3 spur reduction with both third-order and ninth-order sub-band DPDs are demonstrated, using a real commercial mobile PA operating at +20 dBm. A multicluster TX scenario with 1 MHz allocated per cluster and 10 MHz cluster spacing. In (b), both IM3 and IM5 spurs are predistorted separately as well as simultaneously using ninth-order sub-band DPDs. The measured PA is a commercial off-the-shelf small-cell base station PA, operating at +25 dBm output power. A multicluster TX scenario with 2 MHz allocated per cluster and 8 MHz cluster spacing.

B. RF Measurement Examples

The sub-band DPD solution is next tested through actual RF measurements using a commercial LTE-Advanced mobile terminal power amplifier designed for LTE UL band 25 (1850 – 1915 MHz). The RF transceiver used is a National Instruments (NI) PXIe-5645R vector signal transceiver (VST). The digital baseband waveform is first generated locally on the computer, then transferred to the VST to perform I/Q modulation at 1880 MHz. The VST output signal, with -10 dBm power, is then fed to the

mobile PA with output power of +20 dBm. The PA output at considered IM subband is observed with the VST, through a 40 dB attenuator. The observed and filtered baseband I/Q samples, together with the transmitted samples, are then used by the computer for DPD learning. The DPD learning is performed with a sequence of 50k samples after which the resulting obtained parameters are applied for measuring and quantifying the PA output. The DPD learning algorithm is based on an extension of [9], where now also fifth, seventh and ninth-order nonlinearities are considered at IM3 sub-band in addition to third-order nonlinearities. Fig. 5(a) shows the power spectral density at the PA output with and without using the sub-band DPD. The signal used is a multicluster LTE-A signal with 1 MHz per cluster and 10 MHz cluster separation. The intermodulation distortion at the considered IM3 sub-band is suppressed by 20 dB with the higher order sub-band DPD, and giving an additional 10 dB gain compared to the basic third order sub-band DPD.

For further demonstration, another measurement example using an off-the-shelf small-cell base station PA[5] is presented in Fig. 5(b). In this example, the LTE-A cluster bandwidths are 2 MHz each, with 8 MHz cluster separation. Here, both IM3 and IM5 spurs are separately predistorted using ninth-order sub-band DPDs. The distortion at the IM3 and IM5 sub-bands is successfully suppressed by 20 dB and 12 dB, respectively. The power spectrum with simultaneous deployment of IM3 and IM5 sub-band DPDs is also shown in Fig. 5(b), demonstrating sufficient spur suppression in this case as well.

VI. Conclusions

In this article, we considered the problem of transmitter power amplifier induced spurious emissions with non-contiguous carrier aggregation, and discussed low-complexity digital predistortion for their mitigation in the mobile terminal transmitter. For non-contiguous CA transmissions, a recently proposed sub-band DPD structure was shown to yield linearization results beyond the conventional full-band DPD solution, while also reducing the computational complexity in a substantial manner. The example results indicate and demonstrate that with sub-band DPD, the spurious emission limits can be met with much smaller power back-offs. Thus, by employing sub-band DPD, the uplink coverage, throughput and PA efficiency need not be sacrificed in order to meet the emission limits. The sub-band DPD techniques can also be employed in protecting the FDD terminal receiver from desensitization, as well as in protecting the primary users in cognitive radio networks. This article is seeking to spark discussion, raise awareness and catalyze further research in the field of reduced-complexity DPD for non-contiguous transmissions, in particular for mobile devices.

[5]The measurement setup for the basestation PA example is provided by an online weblab sponsored by National Instruments and Chalmers University of Technology, at http://dpdcompetition.com/access-weblab/

REFERENCES

[1] *LTE Evolved Universal Terrestrial Radio Access (E-UTRA): User Equipment (UE) radio transmission and reception*, 3GPP TS 36.101 V12.4.0 (Release 12), June 2014.

[2] *Cognitive Wireless RAN Medium Access Control (MAC) and Physical Layer (PHY) specifications: Policies and procedures for operation in the TV Bands*, IEEE Standard 802.22-2011, July 2011.

[3] C. S. Park, L. Sundström, A. Wallen, and A. Khayrallah, "Carrier aggregation for LTE-advanced: design challenges of terminals," *IEEE Communications Magazine*, Dec. 2013, pp. 76–84.

[4] *Unwanted emissions in the spurious domain*, Recommendation ITU-R SM.329-12, Sept. 2012.

[5] F. M. Ghannouchi and O. Hammi, "Behavioral modeling and predistortion," *IEEE Microwave Magazine*, pp. 52–64, Dec. 2009.

[6] P. Roblin, C. Quindroit, N. Naraharisetti, S. Gheitanchi, and M. Fitton, "Concurrent linearization," *IEEE Microwave Magazine*, pp. 75–91, Nov. 2013.

[7] J. Kim, P. Roblin, D. Chaillot, and Z. Xie, "A generalized architecture for the frequency-selective digital predistortion linearization technique," *IEEE Transactions on Microwave Theory and Techniques*, vol. 61, pp. 596–605, Jan. 2013.

[8] S. Bassam, M. Helaoui, and F. Ghannouchi, "Channel-selective multi-cell digital predistorter for multi-carrier transmitters," *IEEE Transactions on Microwave Theory and Techniques*, vol. 60, pp. 2344–2352, Aug. 2012.

[9] M. Abdelaziz, L. Anttila, A. Mohammadi, F. Ghannouchi, and M. Valkama, "Reduced-complexity power amplifier linearization for carrier aggregation mobile transceivers," in *IEEE International Conference on Acoustics, Speech, and Signal Processing* (ICASSP'14), Florence, Italy, May 2014.

[10] M. Abdelaziz, C. Tarver, K. Li, L. Anttila, M. Valkama, and J. Cavallaro, "Sub-band Digital Predistortion for Noncontiguous Transmissions: Algorithm Development and Real-Time Prototype Implementation," Accepted in *49th Asilomar Conf. Signals, Systems, and Computers, Pacific, Grove, CA, USA*, Nov. 2015.

[11] Z. Fu, L. Anttila, M. Abdelaziz, M. Valkama, and A. Wyglinski, "Frequency-Selective Digital Predistortion for Unwanted Emission Reduction," *IEEE Transactions on Communications*, vol. 63, pp. 254–267, Jan. 2015.

[12] C. Yu, L. Guan, E. Zhu, and A. Zhu, "Band-limited Volterra series-based digital predistortion for wideband RF power amplifiers," *IEEE Transactions on Microwave Theory and Techniques*, vol. 60, pp. 4198–4208, Dec. 2012.

[13] R. Braithwaite, "Closed-Loop Digital Predistortion (DPD) Using an Observation Path With Limited Bandwidth," *IEEE Transactions on Microwave Theory and Techniques*, vol. 63, pp. 726–736 , Feb. 2015.

[14] A. S. Tehrani, H. Cao, S. Afsardoost, T. Eriksson, M. Isaksson, and C. Fager, "A Comparative Analysis of the Complexity/Accuracy Tradeoff in Power Amplifier Behavioral Models," *IEEE Transactions on Microwave Theory and Techniques*, vol. 58, pp. 1510–1520, June 2010.

[15] M. Saint-Laurent, et. al, "A 28 nm DSP Powered by an On-Chip LDO for High-Performance and Energy-Efficient Mobile Applications," *IEEE Journal of Solid-State Circuits*, vol. 50, pp. 81–91, Jan. 2015.

Publication 2

M. Abdelaziz, L. Anttila, C. Tarver, K. Li, J. Cavallaro, and M. Valkama, "Low-complexity Subband Digital Predistortion for Spurious Emission Suppression in Noncontiguous Spectrum Access," *IEEE Transactions on Microwave Theory and Techniques*, vol. 64, no. 11, pp. 3501-3517, Nov. 2016.

Low-Complexity Sub-band Digital Predistortion for Spurious Emission Suppression in Noncontiguous Spectrum Access

Mahmoud Abdelaziz, *Student Member, IEEE,* Lauri Anttila, *Member, IEEE,*
Chance Tarver, *Student Member, IEEE,* Kaipeng Li, *Student Member, IEEE,* Joseph R. Cavallaro, *Fellow, IEEE,*
Mikko Valkama, *Senior Member, IEEE*

***Abstract*—Noncontiguous transmission schemes combined with high power-efficiency requirements pose big challenges for radio transmitter and power amplifier (PA) design and implementation. Due to the nonlinear nature of the PA, severe unwanted emissions can occur, which can potentially interfere with neighboring channel signals or even desensitize the own receiver in frequency division duplexing (FDD) transceivers. In this article, to suppress such unwanted emissions, a low-complexity sub-band DPD solution, specifically tailored for spectrally noncontiguous transmission schemes in low-cost devices, is proposed. The proposed technique aims at mitigating only the selected spurious intermodulation distortion components at the PA output, hence allowing for substantially reduced processing complexity compared to classical linearization solutions. Furthermore, novel decorrelation based parameter learning solutions are also proposed and formulated, which offer reduced computing complexity in parameter estimation as well as the ability to track time-varying features adaptively. Comprehensive simulation and RF measurement results are provided, using a commercial LTE-Advanced mobile PA, to evaluate and validate the effectiveness of the proposed solution in real world scenarios. The obtained results demonstrate that highly efficient spurious component suppression can be obtained using the proposed solutions.**

***Index Terms*—Adaptive filters, carrier aggregation, digital predistortion, frequency division duplexing, nonlinear distortion, power amplifier, software defined radio, spectrally agile radio, spurious emission, 3GPP LTE-Advanced.**

I. Introduction

Spectrum scarcity and ever-increasing data rate requirements are the two main motivating factors behind introducing carrier aggregation (CA) in modern wireless communication systems, such as 3GPP LTE-Advanced [1], [2]. In CA transmission, multiple component carriers (CCs) at different RF frequencies are adopted simultaneously, either within the same RF band (intraband CA), or at different RF bands (interband CA) [3]. While interband CA naturally leads to a *non-contiguous transmit spectrum*, this can also happen in the intraband CA case when the adopted component carriers are located in a non-contiguous manner. Adopting non-contiguous CA provides lots of flexibility in RF spectrum use, but also poses substantial challenges in the transmitter design, especially in lower-cost devices such as LTE-Advanced user equipment (UE). Moreover, multicarrier type modulations with very large peak-to-average power ratio (PAPR) are used in most state-of-the-art wireless communication systems. When combined with noncontiguous transmission schemes and high power-efficiency requirements, controlling the transmitter unwanted emissions due to power amplifier (PA) nonlinearity becomes a true challenge [4]–[6].

In [3], a comparison of different transmitter architectures for CA based transmission schemes was presented, showing that it is more power efficient to combine the CCs before the PA, and thus use only a single PA, instead of having a separate PA for each CC. This is also technically feasible, especially in the intraband CA case. The power savings can be quite significant since the overall transmitter efficiency is dominated by the PA [3], and is particularly critical in mobile terminals and other lower-cost devices, such as small-cell base-stations, with limited computing and cooling capabilities [7], [8]. However, the power efficiency gained from using a single PA for all CCs comes at the expense of more severe unwanted emissions, stemming from the PA nonlinear characteristics, that can occur at adjacent channels or bands, or even at own receiver band in FDD transceiver case [4]–[6], [9].

The levels of different unwanted emissions are, in general, regulated by the standardization bodies and ITU-R [10]. It has been recently demonstrated that in the context of LTE-Advanced mobile transmitter with noncontiguous CA or multicluster type transmission, the PA nonlinearities lead to spurious emissions that can seriously violate the given spectrum and spurious emission limits if not properly controlled [2], [4]–[6]. Furthermore, in FDD devices, in addition to violating the general spurious emission limits, the generated spurious components can also overlap with the device's own receive band, causing own receiver desensitization [4], [9], [11], [12]. One obvious solution to decrease the levels of unwanted emissions is to back off the transmit power from

Mahmoud Abdelaziz, Lauri Anttila, and Mikko Valkama are with the Department of Electronics and Communications Engineering, Tampere University of Technology, Tampere, Finland.

Chance Tarver, Kaipeng Li, and Joseph R. Cavallaro are with the Department of Electrical and Computer Engineering, Rice University, Houston, TX.

This work was supported by the Finnish Funding Agency for Technology and Innovation (Tekes) under the project "Future Small-Cell Networks using Reconfigurable Antennas (FUNERA)", and by the Linz Center of Mechatronics (LCM) in the framework of the Austrian COMET-K2 programme. The work was also funded by the Academy of Finland under the projects 288670 "Massive MIMO: Advanced Antennas, Systems and Signal Processing at mm-Waves", 284694 "Fundamentals of Ultra Dense 5G Networks with Application to Machine Type Communication", and 301820 "Competitive Funding to Strengthen University Research Profiles". This work was also supported in part by the US National Science Foundation under grants ECCS-1408370, CNS-1265332, and ECCS-1232274.

its saturation region. In 3GPP UE terminology, this is known as Maximum Power Reduction (MPR), and MPR values up to 16 dB are allowed in some use cases for mobile terminals [2]. However, this approach will end up yielding a significantly lower PA efficiency as well as a substantial reduction in the network coverage. There is thus a clear need for alternative PA linearization solutions which do not have such drastic adverse effects.

Digital predistortion (DPD) is, in general, one of the most effective solutions for mitigating transmitter nonlinear distortion. There have been substantial research efforts in the past 20 years in developing ever more efficient and elaborate DPD techniques, mostly for high-end macro base-station type of devices. The conventional DPD approaches seek to linearize the full composite transmit signal, and we thus refer to such solutions as full-band DPD in this article. There have also been a handful of recent works on efficient concurrent linearization techniques for multi-band transmitters that employ only a single PA [13]–[15]. These works assume that the component carriers are separated by a large distance such that the spurious emissions are filtered out by the transmit RF filter, and hence linearization of only the main carriers is pursued.

Complementary to such methods, the scope of this paper is to introduce a low-complexity DPD solution for suppressing the spurious emissions in non-contiguous transmission cases, while not concentrating specifically on the linearization of the main component carriers. Hereafter, we will refer to such linearization solutions as *sub-band DPD*. This approach is motivated by the following two factors. First, the emission limits in the spurious region are generally stricter than in the spectral regrowth region around the component carriers, and are thus more easily violated. This has been recognized also in 3GPP recently, in the context of intraband noncontiguous carrier aggregation [2], [4]–[6]. Moreover, even in interband carrier aggregation scenarios in FDD devices, some of the spurious components can be hitting the own RX band causing own receiver desensitization [11]. Second, by concentrating the linearization efforts to the most critical spurious emissions only, the processing and instrumentation requirements can be significantly relaxed, thus potentially facilitating the DPD processing also in mobile terminals and other lower-cost devices. This applies not only to the DPD main path processing complexity but also to the feedback receiver instrumentation complexity which can also be substantially reduced.

There have been some recent studies in the literature that consider the mitigation of the spurious emissions explicitly. In [16]–[18], such processing was added to complement a concurrent linearization system while assuming a frequency-flat PA response within the spurious sub-band. In [16], [17], the DPD parameter estimation was done offline, based on extracting the quasi-memoryless PA parameters using large-signal network analyzer (LSNA) measurements, and covering up to fifth-order processing. In [18], a memoryless least-squares fit between the observed intermodulation distortion (IMD) at the considered sub-band and certain basis functions was performed. The basis functions were generated using a wideband composite carrier baseband equivalent signal, followed by sub-band filtering, implying a very high sample rate and processing complexity, especially for widely spaced carriers. The estimated and regenerated IMD was then applied at the PA input, oppositely phased, such that it is canceled at the PA output. In [19], [20], on the other hand, third-order nonlinearities at the IM3 sub-bands were specifically targeted, through explicit, low-rate, behavioral modeling of the baseband equivalent IM3 sub-band emissions. Furthermore, the parameter estimation of the DPD was based on a closed-loop feedback with a decorrelation-based learning rule, which was shown to have better linearization performance compared to the third-order inverse solution in [16] in terms of the spurious emission suppression. Moreover, an FPGA implementation of this third-order decorrelation-based sub-band DPD was presented in [21], demonstrating fast and reliable performance under real time constraints. A recent overview article [22] highlighted the main principles and advantages of such low complexity sub-band DPD solutions, while not concentrating on the details of the DPD processing or parameter estimation and adaptation algorithms at technical level. In [23], on the other hand, a flexible full-band DPD solution was also proposed by the authors which can optimize the DPD coefficients to minimize the nonlinear distortion at a particular frequency or sub-band in the out-of-band or spurious regions. However, like other full-band DPD techniques, it requires very high sampling rates in the transmitter and feedback receiver when the carrier spacing between the CCs increases.

In this article, we extend the elementary third-order IM3 sub-band DPD solution, proposed by the authors in [19], [20], in two ways. First, the third-order IM3 sub-band DPD is extended to incorporate higher-order processing based on explicit modeling of the higher-order spurious components at the IM3 sub-band. This will enhance the IM3 spurious emission suppression considerably. Furthermore, we also extend the sub-band DPD solution to include higher-order sub-bands, i.e., IM5, IM7, etc., thus offering more flexibility and linearization capabilities beyond the basic IM3 sub-band. All the proposed solutions are derived for wideband nonlinear PAs with memory. Furthermore, we also formulate novel decorrelation-based parameter estimation methods, covering both sample-adaptive and block-adaptive learning rules, to efficiently identify the needed DPD parameters with low complexity. The proposed learning solutions are also shown to offer better performance than the earlier proposed third-order or fifth-order inverse based methods. We also provide comprehensive simulation and RF measurement results, using a commercial LTE-Advanced mobile PA, to evaluate and validate the effectiveness of the proposed solutions in real world scenarios.

The rest of this article is organized as follows: Section II presents the mathematical modeling of the different considered spurious components at different sub-bands, produced by a nonlinear PA with memory. Stemming from this modeling, also the corresponding core processing principles of the proposed DPD solutions at different sub-bands are formulated. Then, Section III presents the proposed DPD parameter learning solutions, covering both sample-adaptive and block-adaptive decorrelation solutions at different sub-bands. Section IV addresses then different implementation alternatives of the proposed sub-band DPD concept, and also

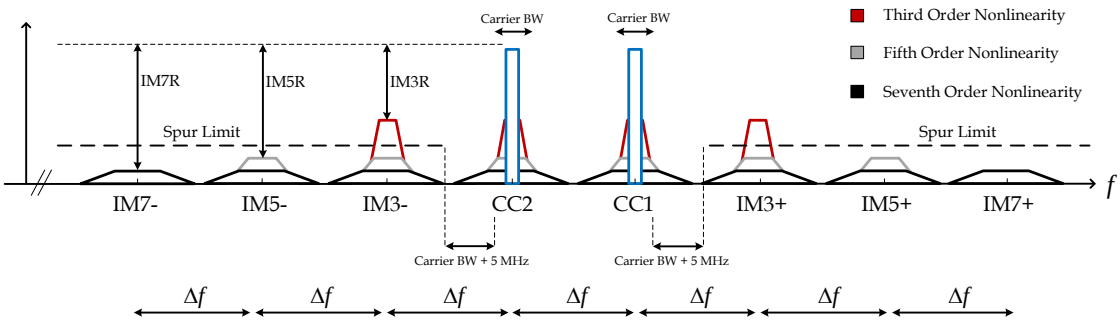

Fig. 1. Illustration of different intermodulation distortion components created by a nonlinear PA when excited with a non-contiguous CA signal with two component carriers. Here, nonlinear distortion components up to order 7 are shown.

analyzes the computing complexity of the sub-band DPD in terms of the number of floating point operations together with some hardware complexity aspects. Finally, Sections V and VI report comprehensive simulation and RF measurement results, evidencing excellent spurious emission suppression in different realistic scenarios.

II. Spurious Component Modeling and Proposed Sub-band DPD Processing

In this manuscript, we assume a practical case of non-contiguous carrier aggregation with two component carriers. When such noncontiguous dual-carrier signal is applied at the PA input, the PA nonlinearity leads to intermodulation distortion at different sub-bands, as shown in Fig. 1. Assuming a CC separation of Δf, in addition to the spectral regrowth around the main carriers, intermodulation between the two CCs yields strong IMD at integer multiples of Δf from the main CCs. In this article, we refer to the intermodulation (IM) sub-bands located at $\pm\Delta f$ from the main CCs as the *IM3 sub-bands*. Similarly, the *IM5 sub-bands* are located at $\pm 2\Delta f$ from the main CCs, and so on. In general, each IM sub-band includes nonlinear distortion components of different orders as shown in Fig. 1. For example, in the case of a seventh-order PA nonlinearity, the IM3 sub-band contains third, fifth and seventh-order nonlinearities, while the IM5 sub-band contains fifth and seventh-order components.

In this section, we start with the fundamental modeling of the nonlinear distortion at the IM3 sub-band as a concrete example. Stemming from that modeling, we then formulate the basic processing of the proposed IM3 sub-band DPD. After that, the modeling is extended to cover the nonlinear distortion components at the higher-order IM sub-bands, followed by the corresponding higher-order sub-band DPD processing. The actual parameter estimation and learning algorithms for the proposed sub-band DPD structures are then presented in details in Section III. In all the modeling and developments, we adopt the widely-used wideband Parallel Hammerstein (PH) PA model [24] to describe the fundamental nonlinear behavior of the PA, as it has been shown to model accurately the measured nonlinear behavior of different classes of true PAs.

A. Spurious Component Modeling at IM3 Sub-bands

The modeling is carried out at composite baseband equivalent level, where the two component carriers are assumed to be separated by $2f_{IF}$. The composite baseband equivalent input and output signals of the P^{th} order Parallel Hammerstein PA model, with monomial nonlinearities and FIR branch filters, respectively, read

$$x(n) = x_1(n)e^{j2\pi\frac{f_{IF}}{f_s}n} + x_2(n)e^{-j2\pi\frac{f_{IF}}{f_s}n}, \tag{1}$$

$$y(n) = \sum_{\substack{p=1\\ p\ \text{odd}}}^{P} f_{p,n} \star |x(n)|^{p-1}x(n), \tag{2}$$

where $x_1(n)$ and $x_2(n)$ are the baseband component carrier signals, $f_{p,n}$ denotes the PH branch filter impulse responses of order p, and $\star$ is the convolution operator. Intermodulation between the two component carriers leads to the appearance of IMD components at $\pm 3f_{IF}$, $\pm 5f_{IF}$, etc., as shown in Fig. 1 for the corresponding RF spectrum.

As a concrete example, let us analyze the IMD at $\pm 3f_{IF}$. Direct substitution of (1) in (2) allows extracting the baseband equivalent distortion terms at the IM3 sub-bands, which, through straight-forward manipulations, yields

$$y_{IM3_\pm}(n) = \sum_{\substack{p=3\\ p\ \text{odd}}}^{P} f_{3\pm,p,n} \star u_{3\pm,p}(n). \tag{3}$$

Here, $f_{3\pm,p,n}$ denote the baseband equivalent impulse responses corresponding to the wideband PH PA model filters $f_{p,n}$, evaluated at the IM3$\pm$ sub-bands, formally defined as

$$f_{3\pm,p,n} = LPF\{e^{\mp j2\pi\frac{3f_{IF}}{f_s}n} f_{p,n}\}, \tag{4}$$

with $LPF\{.\}$ denoting an ideal low pass filtering operation with a passband width P times the bandwidth of the wider CC. Furthermore, $u_{3+,p}(n)$ and $u_{3-,p}(n)$ in (3) are the corresponding p^{th} order static nonlinear (SNL) basis functions, related to the nonlinear distortion at the IM3+ and IM3- sub-bands, respectively. Assuming then an 11^{th} order PA model (i.e., $P = 11$), as a concrete high-order example, the IM3+ sub-band basis functions read

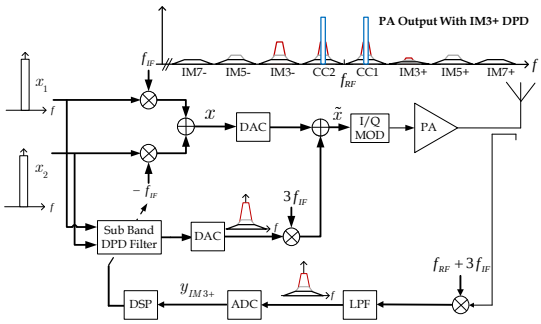

Fig. 2. The proposed sub-band DPD processing principle focusing on the IM3+ sub-band. Thick lines are used to indicate complex I/Q processing. For presentation simplicity, TX filtering between the feedback coupler and the antenna is not shown.

$$u_{3+,3}(n) = x_2^*(n)x_1^2(n) \tag{5}$$

$$u_{3+,5}(n) = u_{3+,3}(n) \times (2|x_1(n)|^2 + 3|x_2(n)|^2) \tag{6}$$

$$u_{3+,7}(n) = u_{3+,3}(n) \times (3|x_1(n)|^4 + 6|x_2(n)|^4 + 12|x_1(n)|^2|x_2(n)|^2) \tag{7}$$

$$u_{3+,9}(n) = u_{3+,3}(n) \times (4|x_1(n)|^6 + 10|x_2(n)|^6 + 30|x_1(n)|^4|x_2(n)|^2 + 40|x_1(n)|^2|x_2(n)|^4) \tag{8}$$

$$u_{3+,11}(n) = u_{3+,3}(n) \times (5|x_1(n)|^8 + 15|x_2(n)|^8 + 60|x_1(n)|^6|x_2(n)|^2 + 100|x_1(n)|^2|x_2(n)|^6 + 150|x_1(n)|^4|x_2(n)|^4). \tag{9}$$

The corresponding basis functions for the IM3- sub-band, i.e., $u_{3-,p}(n)$, can be obtained by simply interchanging $x_1(n)$ and $x_2(n)$ in the above expressions. Next, these behavioral modeling results are utilized to formulate the proposed IM3 sub-band DPD concept, specifically tailored to suppress the distortion at the IM3 sub-band.

B. Proposed IM3 Sub-band DPD Principle

For presentation purposes, we focus here on suppressing the spurious emissions at the IM3+ sub-band, while the corresponding emissions at the IM3- sub-band can also be easily mitigated using a very similar structure with minor changes as will be elaborated later in Section II-C. The key idea of the sub-band DPD concept is to inject a proper additional low-power cancellation signal, with structural similarity to (3) and located at $+3f_{IF}$, into the PA input, such that the level of the IM3+ term at the PA output is reduced. Now, stemming from the IMD structure in (3), an appropriate digital injection signal can be obtained by adopting the IM3+ basis functions $u_{3+,p}(n)$ in (5)-(9), combined with proper filtering using a bank of sub-band DPD filters $\alpha_{3+,p,n}$. Incorporating such sub-band DPD processing with polynomial order Q, the composite baseband equivalent PA input signal reads

$$\tilde{x}(n) = x(n) + \left[\sum_{\substack{p=3 \\ p \text{ odd}}}^{Q} \alpha_{3+,p,n} \star u_{3+,p}(n)\right] e^{j2\pi \frac{3f_{IF}}{f_s} n} \tag{10}$$

Here, and in the continuation, we use $\tilde{(.)}$ variables to indicate sub-band DPD processing and the corresponding predistorted signals. This DPD processing principle is illustrated in Fig. 2 at a conceptual level, where the TX/RX duplexer filters are omitted for simplicity of the presentation since they do not directly impact the sub-band DPD processing or learning. Similar convention is followed also in other figures. Different implementation alternatives as well as the parameter learning and feedback receiver aspects are addressed in more details in Sections III and IV.

C. Generalization to Higher-Order IM Sub-bands

The direct substitution of (1) in (2) leads to the appearance of spurious intermodulation terms also at higher-order IM sub-bands, in addition to the previously considered IM3 sub-bands, as illustrated already in Fig. 1. These higher-order sub-band emissions can also be harmful, since they can violate the emission limits, cause own receiver desensitization, or both. Thus, developing a sub-band DPD solution that can tackle also the distortion at these higher-order IM sub-bands with feasible complexity is important. Similar to the above IM3+ sub-band developments, we next extract the IMD terms at the higher-order IM sub-bands. The baseband equivalent IMD terms at the IM5+, IM7+, IM9+, and IM11+ sub-bands, as concrete examples, can be extracted using (1) and (2), interpreted at proper sub-bands, yielding

$$y_{IM5_+}(n) = \sum_{\substack{p=5 \\ p \text{ odd}}}^{P} f_{5+,p,n} \star u_{5+,p}(n) \tag{11}$$

$$y_{IM7_+}(n) = \sum_{\substack{p=7 \\ p \text{ odd}}}^{P} f_{7+,p,n} \star u_{7+,p}(n) \tag{12}$$

$$y_{IM9_+}(n) = \sum_{\substack{p=9 \\ p \text{ odd}}}^{P} f_{9+,p,n} \star u_{9+,p}(n) \tag{13}$$

$$y_{IM11_+}(n) = \sum_{\substack{p=11 \\ p \text{ odd}}}^{P} f_{11+,p,n} \star u_{11+,p}(n). \tag{14}$$

In the above models, $f_{5+,p,n}$, $f_{7+,p,n}$, $f_{9+,p,n}$, and $f_{11+,p,n}$ denote the baseband equivalent impulse responses corresponding to the wideband PA model filters $f_{p,n}$ in (2), evaluated at the IM5+, IM7+, IM9+, and IM11+ sub-bands, respectively. These are formally obtained similar to (4) but replacing $3f_{IF}$ with either $5f_{IF}$, $7f_{IF}$, $9f_{IF}$, or $11f_{IF}$, respectively. The p^{th} order basis functions at the these higher-order IM sub-bands, denoted by $u_{5+,p}(n)$, $u_{7+,p}(n)$, $u_{9+,p}(n)$, and $u_{11+,p}(n)$, and assuming again an 11^{th} order PH PA model, read

$$u_{5+,5}(n) = (x_2(n)^*)^2 x_1(n)^3 \quad (15)$$

$$u_{5+,7}(n) = u_{5+,5}(n)(4|x_2(n)|^2 + 3|x_1(n)|^2) \quad (16)$$

$$u_{5+,9}(n) = u_{5+,5}(n)(10|x_2(n)|^4 + 6|x_1(n)|^4 + 20|x_1(n)|^2|x_2(n)|^2) \quad (17)$$

$$u_{5+,11}(n) = u_{5+,5}(n)(20|x_2(n)|^6 + 10|x_1(n)|^6 + 75|x_2(n)|^4|x_1(n)|^2 + 60|x_2(n)|^2|x_1(n)|^4) \quad (18)$$

$$u_{7+,7}(n) = (x_2(n)^*)^3 x_1(n)^4 \quad (19)$$

$$u_{7+,9}(n) = u_{7+,7}(n)(5|x_2(n)|^2 + 4|x_1(n)|^2) \quad (20)$$

$$u_{7+,11}(n) = u_{7+,7}(n)(15|x_2(n)|^4 + 10|x_1(n)|^4 + 30|x_2(n)|^2|x_1(n)|^2) \quad (21)$$

$$u_{9+,9}(n) = (x_2(n)^*)^4 x_1(n)^5 \quad (22)$$

$$u_{9+,11}(n) = u_{9+,9}(n)(6|x_2(n)|^2 + 5|x_1(n|^2) \quad (23)$$

$$u_{11+,11}(n) = (x_2(n)^*)^5 x_1(n)^6. \quad (24)$$

The corresponding baseband equivalent IMD terms at the negative IM sub-bands can be obtained by simply interchanging $x_1(n)$ and $x_2(n)$ in (15)-(24).

Then, stemming from the distortion structure in (11)-(14), and adopting similar ideology as in the previous IM3 sub-band DPD case, a natural injection signal for suppressing the spur components at higher-order IM sub-bands can be obtained by properly filtering and combining the above higher-order sub-band basis functions. The sub-band specific filters for the p^{th} order basis functions are denoted with $\alpha_{5+,p,n}$, $\alpha_{7+,p,n}$, $\alpha_{9+,p,n}$, and $\alpha_{11+,p,n}$. Incorporating such DPD processing with DPD polynomial order Q, and aggregating at the same time parallel sub-band DPDs simultaneously for the IM3+, IM5+, and IM7+ sub-bands, as a concrete example, the composite baseband equivalent PA input signal now reads

$$\tilde{x}(n) = x(n) + \left[\sum_{\substack{p=3 \\ p \text{ odd}}}^{Q} \alpha_{3+,p,n} \star u_{3+,p}(n)\right] e^{j2\pi \frac{3f_{IF}}{f_s} n} + \left[\sum_{\substack{p=5 \\ p \text{ odd}}}^{Q} \alpha_{5+,p,n} \star u_{5+,p}(n)\right] e^{j2\pi \frac{5f_{IF}}{f_s} n} + \left[\sum_{\substack{p=7 \\ p \text{ odd}}}^{Q} \alpha_{7+,p,n} \star u_{7+,p}(n)\right] e^{j2\pi \frac{7f_{IF}}{f_s} n} \quad (25)$$

In general, the achievable suppression of the distortion at different IM sub-bands depends directly on the selection and optimization of the different filters $\alpha_{3+,p,n}$, $\alpha_{5+,p,n}$, $\alpha_{7+,p,n}$, and so on. This is addressed in detail in the next section.

III. Sub-band DPD Parameter Learning Using the Decorrelation Principle

In this section, based on the previous spurious component modeling and the proposed sub-band DPD principle, we formulate computing feasible and highly efficient estimation algorithms for learning and optimizing the sub-band DPD filter coefficients such that the spurious emissions are minimized at the considered IM sub-bands. We start by deriving some analytical reference solutions, taking the third-order IM3 sub-band DPD as a simple and tractable example, in order to demonstrate that minimizing the IM3 power is essentially identical to decorrelating the IM3 observation against the corresponding sub-band DPD basis functions. Then, both sample-adaptive and block-adaptive decorrelation based learning rules are devised, covering the general cases of higher-order processing with memory at IM3 and higher-order IM sub-bands.

A. Analytical Reference Solutions

In this subsection, we derive three analytical reference solutions for calculating the IM3 sub-band DPD coefficients. The considered approaches are the third-order inverse solution, also adopted in [16], the IM3 power minimization solution, and the analytical IM3 decorrelation-based solution. To keep the analytical developments simple and tractable, we consider a simplified case with a third-order memoryless IM3+ sub-band DPD and a third-order memoryless PA. The actual sample-adaptive and block-adaptive decorrelation based learning solutions, devised later in this section, are formulated for the general cases of higher-order processing with memory.

Now, starting with the dual carrier signal in (1), and limiting the study to the simplified case of a third-order memoryless IM3+ sub-band DPD and a third-order memoryless PA, the basic signal models are given by (26)-(30).

$$y(n) = f_1 x(n) + f_3 |x(n)|^2 x(n), \quad (26)$$

$$u(n) = x_2^*(n) x_1^2(n), \quad (27)$$

$$y_{IM3_+}(n) = f_3 u(n), \quad (28)$$

$$\tilde{x}(n) = x(n) + \alpha u(n) e^{j2\pi \frac{3f_{IF}}{f_s} n}, \quad (29)$$

$$\tilde{y}_{IM3_+}(n) = (f_3 + f_1\alpha)u(n) + 2f_3\alpha(|x_1(n)|^2 + |x_2(n)|^2)u(n) + f_3|\alpha|^2\alpha|x_1(n)|^4|x_2(n)|^2 u(n). \quad (30)$$

Here, f_1 and f_3 are the memoryless PA model parameters, α denotes the memoryless sub-band DPD parameter to be optimized, while $y_{IM3_+}(n)$ and $\tilde{y}_{IM3_+}(n)$ refer to the baseband equivalent PA output at the positive IM3 sub-band without and with sub-band DPD, respectively.

Now, as (30) clearly shows, the IM3 sub-band distortion at the PA output, with DPD adopted, depends directly on, and can thus be controlled by, the DPD coefficient α. In the well-known *third-order inverse solution*, the DPD parameter α is selected such that the third-order term in (30) is canceled, i.e., $f_3 + f_1\alpha = 0$. The corresponding solution, denoted by α_{inv}, thus reads

$$\alpha_{inv} = -f_3/f_1. \quad (31)$$

However, this will not remove all the distortion, because higher-order terms will be created due to the predistortion, as shown in (30).

A more elaborate method for selecting the DPD parameter α is the one that minimizes the power of the total IM3 sub-band signal, $\tilde{y}_{IM3_+}(n)$, referred to as the *minimum IM3 power* or *minimum mean-squared error (MMSE)* solution in the continuation. For notational convenience, we define the

so-called error signal as $e(n) = \tilde{y}_{IM3_+}(n)$, as with ideal predistortion the IM3 sub-band signal would be zero, and thus the optimization means minimizing the power of this error signal. The detailed derivation of the optimum DPD parameter which minimizes the mean squared error $\mathbf{E}[|e(n)|^2]$ is given in Appendix A, yielding

$$\alpha_{MMSE} = \frac{-\left[f_1 f_3^* \mathbf{E}_{42} + 2|f_3|^2(\mathbf{E}_{62} + \mathbf{E}_{44})\right]^*}{[|f_1|^2\mathbf{E}_{42} + 4\mathbb{R}(f_1 f_3^*)(\mathbf{E}_{62} + \mathbf{E}_{44}) + 4|f_3|^2(\mathbf{E}_{46} + 2\mathbf{E}_{64} + \mathbf{E}_{82})]^*}, \tag{32}$$

where $\mathbf{E}_{ij}$ refers to the products of the CC signals' higher-order moments of the form $\mathbf{E}[|x_1|^i]\mathbf{E}[|x_2|^j]$, while $\mathbf{E}[.]$ denotes the statistical expectation operator.

As will be shown with concrete examples in Section V, this MMSE solution provides better linearization performance compared to the third-order inverse solution. However, as shown in (32), the analytical MMSE solution requires the knowledge of various higher-order moments of the CC signals. Furthermore, the above solution is valid only in the case of a memoryless third-order nonlinear system, beyond which obtaining an analytical expression for the DPD coefficients becomes overly tedious. Thus, to relax these constraints, an alternative solution, based on minimizing the correlation between the IM3 sub-band observation and the third-order basis function $u(n) = x_2^*(n)x_1^2(n)$ was initially discussed in [19], and will be extended to higher nonlinearity orders and higher-order IM sub-bands in this paper. The analytical reference solution for the decorrelation-based sub-band DPD structure is obtained by setting the correlation between the error signal, $e(n)$, and the third-order basis function, $u(n) = x_2^*(n)x_1^2(n)$, to zero, i.e., $\mathbf{E}[e(n)u^*(n)] = 0$. Then, through straightforward algebraic manipulations, the decorrelation-based DPD coefficient, denoted by α_o, can be shown to read

$$\alpha_o = \frac{-f_3}{f_1 + 2f_3(\frac{\mathbf{E}_{60}}{\mathbf{E}_{40}} + \frac{\mathbf{E}_{04}}{\mathbf{E}_{02}})}. \tag{33}$$

Assuming then, for simplicity, that the CC baseband equivalents are complex Gaussians, (33) simplifies to

$$\alpha_o = \frac{-f_3}{f_1 + 2f_3(3\sigma_{x,1}^2 + 2\sigma_{x,2}^2)}, \tag{34}$$

where $\sigma_{x,1}^2 = \mathbf{E}[|x_1|^2]$ and $\sigma_{x,2}^2 = \mathbf{E}[|x_2|]^2$ are the variances of the two CCs [19].

A clear advantage of the decorrelation-based approach compared to the earlier MMSE solution lies in the simple and straightforward adaptive filtering based practical computing solutions, sketched initially in [19] for simple third-order processing at IM3, which do not require any prior knowledge about signal moments or any other parameters. Furthermore, opposed to the MMSE solution, the decorrelation based approach can be easily extended to include higher-order nonlinearities and memory effects, at both the IM3 sub-band as well as the other higher-order IM sub-bands, as will be described in details in the next subsection.

B. Sample-Adaptive Decorrelation-based Learning

In this subsection, we provide the actual sample-adaptive learning rules for both IM3 and higher-order IM sub-band DPD structures with memory, whose basic operating principles were described in Section II. To facilitate the learning, we assume a feedback or observation receiver measuring the particular IM sub-band whose sub-band DPD filter coefficients are currently under learning. Notice that opposed to classical wideband DPD principles, where a wideband observation receiver is typically needed, a more narrowband receiver is sufficient here since only the particular IM sub-band is observed. As both the IM3 and the higher-order IM sub-band DPDs are based on multiple strongly correlated basis functions, given in (5)-(9) and (15)-(24), respectively, we start by introducing a basis function orthogonalization procedure, after which the actual proposed adaptive decorrelation algorithms are described.

1) Basis Function Orthogonalization: When a nonlinearity order higher than the IM sub-band order is considered, multiple basis functions are adopted in the sub-band DPD processing, as described in Section II. Taking as an example case the IM3+ sub-band, the SNL basis functions $u_{3+,p}(n)$, $p = 1, 3, ..., Q$, given in (5)-(9), are highly correlated. This can negatively impact the convergence and stability of the adaptive decorrelation-based learning. Therefore, the SNL basis functions are first orthogonalized [25], which yields a new set of DPD basis functions $s_{3+,p}(n)$, $p = 1, 3, ..., Q$, written formally at sample level as

$$\mathbf{s}_{3+}(n) = \mathbf{W}\mathbf{u}_{3+}(n), \tag{35}$$

where

$$\mathbf{u}_{3+}(n) = [u_{3+,3}(n)\ u_{3+,5}(n)\ ...\ u_{3+,Q}(n)]^T, \tag{36}$$

$$\mathbf{s}_{3+}(n) = [s_{3+,3}(n)\ s_{3+,5}(n)\ ...\ s_{3+,Q}(n)]^T, \tag{37}$$

$$\mathbf{W} = \begin{bmatrix} 1 & 0 & 0 & 0 & 0 \\ w_{5,3} & w_{5,5} & 0 & 0 & 0 \\ w_{7,3} & w_{7,5} & w_{7,7} & \dots & 0 \\ \vdots & \vdots & \vdots & \ddots & \vdots \\ w_{Q,3} & w_{Q,5} & w_{Q,7} & \dots & w_{Q,Q} \end{bmatrix}. \tag{38}$$

The lower triangular matrix $\mathbf{W}$ can be obtained, e.g., through Gram-Schmidt orthogonalization, QR or singular value decomposition, or using a lower complexity iterative orthogonalization algorithm [26].

Similarly, the SNL basis functions in (15)-(24) corresponding to the higher-order IM sub-bands are also orthogonalized, to obtain new sets of orthogonal basis functions $\mathbf{s}_{5+}(n)$, $\mathbf{s}_{7+}(n)$, etc.

2) Adaptive Learning for IM3+ Sub-band: We now present the actual sample-adaptive decorrelation based learning algorithm for the IM3+ sub-band DPD coefficients. For notational convenience, we introduce the following vectors

$$\boldsymbol{\alpha}_{3+,l}(n) = [\alpha_{3+,3,l}(n)\ \alpha_{3+,5,l}(n)\ ...\ \alpha_{3+,Q,l}(n)]^T, \tag{39}$$

$$\bar{\boldsymbol{\alpha}}_{3+}(n) = [\boldsymbol{\alpha}_{3+,0}(n)^T\ \boldsymbol{\alpha}_{3+,1}(n)^T\ ...\ \boldsymbol{\alpha}_{3+,N}(n)^T]^T, \tag{40}$$

$$\bar{\mathbf{s}}_{3+}(n) = [\mathbf{s}_{3+}(n)^T\ \mathbf{s}_{3+}(n-1)^T\ ...\ \mathbf{s}_{3+}(n-N)^T]^T, \tag{41}$$

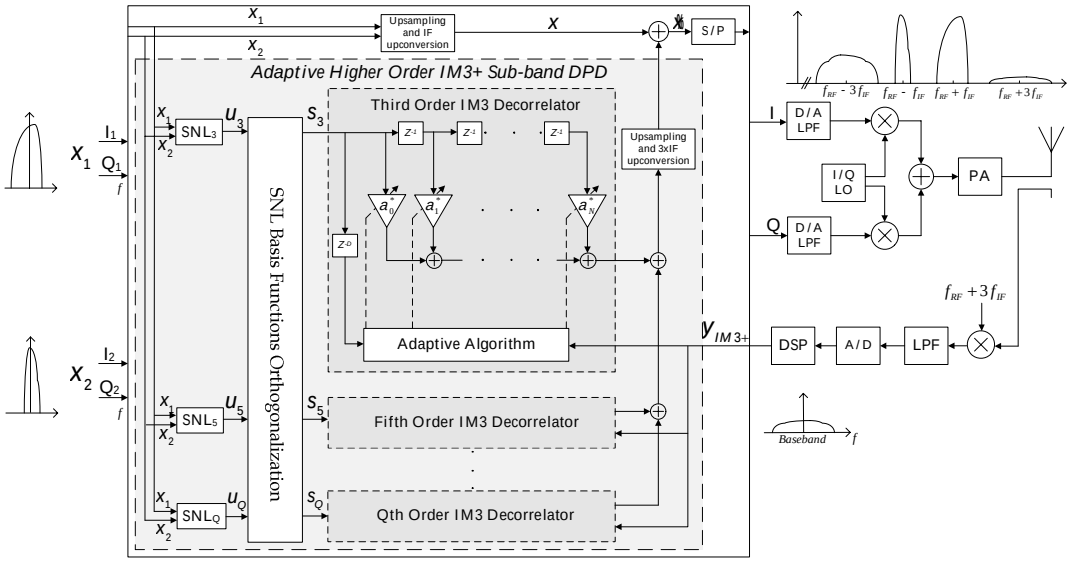

Fig. 3. Detailed block diagram of the sample-adaptive decorrelation-based IM3+ sub-band DPD with higher-order nonlinearities and memory.

where now $\alpha_{3+,p,l}(n)$ denotes the l^{th} adaptive filter coefficient of the p^{th} order orthogonalized IM3+ basis function $s_{3+,p}(n)$ at time index n, and N denotes the adaptive filter memory depth. Furthermore, the vectors $\bar{\boldsymbol{\alpha}}_{3+}(n)$ and $\bar{\mathbf{s}}_{3+}(n)$ incorporate all the coefficients and basis function samples up to polynomial order Q. Adopting this notation, the instantaneous sample of the composite baseband equivalent PA input signal $\tilde{x}(n)$ now reads

$$\tilde{x}(n) = x(n) + \tilde{x}_{3+}(n)e^{j2\pi\frac{3f_{IF}}{f_s}n}, \tag{42}$$

where the instantaneous sample of the baseband equivalent IM3+ injection signal $\tilde{x}_{3+}(n)$ reads

$$\tilde{x}_{3+}(n) = \bar{\boldsymbol{\alpha}}_{3+}(n)^H \bar{\mathbf{s}}_{3+}(n). \tag{43}$$

Then, in order to adaptively update the filter coefficients $\bar{\boldsymbol{\alpha}}_{3+}(n)$, the IM3+ sub-band is observed with the feedback receiver, and the coefficient is updated as

$$\bar{\boldsymbol{\alpha}}_{3+}(n+1) = \bar{\boldsymbol{\alpha}}_{3+}(n) - \frac{\mu}{||\bar{\mathbf{s}}_{3+}(n)||^2 + C}\bar{\mathbf{s}}_{3+}(n)e^*_{3+}(n), \tag{44}$$

where $e_{3+}(n) = \tilde{y}_{IM3_+}(n)$ denotes the baseband equivalent observation of the PA output at the IM3+ sub-band with the current DPD coefficients. The scaling factor $||\bar{\mathbf{s}}_{3+}(n)||^2 + C$ normalizing the learning step-size μ in (44) is philosophically similar to that of the Normalized Least Mean Square (NLMS) algorithm, in effect making the learning characteristics more robust against the input data dynamics.

The proposed coefficient update in (44) is seeking to decorrelate the IM3+ observation and the adopted orthogonalized basis functions. This type of learning algorithm can also be interpreted as a stochastic Newton root search in the objective function $J(\bar{\boldsymbol{\alpha}}_{3+}) = \mathbf{E}[\tilde{x}_{3+}(n)e^*_{3+}(n)]$, where the target is to search for the DPD coefficients $\bar{\boldsymbol{\alpha}}_{3+}$ that minimize the ensemble correlation between $e_{3+}(n)$ and the baseband equivalent of the IM3+ injection signal $\tilde{x}_{3+}(n)$ in (43). The overall processing flow is graphically illustrated in Fig. 3.

3) Adaptive Learning for Higher-Order IM Sub-bands: We now extend the decorrelation based learning to higher-order IM sub-bands. First, adopting vector-based notations again, we introduce the following vectors for notational convenience

$$\boldsymbol{\alpha}_{5+,l}(n) = [\alpha_{5+,5,l}(n)\ \alpha_{5+,7,l}(n)\ \ldots\ \alpha_{5+,Q,l}(n)]^T, \tag{45}$$
$$\boldsymbol{\alpha}_{7+,l}(n) = [\alpha_{7+,7,l}(n)\ \alpha_{7+,9,l}(n)\ \ldots\ \alpha_{7+,Q,l}(n)]^T, \tag{46}$$
$$\bar{\boldsymbol{\alpha}}_{5+}(n) = [\boldsymbol{\alpha}_{5+,0}(n)^T\ \boldsymbol{\alpha}_{5+,1}(n)^T\ \ldots\ \boldsymbol{\alpha}_{5+,N}(n)^T]^T, \tag{47}$$
$$\bar{\boldsymbol{\alpha}}_{7+}(n) = [\boldsymbol{\alpha}_{7+,0}(n)^T\ \boldsymbol{\alpha}_{7+,1}(n)^T\ \ldots\ \boldsymbol{\alpha}_{7+,N}(n)^T]^T, \tag{48}$$
$$\mathbf{s}_{5+}(n) = [s_{5+,5}(n)\ s_{5+,7}(n)\ \ldots\ s_{5+,Q}(n)]^T, \tag{49}$$
$$\mathbf{s}_{7+}(n) = [s_{7+,7}(n)\ s_{7+,9}(n)\ \ldots\ s_{7+,Q}(n)]^T, \tag{50}$$
$$\bar{\mathbf{s}}_{5+}(n) = [\mathbf{s}_{5+}(n)^T\ \mathbf{s}_{5+}(n-1)^T\ \ldots\ \mathbf{s}_{5+}(n-N)^T]^T, \tag{51}$$
$$\bar{\mathbf{s}}_{7+}(n) = [\mathbf{s}_{7+}(n)^T\ \mathbf{s}_{7+}(n-1)^T\ \ldots\ \mathbf{s}_{7+}(n-N)^T]^T. \tag{52}$$

Then, similar to $\tilde{x}_{3+}(n)$ in (43), the baseband equivalents of the IM5+ and IM7+ sub-band DPD injection signals, denoted by $\tilde{x}_{5+}(n)$ and $\tilde{x}_{7+}(n)$, respectively, read

$$\tilde{x}_{5+}(n) = \bar{\boldsymbol{\alpha}}_{5+}(n)^H \bar{\mathbf{s}}_{5+}(n),\ \tilde{x}_{7+}(n) = \bar{\boldsymbol{\alpha}}_{7+}(n)^H \bar{\mathbf{s}}_{7+}(n). \tag{53}$$

Thus, the composite baseband equivalent PA input signal when the IM3+, IM5+, and IM7+ sub-band DPDs are all included, reads

$$\tilde{x}(n) = x(n) + \tilde{x}_{3+}(n)e^{j2\pi\frac{3f_{IF}}{f_s}n} + \tilde{x}_{5+}(n)e^{j2\pi\frac{5f_{IF}}{f_s}n} + \tilde{x}_{7+}(n)e^{j2\pi\frac{7f_{IF}}{f_s}n}. \tag{54}$$

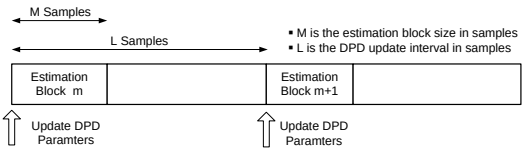

Fig. 4. Block-adaptive DPD learning concept. The DPD parameters estimated in the current estimation block m are applied in the sub-band DPD main path processing during the next block.

Then, similar to the IM3+ coefficient update in (44), the higher-order IM5+ and IM7+ coefficient updates read

$$\bar{\boldsymbol{\alpha}}_{5+}(n+1) = \bar{\boldsymbol{\alpha}}_{5+}(n) - \frac{\mu}{||\bar{\mathbf{s}}_{5+}(n)||^2 + C}\,\bar{\mathbf{s}}_{5+}(n)e^*_{5+}(n), \quad (55)$$

$$\bar{\boldsymbol{\alpha}}_{7+}(n+1) = \bar{\boldsymbol{\alpha}}_{7+}(n) - \frac{\mu}{||\bar{\mathbf{s}}_{7+}(n)||^2 + C}\,\bar{\mathbf{s}}_{7+}(n)e^*_{7+}(n), \quad (56)$$

where $e_{5+}(n) = \tilde{y}_{IM5_+}(n)$ and $e_{7+}(n) = \tilde{y}_{IM7_+}(n)$ denote the baseband equivalents of the PA output at the IM5+ and IM7+ sub-bands, with the corresponding sub-band DPDs included adopting the current coefficients, $\bar{\boldsymbol{\alpha}}_{5+}(n)$ and $\bar{\boldsymbol{\alpha}}_{7+}(n)$, respectively. From the learning perspective, observing a single IM sub-band at a time is the most obvious alternative, which means that the learning for multiple sub-band DPDs happens one at a time. Furthermore, extending the decorrelation-based learning for the negative IM sub-bands is straight-forward. This can be obtained by interchanging $x_1(n)$ and $x_2(n)$ in the SNL basis functions expressions, and observing the PA output at the corresponding negative IM sub-bands.

C. Block-Adaptive Decorrelation-based Learning

As Fig. 3 illustrates, the previous sample-adaptive decorrelation-based learning concept is in principle a closed-loop feedback system with nonlinear adaptive processing inside the loop. During the DPD learning phase, and under the potential hardware processing and latency constraints, the DPD parameter convergence and consequently the DPD linearization performance can be affected, especially if the learning loop delay becomes large. Stemming from this, an alternative and new block-adaptive decorrelation-based learning solution is developed next.

The proposed block-adaptive learning rule implies defining two distinct blocks in the processing, as illustrated in Fig. 4. A single update cycle of the learning algorithm will utilize M samples whereas the DPD parameter update interval is L samples, with $M \leq L$. Thus, by proper choice of M and L, arbitrarily long loop delays can in principle be tolerated, facilitating stable operation under various hardware and software processing latency constraints. Notice that proper timing synchronization between the observation receiver output and the basis functions is, in general, needed, which can be accomplished prior to executing the actual coefficient learning procedure.

Now, assuming an estimation block size of M samples and DPD filter memory depth of N per each of the IM3+ orthogonalized basis functions, the following vectors and matrices,

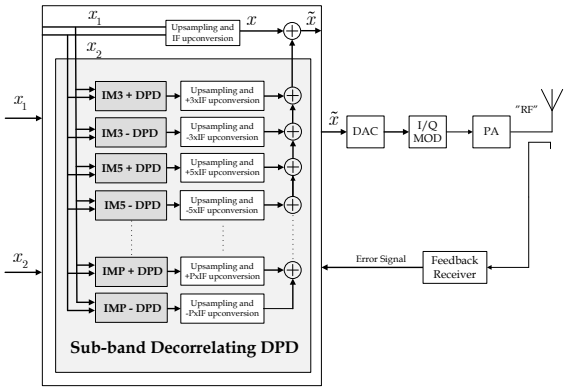

(a) Sub-band DPD Architecture I: Digital IF injection

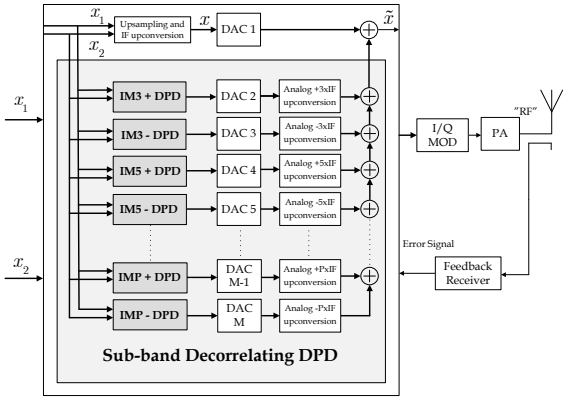

(b) Sub-band DPD Architecture II: Analog IF injection

Fig. 5. Overall sub-band DPD architecture with multiple IM sub-bands included. Thick lines indicate complex I/Q processing.

which stack all the samples and the corresponding DPD filter coefficients within block m, can be defined:

$$\mathbf{s}_{3+}(n_m) = [s_{3+,3}(n_m)\ \ s_{3+,5}(n_m)\ \ \ldots\ \ s_{3+,Q}(n_m)]^T, \quad (57)$$

$$\bar{\mathbf{s}}_{3+}(n_m) = [\mathbf{s}_{3+}(n_m)^T\ \ \ldots\ \ \mathbf{s}_{3+}(n_m - N)^T]^T, \quad (58)$$

$$\mathbf{S}_{3+}(m) = [\bar{\mathbf{s}}_{3+}(n_m)\ \ \ldots\ \ \bar{\mathbf{s}}_{3+}(n_m + M - 1)], \quad (59)$$

$$\boldsymbol{\alpha}_{3+,l}(m) = [\alpha_{3+,3,l}(m)\ \ \alpha_{3+,5,l}(m)\ \ \ldots\ \ \alpha_{3+,Q,l}(m)]^T, \quad (60)$$

$$\bar{\boldsymbol{\alpha}}_{3+}(m) = [\boldsymbol{\alpha}_{3+,0}(m)^T\ \ \boldsymbol{\alpha}_{3+,1}(m)^T\ \ \ldots\ \ \boldsymbol{\alpha}_{3+,N}(m)^T]^T. \quad (61)$$

Here, the index of the first sample of block m is denoted by n_m. The block-adaptive IM3+ sub-band DPD coefficient update then reads

$$\mathbf{e}_{3+}(m) = [\tilde{y}_{IM3_+}(n_m)\ \ldots\ \tilde{y}_{IM3_+}(n_m + M - 1)]^T, \quad (62)$$

$$\bar{\boldsymbol{\alpha}}_{3+}(m+1) = \bar{\boldsymbol{\alpha}}_{3+}(m) - \frac{\mu}{||\mathbf{S}_{3+}(m)||^2 + C}\,\mathbf{S}_{3+}(m)\mathbf{e}^*_{3+}(m), \quad (63)$$

where $\mathbf{e}^*_{3+}(m)$ refers to the element-wise conjugated error signal vector, while $\mathbf{S}_{3+}(m)$ denotes the filter input data matrix, all within the processing block m. The obtained new

TABLE I
COMPARISON OF RUNNING COMPLEXITIES OF NINTH ORDER SUB-BAND AND FULL-BAND DPDS. TWO 1 MHZ CCS WITH 20 MHZ CARRIER SPACING IS ASSUMED. DPD SAMPLE RATE IS 189 MSPS FOR THE FULL-BAND AND 9 MSPS FOR THE SUB-BAND DPD.

	Sub-band DPD				**Full-band DPD**
	IM3+/- Sub-band	IM5+/- Sub-band	IM7+/- Sub-band	IM9+/- Sub-band	Full-band
Basis Function Generation FLOPs	37	40	45	48	11
DPD Filtering FLOPs	$32(N_1{+}1)$ - 2	$24(N_1{+}1)$ - 2	$16(N_1{+}1)$ - 2	$8(N_1{+}1)$ - 2	$40(N_2{+}1)$ - 2
Total Number of FLOPs	$32(N_1{+}1)$ + 35	$24(N_1{+}1)$ + 38	$16(N_1{+}1)$ + 43	$8(N_1{+}1)$ + 46	$40(N_2{+}1)$ + 9
GFLOPS ($N_1 = 1$, $N_2 = 3$)	**0.891**	**0.774**	**0.675**	**0.558**	**31.941**

DPD coefficients $\bar{\alpha}_{3+}(m+1)$ are then applied on the next block of L samples as illustrated in Fig. 4. While the above presentation describes the block-adaptive learning only at the IM3+ sub-band, extending the principle to higher-order IM sub-bands is straightforward, and thus not explicitly shown.

IV. IMPLEMENTATION ASPECTS AND COMPLEXITY ANALYSIS

One of the main advantages of the proposed decorrelation-based sub-band DPD technique is its reduced complexity compared to the classical full-band DPD processing, especially in scenarios where the CCs are widely spaced and thus very high speed ADCs and DACs are required in the classical solutions. In this section, we first address some implementation aspects of the proposed sub-band DPD concept. We then provide a thorough comparison of the computing and hardware complexity perspectives between the full-band and the proposed sub-band DPDs. Finally, some system power efficiency considerations are also presented, with particular focus on low-cost mobile devices.

A. Sub-band DPD Implementation Alternatives

Fig. 5 shows two alternative architectures of the overall sub-band DPD processing with multiple IM sub-bands. The first architecture shown in Fig. 5(a) adds an upsampling and digital IF upconversion block after each sub-band DPD stage in order to digitally place the generated injection signals at proper intermediate frequencies. After adding the sub-band DPD outputs in the digital domain, a single wideband DAC per I and Q branch is used after which the signal is upconverted to RF and amplified by the PA.

The second architecture in Fig. 5(b) adds the outputs of the sub-band DPDs in the analog domain, implying that each sub-band DPD is followed by a narrow-band DAC per I and Q branch, together with an analog complex IF upconversion. A common I/Q RF modulator is then used for all sub-bands prior to the PA module.

Both of these two architectures have their own advantages and disadvantages. In particular, if the carrier spacing between the component carriers is not very large, architecture I is likely to be more suitable. On the other hand, when the carrier spacing starts to increase, using a single wideband DAC may not be efficient from cost and power consumption perspectives, so in this case architecture II is likely to be more attractive. However, some extra processing may be required in this architecture in order to achieve proper synchronization between the DACs. This forms an interesting topic for future research.

A common advantage of both architectures is that each sub-band DPD block can be switched on or off according to the prevailing emission levels and limits at the considered sub-bands. Such flexibility is not available in the classical full-band DPD solutions since, by design, a full-band predistorter always tries to linearize the full composite transmit band. With the sub-band DPD concept, the linearization can be flexibly tailored and optimized to those frequencies which are the most critical from the emission limits perspective.

B. Sub-band versus Full-band DPD Running Complexity

In general, the computational complexity of any DPD can be classified into three main parts [24]: identification complexity, adaptation complexity and running complexity. The identification part is basically the estimation complexity of the DPD parameters, while the adaptation complexity includes the required processing in order to adapt to new operating conditions or device aging. Finally, the running complexity, which is the most critical especially for mobile-type devices, involves the number of computations done per second while the DPD is operating. In this subsection, we will focus on the DPD running complexity in details, while the DPD parameter identification and feedback receiver complexity perspectives are shortly discussed in section IV-C. For a quantitative comparison of the running complexities, we shall use the number of floating point operations (FLOPs) per sample, the number of DPD coefficients, and the required sample rate in the predistortion path as the main quantitative metrics.

In general, the running complexity is divided into two main parts: the first is the basis function generation, and the second is the actual predistortion filtering using the basis functions [24]. The number of FLOPs required to perform these two operations is shown in Table I for ninth-order sub-band and full-band DPDs, respectively, where N_1 and N_2 are the corresponding memory depths per adopted basis function. The full-band DPD architecture that we use also in our comparative performance simulations in Section V, and which is also widely applied otherwise, is based on the PH architecture with ninth order nonlinearity, while the sub-band DPD is based on architecture II shown in Fig. 5(b). Frequency selectivity of the nonlinear PA is another important factor to be considered when comparing the two DPD architectures. This implies that when memory effects of the PA are considered, substantially longer filters are needed for the full-band DPD compared to the sub-band DPD for a certain performance requirement. In the complexity analysis, in the sub-band DPD case, we thus assume a memory depth of 1 per basis function,

while a memory depth of 3 is assumed for the full-band PH DPD per basis function.

A substantial reduction in the needed sample rates can be achieved when adopting the sub-band DPD. As a concrete example, if we consider a challenging LTE-A UL scenario of two 1 MHz CCs with 20 MHz carrier spacing, the required sample rate by the full-band DPD is $9\times(20+1) = 189MSPS$, while for the sub-band DPD it becomes $9 \times 1 = 9MSPS$. Consequently, as shown in Table I, a huge reduction in the number of FLOPs per second (FLOPS) can be achieved using the sub-band DPD. Furthermore, the processing complexity of the sub-band DPD solution is clearly feasible for modern mobile device processing platforms, in terms of the GFLOPS count, while that of the classical fullband DPD is clearly infeasible. However, in some scenarios, when the carrier spacing between the CCs is decreased and/or the CC bandwidth increases, the benefit from using the sub-band DPD approach is reduced since the sample rates of the sub-band and full-band DPD will become more comparable. Notice also that, e.g., in interband CA cases, one can adopt a concurrent 2D-DPD [13], [14] to linearize the main carriers, which can then be easily complemented with the sub-band DPD processing to protect the own receiver if TX filtering does not offer sufficient isolation. Such a scenario could take place, e.g., in uplink Band 1 (1920-1980 MHz) + Band 3 (1710-1785 MHz) interband CA where it is technologically feasible to adopt a single multiband/multimode PA module for amplification. In such scenario, the IM3 sub-band is then directly at the own RX frequencies of Band 1 (2110-2170 MHz).

C. Feedback Receiver and Parameter Estimation Complexity

In addition to the complexity reduction in the DPD main processing path, the complexity of the feedback or observation receiver, used for DPD parameter estimation and adaptation, is also greatly reduced. In order to estimate, e.g., the parameters of the IM3+ sub-band DPD, we only need to observe the IM3+ sub-band at the PA output, instead of observing the full-band (including all the IM sub-bands) which is the case in the full-band DPD. This reduces the cost, complexity and power consumption in the feedback path allowing use of simpler instrumentation, in particular the ADC. Moreover, only a single observation receiver is required, even if linearizing multiple sub-bands, since the parameter learning and corresponding observation of the PA output can be done sequentially, in a per sub-band manner. Finally, in terms of the parameter estimation algorithmic complexity, the proposed decorrelation based solutions are extremely simple, when compared to any classical full-band DPD related method, such as least-squares based parameter fitting and indirect learning architecture [8] that are commonly adopted.

D. Overall Transmitter Power Efficiency Perspectives

When a DPD is adopted, a less linear but more efficient PA, that can operate near its saturation region, can generally be used. However, the overall power efficiency of the device is only improved if the extra power consumed by the DPD stage is less than the power savings due to increased PA efficiency. Here, we address this aspect from a mobile device perspective.

We consider a practical scenario where the transmit power at the output of the mobile PA is +26 dBm (i.e., 400 mW), stemming from 3GPP LTE-Advanced requirements [2], [5], and assuming that the Tx duplexer filter and connector insertion losses are 3 dB. Then, good examples of practical PA power efficiency figures when operating in highly nonlinear or linear modes are around 35% and 20% (or even less), respectively. This means that the power consumed by the highly nonlinear PA is roughly 1150 mwatt, while the corresponding linear PA consumes roughly 2000 mwatt. In other words, adopting a highly power-efficient nonlinear PA saves 850 mwatt of power in this particular example. Then, in order to suppress the spurious emissions at the PA output, in the nonlinear PA case, we adopt the sub-band DPD solution.

In [27], a state of the art 28 nm implementation of the Qualcomm Hexagon DSP capable of supporting up to 4.8 GFLOPS at 1.2 GHz is reported, which is more than enough for carrying out the needed sub-band DPD processing for the IM3 and IM5 sub-bands in our example. In the full-band DPD case, on the other hand, which requires 31.9 GFLOPS as shown in Table I, this is clearly insufficient. The power consumption of the DSP platform in [27] is shown to be approximately 100 mwatt, when running at 840 MHz (i.e., 3.36 GFLOPS assuming 4 FLOPS per cycle), which is again sufficient for linearizing the IM3 and IM5 sub-bands in our example. Thus, adopting the nonlinear PA already saves 850 milliwatt, when it comes to the PA interface, as explained above, while when complemented with the sub-band DPD processing for enhanced linearity, only 100 milliwatt of additional power is consumed. Thus, the overall power budget and power-efficiency are clearly in favor of using a highly nonlinear PA, complemented with the sub-band DPD structure, even in a mobile device with non-contiguous uplink carrier aggregation. Furthermore, if the sub-band DPD processing is implemented using a dedicated hardware solution (e.g., a digital ASIC), an even more power-efficient DPD stage can most likely be realized.

V. Simulation Results

In this section, a quantitative performance analysis of the proposed sub-band DPD solution is presented using Matlab simulations with practical models for mobile-like PAs designed for low-cost devices. In general, we quantify the suppression of intermodulation power at the IM3 and IM5 sub-bands through the power ratios relative to the component carrier wanted signal power as shown in Fig. 1, which are defined as

$$IM3R = 10\log_{10}\frac{P_{wanted}}{P_{IM3}},\ IM5R\ = 10\log_{10}\frac{P_{wanted}}{P_{IM5}}. \tag{64}$$

The inband transmit waveform purity is measured through the error vector magnitude (EVM), which is defined as

$$EVM_{\%} = \sqrt{\frac{P_{error}}{P_{ref}}} \times 100\%. \tag{65}$$

TABLE II
COMPARISON OF IM3+ SUPPRESSION AND EVM OF THIRD-ORDER INVERSE, MMSE AND DECORRELATION-BASED ANALYTICAL SUB-BAND DPD SOLUTIONS AT +23 DBM PA OUTPUT POWER

	Positive IM3R [dBc]	EVM [%]
No DPD	28.8342	1.9711
Third-order Inverse	41.9230	1.8912
Analytical Decorrelation-based	51.8248	1.8914
Analytical MMSE	51.8468	1.8917

Here, P_{error} is the power of the error signal, while P_{ref} is the reference power of the ideal symbol constellation. The error signal is defined as the difference between the ideal symbol values and the corresponding synchronized and equalized samples at the PA output, both normalized to have identical linear gains.

A. Comparison of Analytical IM3 Sub-band DPD Solutions

In Section III-A, analytical reference expressions for the third-order inverse, minimum MSE, and decorrelation-based sub-band DPD solutions were presented. In this subsection, we shortly evaluate and compare the performance of these analytical solutions, assuming a third-order memoryless PA and known parameters, and focus only on the positive IM3 sub-band for simplicity. The memoryless PA model has been identified using a true mobile PA, with transmit power of +23dBm. The main objective is to compare the performance of the three analytical solutions in terms of linearization performance, and thereon to verify that the decorrelation based solution is essentially identifcal to the minimum MSE solution.

The signal used in this performance evaluation is composed of two 1MHz LTE-A UL SC-FDMA CCs with QPSK data modulation, and the CC spacing is 10MHz. The obtained results shown in Table II demonstrate that the decorrelation-based solution is giving almost the same performance as the minimum MSE solution, and also that both of them are substantially better than the classical third-order inverse solution [16] in terms of the IMD suppression at the considered sub-band. It can also be seen from Table II that the EVM is essentially not affected by the sub-band DPD processing.

B. P^{th}-order Inverse vs. Decorrelation-based IM3 Sub-band DPD Solutions

Next we evaluate and compare the performance of 5th-order inverse and decorrelation-based IM3 sub-band DPD solutions. The 5th-order inverse reference solution for IM3+ sub-band is derived in Appendix B. In these simulations, the transmit waveform is again composed of two 1 MHz LTE-A UL SC-FDMA component carriers with QPSK data modulation, and the CC spacing is 10 MHz. The PA model, in turn, is a memoryless 5th-order model whose parameters have been identified using a true mobile PA transmitting at +23 dBm. The 5th-order inverse DPD is using known parameters, while the decorrelation-based one is adopting the proposed sample-adaptive learning described in detail in Section IV.

The PA output spectra with different solutions are illustrated in Fig. 6. It can clearly be seen that the decorrelation-based

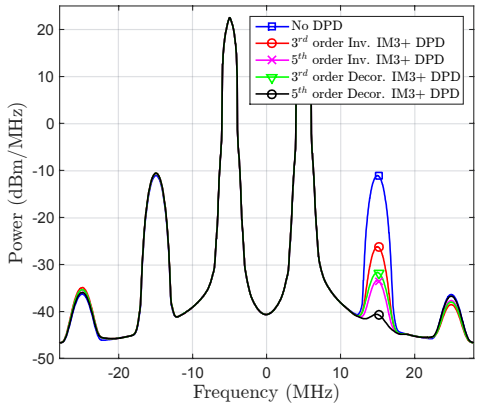

Fig. 6. Baseband equivalent PA output spectrum at +23 dBm with two 1 MHz LTE-A UL carriers and 10 MHz CC separation using a fifth-order memoryless PA. P^{th}-order inverse and decorrelation-based IM3+ sub-band DPD solutions are compared, with both third-order and fifth-order nonlinear processing.

sub-band DPD substantially outperforms the P^{th}-order inverse based sub-band DPD, in both third and fifth-order cases, despite the fact that the P^{th}-order inverse solutions are using known parameters. The reason is that the inverse solutions cancel only the third and fifth order terms, as described in Appendix B, but do not suppress the other induced higher-order terms, which have structural similarity and correlation with the third and fifth-order basis functions. On the other hand, the proposed decorrelation-based solution takes this explicitly into account, and thus achieves clearly better spurious emission suppression. The figure also illustrates that the performance of the fifth-order decorrelation-based sub-band DPD is clearly better than that of the third-order one.

In the remaining parts of this section, we shall focus on more detailed performance evaluations of the proposed decorrelation-based sub-band DPD solution, incorporating memory both in the PA and in the predistortion processing. From now on, we refer to the decorrelation-based sub-band DPD simply as 'sub-band DPD', to simplify the presentation.

C. Performance of Proposed Higher-Order Sub-band DPD at IM3, IM5 and IM7

In this subsection, we evaluate the performance of the proposed sub-band DPD in the more realistic case of having memory in the PA. The PA model is a 9th-order parallel Hammerstein model, with four memory taps per branch, and the parameters have been identified using measurements with a true mobile PA transmitting at +24 dBm. The sub-band DPD structure contains now also memory, with two taps ($N = 1$) per basis function. Block-adaptive learning principle is adopted, with 200 blocks each containing 1000 samples. The transmit waveform is otherwise identical to earlier cases, but the CC separation is now 12 MHz.

Fig. 7 shows the effectiveness of the proposed higher-order sub-band DPDs, here processing the IM3+ sub-band,

TABLE III
COMPARISON OF QUANTITATIVE RUNNING COMPLEXITY AND LINEARIZATION PERFORMANCE OF FULL-BAND VERSUS SUB-BAND DPD. TWO 1 MHZ LTE-A UL CARRIERS WITH QPSK DATA MODULATION AND 20 MHZ CARRIER SPACING ARE USED.

	DPD Running Complexity			Transmitter Performance			
	Coeffs	Fs [MSPS]	GFLOPS	EVM [%]	Positive IM3R [dBc]	Positive IM5R [dBc]	Output Power [dBm]
No DPD	N/A	N/A	N/A	1.2527	35.5744	56.4272	+20
Full-Band ILA DPD	20	189	31.941	0.1058	61.9428	63.9842	+19
IM3+ Sub-Band DPD	8	9	0.891	1.2489	68.3291	N/A	+20
IM5+ Sub-Band DPD	6	9	0.774	1.2529	N/A	71.9823	+20

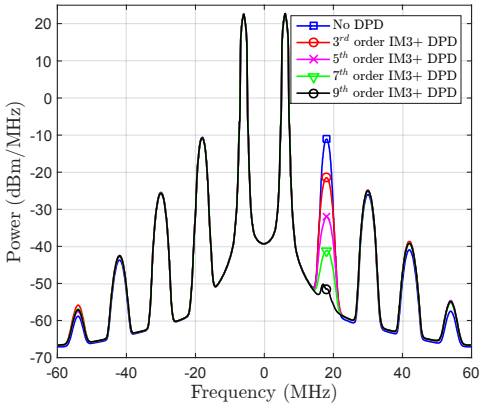

Fig. 7. Baseband equivalent PA output spectrum at +24 dBm with two 1 MHz LTE-A UL carriers and 12 MHz CC separation using a ninth-order PA with memory. Different orders of the IM3+ sub-band DPD are compared, with memory depth equal to 1 per DPD SNL basis function.

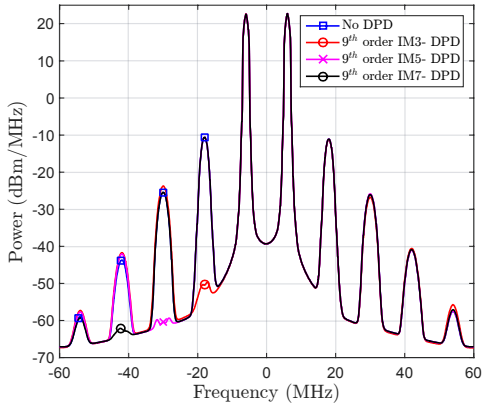

Fig. 9. Baseband equivalent of two 1 MHz LTE-A UL carriers with 12 MHz separation using a ninth order PH PA extracted from a real mobile PA at +24 dBm. Ninth order negative IM3, IM5, and IM7 sub-band DPD solutions are shown, with memory depth equal to 1 per DPD SNL basis function.

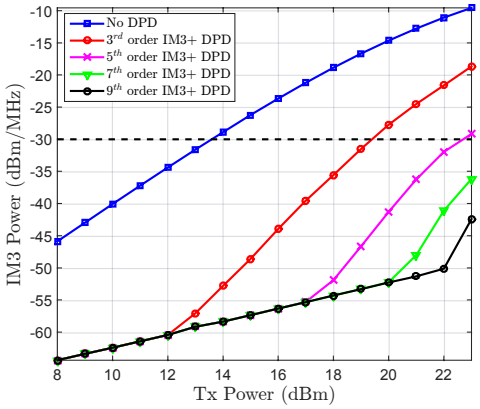

Fig. 8. IM3 spurious emissions vs. TX power using different orders of the IM3+ sub-band DPD processing, with memory depth equal to 1 per DPD SNL basis function. A ninth-order PA with memory is used, and 2 dB Tx filter insertion loss is assumed.

compared to the basic third-order solution presented earlier in [20]. Up to 40 dB suppression for the IM3 spurious emissions is shown when adopting ninth-order processing, something that has not been reported before in any prior works using a practical PA model with memory effects. Fig. 8 shows then how the IM3 spurious emission level changes with varying the TX power and using different sub-band DPD orders. The IM3 spurious emissions are clearly below the general spurious emission limit (-30 dBm/MHz) even at very high TX powers up to +23 dBm, when using a seventh-order, or higher, sub-band DPD.

Another main contribution in this paper is the extension of the IM3 sub-band DPD solution to include also higher-order IM sub-bands. Fig. 9 shows the performance of the negative IM5 and IM7 sub-band DPDs, in addition to the negative IM3 sub-band DPD, when ninth-order nonlinear processing is adopted in the sub-band DPDs. Up to 40 dB, 35 dB, and 18 dB of suppression is achieved at the negative IM3, IM5, and IM7 sub-bands, respectively. This shows the effectiveness of the proposed solutions in processing and suppressing also the spurious emissions at higher IM sub-bands.

D. Full-Band versus Sub-band DPD Complexity and Performance Analysis

In this subsection, we compare the performance of our proposed sub-band DPD technique against that of a classical full-band DPD adopting parallel Hammerstein based wideband linearization and indirect learning architecture (ILA). The

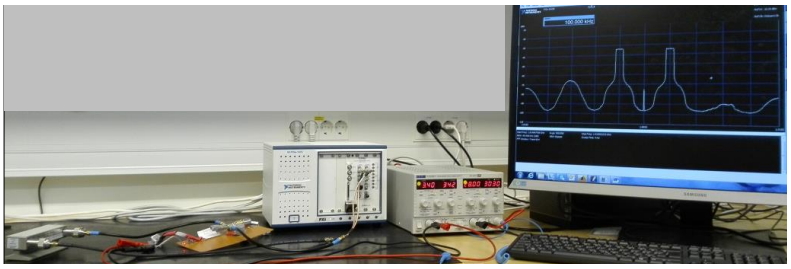

(a)

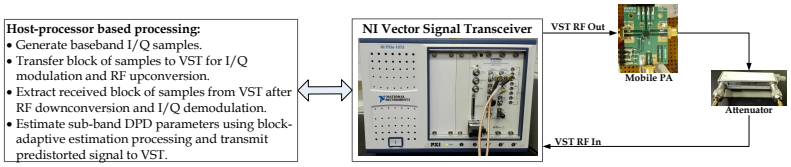

(b)

Fig. 10. Hardware setup used in the RF measurements for testing and evaluating the proposed sub-band DPD.

evaluation considers the linearization performance, complexity, and transmitter efficiency utilizing our earlier complexity analysis results reported in Section IV. The ninth-order full-band PH ILA DPD uses 100k samples for parameter learning, per ILA iteration, with a total of 2 ILA iterations, and the number of memory taps per PH branch is 4. The ninth-order block-adpative sub-band DPD, in turn, uses also a total of 200k samples with block size $M = 1000$, and adopts two memory taps per DPD SNL basis function.

The results are collected in Table III, which shows that in addition to the significantly lower complexity measured by the number of GFLOPS, the sub-band DPD achieves better linearization performance in terms of spurious IMD suppression at the considered IM3 and IM5 sub-bands. On the other hand, the full-band DPD outperforms the sub-band DPD in terms of the inband distortion mitigation (i.e., EVM). This is expected, since the full-band DPD linearizes the whole transmit band, including the main CCs and the IMD spurious emissions. However, the EVM with the sub-band DPD is only around 1.25% which is by far sufficient for modulations at least up to 64-QAM. Additionally, the full-band DPD based on the ILA structure requires an additional 1 to 2 dB back off to guarantee stable operation, which is not required in the sub-band DPD. Thus the transmitter becomes more power efficient when using the sub-band DPD as shown in Table III. For fairness, it is to be acknowledged that a full-band DPD can typically enhance the EVM and ACLR, while the sub-band DPD concept is specifically targeting only the spurious emissions.

VI. RF Measurement Results

In order to further demonstrate the operation of the proposed sub-band DPD solution, we next report results of comprehensive RF measurements using a commercial LTE-Advanced mobile terminal PA together with a vector signal transceiver (VST), which is implementing the RF modulation and demodulation. The actual sub-band DPD processing and parameter learning algorithms are running on a host processor.

The ACPM-5002-TR1 mobile power amplifier used in our measurements is designed for LTE-A UL band 25 (1850-1915 MHz), with 29 dB gain. The National Instruments (NI) PXIe-5645R VST includes both a vector signal generator (VSG), and a vector signal analyzer (VSA) with 80 MHz instantaneous bandwidth. In these experiments, the digital baseband waveform is divided into 50 blocks of size $M = 10k$ samples which are first generated locally on the host processor, and then transferred to the VSG to perform RF I/Q modulation at the desired power level at the PA input. The VST RF output is then connected to the input port of the external power amplifier, whose output port is connected to the VST RF input through a 40 dB attenuator, implementing the observation receiver as illustrated also in Fig. 10. The VSA performs RF I/Q demodulation to bring the signal back to baseband. The baseband I/Q observation block is then filtered to select the IM3 sub-band which is used for block-based sub-band DPD learning, after proper alignment with the locally generated basis functions, as explained in Section III-C. The sub-band DPD block size M used in these experiments is $10k$, and the DPD memory depth N is 1.

In general, two different intra-band LTE-A CA RF measurement examples are demonstrated in this subsection. The first experiment demonstrates the violation of the spurious emission limit due to the inband emission of the IM3+ spur, thus not being attenuated by the TX filter. The second experiment demonstrates an own RX desensitization example, in FDD transceiver context, where the IM3+ spur is located at the own RX band (1930-1995 MHz) and is not sufficiently attenuated by the duplexer TX filter. Notice that in principle, when tackling specifically the own RX desensitization problem with the proposed sub-band DPD solution, the main receiver of

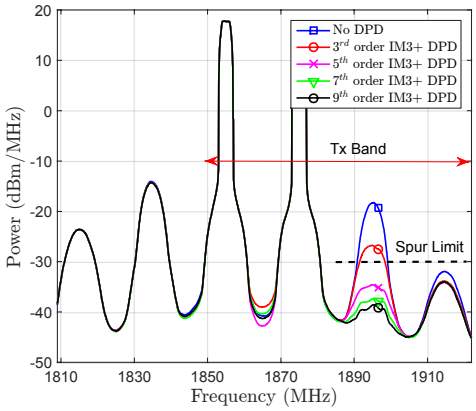

Fig. 11. An LTE-A band 25 RF measurement example at the UE PA output showing the gain from using an IM3+ sub-band DPD. IM3 spur reduction with third, fifth, seventh, and ninth-order sub-band DPDs are demonstrated, using a real commercial mobile PA operating at +25 dBm. An LTE-A UL CA signal with two 3 MHz CCs and 20 MHz carrier spacing is used.

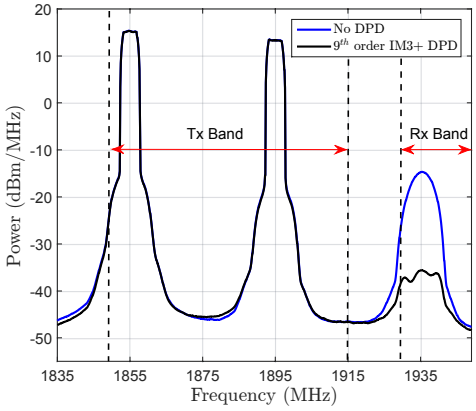

Fig. 12. An LTE-A band 25 RF measurement example at the UE PA output showing the gain from using a ninth-order IM3+ sub-band DPD when the IM3+ is falling at own RX band. An LTE-A UL CA signal with two 5 MHz CCs and 40 MHz carrier spacing is used with a real commercial mobile PA operating at +25 dBm.

the FDD device could potentially be used as the observation receiver (i.e., learning the sub-band DPD coefficients without an extra auxiliary/observation receiver). However, such an approach would indeed be applicable only in the own RX desensitization case, while when mitigating other harmful emissions, an auxiliary observation receiver would anyway have to be adopted. Thus, in these RF measurements, we adopt the auxiliary receiver based approach, while consider further developments of the main receiver based parameter learning as an important topic for our future work.

A. Spurious Emission Limit Violation

Fig. 11 shows the measured power spectral density at the PA output using the IM3 sub-band DPD with different orders. The adopted waveform is an intra-band CA LTE-A UL signal with 3 MHz per CC and 20 MHz carrier spacing. The power level at the PA output in this example is +25 dBm. The intermodulation distortion at the IM3+ sub-band is emitted inband, since the total TX band covers 1850-1915 MHz, and is clearly violating the spurious emission limit (-30 dBm/MHz) when no DPD is used. When using the sub-band DPD, the spurious emission level is well below the emission limit, given that at least 5th-order processing is deployed. In general, more than 20 dB of measured spurious emission suppression is achieved with the ninth order IM3 sub-band DPD, thus giving more than 10 dB additional gain compared to the basic third-order sub-band DPD as shown in Fig. 11. Notice that there is no need for predistorting the IM3- sub-band in this example, since those emissions will be filtered out by the TX filter.

B. Own Receiver Desensitization

Fig. 12 illustrates another LTE-A intra-band CA UL band 25 example, now with 5 MHz CC bandwidths and 40 MHz carrier spacing. The duplexing distance at LTE-A band 25 is only 80 MHz, thus the IM3+ spur at 1935 MHz in this example is falling on the own RX band, and therefore potentially desensitizing the own receiver. The power level at the PA output in this example is +25 dBm.

Then, by adopting a ninth-order IM3+ sub-band DPD, more than 20 dB of spurious emission suppression is achieved, as can be seen in Fig. 12. Again, two taps ($N = 1$) per basis function are used, and block-adaptive parameter learning is deployed. Fig. 13 shows the real-time convergence of the sub-band DPD coefficients for the third, fifth, seventh, and ninth-order basis functions, respectively. It can be seen that the coefficients converge in a stable manner in a real RF environment due to the orthogonalization of the SNL basis functions, as explained in Section III-B.

In general, assuming a UE duplexer TX filter with 65 dB attenuation at the own RX band (e.g., ACMD-6125 Band 25 LTE-A UE Duplexer), the integrated power of the IM3+ spur at the RX band without DPD will be approximately -73 dBm/5MHz. This is 25 dB above the effective RX noise floor when assuming 9 dB UE RX noise figure (NF) [28]. This would thus cause significant own receiver desensitization that could lead to a complete blocking of the desired RX signal. On the other hand, when the proposed IM3+ sub-band DPD is deployed, the integrated power of the IM3+ spur at the RX band will be approximately -95 dBm/5MHz, which is only 3 dB above the effective RX noise floor, as shown also in Fig. 14. Though the residual spur is still slightly above the effective RX noise floor, the sensitivity degradation is substantially relaxed, despite operating at a maximum PA output power of +25 dBm. We elaborate on this further in Fig. 14, showing the integrated power of the IM3+ spur at the RX LNA input while changing the PA output power level. With a ninth order sub-band DPD, we can transmit up to +18 dBm PA output power with an effectively perfectly linear TX, in terms of IM3+ spur

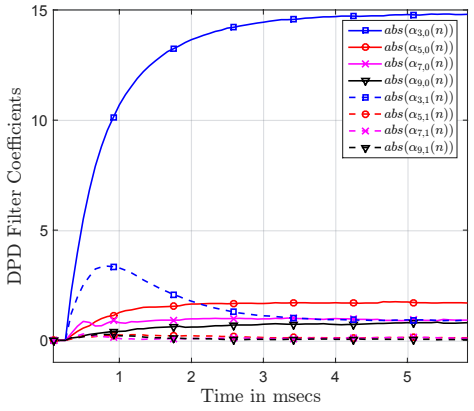

Fig. 13. Convergence of the ninth-order sub-band DPD coefficients, with memory depth $N = 1$ per basis function, when the positive IM3 sub-band is considered and block-adaptive learning is deployed. An RF measurement example with two 5 MHz LTE-A UL CCs and 40 MHz carrier spacing is used with a real commercial mobile PA operating at +25 dBm.

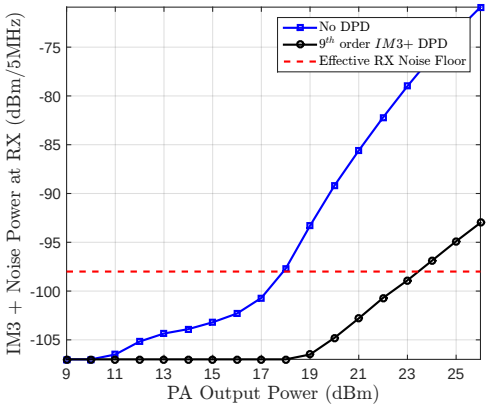

Fig. 14. Integrated IM3+ sub-band power at own RX LNA input over 5 MHz vs. PA output power using ninth order IM3+ sub-band DPD processing, with memory depth equal to 1 per DPD SNL basis function. A commercial mobile PA operating at LTE band 25 is used in the RF measurements, and 65 dB duplexer TX filter attenuation [**?**] is assumed at the RX band.

level, compared to +10 dBm PA output power without DPD. Additionally, with DPD, the integrated IM3+ power is less than the effective RX noise floor up to +23 dBm PA output power, while without DPD it is already 20 dB above the noise floor at the same power level.

VII. Conclusions

In this article, a novel low-complexity sub-band digital predistortion (DPD) solution was proposed for suppressing unwanted spurious emissions in non-contiguous spectrum access. Novel decorrelation based adaptive parameter learning methods were also formulated, allowing efficient estimation and tracking with low computational complexity. All algorithm derivations and modeling were carried out in the general case of having memory in the PA as well as in the sub-band DPD processing. Different nonlinear distortion and processing orders, beyond classical third-order cases, were also reported. The proposed technique can find application in suppressing inband spurs which would violate the spurious emission limit, suppressing out-of-band spurs falling, e.g., on the own receiver band, or in protecting primary user transmissions in cognitive radio systems. A quantitative complexity analysis was presented, comparing the proposed solution to conventional full-band DPD solutions available in the literature. The performance was evaluated in a comprehensive manner, showing excellent linearization performance despite the considerably reduced complexity compared to classical full-band solutions. Finally, extensive RF measurement results using a commercial LTE-Advanced mobile power amplifier were reported, evidencing up to 22 dB suppression of the most problematic third-order spurious emissions.

Appendix A: Analytical MMSE Solution for Third-Order IM3 Sub-band DPD

Here, we derive the analytical minimum mean-square error solution shown in (32), which is used as a reference solution in simulations in Section V-A. We first define the so-called error signal as $e(n) = \tilde{y}_{IM3_+}(n)$, since with ideal predistortion the IM3+ sub-band signal would be zero, and thus the optimization means minimizing the power of this error signal. From (30), the error signal reads

$$e(n) = (f_3 + f_1\alpha)u(n) + 2f_3\alpha(|x_1(n)|^2 + |x_2(n)|^2)u(n) + f_3|\alpha|^2\alpha|x_1(n)|^4|x_2(n)|^2u(n), \quad (66)$$

where f_1 and f_3 are the third-order memoryless PA model parameters, α denotes the DPD coefficient to be optimized, and $x_1(n)$ and $x_2(n)$ are the baseband equivalents of the two component carriers. The statistical expectation $\mathbf{E}[|e(n)|^2] = \mathbf{E}[e(n)e^*(n)]$, assuming that the component carrier signals $x_1(n)$ and $x_2(n)$ are statistically independent, and ignoring some high-order vanishingly small terms, then reads

$$\mathbf{E}[e(n)e^*(n)] = \mathbf{E}_{42}\left[|f_3|^2 + |f_1|^2|\alpha|^2 + \alpha f_1 f_3^* + \alpha^* f_1^* f_3\right] + (2\mathbf{E}_{62} + 2\mathbf{E}_{44})\left[|f_3|^2(\alpha + \alpha^*) + |\alpha|^2(f_1 f_3^* + f_1^* f_3)\right] + (4\mathbf{E}_{46} + 8\mathbf{E}_{64} + 4\mathbf{E}_{82})|f_3|^2|\alpha|^2, \quad (67)$$

where $\mathbf{E}_{ij}$ is used as a shorthand notation for $\mathbf{E}[|x_1|^i]\mathbf{E}[|x_2|^j]$. Now, differentiating (67) with respect to α, yields

$$\frac{\partial}{\partial\alpha}\mathbf{E}[e(n)e^*(n)] = \mathbf{E}_{42}\left[\alpha^*|f_1|^2 + f_1 f_3^*\right] + (2\mathbf{E}_{62} + 2\mathbf{E}_{44})\left[|f_3|^2 + \alpha^*(f_1 f_3^* + f_1^* f_3)\right] + (4\mathbf{E}_{46} + 8\mathbf{E}_{64} + 4\mathbf{E}_{82})|f_3|^2\alpha^*. \quad (68)$$

Then, setting (68) to zero and solving for α yields the optimal MMSE DPD parameter, given by

$$\alpha_{MMSE} = \frac{-\left[f_1 f_3^* \mathbf{E}_{42} + 2|f_3|^2(\mathbf{E}_{62}+\mathbf{E}_{44})\right]^*}{\left[|f_1|^2\mathbf{E}_{42} + 4\mathbb{R}(f_1 f_3^*)(\mathbf{E}_{62}+\mathbf{E}_{44}) + 4|f_3|^2(\mathbf{E}_{46}+2\mathbf{E}_{64}+\mathbf{E}_{82})\right]^*}, \tag{69}$$

where $\mathbb{R}(.)$ denotes the real-part operator. This concludes the proof.

Appendix B: Analytical Fifth-Order Inverse Based IM3 Sub-band DPD Solution

Here, we derive the 5^{th} order inverse solution for the IM3+ sub-band DPD, to be used as a reference solution in the simulations in Section V-B. The output of a memoryless 5^{th} order polynomial PA model is

$$y(n) = f_1 x(n) + f_3|x(n)|^2 x(n) + f_5|x(n)|^4 x(n), \tag{70}$$

where f_1, f_3 and f_5 are the polynomial coefficients, and $x(n)$ is the composite baseband equivalent input signal, as given in (1). Through direct substitution of (1) in (70), the baseband equivalent IM3+ distortion term, located at three times the IF frequency, can be extracted and reads

$$\begin{aligned} y_{IM3_+}(n) = {} & f_3(x_2^*(n)x_1^2(n)) \\ & + 2f_5|x_1(n)|^2(x_2^*(n)x_1^2(n)) \\ & + 3f_5|x_2(n)|^2(x_2^*(n)x_1^2(n)). \end{aligned} \tag{71}$$

Stemming from the signal structure in (71), the sub-band DPD injection signal is composed of three basis functions of the form $x_2^*(n)x_1^2(n)$, $|x_1(n)|^2x_2^*(n)x_1^2(n)$ and $|x_2(n)|^2x_2^*(n)x_1^2(n)$. In case of fifth-order inverse based sub-band DPD, these basis functions are multiplied by proper coefficients such that all the distortion terms at the IM3+ sub-band at the PA output, up to order five, are cancelled. Thus, incorporating such DPD processing, yet with arbitrary coefficients, the composite baseband equivalent PA input signal reads

$$\begin{aligned} \tilde{x}(n) = {} & x_1(n)e^{j2\pi\frac{f_{IF}}{f_s}n} + x_2(n)e^{-j2\pi\frac{f_{IF}}{f_s}n} \\ & + \alpha_{3,inv}(x_2^*(n)x_1^2(n))e^{j2\pi\frac{3f_{IF}}{f_s}n} \\ & + \alpha_{51,inv}|x_1(n)|^2(x_2^*(n)x_1^2(n))e^{j2\pi\frac{3f_{IF}}{f_s}n} \\ & + \alpha_{52,inv}|x_2(n)|^2(x_2^*(n)x_1^2(n))e^{j2\pi\frac{3f_{IF}}{f_s}n}, \end{aligned} \tag{72}$$

where the subscript inv in the coefficients is emphasizing the P^{th}-order inverse based solution. Substituting (72) in (70), and extracting the third and fifth order IM3+ terms, yields

$$\begin{aligned} \tilde{y}_{IM3_+}(n) = {} & (f_1\alpha_{3,inv} + f_3)x_2^*(n)x_1^2(n) \\ & + (f_1\alpha_{51,inv} + 2f_3\alpha_{3,inv} + 2f_5)|x_1(n)|^2(x_2^*(n)x_1^2(n)) \\ & + (f_1\alpha_{52,inv} + 2f_3\alpha_{3,inv} + 3f_5)|x_2(n)|^2(x_2^*(n)x_1^2(n)). \end{aligned} \tag{73}$$

From (73), we now can easily obtain the fifth-order inverse coefficients that null the third and fifth-order terms, yielding

$$\alpha_{3,inv} = -\frac{f_3}{f_1},$$

$$\alpha_{51,inv} = 2\frac{f_3^2}{f_1^2} - 2\frac{f_5}{f_1},\ \alpha_{52,inv} = 2\frac{f_3^2}{f_1^2} - 3\frac{f_5}{f_1}.$$

This concludes the derivation.

References

[1] S. Parkvall, A. Furuskar, and E. Dahlman, "Evolution of LTE toward IMT-advanced," *IEEE Commun. Mag.*, vol. 49, no. 2, pp. 84–91, February 2011.

[2] *LTE Evolved Universal Terrestrial Radio Access (E-UTRA) User Equipment (UE) radio transmission and reception, 3GPP TS 36.101 V12.4.0 (Release 12)*, June 2014.

[3] S.A. Bassam, W. Chen, M. Helaoui, and F.M. Ghannouchi, "Transmitter architecture for CA: Carrier Aggregation in LTE-Advanced systems," *IEEE Microw. Mag.*, vol. 14, no. 5, pp. 78–86, July 2013.

[4] C. Park, L. Sundström, A. Wallen, and A. Khayrallah, "Carrier aggregation for LTE-advanced: Design challenges of terminals," *IEEE Commun. Mag.*, vol. 51, no. 12, pp. 76–84, Dec. 2013.

[5] R4-121205, "Way forward for non-contiguous intraband transmitter aspects.", 3GPP Tech. Rep., Feb. 2013.

[6] R4-124353, "Non-contiguous intraband unwanted emission.", 3GPP Tech. Rep., Feb. 2013.

[7] H. Gandhi, D. Greenstreet, and J. Quintal, "Digital Radio Front-End strategies provide game-changing benefits for small cell base stations," Tech. Rep., Texas Instruments, May 2013.

[8] L. Guan and A. Zhu, "Green communications: Digital predistortion for wideband RF power amplifiers," *IEEE Microw. Mag.*, vol. 15, no. 7, pp. 84–89, Dec. 2014.

[9] R4-123797, "UE reference sensitivity requirements with two UL carriers.," 3GPP Tech. Rep., Feb. 2013.

[10] *International Telecommunication Union Radio Communication Sector, Recommendation ITU-R SM.329-12 Unwanted emissions in the spurious domain.*.

[11] Chao Yu, Wenhui Cao, Yan Guo, and A. Zhu, "Digital Compensation for Transmitter Leakage in Non-Contiguous Carrier Aggregation Applications With FPGA Implementation," *IEEE Trans. Microw. Theory Techn.*, vol. 63, no. 12, pp. 4306–4318, Dec 2015.

[12] A. Kiayani, M. Abdelaziz, L. Anttila, V. Lehtinen, and M. Valkama, "Digital Mitigation of Transmitter-Induced Receiver Desensitization in Carrier Aggregation FDD Transceivers," *IEEE Trans. Microw. Theory Techn.*, vol. 63, no. 11, pp. 3608–3623, Nov 2015.

[13] S.A. Bassam, F.M. Ghannouchi, and M. Helaoui, "2-D Digital Predistortion (2-D-DPD) architecture for concurrent dual-band transmitters," *IEEE Trans. Microw. Theory Techn.*, vol. 59, no. 10, pp. 2547–2553, Oct. 2011.

[14] P. Roblin, C. Quindroit, N. Naraharisetti, S. Gheitanchi, and M. Fitton, "Concurrent linearization," *IEEE Microw. Mag.*, vol. 14, no. 7, pp. 75–91, Nov. 2013.

[15] Y. Liu, J. Yan, and P. Asbeck, "Concurrent dual-band digital predistortion with a single feedback loop," *IEEE Trans. Microw. Theory Techn.*, vol. 63, no. 5, pp. 1556–1568, May 2015.

[16] P. Roblin, S. K. Myoung, D. Chaillot, Y. G. Kim, A. Fathimulla, J. Strahler, and S. Bibyk, "Frequency-selective predistortion linearization of RF power amplifiers," *IEEE Trans. Microw. Theory Techn.*, vol. 56, no. 1, pp. 65–76, Jan. 2008.

[17] J. Kim, P. Roblin, D. Chaillot, and Z. Xie, "A generalized architecture for the frequency-selective digital predistortion linearization technique," *IEEE Trans. Microw. Theory Techn.*, vol. 61, no. 1, pp. 596–605, Jan. 2013.

[18] S.A. Bassam, M. Helaoui, and F.M. Ghannouchi, "Channel-selective multi-cell digital predistorter for multi-carrier transmitters," *IEEE Trans. Microw. Theory Techn.*, vol. 60, no. 8, pp. 2344–2352, Aug. 2012.

[19] M. Abdelaziz, L. Anttila, A. Mohammadi, F. Ghannouchi, and M. Valkama, "Reduced-complexity power amplifier linearization for carrier aggregation mobile transceivers," in *IEEE International Conference on Acoustics, Speech, and Signal Processing*, pp. 3908–3912, May 2014.

[20] M. Abdelaziz, L. Anttila, J.R. Cavallaro, S. Bhattacharyya, A. Mohammadi, F.M. Ghannouchi, M. Juntti, and M. Valkama, "Low-complexity digital predistortion for reducing power amplifier spurious emissions in spectrally-agile flexible radio," in *9th International Conference on Cognitive Radio Oriented Wireless Networks*, pp. 323–328, June 2014.

[21] M. Abdelaziz, C. Tarver, K. Li, L. Anttila, R. Martinez, M. Valkama, J. R. Cavallaro, "Sub-band digital predistortion for noncontiguous transmissions: Algorithm development and real-time prototype implementation," in *49th Asilomar Conference on Signals, Systems and Computers*, pp. 1180–1186, Nov. 2015.

[22] M. Abdelaziz, Z. Fu, L. Anttila, A. M. Wyglinski and M. Valkama, "Digital predistortion for mitigating spurious emissions in spectrally agile radios," *IEEE Commun. Mag.*, vol. 54, no. 3, pp. 60–69, March 2016.

[23] Z. Fu, L. Anttila, M. Abdelaziz, M. Valkama, and A. M. Wyglinski, "Frequency-Selective Digital Predistortion for Unwanted Emission Reduction," *IEEE Trans. Commun.*, vol. 63, no. 1, pp. 254–267, Jan. 2015.

[24] A.S. Tehrani, H. Cao, S. Afsardoost, T. Eriksson, M. Isaksson, and C. Fager, "A comparative analysis of the complexity/accuracy tradeoff in power amplifier behavioral models," *IEEE Trans. Microw. Theory Techn.*, vol. 58, no. 6, pp. 1510–1520, June 2010.

[25] H. Qian, S. Yao, H. Huang, and W. Feng, "A low-complexity digital predistortion algorithm for power amplier linearization," *IEEE Trans. Broadcast.*, vol. 60, no. 4, pp. 670–678, Dec. 2014.

[26] W. Hoffmann, "Iterative algorithms for Gram Schmidt orthogonalization," *Computing*, vol. 41, no. 4, pp. 335–348, 1989.

[27] M. Saint-Laurent et al., "A 28 nm DSP powered by an on-chip LDO for high-performance and energy-efficient mobile applications," *IEEE J. Solid-State Circuits*, vol. 50, no. 1, pp. 81–91, Jan 2015.

[28] *LTE Evolved Universal Terrestrial Radio Access (E-UTRA) RF system scenarios, 3GPP TR 36.942 V10.2.0 (Release 10)*, May 2011.

Mahmoud Abdelaziz (S'13) received the B.Sc. degree (with honors) and M.Sc. degree in Electronics and Electrical Communications Engineering from Cairo University, Egypt, in 2006 and 2011. He is currently pursuing the Doctoral degree at Tampere University of Technology, Finland where he works as a researcher with the Department of Electronics and Communications. From 2007 to 2012 he has been working as a communication systems and signal processing engineer at Newport Media, as well as other companies in the wireless industry. His research interests include statistical and adaptive signal processing in flexible radio transceivers, wideband digital pre-distortion, and cognitive radio systems.

Lauri Anttila (S'06, M'11) received the M.Sc. degree and D.Sc. (Tech) degree (with honors) in electrical engineering from Tampere University of Technology (TUT), Tampere, Finland, in 2004 and 2011. Currently, he is a Senior Research Fellow at the Department of Electronics and Communications Engineering at TUT. His research interests are in signal processing for wireless communications, in particular radio implementation challenges in 5G cellular radio and full-duplex radio, flexible duplexing techniques, and transmitter and receiver linearization. He has co-authored over 60 peer reviewed articles in these areas, as well as two book chapters.

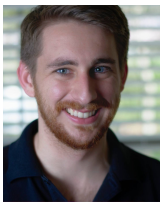

Chance Tarver received a B.S. degree in electrical engineering from Louisiana Tech University, Ruston, LA, in 2014, and his M.S. degree in electrical and computer engineering in 2016 from Rice University, Houston, TX. He is currently a Ph.D. student in the Department of Electrical and Computer Engineering at Rice University. His research interests include software defined radio and signal processing for wireless communications.

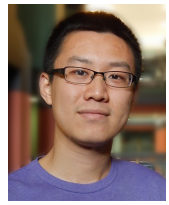

Kaipeng Li (S'14) received his B.S. degree in physics from Nanjing University, Nanjing, China, in 2013, and his M.S. degree in electrical and computer engineering from Rice University in 2015. He is currently a Ph.D. candidate in the Department of Electrical and Computer Engineering at Rice University, Houston, Texas. His research interests include digital signal processing, parallel computing on GPGPU and multicore CPU, software-defined radios and massive MIMO systems.

Joseph R. Cavallaro (S'78, M'82, SM'05, F'15) received the B.S. degree from the University of Pennsylvania, Philadelphia, PA, in 1981, the M.S. degree from Princeton University, Princeton, NJ, in 1982, and the Ph.D. degree from Cornell University, Ithaca, NY, in 1988, all in electrical engineering. From 1981 to 1983, he was with AT&T Bell Laboratories, Holmdel, NJ. In 1988, he joined the faculty of Rice University, Houston, TX, where he is currently a Professor of electrical and computer engineering. His research interests include computer arithmetic, and DSP, GPU, FPGA, and VLSI architectures for applications in wireless communications. During the 1996-1997 academic year, he served at the National Science Foundation as Director of the Prototyping Tools and Methodology Program. He was a Nokia Foundation Fellow and a Visiting Professor at the University of Oulu, Finland in 2005 and continues his affiliation there as an Adjunct Professor. He is currently the Director of the Center for Multimedia Communication at Rice University. He is a Fellow of the IEEE and a Member of the IEEE SPS TC on Design and Implementation of Signal Processing Systems and the Chair-Elect of the IEEE CAS TC on Circuits and Systems for Communications. He is currently an Associate Editor of the IEEE Transactions on Signal Processing, the IEEE Signal Processing Letters, and the Journal of Signal Processing Systems. He was Co-chair of the 2004 Signal Processing for Communications Symposium at the IEEE Global Communications Conference and General/Program Co-chair of the 2003, 2004, and 2011 IEEE International Conference on Application-Specific Systems, Architectures and Processors (ASAP), General/Program Co-chair for the 2012, 2014 ACM/IEEE GLSVLSI, Finance Chair for the 2013 IEEE GlobalSIP conference, and TPC Co-Chair of the 2016 IEEE SiPS workshop. He was a member of the IEEE CAS Society Board of Governors during 2014.

Mikko Valkama (S'00, M'01, SM'15) was born in Pirkkala, Finland, on November 27, 1975. He received the M.Sc. and Ph.D. Degrees (both with honors) in electrical engineering (EE) from Tampere University of Technology (TUT), Finland, in 2000 and 2001, respectively. In 2002, he received the Best Ph.D. Thesis -award by the Finnish Academy of Science and Letters for his dissertation entitled "Advanced I/Q signal processing for wideband receivers: Models and algorithms". In 2003, he was working as a visiting researcher with the Communications Systems and Signal Processing Institute at SDSU, San Diego, CA. Currently, he is a Full Professor and Department Vice-Head at the Department of Electronics and Communications Engineering at TUT, Finland. His general research interests include communications signal processing, estimation and detection techniques, signal processing algorithms for software defined flexible radios, cognitive radio, full-duplex radio, radio localization, 5G mobile cellular radio, digital transmission techniques such as different variants of multicarrier modulation methods and OFDM, and radio resource management for ad-hoc and mobile networks.

Publication 3

M. Abdelaziz, L. Anttila, A. Kiayani, and M. Valkama, "Decorrelation-based concurrent digital predistortion with a single feedback path," *IEEE Transactions on Microwave Theory and Techniques*, vol. PP, no. 99, pp. 1-14, June 2017.

Decorrelation-based Concurrent Digital Predistortion with a Single Feedback Path

Mahmoud Abdelaziz, *Student Member, IEEE,* Lauri Anttila, *Member, IEEE,* Adnan Kiayani, *Member, IEEE,* Mikko Valkama, *Senior Member, IEEE,*

***Abstract*—In this article, a novel decorrelation-based concurrent digital predistortion (DPD) solution is proposed for dual-band transmitters employing a single wideband power amplifier (PA), and utilizing only a single feedback receiver path. The proposed decorrelation-based parameter learning solution is both flexible and simple, and operates in a closed-loop manner, opposed to the widely-applied indirect learning architecture. The proposed decorrelation-based learning and DPD processing can also be effectively applied to more ordinary single carrier/band transmissions, as well as generalized to more than two transmit bands. Through a comprehensive analysis covering both the DPD parameter learning and the main path processing, it is shown that the complexity of the proposed concurrent DPD is substantially lower compared to the other state-of-the-art concurrent DPD methods. Extensive set of simulation and RF measurement results are also presented, using base-station PAs as well as a commercial LTE-Advanced mobile PA, to evaluate and validate the effectiveness of the proposed DPD solution in various real world scenarios, incorporating both single-band and dual-band transmitter cases. The simulation and RF measurement results demonstrate excellent linearization performance of the proposed concurrent DPD, even outperforming current state-of-the-art methods, despite the significantly lower complexity.**

***Index Terms*—Adaptive filters, carrier aggregation, concurrent linearization, digital predistortion, dual band power amplifiers, frequency division duplexing, nonlinear distortion, spectrally agile radio, 3GPP LTE-Advanced.**

I. Introduction

SPECTRUM aggregation improves the achievable bit-rates and the efficiency of the radio spectrum utilization, but also poses substantial challenges in the transmitter design, especially in low-cost devices such as mobile terminals and small-cell base-stations [1]. In order to enhance the power and cost efficiencies of such wideband transmitters, e.g., carrier aggregation (CA) transmitters in 3GPP LTE-Advanced, the component carriers (CCs) should be combined prior to the power amplifier (PA) [2], in particular in cases where the CCs are still relatively close in frequency. However, this leads to additional unwanted emissions due to inter-modulation between the CCs, as a result of the PA nonlinearity [3], as shown in Fig. 1.

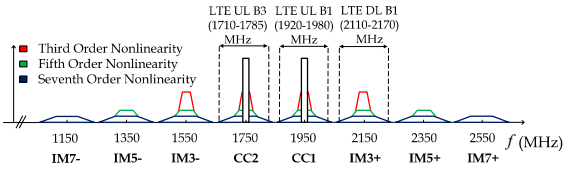

Fig. 1. Illustration of different distortion components created by a nonlinear PA when excited with a non-contiguous CA signal with two component carriers. In this LTE-A UL interband CA example, the CCs are at LTE UL bands 1 and 3. In addition to the EVM and ACLR degradation due to distortion components at and around the main CCs, the IM3+ spur lies at the own RX frequencies of Band 1, causing own RX desensitization.

Three kinds of unwanted emissions result from the nonlinear behavior. The first is emitted in-band, right on top of each CC, thus degrading the in-band error vector magnitude (EVM). The second kind of emissions are out-of-band (OOB) emissions which are emitted in the adjacent channels, thus degrading the adjacent channel leakage ratio (ACLR). The third kind of unwanted emissions are those emitted in the spurious domain, beyond the adjacent channel region which can seriously violate the given spurious emission limits [1], [4]–[6]. Furthermore, in FDD devices, the generated spurious components can also overlap with the device's own receive band, causing receiver desensitization [1], [7]–[9], as demonstrated in Fig. 1

In the recent literature, there have been some works on efficient concurrent digital predistortion (DPD) techniques for CA transmitters that employ only a single PA [3], [10]–[16]. These works assume that the CCs are separated by a relatively large distance such that the spurious emissions are filtered out by the transmit RF filter, and hence linearization of only the main carriers is pursued. The advantage of such concurrent DPD techniques is the reduced sampling rates of both the DAC and ADC in the DPD system, compared to conventional full-band DPD which linearizes the whole aggregated spectrum at a significantly higher sampling rate. However, most of the concurrent DPD techniques developed so far are based on the indirect learning architecture (ILA) when it comes to the DPD parameter estimation, which requires the observation of both CCs at the same time in order to compute the post inverse solution, thus calling for two feedback receivers for proper DPD operation [3], [10]–[12].

Manuscript received January 17, 2017. Mahmoud Abdelaziz, Lauri Anttila, Adnan Kiayani, and Mikko Valkama are with the Laboratory of Electronics and Communications Engineering, Tampere University of Technology, Tampere, Finland.

This work was supported by the Finnish Funding Agency for Technology and Innovation (Tekes) under the project "Future Small-Cell Networks using Reconfigurable Antennas (FUNERA)", and by the Linz Center of Mechatronics (LCM) in the framework of the Austrian COMET-K2 programme. The work was also funded by Tekes, Nokia Bell Labs, Huawei Technologies Finland, TDK-EPCOS, Pulse Finland and Sasken Finland under the 5G TRx project, and by the Academy of Finland under the projects 288670 "Massive MIMO: Advanced Antennas, Systems and Signal Processing at mm-Waves", 284694 "Fundamentals of Ultra Dense 5G Networks with Application to Machine Type Communication", and 301820 "Competitive Funding to Strengthen University Research Profiles".

In this paper, a novel reduced-complexity concurrent DPD solution with a *single feedback receiver* is proposed for dual-band transmitters. The proposed DPD main path processing is based on modeling and injecting the unwanted emissions within and around the main CCs into the PA input with opposite phase, such that the unwanted inband and adjacent channel emissions are canceled at the PA output. The parameter learning is based on a closed-loop feedback system, instead of ILA, with a very simple decorrelation-based learning rule, which aims to minimize the correlation between the nonlinear distortion observed at the PA output (per CC) and specific locally generated baseband nonlinear basis functions. This enables learning the DPD parameters separately for each CC, utilizing only a single feedback receiver.

There have been some recent research efforts in the existing literature utilizing only a single feedback receiver for parameter estimation in the concurrent DPD context [14]–[16]. In all these solutions, however, the PA behavioral model has to be extracted first and then used in the ILA-based learning. Such extra step, which significantly adds to the learning complexity, is not required in the proposed DPD solution. Overall, like will be shown through detailed complexity comparison, the proposed decorrelation-based DPD learning is substantially less complex compared to the ILA-based learning, while offering similar or even slightly enhanced linearization performance.

In general, the decorrelation-based DPD learning was originally introduced by the authors in [17], [18] for mitigating the emissions at the spurious intermodulation (IM) sub-bands only (i.e., IM3, IM5, etc., sub-bands), while not considering the nonlinear distortion at and around the main carriers. Consequently, the EVM and ACLR degradations due to PA nonlinearity were not tackled at all in [17], [18]. The concurrent DPD solution proposed in this article is, in turn, specifically developed and tailored to mitigate the distortion at and around the main carriers.

Moreover, the proposed concurrent DPD can be complemented with the spurious domain DPD developed in [17], [18] to obtain a complete and highly flexible DPD structure which can target the unwanted emissions at any sub-band, whether at or around the main CCs or at any spurious domain IM sub-band, while using only a single feedback observation receiver. Such complete solution is very flexible in the sense that it allows for linearizing any sub-bands of choice, based on the target application and linearization requirements.

An alternative, flexible ILA-based concurrent DPD solution was also introduced in [19]. However, this solution requires significant extra processing in order to guide the DPD to linearize only the targeted sub-band(s). In particular, direct modeling at the sub-band(s) that we do not eventually seek to linearize, is required in [19]. Such extra processing step is not required in the solution proposed in this paper. Furthermore, in [20], a flexible full-band DPD solution, which optimizes the DPD coefficients to minimize the nonlinear distortion at a particular frequency or sub-band, was proposed. However, like other full-band DPD techniques, it requires very high sampling rates in the transmitter and feedback receiver when the carrier spacing between CCs increases. On the other hand, the proposed solution in this paper does not have such drawbacks.

The rest of this article is organized as follows: Section II presents the mathematical modeling of the nonlinear distortion in a practical dual-band scenario. Stemming from this nonlinear distortion model, the proposed concurrent DPD main path processing is formulated. Then, Section III presents the proposed concurrent DPD parameter learning solution, building on the closed-loop decorrelation approach. Section IV then presents an extended decorrelation-based DPD architecture where the main component carriers as well as any other harmful nonlinear distortion products at other sub-bands are suppressed. A detailed complexity analysis and comparison with state-of-the-art single feedback concurrent DPD techniques are then presented in Section V. Sections VI and VII report comprehensive simulation-based as well as practical RF measurement results of the proposed DPD solution, respectively, incorporating both LTE/LTE-Advanced base-station and user equipment side PAs. Finally, Section VIII summarizes the main findings of this article.

II. Nonlinearity Modeling and Proposed DPD Processing

In this section, the modeling of the nonlinear distortion at and around the main carriers is performed in a practical case of non-contiguous carrier aggregation with two component carriers. The basic processing of the proposed concurrent DPD is then formulated stemming from that model. In principle, the proposed DPD can also be generalized to more than two component carriers. However, we will limit the discussion in this paper to the two-component carrier scenario for the sake of presentation compactness. The Parallel Hammerstein (PH) PA model, with odd-order nonlinearities, is adopted in all the modeling and DPD developments, since it has been shown to accurately model the nonlinear behavior of various classes of real PAs [21]. However, we wish to emphasize that the proposed concurrent DPD is compatible with other PA behavioral models as well, e.g., the Volterra model [21].

A. Nonlinear Distortion Modeling around the Main Carriers

We perform the modeling at the composite baseband equivalent level, in which the frequency spacing between the two component carriers is assumed to be $2f_{IF}$. A separate direct conversion TX chain is assumed per CC, and thus in the considered TX architecture, there is no IF upconversion, while the notation f_{IF} simply refers in this manuscript to half the carrier spacing between the two CCs at RF.

Assuming a P^{th} order PH PA model, with monomial nonlinearities and FIR branch filters, the composite baseband equivalent signals at the PA input and output, respectively, read

$$x(n) = x_1(n)e^{j2\pi\frac{f_{IF}}{f_s}n} + x_2(n)e^{-j2\pi\frac{f_{IF}}{f_s}n}, \tag{1}$$

$$y(n) = \sum_{\substack{p=1 \\ p,\ \text{odd}}}^{P} f_{p,n} \star |x(n)|^{p-1}x(n), \tag{2}$$

where $x_1(n)$ and $x_2(n)$ denote the baseband component carrier signals, $f_{p,n}$ denotes the p^{th} order PH branch filter impulse response, and $\star$ is the convolution operator.

The baseband equivalent distortion terms at and around the main CCs can be extracted by the direct substitution of (1) in (2), which yields

$$y_{\pm}(n) = \sum_{\substack{p=1 \\ p,\ \text{odd}}}^{P} f_{\pm,p,n} \star u_{\pm,p}(n), \tag{3}$$

where $f_{\pm,p,n}$ denote the baseband equivalent impulse responses corresponding to the wideband PH PA model filters $f_{p,n}$, evaluated around $x_1(n)$ and $x_2(n)$ respectively, and defined as

$$f_{\pm,p,n} = h_{P,n}^{LPF} \star \{e^{\mp j2\pi \frac{f_{IF}}{f_s} n} f_{p,n}\}, \tag{4}$$

with $h_{P,n}^{LPF}$ denoting an ideal low pass filter with passband width P times the bandwidth of the wider component carrier. Meanwhile, $u_{\pm,p}(n)$ in (3) denote the corresponding p^{th} order static nonlinear (SNL) basis functions, related to the nonlinear distortion around $x_1(n)$ and $x_2(n)$, respectively. Assuming a ninth-order PA model (i.e., $P = 9$), the SNL basis functions representing the nonlinear distortion around the first CC $x_1(n)$, as a concrete example, read

$$u_{+,1}(n) = x_1 \tag{5}$$
$$u_{+,3}(n) = x_1|x_1|^2 + 2x_1|x_2|^2 \tag{6}$$
$$u_{+,5}(n) = x_1|x_1|^4 + 3x_1|x_2|^4 + 6x_1|x_1|^2|x_2|^2 \tag{7}$$
$$u_{+,7}(n) = x_1|x_1|^6 + 4x_1|x_2|^6 + 12x_1|x_1|^4|x_2|^2 + 18x_1|x_1|^2|x_2|^4 \tag{8}$$
$$u_{+,9}(n) = x_1|x_1|^8 + 5x_1|x_2|^8 + 20x_1|x_1|^6|x_2|^2 + 40x_1|x_1|^2|x_2|^6 + 60x_1|x_1|^4|x_2|^4 \tag{9}$$

The time index (n) has been excluded from $x_1(n)$ and $x_2(n)$ in (5)-(9) only to simplify the presentation. Similarly, the corresponding basis functions for the second CC x_2 (i.e., $u_{-,p}(n)$) can be obtained by interchanging x_1 and x_2 in the above expressions. It is worth mentioning that similar basis function expressions have been developed in [22] but up to seventh order nonlinearity only. Moreover, in [22] these basis functions were presented as a simplification of the basis functions in [10] without assuming a particular PA model with memory. In this work, we thus show that (5)-(9) represent the exact basis functions when a PH PA model is assumed. Next, the behavioral model in (3)-(9) is utilized to formulate the proposed injection based concurrent DPD concept, specifically tailored to suppress the distortion at and around the main carriers.

B. Proposed Concurrent DPD Processing

Since we are mostly concerned with the nonlinear distortion at and around the main carriers, we first rewrite equation (3) to separate the linear part from the nonlinear terms as

$$y_{\pm}(n) = f_{\pm,1,n} \star u_{\pm,1}(n) + \sum_{\substack{p=3 \\ p,\ \text{odd}}}^{P} f_{\pm,p,n} \star u_{\pm,p}(n). \tag{10}$$

The main idea of the proposed concurrent DPD processing is then to inject an additional low-power cancellation signal, with similar structure to the nonlinear terms in (10), into the PA input, such that the nonlinear distortion at and around the main carriers is mitigated at the PA output. Therefore, we can obtain an appropriate digital injection signal, to mitigate the nonlinear distortion terms around $x_1(n)$, by adopting the SNL basis functions $u_{+,p}(n)$, $p > 1$, in (6)-(9), combined with a proper bank of DPD filters $\alpha_{+,p,n}$. Similarly, an additional digital injection signal can be applied at the PA input to mitigate the nonlinear distortions around $x_2(n)$ by applying another bank of DPD filters $\alpha_{-,p,n}$ together with the SNL basis functions $u_{-,p}(n)$. This flexibility in operation is one advantage of the proposed DPD principle, since it is not necessarily required in all scenarios to mitigate the distortions around both CCs. For example, the EVM and/or ACLR requirements can be, in general, different between the two CCs, and thus only one of the two CCs might need predistortion. This flexibility can reduce power consumption, which is especially important for small devices.

In general, incorporating such concurrent DPD processing for both main carriers $x_1(n)$ and $x_2(n)$ with polynomial order Q, the composite baseband equivalent PA input signal reads

$$\tilde{x}(n) = x(n) + \left(\sum_{\substack{q=3 \\ q,\ \text{odd}}}^{Q} \alpha_{+,q,n}^{*} \star u_{+,q}(n) \right) e^{j2\pi \frac{f_{IF}}{f_s} n} + \left(\sum_{\substack{q=3 \\ q,\ \text{odd}}}^{Q} \alpha_{-,q,n}^{*} \star u_{-,q}(n) \right) e^{-j2\pi \frac{f_{IF}}{f_s} n} \tag{11}$$

We use $\tilde{(.)}$ variables here, and in the continuation, to indicate DPD processing and the corresponding predistorted signals. Notice that while the polynomial order Q in (11) is assumed identical for both CCs, mainly for notational simplicity, it can easily be set also independently in practice for the two CCs if, e.g., the linearization performance is to be tailored in a per CC manner. Furthermore, the achievable mitigation of the nonlinear distortion around the main carriers depends directly on the estimation and optimization of the concurrent DPD filter coefficients $\alpha_{\pm,q,n}$. This is addressed in detail in the next section. It is also to be noted that the linear basis function in (5) is not used in the proposed DPD, which reduces the required number of DPD coefficients. Thus, both the DPD learning and main path complexities are reduced. The reason for not including (5) is that the primary objective of the DPD is to mitigate the nonlinear distortions only, while the linear distortions can be considered part of the overall communications channel, which is always equalized at the receiver side. Meanwhile, the concurrent DPD solutions in [3], [10]–[16] utilize the ILA, which requires using the linear term for a correct post-inverse estimation.

III. Closed-Loop Parameter Learning Using the Decorrelation Principle

In this section, we build upon the previous nonlinear distortion modeling and the proposed concurrent DPD processing in order to formulate a highly efficient and computationally

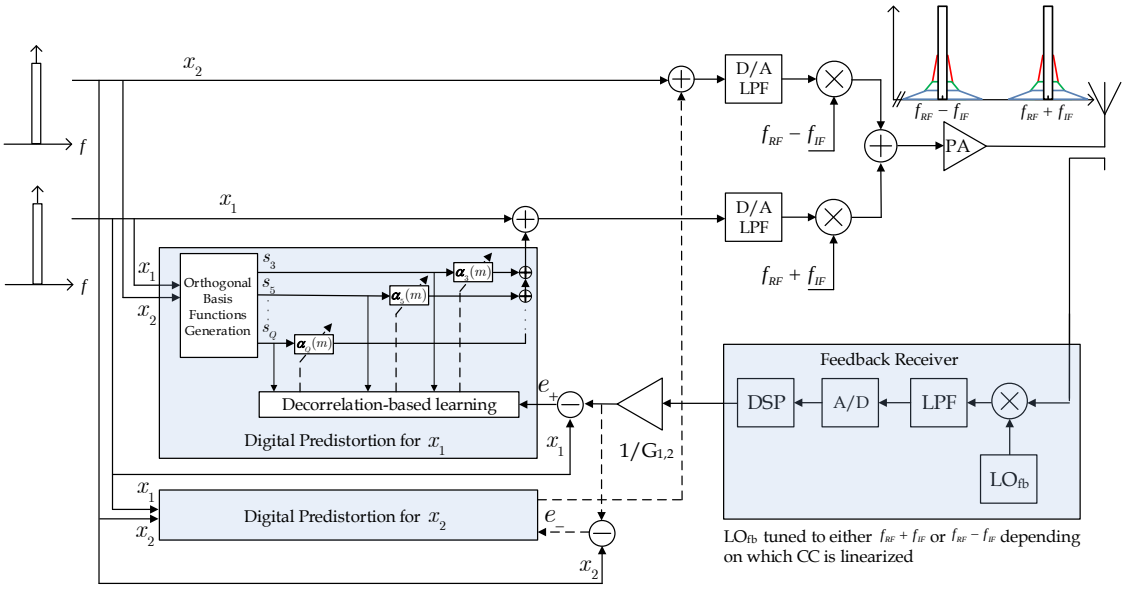

Fig. 2. Block diagram of the adaptive decorrelation-based concurrent DPD adopting closed-loop learning with a single feedback observation receiver. The PA distortion is observed in a per-CC manner and the DPD coefficients $\boldsymbol{\alpha}_q(m)$ of a given CC are adaptively estimated using the decorrelation-based learning rule. The orthogonalized basis functions s_q representing the nonlinear distortion at the considered CC are filtered with the corresponding DPD coefficients and then injected at the PA input. This process is iterated, per CC, until the coefficients converge to the desired value at which the correlation between the PA observation and the basis function samples is minimized.

feasible closed-loop estimation algorithm for learning the concurrent DPD filter coefficients, based on the decorrelation principle. We formulate the DPD parameter optimization task here as minimizing the correlation between the nonlinear distortion at and around the considered main carrier, and the basis functions representing the nonlinear distortion.

The DPD learning is performed one carrier at a time, while utilizing only a single feedback receiver. On one hand, this requires twice the learning time when compared to the dual feedback approach. On the other hand, the PA characteristics usually vary in the order of seconds or tens of seconds [23]. This is much slower than the DPD learning time which is in the order of milliseconds, as demonstrated in Section VI, which means that such per-CC learning is well justified.

In order to extract the nonlinear distortion around each of the main carriers, the useful or linear signal components have to be properly subtracted from the observations at the PA output. This requires an estimate of the complex linear gain of the PA, per CC, which can easily be obtained using simple linear estimation techniques (e.g., least squares). The baseband equivalent nonlinear distortion terms, denoted by $e_{\pm}(n)$ at the PA output around $x_1(n)$ and $x_2(n)$, respectively, can then be calculated as follows

$$e_+(n) = h_{Q,n}^{LPF} \star \{y(n)e^{-j2\pi \frac{f_{IF}}{f_s} n}\}/G_1 - x_1(n) \qquad (12)$$

$$e_-(n) = h_{Q,n}^{LPF} \star \{y(n)e^{j2\pi \frac{f_{IF}}{f_s} n}\}/G_2 - x_2(n), \qquad (13)$$

where G_1 and G_2 are the estimated complex linear gains of the PA for $x_1(n)$ and $x_2(n)$, respectively, while $h_{Q,n}^{LPF}$ denotes the lowpass filtering impulse response of the feedback receiver chain with a passband width of Q times the bandwidth of the wider CC.

The next step is to locally generate the combined basis functions in (6)-(9) and their delayed replicas, and apply the decorrelation-based learning principle. As the name indicates, the learning is based on finding the DPD filter coefficients $\alpha_{\pm,q,n}$ in (11) that minimize the correlation between the extracted nonlinear distortion at the PA output, given in (12) and (13), and the locally generated basis functions, as also illustrated in Fig. 2.

In general, the basis functions in (5)-(9) are mutually correlated and thus a basis function orthogonalization procedure is required in order to have a faster and smoother convergence of the DPD parameter estimates during the learning process, as well as better numerical properties for hardware implementation [24]. In principle, any suitable orthogonalization procedure can be adopted, e.g., Gram-Schmidt, QR or singular value decomposition based, or using a lower complexity iterative orthogonalization algorithm [25]. The orthogonalized versions of the SNL basis functions $u_{\pm,q}(n)$ are denoted in the following by $s_{\pm,q}(n)$.

Then, assuming a DPD filter memory order of N_q per each of the new orthogonal basis functions $s_{\pm,q}(n)$, and an estimation block size of M samples, we combine all the samples and the corresponding DPD filter coefficients, within

processing block m, into the following vectors and matrices:

$$\mathbf{s}_{\pm,q}(n_m) = [s_{\pm,q}(n_m) \; ... \; s_{\pm,q}(n_m - N_q)], \tag{14}$$

$$\mathbf{S}_{\pm,q}(m) = [\mathbf{s}_{\pm,q}(n_m)^T \; ... \; \mathbf{s}_{\pm,q}(n_m + M - 1)^T]^T, \tag{15}$$

$$\mathbf{S}_{\pm}(m) = [\mathbf{S}_{\pm,3}(m) \; \mathbf{S}_{\pm,5}(m) \; ... \; \mathbf{S}_{\pm,Q}(m)], \tag{16}$$

$$\boldsymbol{\alpha}_{\pm,q}(m) = [\alpha_{\pm,q,0}(m) \; \alpha_{\pm,q,1}(m) \; ... \; \alpha_{\pm,q,N_q}(m)]^T, \tag{17}$$

$$\bar{\boldsymbol{\alpha}}_{\pm}(m) = [\boldsymbol{\alpha}_{\pm,3}(m)^T \; \boldsymbol{\alpha}_{\pm,5}(m)^T \; ... \; \boldsymbol{\alpha}_{\pm,Q}(m)^T]^T, \tag{18}$$

where n_m denotes the index of the first sample within block m. The block-adaptive decorrelation-based DPD coefficient update, with learning rate μ, then reads

$$\bar{\boldsymbol{\alpha}}_{\pm}(m+1) = \bar{\boldsymbol{\alpha}}_{\pm}(m) - \mu \, [\mathbf{e}_{\pm}(m)^H \mathbf{S}_{\pm}(m)]^T, \tag{19}$$

where $\mathbf{e}_{\pm}(m) = [e_{\pm}(n_m) \;\; ... \;\; e_{\pm}(n_m + M - 1)]^T$ and $\mathbf{S}_{\pm}(m)$ denote the error signal vector and the filter input data matrix, respectively, all within the processing block m. The updated DPD coefficients $\bar{\boldsymbol{\alpha}}_{\pm}(m+1)$ are then used to filter the next block of M samples, and the process is iterated until convergence. The DPD parameter update interval can be chosen to be L samples, with $M \leq L$. This adds more flexibility to the proposed solution, and allows for tolerating arbitrarily long loop delays through the proper selection of M and L. This, in turn, facilitates stable operation under various hardware and software processing latency constraints, as demonstrated in [26] in the context of DPD for spurious emissions mitigation at the IM sub-bands. In general, this computing-efficient coefficient learning approach has been observed, in both simulations and RF measurements, to be stable and to converge reliably assuming that the step-size μ is chosen properly.

IV. Extended DPD solution and Feedback Receiver Aspects

A. Decorrelation-based DPD solution for all sub-bands

In this section, an extended decorrelation-based sub-band DPD solution is presented. It combines the processing developed in the previous sections for concurrent linearization, and the authors' earlier work in [18] for spurious domain linearization. Such complete sub-band DPD solution has the capability to suppress nonlinear distortion in non-contiguous CA/multi-band transmitters in a flexible and efficient manner, at and around the main carriers as well as in the spurious domain, using the decorrelation-based learning rule and a single feedback receiver operating at a lower sample rate. The leading principle in the parameter learning is to minimize the correlation between the distortion at the main CCs, and/or at any of the IM sub-bands, and specific low-rate baseband SNL basis functions representing the nonlinear distortion at the corresponding sub-bands. The SNL basis functions representing the nonlinear distortion at the IM sub-bands were already derived in [18], and are denoted by $u_{b\pm,q}(n)$, where $b = 3, 5, ..., B$ is the sub-band index (i.e., $b = 3$ for the IM3 sub-bands, $b = 5$ for the IM5 sub-bands, etc.).

Incorporating now the sub-band DPD processing with DPD polynomial order Q, and aggregating at the same time the linearization processing at all sub-bands simultaneously, the composite baseband equivalent PA input signal, assuming that $Q \geq B$, reads then

$$\begin{aligned}\tilde{x}(n) = x(n) &+ \left(\sum_{\substack{q=3 \\ q,\ \text{odd}}}^{Q} \alpha^*_{+,q,n} \star s_{+,q}(n) \right) e^{j2\pi \frac{f_{LE}}{f_s} n} \\ &+ \left(\sum_{\substack{q=3 \\ q,\ \text{odd}}}^{Q} \alpha^*_{-,q,n} \star s_{-,q}(n) \right) e^{-j2\pi \frac{f_{LE}}{f_s} n} \\ &+ \sum_{\substack{b=3 \\ b,\ \text{odd}}}^{B} \left(\sum_{\substack{q=b \\ q,\ \text{odd}}}^{Q} \alpha^*_{b+,q,n} \star s_{b+,q}(n) \right) e^{j2\pi \frac{b \times f_{LE}}{f_s} n} \\ &+ \sum_{\substack{b=3 \\ b,\ \text{odd}}}^{B} \left(\sum_{\substack{q=b \\ q,\ \text{odd}}}^{Q} \alpha^*_{b-,q,n} \star s_{b-,q}(n) \right) e^{-j2\pi \frac{b \times f_{LE}}{f_s} n}\end{aligned} \tag{20}$$

where $s_{b\pm,q}(n)$ are the q^{th} order orthogonalized versions of the SNL basis functions $u_{b\pm,q}(n)$ at the b^{th} sub-band, and $\alpha_{b\pm,q,n}$ are the corresponding DPD filters to be estimated using the block-adaptive learning solution which will be described next. Notice that, in (20), for notational simplicity, the DPD orders at different sub-bands are assumed to be identical, while in reality they can easily be set independently based on the corresponding linearization requirements.

The block-adaptive decorrelation-based DPD coefficient update for the b^{th} sub-band reads

$$\bar{\boldsymbol{\alpha}}_{b\pm}(m+1) = \bar{\boldsymbol{\alpha}}_{b\pm}(m) - \mu \, [\mathbf{e}_{b\pm}(m)^H \mathbf{S}_{b\pm}(m)]^T, \tag{21}$$

where $\mathbf{S}_{b\pm}(m)$ and $\bar{\boldsymbol{\alpha}}_{b\pm}(m)$ are defined as in (16) and (18), using the orthogonalized basis functions corresponding to the b^{th} sub-band. The error signal vector is denoted by $\mathbf{e}_{b\pm}(m) = [e_{b\pm}(n_m) \;\; ... \;\; e_{b\pm}(n_m + M - 1)]^T$. For $b = 1$, $e_{\pm}(n)$ are defined in (12) and (13), while for the IM sub-bands $b = 3, 5, ..., B$, $e_{b\pm}(n) = \tilde{y}_{IMb_{\pm}}(n)$, which denotes the baseband equivalents of the PA output at the b^{th} sub-bands, with the corresponding sub-band DPD processing included adopting the current coefficients, $\bar{\boldsymbol{\alpha}}_{b\pm}(n)$. In other words, at the actual IM sub-bands, the error signal in the learning is directly the observed PA output since the ideal linear signal term is, by definition, zero.

Thus, as we can see from (21), the DPD learning for all the sub-bands including the main carriers is adopting the simple decorrelation principle. And since the learning is done one sub-band at a time, a single computing engine or correlator can be reused in the actual hardware implementation for the different sub-bands. This learning scheme thus provides a very simple, cost-effective, and high performance solution, as will also be demonstrated through the simulations and RF measurement results in Sections VI and VII, respectively.

TABLE I
DPD MAIN PATH PROCESSING COMPUTATIONAL COMPLEXITY COMPARISON. THE OVERSAMPLING FACTOR $R = Q$ WITHOUT FILTERED BASIS FUNCTIONS, AND $R < Q$ WITH FILTERED BASIS FUNCTIONS.

	BF generation (FLOP/sample)	BF extra filtering, if $R < Q$ (FLOP/sample)	DPD main path processing (FLOP/sample)	Minimum processing sample rate (Msps)
1-Full-band DPD	$Q+2$	$\sum_{q=3}^{Q}[4N_b+2]R/q$	$(Q+1)(4N+3)$	$R(W_1+W_2+\Delta f)$
2-[10]	$6+4\sum_{q=3}^{Q} q$	$2\sum_{q=3}^{Q}[4N_b+2]R/q$	$2(Q+1)(4N+3)$	$R \times max(W_1, W_2)$
3-[14], [15]	$6+4\sum_{q=3}^{Q} q$	$2\sum_{q=3}^{Q}[4N_b+2]R/q$	$2(Q+1)(4N+3)$	$R \times max(W_1, W_2)$
4-[16]	$Q+2$	$2\sum_{q=3}^{Q}[4N_b+2]R/q$	$(Q+1)(4N+3)+2(5N_s+6)$	$R(W_1+W_2)$
5-This work	$6+4\sum_{q=3}^{Q} q$	$2\sum_{q=3}^{Q}[4N_b+2]R/q$	$2(Q-1)(4N+3)$	$R \times max(W_1, W_2)$

TABLE II
DPD LEARNING COMPLEXITY COMPARISON.

	PA estimation (FLOP/M samples)	BF generation (FLOP/KM samples)	DPD estimation (FLOP/KM samples)	Minimum learning sample rate (Msps)
1-Full-band DPD One feedback RX	0	$KM[Q+2]$	$4K[(M+(Q+1)(N+1)/6) \times(Q+1)^2(N+1)^2/4]$	$R(W_1+W_2+\Delta f)$
2-[10] Two feedback RXs	0	$KM[6+4\sum_{q=3}^{Q} q]$	$4K[(M+(Q+1)(N+1)/3) \times(Q+1)^2(N+1)^2]$	$R \times max(W_1, W_2)$
3-[14], [15] One feedback RX	$4[(M+(Q+1)(N+1)/3) \times(Q+1)^2(N+1)^2]+ 8M(Q+1)(N+1)-2M$	$KM[6+4\sum_{q=3}^{Q} q]$	$4K[(M+(Q+1)(N+1)/3) \times(Q+1)^2(N+1)^2]$	$R \times max(W_1, W_2)$
4-[16] One feedback RX	$4[(M+(Q+1)(N+1)/6) \times(Q+1)^2(N+1)^2/4]+ 4M(Q+1)(N+1)-2M$	$KM[Q+2]$	$4K[(M+(Q+1)(N+1)/6) \times(Q+1)^2(N+1)^2/4]$	$R(W_1+W_2)$
5-This work One feedback RX	$16M-4$	0	$4K[(2M+1)(Q-1)(N+1)-M]$	$R \times max(W_1, W_2)$

B. Decorrelation-based DPD Solution for Single CC/Band Scenarios

The same decorrelation-based DPD learning algorithm can be used, not only in the earlier considered dual carrier/band scenarios, but also in more classical single CC/band transmitters. This can be achieved by simply setting $x_2(n) = 0$ in (6)-(9), and thus $x_1(n)$ becomes the main/only carrier of interest. The decorrelation-based learning can then minimize the correlation between the single CC -based basis functions and the nonlinear distortion around the main carrier $x_1(n)$ using the same learning rule as explained earlier, while setting $f_{IF} = 0$. This single CC mode of operation can also be used when the carrier spacing between the two CCs gets narrower, by interpreting the composite baseband signal as one arbitrary baseband waveform centered at zero frequency. This approach naturally assumes that the sample rate for processing the composite signal as a whole is still feasible, implying then also that all sub-bands are processed and linearized simultaneously. This further emphasizes the flexibility of the proposed DPD solution for different transmission scenarios and system aspects. In this context, it is also worth mentioning that the work in [27] proposes a concurrent DPD for scenarios in which the CCs are narrowly spaced. This approach uses a multiple-input multiple-output Volterra DPD structure with filtered basis functions, thus reducing the sample rates required by the DAC and ADC in the DPD system.

C. DPD Feedback Receiver Aspects

In order to further reduce the complexity of the proposed DPD with Q^{th} order DPD processing, a narrower BW feedback receiver can be used even when higher-order nonlinearities are included in the estimation and linearization processing. In other words, the feedback receiver sample rate of a Q^{th} order DPD can be chosen to be R times the BW of the wider linearized CC, where $R < Q$. As an example, in a dual carrier scenario, if the BW of each CC is 20 MHz, and a ninth-order ($Q = 9$) concurrent DPD is adopted, the observed PA output can be filtered such that only, e.g., 60 MHz is captured per CC (i.e., $R = 3$), instead of $9 \times 20 = 180$ MHz. This can further reduce the complexity of the feedback receiver in the proposed DPD architecture, in particular the feedback ADC, while still providing very good linearization performance, as will be shown in the RF measurement examples. Similarly, in the DPD main path processing, the SNL basis functions can be filtered to reduce the DPD sample rate and thus complexity, as will be described in more details in Section V. A similar idea, based on filtering the DPD basis functions, was also proposed in [28] as a way of reducing the DPD complexity in ordinary ILA-based DPD learning architectures.

V. COMPLEXITY ANALYSIS AND COMPARISON AGAINST STATE-OF-THE-ART

This section presents a detailed quantitative comparison between the complexities of the single feedback concurrent DPD proposed in this article, and the existing state-of-the-art single feedback concurrent DPDs in [14]–[16]. The complexities of the dual feedback concurrent DPD, as in [10], and the classical full-band DPD are also presented for reference. The number of floating point operations (FLOP) is used to

quantify the complexity of each DPD technique [21]. Moreover, both the DPD main path processing complexity and the parameter learning complexity are considered in the analysis and comparisons, as shown in Tables I and II, respectively. To the best of the authors' knowledge, this is the first time that such a comprehensive complexity analysis of the state-of-the-art single feedback concurrent DPD techniques is reported in the literature.

The following assumptions are made in all of the considered DPD techniques in order to ensure a fair comparison:

- A dual carrier scenario is considered, and the DPD is linearizing both CCs. A separate analog TX chain for each CC and a shared PA are assumed for generating the dual-carrier RF signal.
- In principle, any suitable nonlinear model can be used. However, for fairness of comparison, the basis functions derived in this work stemming from the PH PA model, in (5)-(9), are used in all the considered concurrent DPD techniques.
- A suitable orthogonalization processing is applied to the basis functions in all the considered techniques for better numerical properties and stability in the DPD parameter estimation [29], [30]. The complexity of the orthogonalization process is identical in all cases and is thus excluded in the analysis.
- Proper synchronization is required between the PA output observation and the baseband basis function samples in all methods, and thus the synchronization complexity is also excluded from the comparison. However, it is worth mentioning that some extra effort is required for synchronization in the methods proposed in [14], [15] when compared to the other considered methods, as explained in [14].

The notations used in the complexity analysis are consistent with the notations throughout the paper, along with some additional symbols that are all summarized here: Q denotes the DPD nonlinearity order. N denotes the DPD filter memory order, where it is assumed that each q^{th} order DPD filter $\alpha_{\pm,q,n}$ has $N+1$ memory taps, for simplicity. M denotes the estimation block size in both the block-adaptive filtering used in this work, as well as the block LS estimation. K denotes the number of block-adaptive iterations in this work, as well as the number of ILA iterations in ILA-based DPD learning. W_1, W_2, denote the bandwidths of the first and second CCs respectively, while the carrier spacing is denoted with Δf. Finally, N_s denotes the memory depth of the filters used in [16] for carrier separation and relocation before transmitting each CC on separate TX chains. These filters are assumed to be FIR filters with symmetrical coefficients.

In case of applying additional filtering to the basis functions (BFs) to reduce the DPD processing sample rate, as explained in Section IV-C, the symbol R denotes the amount of oversampling applied in the basis functions generation compared to the original CC bandwidths W_1 and W_2. In the normal scenario without filtered BFs, this oversampling factor $R = Q$, otherwise $R < Q$. N_b denotes the memory depth of the BF bandlimitation filter used for filtering the basis functions, which is assumed to be a computationally efficient polyphase FIR decimator structure [31].

The results of the complexity analysis are presented in Tables I and II, with the main findings being the following:

- The DPD main path processing complexity of the solution developed in this work is lower than in any of the other techniques. This is because the proposed DPD solution does not require processing of the linear basis function, opposed to all other methods, as explained in Section II. This is reflected on the third column of Table I.
- When compared to the single feedback concurrent DPD in [16], the proposed DPD has significantly lower main path complexity, despite having greater basis function generation complexity. In [16], a single DPD is used for both CCs, resulting in a higher DPD sample rate. Moreover, two carrier separation and relocation filters are required in [16] to transmit the aggregated carriers on separate TX chains, thus adding to the overall DPD running complexity. These aspects are reflected on the first, third, and fourth columns of Table I.
- The single feedback concurrent DPDs in [14]–[16] require PA direct model extraction, which significantly adds to the DPD learning complexity. On the other hand, in this work only the linear gain of the PA is required, implying substantially lower complexity. This is reflected on the first column of Table II.
- The same basis function samples used in the DPD main path processing can be reused in the decorrelation-based DPD learning in this work, as illustrated in Fig. 2. This is not possible in the other DPD solutions due to the nature of the ILA-based learning which requires a post-inverse estimation whose basis functions are generated from the PA output samples. This is an important difference and is reflected on the second column of Table II.
- DPD parameter estimation developed in this work is significantly less complex than the other methods, which are all ILA-based. This is reflected on the third column of Table II.

Concrete numerical examples of the overall main path processing complexity, in terms of FLOP per second, as well as the learning complexity in terms of FLOP per learning procedure, will be provided in the next section, together with the corresponding linearization performance results.

VI. Simulation Results

In this section, practical carrier aggregation based simulation studies, using a real PA model, are reported in order to quantitatively compare the complexity and performance of the proposed decorrelation-based concurrent DPD and state-of-the-art concurrent DPD methods mentioned in Section V. Both the inband waveform purity and the adjacent channel leakage due to spectral regrowth are quantified using the well-known EVM and ACLR metrics. [4], [32].

The considered dual carrier example is shown in Fig. 3 with two 10 MHz OFDM carriers and 100 MHz carrier spacing. A ninth-order PH PA model is used whose parameters have been identified using RF measurements with a true mobile PA transmitting at +22 dBm. This mobile PA has 29 dB gain, and +31

TABLE III
COMPLEXITY AND PERFORMANCE COMPARISON WITH STATE-OF-THE-ART CONCURRENT DPD METHODS

	Overall DPD complexity					DPD performance of CC1	
	Main path processing (GFLOP/s)	Overall learning complexity (MFLOP)	DPD sample rate (Msps)	Num. of est. samples	Num. of fb. RXs	EVM (%)	ACLR L / R (dBc)
Without DPD	0	0	N/A	N/A	N/A	4.01	35.52 / 36.19
1-Full-band DPD	238.59	108.6	990	30k	1	0.52	53.91 / 51.86
2-[10]	28.98	114	90	30k (per CC)	2	0.53	53.45 / 51.53
3-[14], [15]	28.98	152.4	90	40k (per CC)	1	0.53	53.45 / 51.53
4-[16]	113.94	146.4	180	40k (per CC)	1	0.52	53.00 / 51.55
5-This work	25.02	18.96	90	100k (per CC)	1	0.53	53.87 / 51.64

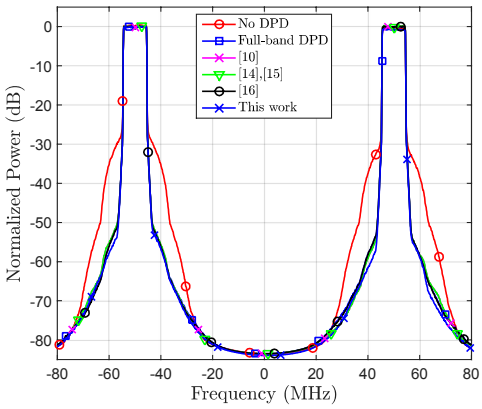

Fig. 3. Normalized PA output spectra of a concurrent noncontiguous intraband CA transmitter with two 10 MHz OFDM carriers with 100 MHz spacing, and 16-QAM subcarrier modulation. The PAPR is 12.5 dB. A ninth-order PH model is used. The PA parameters have been identified using RF measurements with a true mobile PA transmitting at +22 dBm.

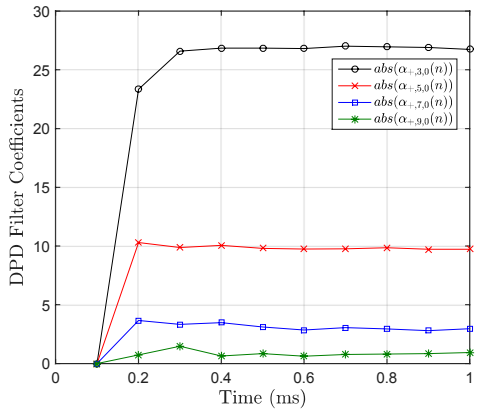

Fig. 4. Example convergence of the first memory taps, per basis function, of the ninth-order decorrelation-based CC1 DPD using a single realization of two 10 MHz OFDM carriers with 100 MHz spacing, and 16-QAM subcarrier modulation. A single learning block corresponds to 0.1 ms in real-time. The ninth-order PA parameters have been identified using RF measurements with a true mobile PA transmitting at +22 dBm.

dBm 1 dB compression point. The adopted parameterizations of the different DPD solutions are as follows: The estimation block size $M = 10k$ samples, and the DPD nonlinearity order $Q = 9$ in all the considered DPD methods. The number of block-adaptive iterations $K = 10$ in the proposed DPD, while the number of ILA iterations $K = 3$ in all the other considered DPD methods. In [10], [14], [15] and in the proposed DPD, the DPD memory order $N = 2$ per CC. Meanwhile, in [16] and in the full-band DPD the two CCs are predistorted with a single DPD, and thus a higher DPD memory order $N = 5$ is used. No filtering of the basis functions is performed in this comparison (i.e., $N_b = 0$). Additionally, in [16], $N_s = 50$.

All the considered DPD methods have almost the same linearization performance as shown in Fig. 3 and in Table III. However, the complexity is clearly in favor of the proposed concurrent DPD solution, showing a notable advantage in both the DPD main path processing complexity and learning complexity. The main path complexity is measured in GFLOP per second (GFLOP/s), while the learning complexity is measured in terms of the overall number of FLOP used in the learning process. The main findings of the complexity comparison in Table III can be summarized as follows: (*i*) The proposed DPD has clearly the lowest main path complexity in GFLOP/s. (*ii*) The number of samples used for DPD coefficients estimation is higher in the proposed DPD compared to the other considered DPD methods, which implies longer learning time. However, the time required for obtaining the correct DPD coefficients, per CC, in the proposed DPD is roughly 0.5 ms which is still very fast compared to the rate of change that can occur in the PA behavior [23], as shown in Fig. 4 for CC1 DPD coefficients. (*iii*) The overall learning complexity of the proposed DPD is significantly lower than all the other considered DPD methods despite using somewhat more samples.

VII. RF MEASUREMENT RESULTS

In this section, we provide results of comprehensive RF measurements using three commercially available power amplifiers, shown in Fig. 5. The first is an LTE-A band 1 base station (BS) PA, and the second is a general purpose wideband PA, suitable for interband CA. The third is an LTE-A band 25 user equipment (UE) PA. The RF measurement examples quantify and demonstrate the performance of the proposed decorrelation-based DPD solution, while other state-of-the-art DPD methods, which are based on the ILA principle for learning, are also implemented for reference.

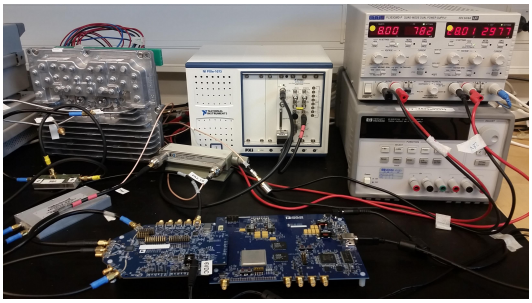

(a) Photo of the RF measurement setup

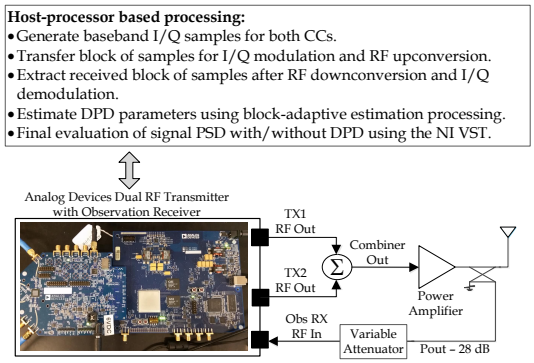

(b) Block diagram of the RF measurement setup

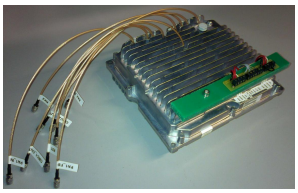

(c) LTE-A DL Band 1 (2110 MHz - 2170 MHz) basestation microwave PA

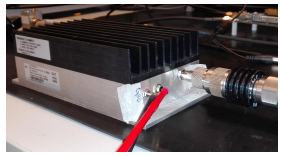

(d) Wideband microwave PA (10 MHz - 4200 MHz) suitable for LTE-A interband CA

(e) LTE-A UL Band 25 (1850 MHz - 1915 MHz) UE microwave PA

Fig. 5. Hardware setup used in the RF measurements for testing and evaluating the proposed decorrelation-based concurrent DPD. The three RF power amplifiers used in the measurements are also shown.

A. RF Measurement Setup

The RF measurement setup is shown in Fig. 5. The Analog Devices evaluation board AD9368-2 has two RF transmitters, each with 250 MHz instantaneous bandwidth, that are used for implementing CA transmission scenarios. The board is also equipped with an observation receiver with 200 MHz instantaneous bandwidth, which is used as the DPD feedback receiver. The board is then connected to a host processor, which implements the baseband signal processing necessary for DPD, as well as the basic baseband waveform processing for the CCs. The digital baseband waveforms of the component carriers are divided into blocks of size $M = 10k$ samples each, which are first generated locally on the host processor, and then transferred to the evaluation board to perform RF I/Q modulation at the desired power level at the PA input. In the noncontiguous CA scenarios, the RF outputs of the two TX chains are combined using an RF combiner, and then connected to the input port of the external power amplifier. The PA output is then extracted via a directional coupler with 28 dB attenuation, and fed to the input of the evaluation board observation receiver, as illustrated also in Fig. 5. An extra variable attenuator is used to adjust the signal power at the directional coupler output to a level suitable for the observation receiver input. The observation receiver performs RF I/Q demodulation to bring the signal back to baseband, which is then used for the DPD learning. In all our measurement examples, the linear gain of the overall RF path, including the external PA and the attenuator, is estimated using block LS in order to be able to extract the nonlinear distortion at the PA output.

The DPD parameters used in the RF measurements are defined as follows: The estimation block size $M = 10k$ samples, and the DPD nonlinearity order $Q = 9$ in all the considered DPD methods. The number of block-adaptive iterations $K = 10$ in the proposed DPD solution, while the number of ILA iterations is $K = 3$ in all the other considered ILA-based reference DPD methods. In [10], [14], [15] and in the proposed DPD, the DPD memory order $N = 1$ per CC (i.e., two taps per basis function). In case a full-band DPD is used to linearize the two aggregated CCs, the DPD memory order $N = 3$ (i.e., four taps per basis function).

B. Base Station Measurements

Three different LTE-A RF measurement scenarios are presented in this section. The first, is a contiguous intraband CA scenario, the second is a noncontiguous intraband CA scenario, while the third is an interband CA scenario. In the first two scenarios, a commercial LTE-A Band 1 (2110-2170 MHz) BS PA is used, shown in Fig. 5(c). The freescale BS PA (model no. MD7IC2250GN) is a Doherty PA with 31 dB gain, and +47 dBm 1 dB compression point. A driver amplifier is used before the Doherty PA with 14 dB gain and +25 dBm 1 dB compression point. In the third scenario, a general-purpose wideband PA with 40 dB gain, and +28 dBm 1 dB compression point is used, as shown in Fig. 5(d). This PA (model no. ZHL-

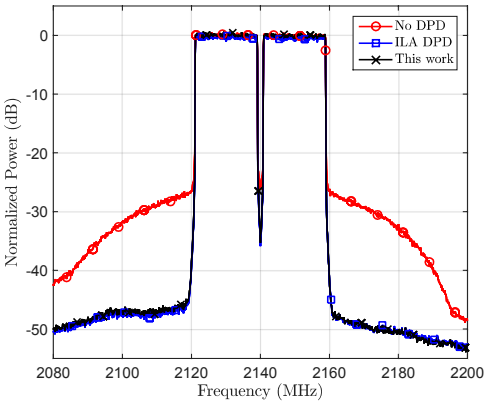

Fig. 6. An RF measurement example at LTE DL Band 1 (2110-2170 MHz) showing the normalized PA output spectra of a contiguous intraband CA transmitter with two 20 MHz OFDM carriers. 16-QAM subcarrier modulation is used per CC. Spectral regrowth and EVM are reduced when using the proposed decorrelation-based DPD with a real commercial base station PA operating at +36 dBm output power.

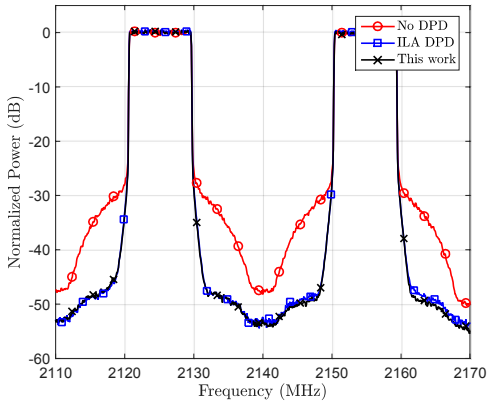

Fig. 8. An RF measurement example at LTE DL Band 1 (2110-2170 MHz) showing the normalized PA output spectra of a concurrent noncontiguous intraband CA transmitter with two 10 MHz OFDM carriers. The CC spacing is 30 MHz, and 16-QAM subcarrier modulation is used. Spectral regrowth and EVM are reduced when using the proposed decorrelation-based concurrent DPD with a real commercial base station PA operating at +34 dBm TX power.

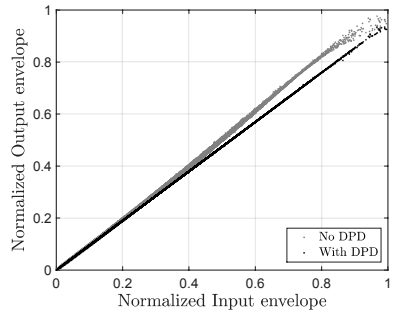

(a) AM AM response

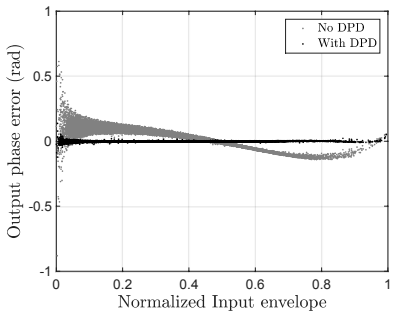

(b) AM PM response

Fig. 7. AM/AM and AM/PM responses of the LTE-A DL Doherty BS PA with (black) and without (gray) the proposed DPD at +36 dBm output power.

4240) is suitable for interband CA, and can, in principle, be adopted, e.g., in femto-cell access points.

1) Contiguous Intraband CA Scenario: An LTE-A Band 1 contiguous intraband CA scenario with two 20 MHz CCs is studied, in which the two aggregated CCs are interpreted as one CC (i.e, CC1), as explained in Section IV-B. The aggregated signal is transmitted via one RF transmitter (TX) chain of the AD evaluation board, and thus no RF combiner is used in this scenario. The block-adaptive DPD processing is implemented on a host processor, using the full-band baseband I/Q samples from the observation receiver, with 200 MHz observation BW. Iterative clipping and filtering -based PAPR reduction is applied to the composite transmit signal in this scenario [33]. The classical ILA-based DPD is also implemented for reference, and compared to the proposed DPD in Fig. 6, with Table IV showing the corresponding ACLR and EVM results. As is obvious, the proposed DPD solution and the existing ILA-based DPD are both providing very similar performance, despite the substantial difference in the computing complexity in favor of the proposed solution, as already demonstrated in Section V. Fig. 7 shows the AM/AM and AM/PM responses of the PA with the proposed DPD (black), and without DPD (gray), in this scenario, measured at +36 dBm average output power.

2) Noncontiguous Intraband CA Scenario: An LTE-A Band 1 noncontiguous intraband CA scenario, with two 10 MHz CCs and 30 MHz carrier spacing, is studied next. Each CC is transmitted via a separate RF chain in this scenario, and an RF combiner is then used to combine the two CCs at the PA input, as also illustrated in Fig. 5. 30 MHz observation BW is used per CC in the proposed DPD learning, which is done sequentially, one CC at a time in this example, unlike in the previous contiguous scenario where the whole aggregated signal was used for learning. The final DPD coefficients after convergence are then applied on each CC before being

TABLE IV
BS RF MEASUREMENT SCENARIOS AND OBTAINED RESULTS

Scenario	DPD Type	EVM [%]	ACLR L / R of CC1 (dBc)	ACLR L / R of CC2 (dBc)	TX Power (dBm)	PAPR (dB)
Contiguous Intraband CA	No DPD	5.65	30.89 / 31.56	N/A	+36	8.8
	ILA DPD	1.97	46.87 / 49.66	N/A	+36	8.8
	This work	2.04	46.95 / 50.12	N/A	+36	8.8
Noncontiguous Intraband CA	No DPD	5.54	36.60 / 36.63	36.41 / 36.36	+34	9.87
	ILA DPD	1.85	49.85 / 48.72	49.99 / 49.85	+34	9.87
	This work	1.93	49.89 / 49.33	49.98 / 49.87	+34	9.87
Noncontiguous Interband CA	No DPD	3.92	35.47 / 36.08	36.36 / 35.95	+23	9.94
	[10]	1.24	48.05 / 48.10	48.16 / 48.12	+22	9.94
	[14], [15]	1.25	48.05 / 48.09	48.15 / 48.12	+22	9.94
	This work	1.28	50.07 / 49.95	49.13 / 49.08	+23	9.94

transmitted via the corresponding TX chains. Iterative clipping and filtering -based PAPR reduction is applied to each CC separately in this scenario. The classical full-band ILA-based DPD is also implemented for reference, with block LS based parameter learning per ILA iteration, and compared to the proposed concurrent DPD in Fig. 8, with Table IV showing the corresponding ACLR and EVM results. The linearization performance numbers are again very similar despite the proposed concurrent DPD being significantly less complex than the full-band ILA-based DPD, as analyzed already in Section V.

3) Interband CA Scenario: For further demonstration and proof-of-concept of the proposed concurrent DPD, a true interband CA scenario is addressed next. The setup is otherwise similar to the previous setup related to the noncontiguous intraband CA scenario, but, in this case, the two aggregated CCs are located at Band 2 (1930-1990 MHz), and Band 4 (2110-2155 MHz), respectively, which is a practical LTE-A interband CA scenario [34]. Furthermore, the general purpose wideband PA is used. Iterative clipping and filtering -based PAPR reduction is again applied to each CC separately. The performance of the proposed single feedback concurrent DPD is compared against two different concurrent DPD techniques: the first is the classical concurrent DPD reported in [10] with two feedback receivers, and the second is the single feedback concurrent DPD developed in [14], [15].

Fig. 9 shows the normalized spectra at the PA output without DPD and with the three considered concurrent DPD techniques, at +23 dBm PA output power. An extra 1 dB backoff is applied in the concurrent DPDs in [10], [14], [15] for proper operation, however, such backoff is not required for the proposed DPD which does not use the ILA principle for learning. The results in Fig. 9 and Table IV again demonstrate very good linearization performance of the proposed concurrent DPD solution, which is even slightly better than the other concurrent DPDs, despite its reduced complexity, as explained in Section V. The same assumptions that were made in Section V are assumed here as well for a fair comparison among the considered concurrent DPD techniques.

C. UE Measurements

Two different LTE-A UE RF measurement scenarios are presented in this section. The first corresponds to 3GPP LTE-A multicluster transmission scenario [4], while the second is a noncontiguous intraband CA scenario where only one of the CCs and one of the IM3 spurs are being linearized, thus demonstrating the flexibility of the proposed DPD. The power amplifier adopted in the UE RF measurements (model no. ACPM-5002-TR1) is designed for LTE-A UL Band 25 (1850-1915 MHz), with 29 dB gain, and +31 dBm 1 dB compression point, as shown in Fig. 5(e).

1) Multicluster Scenario: Fig. 10 demonstrates an RF measurement example corresponding to 3GPP LTE-Advanced multicluster transmission scenario, where the mobile device is accessing a single SC-FDMA based 20 MHz LTE UL carrier with non-contiguous physical resource block (PRB) allocation inside the carrier. The figure shows the normalized spectra at the PA output, with and without the proposed DPD, operating at +24 dBm TX power. A single full-band decorrelation-based DPD is used, in this scenario, to linearize the overall signal composed of the two clusters, with 5 MHz and 10 MHz bandwidths and 5 MHz cluster separation. Iterative clipping and filtering based PAPR reduction is applied to the composite transmit signal. ILA based DPD is also implemented and compared to the proposed DPD in Table V, in terms of the ACLR and EVM, demonstrating similar performance between them.

2) Noncontiguous Intraband CA Scenario: Fig. 11 represents a scenario where also the negative IM3 sub-band is emitted inband (not suppressed by the TX/antenna filter), while the positive IM3 sub-band is out-of-band and can thus be easily filtered by the TX filter. The two SC-FDMA based UL component carriers in this example have 10 MHz and 5 MHz bandwidths, where the 10 MHz CC uses QPSK data modulation, while the 5 MHz CC uses 64QAM data modulation, and is thus much more sensitive to EVM degradation. In this example, the DPD is therefore deliberately configured to linearize only the 5 MHz component carrier and the negative IM3 sub-band, which is emitted inband, to demonstrate the great processing and linearization flexibility. 25 MHz observation BW is used in the proposed DPD learning, such that the DPD coefficients to linearize CC2 and the negative IM3 sub-band are learned sequentially. Iterative clipping and filtering based PAPR reduction is applied to the ideal transmit signal. Table V shows the ACLR, EVM and IM3 spur suppression results in this scenario, evidencing again very high-performance linearization. Notice that the IM spur at the negative IM3 sub-band is also suppressed by around 20 dB through the DPD

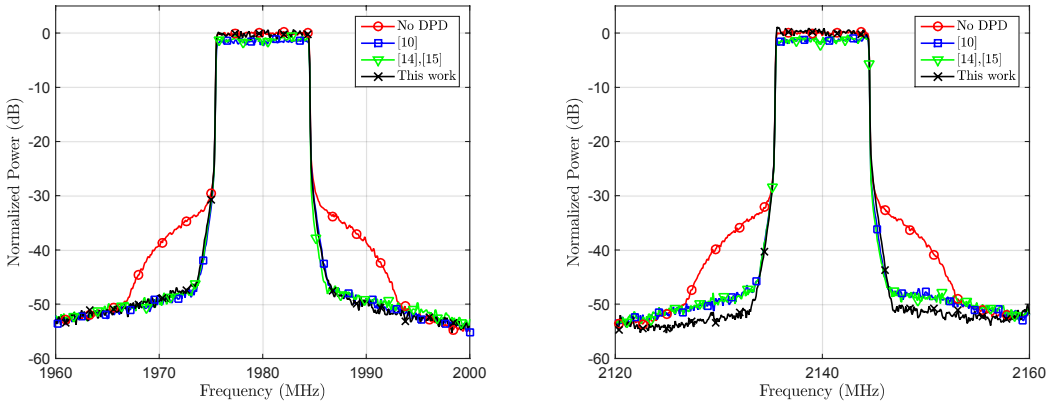

(a) (b)

Fig. 9. A practical LTE-A DL interband CA RF measurement example showing the normalized PA output spectra with and without DPD using a real commercial wideband PA operating at +23 dBm output power. The OFDM CCs are 10 MHz each and transmitted at LTE-A DL bands 2 (1930-1990 MHz) and 4 (2110-2155 MHz) respectively, with 160 MHz CC spacing. 16-QAM subcarrier modulation is used per CC. Spectral regrowth and EVM are reduced when using the proposed decorrelation-based concurrent DPD, which slightly outperforms the concurrent DPDs in [10], [14], [15].

TABLE V
UE RF MEASUREMENT SCENARIOS AND OBTAINED RESULTS

TX Power = +24 dBm **Scenario**	DPD Type	EVM [%]	ACLR L / R of CC1 (dBc)	ACLR L / R of CC2 (dBc)	IM3- spur supression (dB)	PAPR (dB)
Multicluster	No DPD	4.39	32.04 / 34.23	N/A	N/A	8.65
	ILA DPD	0.71	45.98 / 47.31	N/A	N/A	8.65
	This work	0.79	46.28 / 47.28	N/A	N/A	8.65
Noncontiguous Intraband CA	No DPD	3.68	N/A	33.43 / 33.95	0	8.18
	This work	0.73	N/A	50.26 / 50.47	20	8.18

processing, taking it below the general spurious emission limit of -30 dBm/1MHz measurement bandwidth that all RF devices must obey [35].

D. Discussion and Future Work

In this section, we shortly point towards some future work items in the context of the proposed concurrent DPD solution. Despite the fact that the proposed solution is already offering excellent linearization performance at substantially reduced complexity compared to other state-of-the-art concurrent DPD methods, as demonstrated through extensive simulations and RF measurements, there is potentially some room for further improvements.

The fact that the learning of the DPD coefficients for the two CCs is done sequentially can, in principle, cause some inter-dependence between the optimal coefficients of the DPD stages of CC1 and CC2, in particular if the PA is very deep in saturation. Specifically, in very deep saturation, and assuming that the DPD coefficients of CC1 are learned first, then activating the DPD unit of CC2 may cause slight degradation of the linearization of CC1. We hypothesize that then iterating shortly the learning between the CCs can reduce this mutual effect while reaching an improved linearization performance for the CCs. On the other hand, this may require somewhat more learning samples in the overall learning procedure. In the context of the described learning rules, these iterations between the CCs can basically be adopted at the level of the learning block m or then between the K learning blocks of individual CCs, assuming that the observation receiver center-frequency can be adjusted accordingly.

We also wish to acknowledge that it is basically also possible to perform the learning for the two CCs in parallel, instead of sequentially, while still using only a single narrowband observation receiver. However, this will require storing the PA observation samples and basis function samples of one of the two CCs in memory in order to allow learning the DPD coefficients for CC1 and CC2 simultaneously. With such parallel learning, however, the actual parameter learning algorithms are to be re-designed. This is one interesting topic for our future work.

Another interesting point for future work is extending the proposed concurrent DPD to support transmitting more than two component carriers. The decorrelation-based learning, as such, can support any number of bands or CCs, but the basis functions for scenarios with more than two CCs will be different. In this context, it is worth mentioning that a concurrent DPD solution for tri-band CA scenarios has been developed in [36]. The mathematical expressions representing

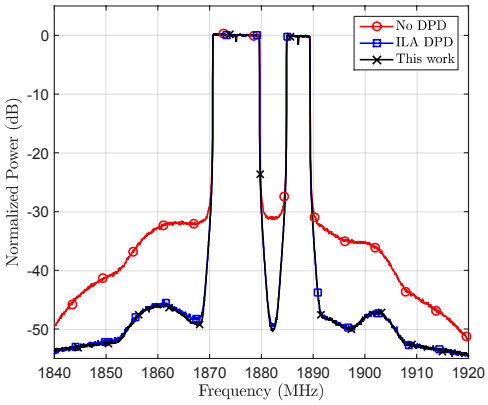

Fig. 10. An RF measurement example at LTE UL band 25 (1850-1915 MHz) showing the normalized spectra of a multicluster 20 MHz SC-FDMA signal with 16-QAM data modulation at 1880 MHz. Spectral regrowth and EVM are reduced when using the proposed decorrelation-based DPD with a real commercial mobile PA operating at +24 dBm output power. ILA based DPD is also implemented and shown for reference.

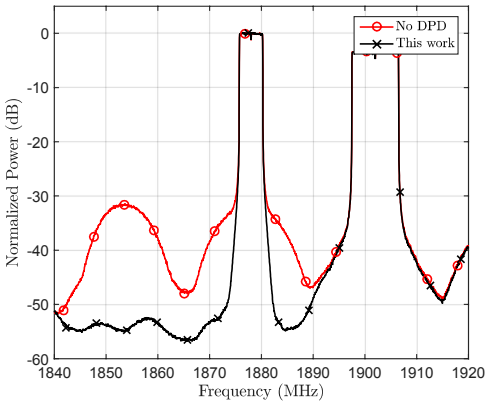

Fig. 11. An RF measurement example at LTE UL band 25 (1850-1915 MHz) showing the normalized PA output spectra of a concurrent noncontiguous intraband CA transmitter with 10 MHz and 5 MHz SC-FDMA component carriers, using QPSK and 64-QAM data modulation respectively. Nonlinear distortion at and around the 5 MHz CC as well as at the IM3- sub-band are reduced when using the proposed decorrelation-based DPD with a real commercial mobile PA operating at +24 dBm output power.

the nonlinear distortion components are derived in [36] from a pruned Volterra model, while the DPD learning is based on the classical indirect learning architecture. Finally, extending the developed concurrent DPD structure and parameter learning principles to account also for I/Q modulators' impairments, e.g., through augmented sets of basis functions, like was done in [37] in more ordinary single-band transmitter context, is one interesting and important future study topic.

VIII. Conclusions

In this article, a novel decorrelation-based concurrent digital predistortion (DPD) solution was proposed for suppressing nonlinear distortion in dual carrier transmitters where a single power amplifier (PA) is used to amplify both carriers. The proposed solution adopts only a single narrowband feedback path, opposed to many earlier concurrent DPD solutions which commonly require a separate feedback path per carrier, such that closed-loop decorrelation based parameter learning is carried out in a per carrier or per band manner. The decorrelation-based closed-loop learning and linearization were also shown to be fully applicable in more classical single carrier or single band transmitters. Furthermore, a flexible overall linearization architecture was introduced where the concurrent linearization at and around the main carriers was complemented with additional predistortion branches to suppress spurious emissions more far away from the main carriers. The combined solution offers great flexibility in mitigating and suppressing nonlinear distortion at any desired sub-band(s), while still using a single feedback receiver. The linearization performance was evaluated in a comprehensive manner using both simulations and actual RF measurements, incorporating both UE side and BS side LTE/LTE-Advanced power amplifiers and different contiguous and non-contiguous transmission scenarios. All experiments demonstrated excellent linearization performance, despite the very simple processing and substantially lower hardware and computing complexities compared to existing solutions.

References

[1] C. Park, L. Sundström, A. Wallen, and A. Khayrallah, "Carrier aggregation for LTE-advanced: Design challenges of terminals," *IEEE Commun. Mag.*, pp. 76–84, Dec. 2013.

[2] S.A. Bassam, W. Chen, M. Helaoui, and F.M. Ghannouchi, "Transmitter architecture for CA: Carrier Aggregation in LTE-Advanced systems," *IEEE Microw. Mag.*, vol. 14, 2013.

[3] P. Roblin, C. Quindroit, N. Naraharisetti, S. Gheitanchi, and M. Fitton, "Concurrent linearization," *IEEE Microw. Mag.*, pp. 75–91, Nov. 2013.

[4] *LTE Evolved Universal Terrestrial Radio Access (E-UTRA) User Equipment (UE) radio transmission and reception, 3GPP TS 36.101 V12.4.0 (Release 12)*, June 2014.

[5] Nokia, "R4-121205 Way forward for non-contiguous intraband transmitter aspects. Available at: http://www.3gpp.org/," Tech. Rep., 3GPP, Feb. 2013.

[6] Nokia, "R4-124353, Non-contiguous intraband unwanted emission. Available at: http://www.3gpp.org/," Tech. Rep., 3GPP, Feb. 2013.

[7] Ericsson and ST-Ericsson, "R4-123797, UE reference sensitivity requirements with two UL carriers. Available at: http://www.3gpp.org/," Tech. Rep., 3GPP, Feb. 2013.

[8] C. Yu, W. Cao, Y. Guo, and A. Zhu, "Digital Compensation for Transmitter Leakage in Non-Contiguous Carrier Aggregation Applications With FPGA Implementation," *IEEE Trans. Microw. Theory Techn.*, vol. 63, no. 12, pp. 4306–4318, Dec 2015.

[9] A. Kiayani, M. Abdelaziz, L. Anttila, V. Lehtinen, and M. Valkama, "Digital Mitigation of Transmitter-Induced Receiver Desensitization in Carrier Aggregation FDD Transceivers," *IEEE Trans. Microw. Theory Techn.*, vol. 63, no. 11, pp. 3608–3623, Nov 2015.

[10] S.A. Bassam, F.M. Ghannouchi, and M. Helaoui, "2-D Digital Predistortion (2-D-DPD) architecture for concurrent dual-band transmitters," *IEEE Trans. Microw. Theory Techn.*, vol. 59, pp. 2547–2553, Oct. 2011.

[11] Y. J. Liu, W. Chen, J. Zhou, B. H. Zhou, and F. M. Ghannouchi, "Digital Predistortion for Concurrent Dual-Band Transmitters Using 2-D Modified Memory Polynomials," *IEEE Trans. Microw. Theory Techn.*, vol. 61, no. 1, pp. 281–290, Jan 2013.

[12] Hua Qian, Saijie Yao, Hao Huang, Xiumei Yang, and Weifeng Feng, "Low complexity coefficient estimation for concurrent dual-band digital predistortion," *IEEE Trans. Microw. Theory Techn.*, vol. 63, no. 10, pp. 3153–3163, Oct 2015.

[13] M. Cabarkapa, N. Neskovic, and D. Budimir, "A Generalized 2-D Linearity Enhancement Architecture for Concurrent Dual-Band Wireless Transmitters," *IEEE Trans. Microw. Theory Techn.*, vol. 61, no. 12, pp. 4579–4590, Dec 2013.

[14] Y. Liu, J. Yan, and P. Asbeck, "Concurrent dual-band digital predistortion with a single feedback loop," *IEEE Trans. Microw. Theory Techn.*, vol. 63, no. 5, pp. 1556–1568, May 2015.

[15] Yuelin Ma and Y. Yamao, "Spectra-Folding Feedback Architecture for Concurrent Dual-Band Power Amplifier Predistortion," *IEEE Trans. Microw. Theory Techn.*, vol. 63, no. 10, pp. 3164–3174, Oct 2015.

[16] C. Yu, J. Xia, X. Zhu, and A. Zhu, "Single-Model Single-Feedback Digital Predistortion for Concurrent Multi-Band Wireless Transmitters," *IEEE Trans. Microw. Theory Techn.*, vol. 63, no. 7, pp. 2211–2224, July 2015.

[17] M. Abdelaziz, L. Anttila, A. Mohammadi, F. Ghannouchi, and M. Valkama, "Reduced-complexity power amplifier linearization for carrier aggregation mobile transceivers," in *IEEE International Conference on Acoustics, Speech, and Signal Processing*, May 2014.

[18] M. Abdelaziz, L. Anttila, C. Tarver, K. Li, J. Cavallaro, and M. Valkama, "Low-Complexity Sub-band Digital Predistortion for Spurious Emission Suppression in Noncontiguous Spectrum Access," *IEEE Trans. Microw. Theory Techn.*, vol. 64, no. 11, pp. 3501–3517, Nov. 2016.

[19] C. Yu, M. Allegue-Martnez, Y. Guo, and A. Zhu, "Output-Controllable Partial Inverse Digital Predistortion for RF Power Amplifiers," *IEEE Trans. Microw. Theory Techn.*, vol. 62, no. 11, pp. 2499–2510, Nov 2014.

[20] Z. Fu, L. Anttila, M. Abdelaziz, M. Valkama, and A. Wyglinski, "Frequency-selective digital predistortion for unwanted emission reduction," *IEEE Trans. Commun.*, vol. 63, no. 1, pp. 254–267, Jan. 2015.

[21] A.S. Tehrani, H. Cao, S. Afsardoost, T. Eriksson, M. Isaksson, and C. Fager, "A comparative analysis of the complexity/accuracy tradeoff in power amplifier behavioral models," *IEEE Trans. Microw. Theory Techn.*, vol. 58, pp. 1510–1520, June 2010.

[22] J. Liu, J. Zhou, W. Chen, B. Zhou, and F.M. Ghannouchi, "Low-complexity 2D behavioural model for concurrent dual-band power amplifiers," *Electronics Letters*, vol. 48, no. 11, pp. 620–621, May 2012.

[23] H. Q. He and M. Faulkner, "Performance of adaptive predistortion with temperature in RF power amplifier linearization," in *Proceedings of the Fifth International Symposium on Signal Processing and Its Applications.*, 1999, vol. 2, pp. 717–720.

[24] S. Haykin, *Adaptive Filter Theory, Fifth Edition*, Pearson, 2014.

[25] W. Hoffmann, "Iterative algorithms for Gram Schmidt orthogonalization," *Computing*, vol. 41, no. 4, pp. 335–348, 1989.

[26] M. Abdelaziz, C. Tarver, K. Li, L. Anttila, M. Valkama, and J. Cavallaro, "Sub-band digital predistortion for noncontiguous transmissions: Algorithm development and real-time prototype implementation," in *49th Asilomar Conf. Signals, Systems, and Computers, Pacific, Grove, CA, USA.*, Nov. 2015.

[27] E. Zenteno and D. Rönnow, "MIMO Subband Volterra Digital Predistortion for Concurrent Aggregated Carrier Communications," *IEEE Trans. Microw. Theory Techn.*, vol. 65, no. 3, pp. 967–979, March 2017.

[28] C. Yu, L. Guan, E. Zhu, and A. Zhu, "Band-Limited Volterra Series-Based Digital Predistortion for Wideband RF Power Amplifiers," *IEEE Trans. Microw. Theory Techn.*, vol. 60, no. 12, pp. 4198–4208, Dec 2012.

[29] R. Raich, Hua Qian, and G. T. Zhou, "Orthogonal polynomials for power amplifier modeling and predistorter design," *IEEE Trans. Veh. Technol.*, vol. 53, no. 5, pp. 1468–1479, Sept 2004.

[30] R. Raich and G. T. Zhou, "Orthogonal polynomials for complex gaussian processes," *IEEE Trans. Signal Process.*, vol. 52, no. 10, pp. 2788–2797, Oct 2004.

[31] Alan V. Oppenheim and Ronald W. Schafer, *Discrete-Time Signal Processing, 3rd Edition*, Prentice Hall, 1999.

[32] E. Dahlman, S. Parkvall, and J. Skold, *4G LTE/LTE-Advanced for Mobile Broadband.*, Elsevier Ltd., 2011.

[33] J. Armstrong, "Peak-to-average power reduction for OFDM by repeated clipping and frequency domain filtering," *Electronics Letters*, vol. 38, no. 5, pp. 246–247, Feb 2002.

[34] *LTE Evolved Universal Terrestrial Radio Access (E-UTRA) Base Station (BS) radio transmission and reception, 3GPP TS 36.104 V12.6.0 (Release 12)*, Feb 2015.

[35] *International Telecommunication Union Radio Communication Sector, Recommendation ITU-R SM.329-12 Unwanted emissions in the spurious domain. Available at: https://www.itu.int/.*

[36] M. Younes, A. Kwan, M. Rawat, and F. M. Ghannouchi, "Linearization of Concurrent Tri-Band Transmitters Using 3-D Phase-Aligned Pruned Volterra Model," *IEEE Trans. Microw. Theory Techn.*, vol. 61, no. 12, pp. 4569–4578, Dec 2013.

[37] L. Anttila, P. Händel, and M. Valkama, "Joint mitigation of power amplifier and I/Q modulator impairments in broadband direct-conversion transmitters," *IEEE Trans. Microw. Theory Techn.*, vol. 58, pp. 730–739, April 2010.

Mahmoud Abdelaziz (S'13) received his B.Sc. (hons.) and M.Sc. degrees in Electronics and Communications Engineering from Cairo University, Egypt, in 2006 and 2011, respectively. He is currently pursuing the D.Sc. degree at Tampere University of Technology, Finland where he works as a researcher with the Department of Electronics and Communications. From 2007 to 2012 he has worked at California-based Newport Media Inc., as well as other companies in the wireless industry. His research interests include statistical and adaptive signal processing in flexible radio transceivers, and wideband digital predistortion.

Lauri Anttila (S'06, M'11) received the M.Sc. degree and D.Sc. (Tech) degree (with honors) in electrical engineering from Tampere University of Technology (TUT), Tampere, Finland, in 2004 and 2011. Currently, he is a Senior Research Fellow at the Department of Electronics and Communications Engineering at TUT. His research interests are in signal processing for wireless communications, in particular radio implementation challenges in 5G cellular radio and full-duplex radio, flexible duplexing techniques, and transmitter and receiver linearization. He has co-authored over 60 peer reviewed articles in these areas, as well as two book chapters.

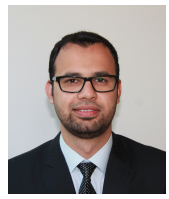

Adnan Kiayani received the B.Sc. degree from COMSATS Institute of Information Technology, Islamabad, Pakistan, in 2006, the M.Sc. degree (with honors) and D.Sc. degree from Tampere University of Technology (TUT), Tampere, Finland, in 2009 and 2015, respectively, all in electrical engineering. He is currently a post-doctoral research fellow at the Department of Electronics and Communications Engineering, TUT, working on the self-interference cancellation in frequency division duplex (FDD) transceivers using digital signal processing (DSP) techniques. His general research interests are in analysis and DSP algorithms for wireless communications, including RF impairments mitigation.

Mikko Valkama (S'00, M'01, SM'15) was born in Pirkkala, Finland, on November 27, 1975. He received the M.Sc. and Ph.D. Degrees (both with honors) in electrical engineering (EE) from Tampere University of Technology (TUT), Finland, in 2000 and 2001, respectively. In 2003, he was working as a visiting researcher with the Communications Systems and Signal Processing Institute at SDSU, San Diego, CA. Currently, he is a Full Professor and Department Vice-Head at the Department of Electronics and Communications Engineering at TUT, Finland. His general research interests include radio communications, radio networks and communications signal processing, with specific emphasis on 5G mobile communications systems.

Publication 4

Z. Fu, L. Anttila, M. Abdelaziz, M. Valkama, and A. M. Wyglinski, "Frequency-Selective Digital Predistortion for Unwanted Emission Reduction," *IEEE Transactions on Communications*, vol. 63, no. 1, pp. 254-267, Jan. 2015.

Frequency-Selective Digital Predistortion for Unwanted Emission Reduction

Zhu Fu, *Student Member, IEEE,* Lauri Anttila, *Member, IEEE,* Mahmoud Abdelaziz, *Member, IEEE,* Mikko Valkama, *Senior Member, IEEE,* Alexander M. Wyglinski, *Senior Member, IEEE*

***Abstract*—In this article, we present a novel digital predistortion (DPD) solution based on a direct learning approach, which is capable of reducing the unwanted emissions resulting from the power amplifier (PA) at any pre-specified frequency located in the transmitter's out-of-band or spurious domain. The proposed scheme is based on evaluating the power spectral density (PSD) of the PA output signal, and optimizing the DPD coefficients iteratively in order to minimize the output PSD around the pre-specified frequency. To highlight the feasibility of the proposed implementation, the predistortion processing is kept as simple as possible, deploying quasi-memoryless polynomial models. Efficient mitigation of unwanted emissions around the target frequency is demonstrated via simulations and actual RF measurements, in both single-carrier and dual-carrier waveform scenarios, using memoryless and memory-based power amplifiers. The proposed DPD solution could potentially be employed in applications such as mobile devices utilizing non-contiguous multi-carrier transmission, where the intermodulation spurs may overlap with the device's own receiver band, or could potentially be violating the spurious emission limits. Another target application is cognitive radio, where the PA may produce unwanted emissions that are interfering with primary user transmissions. To the best of the authors' knowledge, there does not exist a similar technique in the open literature, and thus the purpose of this article is to encourage scientific discussions and technological innovations towards the creation of relatively low-complexity frequency-optimized predistortion techniques employed against selected unwanted emissions produced by the transmitter.**

***Index Terms*—Digital predistortion (DPD), power amplifier (PA), nonlinearity, spurious emission, ACLR, NC-OFDM, carrier aggregation, LTE/LTE-Advanced uplink, frequency division duplexing (FDD), receiver band.**

I. Introduction

RADIO frequency (RF) front-ends of wireless transmitters serve as the interfaces between the antennas and the baseband processing stages. However, these RF front-ends are typically prone to several types of impairments, resulting in the degradation of the overall transceiver performance, such as sensitivity, dynamic range, and unwanted emissions [1], [2]. One important RF front-end component is the power amplifier (PA), which is known to be nonlinear [2] and can potentially generate spectral regrowth [3] when operating near its saturation region. Meanwhile, with the increasing demands for enhancing the performance of digital communication systems operating in challenging channel conditions, as well as enhancing the overall efficiency and flexibility of RF spectrum usage, multicarrier modulation (MCM) is often employed as a physical layer transmission solution. Several examples of commercial systems that use MCM include 3GPP Long term Evolution (LTE) [4] mobile cellular radio and wireless local area networks (WLAN/WiFi) based on the family of IEEE 802.11 wireless standards [5], [6]. Despite its advantages, multicarrier modulation exhibits high peak-to-average power ratio (PAPR) [7] profile. Therefore, the nonlinear behavior of the PA combined with a high PAPR profile often associated with multicarrier transmissions, may yield substantial unwanted emissions that can violate the emission limits, and thus potentially interfere with other signals within the frequency vicinity. Furthermore, in frequency division duplexing (FDD) systems [8], if the PA produces unwanted emissions that happen to overlap with the intended receiver band, it may cause severe receiver desensitization [9], [10] and [11]. This becomes especially problematic when carrier aggregation (CA) is performed, especially with non-contiguous CA-based transmissions, since the duplexing gap is smaller relative to more conventional transmission schemes and the location of the dominant spurious components is more sparse across frequency [9]. Furthermore, understanding and controlling the unwanted emissions of the transmitter is also very important with respect to the implementation of emerging wireless technology such as cognitive radio (CR), where the secondary user (SU) transmitters have strict limitations and constraints designed to interfere with ongoing primary user (PU) transmissions [12], [13]. Hence, minimizing and controlling the unwanted emissions of the SU transmitter across the PU bands is an important requirement.

Linearization is a systematic procedure for reducing an amplifier's distortion and unwanted emissions. While numerous linearization methods have been proposed in the open literature [14], [15] at large scale, digital predistortion (DPD) is recognized as a promising approach due to its accuracy and cost-effectiveness. There has been substantial research into designing DPD techniques for the compensation of PA

Manuscript received April, 2014; revised July, 2014 and September, 2014.

Zhu Fu was with Wireless Innovation Laboratory, Department of Electrical and Computer Engineering, Worcester Polytechnic Institute, Worcester, MA, 01609, USA, when this paper was submitted, and she is now with Qualcomm Atheros Incorporate, San Jose, CA, 95110, USA.

Alexander M. Wyglinski is with Wireless Innovation Laboratory, Department of Electrical and Computer Engineering, Worcester Polytechnic Institute, Worcester, MA, 01609-2280, USA. URL: (http://www.wireless.wpi.edu/).

Lauri Anttila, Mahmoud Abdelaziz, and Mikko Valkama are with the Department of Electronics and Communications Engineering, Tampere University of Technology, Tampere, Finland.

This work was supported by the Finnish Funding Agency for Technology and Innovation (Tekes) under the project "Cross-Layer Modeling and Design of Energy-Aware Cognitive Radio Networks (CREAM)". The work was also funded by the Academy of Finland under the project 251138 "Digitally-Enhanced RF for Cognitive Radio Devices", and the Linz Center of Mechatronics (LCM) in the framework of the Austrian COMET-K2 programme.

nonlinearities in both single-carrier and multi-carrier type waveforms, as reported in [16–20]. Many recent DPD developments have focused on finding efficient variants of the Volterra series in order to model memory effects more accurately [21–25], which are essential as the bandwidth increases, as well as finding efficient ways to decrease the processing sample rates and computational complexity required for predistortion and DPD learning [26], [27], [28].

In general, conventional full-band DPD methods, which primarily aim at linearizing the whole transmission band, require more complex predistortion processing based on the amount of bandwidth being handled or if improved linearization performance is required. The computational complexity of the predistortion process may potentially become prohibitive, especially for battery powered devices [26]. In some cases, the linearization of the whole transmission band may not even be necessary, but linearization of only some specific range of frequencies within the overall transmission band might be of interest. To the best of the authors' knowledge, the current literature on DPD does not address such scenarios explicitly, except for the special case of dual-carrier transmission in [29], as well as adjacent channel leakage related optimization in [27], [28]. To address these shortcomings, this paper proposes a novel predistortion solution that aims to minimize the unwanted emissions resulting from the PA located around a single, pre-specified frequency within the transmission band. The solution is based on analyzing the power spectral density (PSD) of the PA output, and iteratively optimizing the DPD coefficients in order to minimize the output PSD around the target frequency. This proposed approach allows for very simple memoryless predistortion processing, which is critical especially in mobile devices due to computational complexity constraints. Furthermore, to limit the deployment of receiver feedback needed to actively observe or measure the PA output during the DPD learning process, a simple one-shot observation coupled together with a direct learning principle are used as the initial processing stage. This is then combined with an iterative processing approach in order to optimize the DPD coefficients in terms of output PSD minimization at the target frequency. Both simulation-based evaluations as well as actual RF measurements are provided to demonstrate the operation of the proposed solution.

In general, it should be noted that many existing DPD methods, e.g., [24], [30], [31], can certainly reduce the spectral regrowth and unwanted emissions across all frequencies, especially if the bandwidth of the feedback path and processing complexity in the main DPD processing path are not limited. However, conventional DPD solutions cannot readily tailor their linearization capability to an arbitrary subset of frequencies, especially if the processing complexity is limited, but seek to push the unwanted emissions down throughout the entire transmit spectrum. Thus, in this work we take an alternative approach and focus the processing power of the DPD stage, given limited complexity, to the pre-specified frequency. This work can also be seen as a first step towards this direction, as opposed to conventional full bandwidth linearization approaches, and thus one purpose of this article is to encourage scientific discussions and technological innovations towards fairly low-complexity frequency-selective predistortion techniques against selected unwanted emissions of the transmitter.

The rest of this paper is organized as follows: Section II defines the fundamental problem statement, and elaborates further on the motivation of the proposed method. Furthermore, potential use cases are shortly discussed. Section III presents the basic mathematical formulation of our proposed DPD approach for both quasi-memoryless nonlinear PA model and memory-based nonlinear PA model. Section IV describes the proposed procedure for the DPD parameter estimation and optimization, building upon one-shot direct learning and additional iterative processing. Simulation and RF measurement results and comparisons are presented in Section VI, and several concluding remarks are made in Section VII.

II. Problem Statement and Motivation

A. Quantifying Unwanted Emissions

The unwanted emissions in the transmitter output spectrum can be generally divided into three parts: The emissions within the occupied channel bandwidth (also called inband emissions), the out-of-band (OOB) emissions, and the spurious emissions. Fig. 1 illustrates the principal output spectrum of a transmitter, together with the different frequency regions from the unwanted emissions perspective. In this situation, we mostly define and use these concepts according to what has been defined and specified by the International Telecommunication Union Radio Communication Sector (ITU-R), as well as by the 3GPP standardization body within the context of LTE/LTE-Advanced mobile cellular radio [32], [33], [34], [35].

First, the occupied bandwidth is defined as the bandwidth containing 99% of the total integrated mean power of the transmitted spectrum within the assigned channel [35]. The inband transmit waveform purity is typically measured through the error vector magnitude (EVM), which is defined as

$$EVM_{\%} = \sqrt{\frac{P_{error}}{P_{ref}}} \times 100\%, \tag{1}$$

where P_{error} is the power of the error signal, defined as the difference between the ideal symbol values and the corresponding symbol rate complex samples at the PA output, both normalized to same average power, while P_{ref} is the reference power of the ideal symbol constellation. Typically in EVM evaluations, linear distortion of the transmit chain is equalized prior to calculating the error signal [33]. In turn, the OOB emissions are defined here as the unwanted emissions immediately outside the assigned channel bandwidth resulting from the non-linearity in the transmitter but excluding spurious emissions. This OOB emission is usually quantified as the spectrum emissions at the immediate adjacent channels, denoted as $\triangle \mathrm{f}_{\mathrm{OOB}}$, and is measured here with the adjacent channel leakage power ratio (ACLR). The ACLR is defined as the ratio of the transmitted powers within the wanted channel (P_{wanted}) and the adjacent channel ($P_{adjacent}$), respectively

[34], namely

$$ACLR_{dB} = 10\log_{10}\frac{P_{wanted}}{P_{adjacent}}, \quad (2)$$

and it can be calculated separately for left and right adjacent channels. Notice also that in general, depending on the system specifications, the evaluation or measurement bandwidth of the adjacent channel power can be different than that of the wanted signal power [34]. On the other hand, spurious emissions are located at more far-away frequencies, outside the OOB region [4], [32]. Following the ITU-R recommendations [32], which are applicable at all frequencies between 1 - 12.75 GHz, we quantify the spurious emissions as the integrated power over a 1 MHz measurement bandwidth/window, at frequencies beyond the OOB range. While this gives an absolute power measure for the spurious emissions within the measurement bandwidth, we also define the relative spurious emission rejection ratio (SRR) as the ratio of the inband wanted channel power and the spurious emission power (over the 1 MHz measurement bandwidth) at the considered frequency, namely

$$SRR_{dB} = 10\log_{10}\frac{P_{wanted}}{P_{spur}}. \quad (3)$$

Finally, in the special case of non-contiguous carrier aggregation transmission, the third-order and fifth-order cross-modulation or intermodulation *between the carriers*, in addition to the classical regrowth around the individual carriers, are of special interest [33], [35]. Depending on the frequency separation between the aggregated carriers (also called component carriers), say $\triangle f_{CA}$, these IM3 and IM5 regions are respectively located at the distance of $\triangle f_{CA}$ and $2\triangle f_{CA}$, from the center of the appropriate component carrier, as illustrated in Fig. 2. We quantify the rejection of these specific IM3 and IM5 terms through the power ratios relative to the component carrier wanted signal power as

$$IM3R_{dB} = 10\log_{10}\frac{P_{wanted,cc}}{P_{im3}}, \quad (4)$$

$$IM5R_{dB} = 10\log_{10}\frac{P_{wanted,cc}}{P_{im5}}. \quad (5)$$

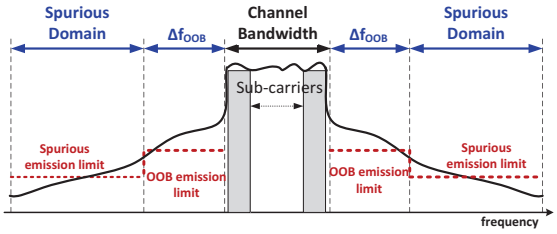

Fig. 1. Transmitter RF spectrum. It is composed of the occupied channel bandwidth, OOB emissions, and the spurious domain.

B. Predistortion Principle and Motivation for Frequency-Selective Optimization

Conventional DPD methods typically seek to linearize the entire transmit spectrum, without specifically tailoring the linearization capabilities to any particular regions of the spectrum. In conventional applications, the target has been mainly to enhance the ACLR and/or EVM but also other spectral regions of the transmitter output are affected, especially when deploying a full-bandwidth feedback receiver for DPD learning combined with full-bandwidth DPD processing in the main transmit path. In general, while processing the signal in a nonlinear manner, additional higher order intermodulation products (IMPs) will occur at the PA output, which result in increased bandwidth as shown in Fig. 3(b). This is due to the nonlinear nature of the predistorter itself, which is in cascade with the nonlinear PA. Hence, the two nonlinearities in this cascade configuration, combined with proper optimization for the DPD processing, will result in reduced power of the original lower-order IMPs but also yield new higher-order nonlinear terms. While these new higher-order terms are often fairly weak, conventional predistortion solutions do not contain explicit mechanisms to control the unwanted emissions at particular subset of frequencies. In other words, there are no easy solutions for performing this trade-off, such as between the strength of the new higher-order products and the orignal unwanted emissions. Thus, especially if the computational complexity of the DPD processing is limited, having the ability to tailor the linearization capability to given subset of frequencies, such as own receiver band in FDD transceivers, would be particularly useful. This is one of the main motivations of this work.

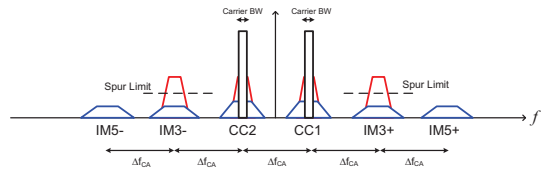

Fig. 2. Illustration of transmitter RF spectrum with two non-contiguously aggregated component carriers (CCs). In addition to classical regrowth around the component carriers, also 3rd and 5th order intermodulation between the carriers are shown.

To elaborate further on wireless systems deployed in FDD mode [33], [36], implying simultaneous transmission and reception per individual transceivers, the ability to protect the sensitive receiver circuitry from a strong transmit signal is a key issue [9], [10] and [11]. As the sensitivity requirements of the receiver itself are typically in the range of -80 dBm to -100 dBm [33], the power limits for transmitter-induced emissions within the receiver band are typically even tighter than the general spurious emission limits [9]. Although a duplex filter is usually implemented to provide suppression of transmitter unwanted emissions occurring at the receiver frequencies, there are increasing challenges and difficulties to obtain sufficient attenuation for these emissions as the duplexing gaps, denoting the center-frequency separation of simultaneous transmission and reception, are becoming increasingly smaller [33], [9]. For instance, in band 20 of the Evolved Universal Terrestrial Radio Access (E-UTRA) operating frequencies [4],

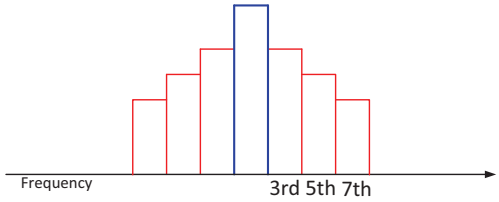

(a) No DPD.

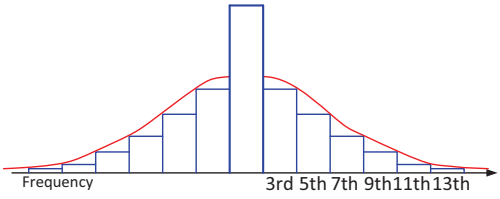

(b) With conventional DPD.

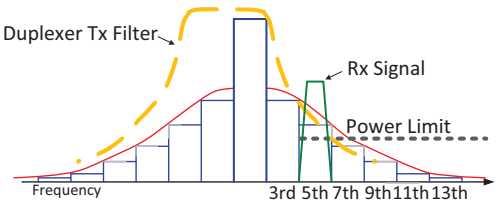

(c) Illustration of spurious emission at own RX.

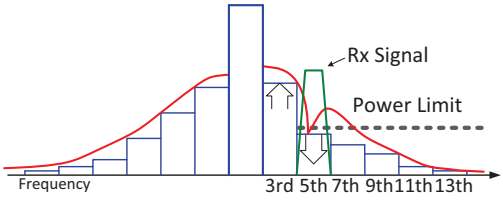

(d) Frequency-selective unwanted emission suppression with proposed DPD solution.

Fig. 3. Example output spectrum of a transmitter (a) with no DPD, (b) with conventional DPD, (c) with conventional DPD but potentially desensitizing own RX in FDD mode, and (d) with proposed DPD optimizing the DPD processing to own RX band in FDD mode.

the uplink frequencies, *i.e.*, user equipment (UE) to base station (BS), and the downlink frequencies, *i.e.*, BS to UE, are specified as 832 MHz - 862 MHz and 791 MHz - 821 MHz, respectively. Thus, the duplex gap for this configuration is only 41 MHz. Then, if a fully allocated 20 MHz LTE uplink carrier is transmitted, the 5th order spectral regrowth at the spurious emission region of the uplink transmitter output will directly fall on top of the receiver band, hence potentially desensitizing the receiver. This is illustrated in Fig. 3(c), where the green spectral component represents the received signal, which coincides with the 5th order regrowth at the transmitter output. Although a duplex filter will suppress the unwanted emissions at the RX band, typically by some 50-60dB in mobile transmitters, the residual power can still be substantial [9].

Deploying classical wideband linearization solutions to provide very high suppression of unwanted emissions at specific frequencies of the transmitter output, in cases such as those described above, easily lead to excessively high computational complexity as the performance cannot be tailored as a function of frequency. In contrast to conventional solutions, our proposed DPD method aims to optimize the suppression of unwanted emissions at arbitrary pre-specified frequencies at the PA output. Ideally, the proposed method is able to generate a 'notch' at any pre-specified frequency of the PA output spectrum by manipulating the DPD coefficients such that the unwanted emissions can be controlled at the target frequency. By imposing additional optimization constraints, the unwanted emissions at other frequencies can be also kept within specified limits, which is based upon the overall degrees of freedom stemming from the deployed processing order in the DPD stage. As illustrated in Fig. 3(d), a notch can be generated at the target frequency, so the power limit, e.g., at own RX band is eventually not violated.

III. Mathematical Problem Formulation and Pre-Distortion Processing

In this section, we conduct the basic mathematical problem formulation in terms of several PA models, available DPD processing, and the resulting PA output spectral density (PSD). The actual DPD coefficient learning and optimization aspects are addressed then in the next section. For notational convenience, we use continuous-time complex baseband equivalent signal notations in the analysis and modeling.

A. Quasi-Memoryless PA model

Assuming a narrowband signal, both PA and DPD can be modeled as truncated complex power series or polynomials. Such models are widely used in the literature, see ([2] and the references therein). The coefficients of the power series are complex such that they can represent both the AM-AM and AM-PM conversion accurately. Thus, the overall 'DPD + PA' system is modeled by a cascade of two memoryless odd order polynomials. The assumed DPD processing with $x(t)$ denoting the complex baseband input waveform and $b_{2\,l-1}$ denoting the coefficient of the $(2\,l-1)^{\text{th}}$ order term is formulated here as

$$z\left(t\right)=\sum_{l=1}^{L}b_{2\,l-1}x\left(t\right)\left|x\left(t\right)\right|^{2\,l-2} \tag{6}$$

$$=\sum_{l=1}^{L}b_{2\,l-1}x\left(t\right)^{l}x^{*}\left(t\right)^{l-1}, \tag{7}$$

where $z\left(t\right)$ represents the DPD output signal. In general, the form in (6) is used in many of the subsequent derivation steps. Similarly, the PA can be modeled as

$$y\left(t\right)=\sum_{p=1}^{P}a_{2\,p-1}z\left(t\right)\left|z\left(t\right)\right|^{2\,p-2}, \tag{8}$$

where $y(t)$ denotes the PA output and $a_{2\,p-1}$ represents the coefficient of the $(2\,p-1)^{\text{th}}$ order term in the PA model. After inserting (6) into (8), we obtain

$$y\left(t\right)=\sum_{k=1}^{Q}c_{2\,k-1}x\left(t\right)\left|x\left(t\right)\right|^{2\,k-2}, \tag{9}$$

where the effective coefficients c_{2k-1} of the overall cascade model consists of PA and DPD coefficients a_{2p-1} and b_{2l-1}, and $Q=(L+1)(P+1)-1$ is the polynomial order of the overall 'DPD+PA' cascade.

In general, our aim is to suppress the PA induced emissions at the N^{th} spectral regrowth or intermodulation region (see Fig. 3). Since the N^{th} and higher than N^{th} order nonlinear terms in (9) generally contribute to the unwanted emissions located at such frequencies, we can truncate $y\left(t\right)$ as

$$y_{tr}\left(t\right)=\sum_{k=\frac{N+1}{2}}^{Q}c_{2\,k-1}x\left(t\right)\left|x\left(t\right)\right|^{2\,k-2}, \tag{10}$$

and use this truncated signal model in the subsequent analysis.

Next, to analyze the power spectral density (PSD) of the PA output signal, we invoke the Wiener-Khinchin theorem [37], which states that the autocorrelation function, $R(\tau)$, and the PSD, $S(f)$, form a Fourier Transform pair. The autocorrelation function of the truncated signal $y_{tr}(t)$ can then be shown to be of the form

$$\begin{aligned}R_{y_{tr}}(\tau)&=E[y_{tr}(t)\,y_{tr}^{*}(t-\tau)]\\&=\sum_{k_1=\frac{N+1}{2}}^{Q}\sum_{k_2=\frac{N+1}{2}}^{Q}c_{2k_1-1}c_{2k_2-1}^{*}R_{x^{2k_1-1}x^{2k_2-1}}(\tau),\end{aligned} \tag{11}$$

where $R_{x^{p}x^{q}}(\tau)=E[\phi_p(t)\,\phi_q^{*}(t-\tau)]$, using the shorthand notation $\phi_p(t)=x\left(t\right)\left|x\left(t\right)\right|^{p-1}$, and $(\cdot)^{*}$ denotes complex conjugation. As it can be observed, the autocorrelation function can be expressed as double summation of the cross-correlation of odd order power terms of the DPD input signal $x(t)$ multiplied by the coefficients c_{2k-1} and c_{2k-1}^{*}. The corresponding PSD of the truncated signal can then be derived through Fourier transform as:

$$S_{y_{tr}}(f)=\sum_{k_1=\frac{N+1}{2}}^{Q}\sum_{k_2=\frac{N+1}{2}}^{Q}c_{2\,k_1-1}c_{2\,k_2-1}^{*}S_{x^{2k_1-1}x^{2k_2-1}}(f). \tag{12}$$

The above expression now shows that suppression of unwanted emission power at certain frequency, say $f=f_0$, can be achieved by properly manipulating and optimizing the coefficients c_{2k-1} to minimize the PSD in (12) evaluated at $f=f_0$. Assuming a known or already estimated PA model coefficients a_{2p-1}, as well as knowledge of the spectral characteristics of the DPD input signal $x(t)$, this is equivalent to optimizing the DPD coefficients b_{2l-1} accordingly. This will be elaborated further in the next section.

B. PA Model with Memory

When dealing with a range of wideband waveforms and transmission schemes, it is necessary to consider the memory effects of the PA, which introduces extra complexity to our investigations. In this study, we employ the Parallel Hammerstein (PH) model with polynomial nonlinearities and FIR filters in order to model the PA with memory. Such models have been shown to have excellent modeling capabilities and accuracy for various types of power amplifiers [38–40]. To keep the analysis tractable and to emphasize low-complexity predistortion processing, we still keep the predistorter memoryless.

In general, the Parallel-Hammerstein PA model is given as

$$y\left(t\right)=\sum_{p=1}^{P}a_{2\,p-1}(t)\star\left(z\left(t\right)\left|z\left(t\right)\right|^{2\,p-2}\right) \tag{13}$$

where $a_p\left(t\right)$ are the model filters (impulse responses), $\star$ denotes convolution and $z\left(t\right)$ denotes the PA input. Inserting next the memoryless DPD output in (6) into (13), the output of the PA can be written as

$$y\left(t\right)=\sum_{k=1}^{Q}c_{2\,k-1}(t)\star\left(x\left(t\right)\left|x\left(t\right)\right|^{2\,k-2}\right), \tag{14}$$

where the filters (impulse responses) $c_{2k-1}(t)$ consist of PA model filters $a_{2p-1}(t)$ and the DPD coefficients b_{2l-1}. An example case of the structure of these filters is given in the next sub-section. Notice that a truncated signal model similar to (10) can be directly obtained here as well.

Under the above Parallel-Hammerstein PA model, the autocorrelation function of the truncated PA output signal can be shown via fairly elementary manipulations, to be of the form

$$\begin{aligned}R_{y_{tr}}(\tau)&=E[y_{tr}(t)\,y_{tr}^{*}(t-\tau)]\\&=\sum_{k_1=\frac{N+1}{2}}^{Q}\sum_{k_2=\frac{N+1}{2}}^{Q}c_{2k_1-1}(\tau)\star c_{2k_2-1}^{*}(-\tau)\\&\qquad\star R_{x^{2k_1-1}x^{2k_2-1}}(\tau),\end{aligned} \tag{15}$$

By the Fourier transform, the corresponding PSD of the truncated signal with the Parallel-Hammerstein PA model yields:

$$\begin{aligned}S_{y_{tr}}(f)=\sum_{k_1=\frac{N+1}{2}}^{Q}\sum_{k_2=\frac{N+1}{2}}^{Q}&C_{2\,k_1-1}(f)\\&C_{2\,k_2-1}^{*}(f)S_{x^{2k_1-1}x^{2k_2-1}}(f),\end{aligned} \tag{16}$$

where $C_i(f)$ denotes the Fourier transform of $c_i(\tau)$. This result shows that the suppression of unwanted emissions at a certain frequency $f=f_0$ can be achieved by manipulating and optimizing $c_{2k-1}(t)$ to minimize the output of (16) at the considered frequency. With *a priori* knowledge of the PA coefficients $a_{2p-1}(t)$ and the spectral characteristics of the input signal $x(t)$, the optimal combination of the DPD coefficients b_{2l-1} can be obtained. This will be elaborated in detail in the next section.

C. Example Study Cases

In this subsection, we apply the general expressions derived in the previous section of this paper to several case studies: (i) 5^{th} order memoryless PA model and a 7^{th} order memoryless DPD, and (ii) 5^{th} order Parallel-Hammerstein PA model and 7^{th} order memoryless DPD. These example cases are selected mostly for the illustration purposes and to keep the presentation tractable and concise, and are also used in the simulation and measurement experiments later on in this paper. However, notice that the selected model and processing orders are just examples, and higher-order solutions can also be easily derived.

1) Quasi-Memoryless PA Case: Assuming a 5^{th} order PA model and a 7^{th} order DPD, the PA output signal from (8) yields

$$y\left(t\right) = c_{1}\, x\left(t\right) + c_{3}\, \left|x\left(t\right)\right|^{2} x\left(t\right) + c_{5}\, \left|x\left(t\right)\right|^{4} x\left(t\right) + \cdots + c_{35}\, \left|x\left(t\right)\right|^{34} x\left(t\right). \tag{17}$$

With the purpose of reducing the unwanted emissions at a target frequency f_0, which is assumed to be located within a third-order regrowth region, (17) is truncated such that

$$y_{tr}\left(t\right) = c_{3}\, \left|x\left(t\right)\right|^{2} x\left(t\right) + c_{5}\, \left|x\left(t\right)\right|^{4} x\left(t\right) + c_{7}\, \left|x\left(t\right)\right|^{6} x\left(t\right) + c_{9}\, \left|x\left(t\right)\right|^{8} x\left(t\right) + c_{11}\, \left|x\left(t\right)\right|^{10} x\left(t\right), \tag{18}$$

In the above expression, we have also employed substantial truncation of the higher order nonlinear terms, and kept only those that will contribute the most to the PA output. By performing this operation, the computation complexity is reduced significantly. The cascaded parameters c_3, c_5, c_7, c_9 and c_{11} of the above model can now be expanded as

$$\begin{aligned}
c_3 &= a_1 b_3 + a_3,\\
c_5 &= a_1 b_5 + 2a_3 b_3 + a_5 + a_3 b_3^*,\\
c_7 &= 2a_3 b_3 b_3^* + a_3 b_3^2 + 2a_5 b_3^* + a_1 b_7 + 2a_3 b_5\\
&\quad + 3a_5 b_3 + a_3 b_5^*,\\
c_9 &= a_3 b_3^2 b_3^* + a_5 (b_3^*)^2 + 2a_3 b_5 b_3^* + 6a_5 b_3^* b_3 + 2a_3 b_3 b_5^*\\
&\quad + 2a_3 b_3 b_5 + 3a_5 b_3^2 + 2a_5 b_5^* + 2a_3 b_7 + 3a_5 b_5 + a_3 b_7^*,\\
c_{11} &= 3a_5 (b_3^*)^2 b_3 + 2a_3 b_3 b_5 b_3^* + 6a_5 b_3^* b_3^2 + a_3 b_3^2 b_5^*\\
&\quad + a_5 b_3^3 + 2a_3 b_3 b_7^* + 2a_5 b_3^* b_5^* + 2a_3 b_7 b_3^* + 6a_5 b_3^* b_5\\
&\quad + 2a_3 b_5 b_5^* + 6a_5 b_5^* b_3 + 2a_3 b_3 b_7 + a_3 b_5^2 + 6a_5 b_3 b_5\\
&\quad + 2a_5 b_7^* + 3a_5 b_7.
\end{aligned} \tag{19}$$

Notice also that if the target frequency f_0 is is located within a fifth-order regrowth region, as opposed to third-order region, then the above expressions can be truncated further by neglecting the third-order term relative to c_3. Next, the auto-correlation and PSD of the truncated signal y_{tr} can be calculated using (11) and (12), but taking into account also the truncation of the higher-order terms. This yields the expression of the PSD to be optimized given by

$$\begin{aligned}
S_{y_{tr}}(f) &= c_3 c_3^* S_{x^3x^3}(f) + c_3 c_5^* S_{x^3x^5}(f) + c_5^* c_5 S_{x^5x^3}(f)\\
&\quad + c_3 c_7^* S_{x^3x^7}(f) + c_3^* c_7 S_{x^7x^3}(f) + c_3 c_9^* S_{x^3x^9}(f)\\
&\quad + c_3^* c_9 S_{x^9x^3}(f) + c_3 c_{11}^* S_{x^3x^{11}}(f) + c_3^* c_{11} S_{x^{11}x^3}(f)\\
&\quad + c_5 c_5^* S_{x^5x^5}(f) + c_5 c_7^* S_{x^5x^7}(f) + c_5^* c_7 S_{x^7x^5}(f)\\
&\quad + c_5 c_9^* S_{x^5x^9}(f) + c_5^* c_9 S_{x^9x^5}(f) + c_5 c_{11}^* S_{x^5x^{11}}(f)\\
&\quad + c_5^* c_{11} S_{x^{11}x^5}(f) + c_7 c_7^* S_{x^7x^7}(f) + c_7 c_9^* S_{x^7x^9}(f)\\
&\quad + c_7^* c_9 S_{x^9x^7}(f) + c_7 c_{11}^* S_{x^7x^{11}}(f) + c_7^* c_{11} S_{x^{11}x^7}(f)\\
&\quad + c_9 c_9^* S_{x^9x^9}(f) + c_9 c_{11}^* S_{x^9x^{11}}(f) + c_9^* c_{11} S_{x^{11}x^9}(f)\\
&\quad + c_{11} c_{11}^* S_{x^{11}x^{11}}(f),
\end{aligned} \tag{20}$$

where the exact expressions for the cascaded parameters c_3, c_5, c_7, c_9 and c_{11} are given in (19), showing their dependency on the optimization variables, i.e., DPD coefficients b_{2l-1}.

2) Parallel-Hammerstein PA Case: Starting with a 7^{th} order memoryless DPD and a 5^{th} order PH PA model with memory filters $a_1\left(t\right)$, $a_3\left(t\right)$ and $a_5\left(t\right)$ for the main, third order and fifth order branches, the PA output signal can be expressed as

$$y\left(t\right) = c_1\left(t\right) \star x\left(t\right) + c_3\left(t\right) \star \left|x\left(t\right)\right|^{2} x\left(t\right) + c_5\left(t\right) \star \left|x\left(t\right)\right|^{4} x\left(t\right) + \cdots + c_{35}(t) \star \left|x\left(t\right)\right|^{34} x\left(t\right). \tag{21}$$

In this example, we will again focus on the third-order regrowth region. Consequently, the truncated output of the PA with only the most relevant terms included can be expressed as

$$y_{tr}\left(t\right) = c_3(t) \star \left|x\left(t\right)\right|^{2} x\left(t\right) + c_5(t) \star \left|x\left(t\right)\right|^{4} x\left(t\right) + c_7 \star \left|x\left(t\right)\right|^{6} x\left(t\right) + c_9(t) \star \left|x\left(t\right)\right|^{8} x\left(t\right) + c_{11}(t) \star \left|x\left(t\right)\right|^{10} x\left(t\right). \tag{22}$$

Notice that if the target frequency is located within the fifth-order regrowth region, the above expression can be further simplified by neglecting the third-order term. Then, after taking the auto-correlation of y_{tr}, the PSD can be evaluated through Fourier transform of the obtained autocorrelation function, yielding

$$\begin{aligned}
S_{y_{tr}}(f) &= C_3(f) C_3^*(f) S_{x^3x^3}(f) + C_3(f) C_5^*(f) S_{x^3x^5}(f)\\
&\quad + C_3^*(f) C_5(f) S_{x^5x^3}(f) + C_3(f) C_7^*(f) S_{x^3x^7}(f)\\
&\quad + C_3^*(f) C_7(f) S_{x^7x^3}(f) + C_3(f) C_9^*(f) S_{x^3x^9}(f)\\
&\quad + C_3^*(f) C_9(f) S_{x^9x^3}(f) + C_3(f) C_{11}^*(f) S_{x^3x^{11}}(f)\\
&\quad + C_3^*(f) C_{11}(f) S_{x^{11}x^3}(f) + C_5(f) C_5^*(f) S_{x^5x^5}(f)\\
&\quad + C_5(f) C_7^*(f) S_{x^5x^7}(f) + C_5^*(f) C_7(f) S_{x^7x^5}(f)\\
&\quad + C_5(f) C_9^*(f) S_{x^5x^9}(f) + C_5^*(f) C_9(f) S_{x^9x^5}(f)\\
&\quad + C_5(f) C_{11}^*(f) S_{x^5x^{11}}(f) + C_5^*(f) C_{11}(f) S_{x^{11}x^5}(f)\\
&\quad + C_7(f) C_7^*(f) S_{x^7x^7}(f) + C_7(f) C_9^*(f) S_{x^7x^9}(f)\\
&\quad + C_7^*(f) C_9(f) S_{x^9x^7}(f) + C_7(f) C_{11}^*(f) S_{x^7x^{11}}(f)\\
&\quad + C_7^*(f) C_{11}(f) S_{x^{11}x^7}(f) + C_9(f) C_9^*(f) S_{x^9x^9}(f)\\
&\quad + C_9(f) C_{11}^*(f) S_{x^9x^{11}}(f) + C_9^*(f) C_{11}(f) S_{x^{11}x^9}(f)\\
&\quad + C_{11}(f) C_{11}^*(f) S_{x^{11}x^{11}}(f),
\end{aligned} \tag{23}$$

where $C_i(f)$ is the Fourier transform of $c_i(\tau)$. These can be expanded and written as

$$\begin{aligned}
C_3(f) &= A_1(f)b_3 + A_3(f),\\
C_5(f) &= A_1(f)b_5 + 2A_3(f)b_3 + A_5(f) + A_3(f)b_3^*,\\
C_7(f) &= 2A_3(f)b_3b_3^* + A_3(f)b_3^2 + 2A_5(f)b_3^* + A_1(f)b_7\\
&\quad + 2A_3(f)b_5 + 3A_5(f)b_3 + A_3(f)b_5^*,\\
C_9(f) &= A_3(f)b_3^2b_3^* + A_5(f)(b_3^*)^2 + 2A_3(f)b_5b_3^*\\
&\quad + 6A_5(f)b_3^*b_3 + 2A_3(f)b_3b_5^* + 2A_3(f)b_3b_5\\
&\quad + 3A_5(f)b_3^2 + 2A_5(f)b_5^* + 2A_3(f)b_7\\
&\quad + 3A_5(f)b_5 + A_3(f)b_7^*,\\
C_{11}(f) &= 3A_5(f)(b_3^*)^2b_3 + 2A_3(f)b_3b_5b_3^* + 6A_5(f)b_3^*b_3^2\\
&\quad + A_3(f)b_3^2b_5^* + A_5(f)b_3^3 + 2A_3(f)b_3b_7^*\\
&\quad + 2A_5(f)b_3^*b_5^* + 2A_3(f)b_7b_3^* + 6A_5(f)b_3^*b_5\\
&\quad + 2A_3(f)b_5b_5^* + 6A_5(f)b_5^*b_3 + 2A_3(f)b_3b_7\\
&\quad + A_3(f)b_5^2 + 6A_5(f)b_3b_5 + 2A_5(f)b_7^* + 3A_5(f)b_7,
\end{aligned} \tag{24}$$

where $A_i(f)$ denotes the Fourier transform of $a_i(t)$, showing again the PSD dependency on the optimization variables, i.e., DPD coefficients b_{2l-1}.

IV. Parameter Estimation and Coefficient Optimization

In this section, the actual coefficient optimization and associated parameter estimation aspects in the context of the proposed predistortion approach are addressed, with the purpose of minimizing the derived PSD of the PA output signal around the pre-specified frequency f_0. In general, as the previous modeling section already indicates, a direct model for the PA is needed in the proposed approach for the purpose of evaluating the output PSD. Hence, we employ a direct modeling approach as opposed to indirect modeling and learning, which is one of the common techniques in DPD context. By deploying direct learning, we can also save substantial energy in terms of using the observation receiver from PA output back to digital baseband. This is because the direct model can be estimated in one stage, without indirect learning type of hardware-intensive iterations. In general, after identifying the direct model for the PA, additional iterative processing at digital baseband can be applied, to finally optimize the DPD coefficients for unwanted emission suppression at the target frequency.

A. Overall Processing Flow

A block-diagram of the overall processing stages is illustrated in Fig. 4. For presentation purposes, the actual digital-analog (D/A), analog-digital (A/D) as well as up- and down-conversion stages are not shown in order to focus on the fundamental elements of the transceiver system from a DPD processing perspective. The first stage around the PA is the direct modeling/learning block, identifying either a memoryless or Parallel-Hammerstein direct-model for the PA at hand. This is done only once using block least-squares (LS) parameter estimation, which is feasible since both the memoryless and Parallel-Hammerstein PA models are linear in parameters [38], [39] and [40], and the identified model parameters are then fed on towards the PSD evaluation, the iterative optimizer, and associated signal processing blocks.

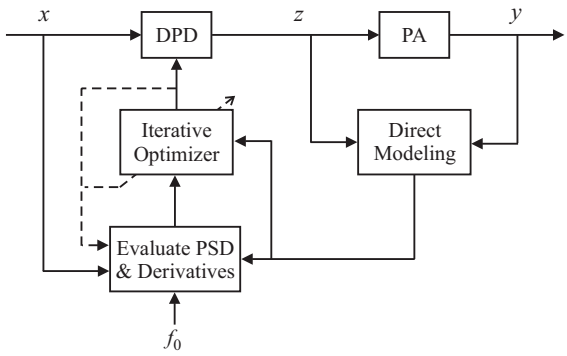

Fig. 4. The proposed overall block-diagram of the predistortion processing including direct PA modeling/learning, evaluation of PSD derivatives and carrying out iterative DPD parameter optimization.

B. PSD Evaluation

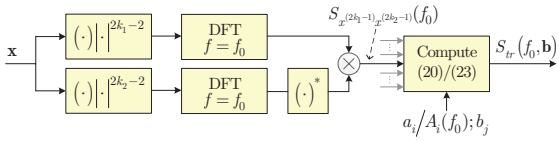

Fig. 5. Block diagram showing the signal processing procedures for evaluating the elementary PSD components at $f = f_0$ between basis functions of order $2k_1 - 1$ and $2k_2 - 1$, and the output PSD. The same elementary PSD components can be also used to calculate the first and second derivatives of the output PSD.

An efficient implementation for the proposed signal processing procedure formulated in Section III for the PSD evaluation of the truncated signal model is shown in Fig. 5 with a block-based approach adopted. Here, the input $\mathbf{x}$ is an N_{bl}-dimensional vector composed of N_{bl} samples of the original complex baseband data. It is transformed into a collection of DPD basis functions that are used in a memoryless $(2K-1)^{th}$ order nonlinear model, and thus we obtain K pieces of N_{bl}-dimensional vectors consisting of the basis function samples $x(n)|x(n)|^{2k-2}$. Based on the pre-specified frequency f_0, around which we aim to minimize the unwanted emissions, only the basis functions associated with the truncated signal are computed. Additionally, instead of calculating the cross-correlations in (11) or (15) in the time domain, a more practical and efficient structure is proposed here based on the fast convolution method [41]. The basis functions are first transformed to the frequency domain, but since we only need to compute the PSD at one specific frequency (f_0), a single point Discrete Fourier Transform (DFT) suffices, which significantly reduces the complexity. To reduce the variance of this approach, the overall block size N_{bl} is divided into equal length DFT sub-blocks over which the averaged single

point DFT is computed. Finally, expression (20) or (23) is evaluated in the last block, which takes as inputs all the elementary PSD's, the PA model coefficients a_i (or $A_i(f_0)$ in the case of the memory PA model), and the DPD parameters b_j. When carefully examining the PSDs in (20) or (23), we can see that out of the 25 PSDs, 20 are complex conjugate pairs and thus they need to be computed only once. The PA model coefficients are already known through previous direct model identification stage, which then leaves only the DPD parameters to be determined. Hence, the output PSD $S_{tr}(f_0)$ becomes a function of the DPD parameter vector $\mathbf{b} = [b_3 \quad b_5 \quad \dots \quad b_{2K-1}]^T$, which we will here denote by $S_{tr}(\mathbf{b})$ for short.

C. Iterative Optimization

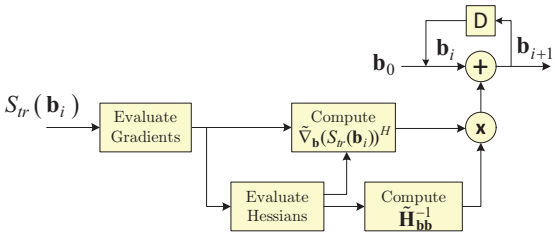

Fig. 6. Implementation of proposed iterative DPD parameter optimization through Newton-Raphson method.

The final step is to optimize the parameter vector $\mathbf{b}$ of the predistorter in order to find $\min(S_{tr}(\mathbf{b}))$. This is a general optimization problem that aims to seek values for certain design or control variables in order to minimize an objective function. In this study, the *Newton-Raphson* method is employed, which seeks the minimum of a function $F(x)$ using both first and second derivatives [42]. In its simplest form, with a single variable x to be optimized, and assuming $F(x)$ holomorphic, it can be described as

$$x_{i+1} = x_i - \frac{F'(x_i)}{F''(x_i)}, \tag{25}$$

where x_0 is an initial estimate of the minimum point of $F(x)$, and (25) is executed in a loop until $|F'(x_i)|$ is sufficiently small [42]. In the current problem, multiple parameters b_{2l-1} are optimized instead of a scalar. Furthermore, since the objective function in our application is real-valued (and therefore strictly-speaking non-holomorphic), we must use the differentiation rules of Wirtinger calculus [43], [44]. In this case, defining the parameter vector $\mathbf{b} = [b_3 \quad b_5 \quad \dots \quad b_{2K-1}]^T$, the updated equation becomes [43]

$$\mathbf{b}_{i+1} = \mathbf{b}_i + \underbrace{\left(\mathbf{H}_{\mathbf{bb}} - \mathbf{H}_{\mathbf{b}^*\mathbf{b}}\mathbf{H}_{\mathbf{b}^*\mathbf{b}^*}^{-1}\mathbf{H}_{\mathbf{bb}^*}\right)^{-1}}_{\tilde{\mathbf{H}}_{\mathbf{bb}}} \underbrace{\left[\mathbf{H}_{\mathbf{b}^*\mathbf{b}}\mathbf{H}_{\mathbf{b}^*\mathbf{b}^*}^{-1}\nabla_{\mathbf{b}^*}(S_{tr}(\mathbf{b}_i))^H - \nabla_{\mathbf{b}}(S_{tr}(\mathbf{b}_i))^H\right]}_{\tilde{\nabla}_{\mathbf{b}}(S_{tr}(\mathbf{b}_i))^H} \tag{26}$$

where the gradients are defined as

$$\nabla_{\mathbf{b}}(S_{tr}(\mathbf{b})) = \frac{\partial S_{tr}(\mathbf{b})}{\partial \mathbf{b}} \qquad \nabla_{\mathbf{b}^*}(S_{tr}(\mathbf{b})) = \frac{\partial S_{tr}(\mathbf{b})}{\partial \mathbf{b}^*} \tag{27}$$

and the Hessian matrices as

$$\mathbf{H}_{\mathbf{bb}} = \frac{\partial}{\partial \mathbf{b}}\left(\frac{\partial S_{tr}(\mathbf{b})}{\partial \mathbf{b}}\right)^H \qquad \mathbf{H}_{\mathbf{b}^*\mathbf{b}} = \frac{\partial}{\partial \mathbf{b}^*}\left(\frac{\partial S_{tr}(\mathbf{b})}{\partial \mathbf{b}}\right)^H$$
$$\mathbf{H}_{\mathbf{bb}^*} = \frac{\partial}{\partial \mathbf{b}}\left(\frac{\partial S_{tr}(\mathbf{b})}{\partial \mathbf{b}^*}\right)^H \qquad \mathbf{H}_{\mathbf{b}^*\mathbf{b}^*} = \frac{\partial}{\partial \mathbf{b}^*}\left(\frac{\partial S_{tr}(\mathbf{b})}{\partial \mathbf{b}^*}\right)^H \tag{28}$$

The principal iterative processing is illustrated in Fig. 6. Notice that for any given DPD order and PA model type (memoryless or PH), the needed derivatives can be precalculated analytically, and then simply evaluated with the PA model parameters at hand and the current DPD coefficient values. Several examples can be easily obtained through the PSD expressions in (23) and (24) for which the first and second derivatives applied to b_3, b_5 and b_7 can be easily analytically calculated, although not shown here due to space constraints. Thus, the same elementary PSD components, whose computations are illustrated in Fig. 5, can be directly deployed to obtain the needed PSD derivatives, together with precalculated analytical expressions for the coefficient derivatives with respect to DPD parameters, being then simply evaluated at the current parameter vector $\mathbf{b}_i$.

In general, if the initial estimate $\mathbf{b}_0$ is reasonably close to the root, the Newton-Raphson Method converges very fast, usually within 3-4 iterations. It should be noted that this is only an indicative number. In this study, we naturally use the direct-modeling inverse, or generally P-th order inverse, as the starting point $\mathbf{b}_0$, as direct identification is anyway needed for the PSD gradient evaluations.

In conclusion, the overall processing can be summarized as follows:

- Initially switching the DPD processing off, transmit a sequence of length N_{bl} samples through the PA and through the observation/feedback receiver in order to identify a direct model for the PA. Due to linear-in-parameters nature of the considered PA models, ordinary least-squares (LS) model fitting over the block of N_{bl} samples can be used. The original transmit sequence can simultaneously be also fed to the PSD evaluation block in order to evaluate the needed correlations and the corresponding elementary PSD components.
- Using the obtained direct PA model, calculate the P-th order inverse DPD as the starting point $\mathbf{b}_0$.
- Using the identified PA parameters and current DPD parameter vector $\mathbf{b}_i$, evaluate $S_{tr}(b)$, the gradients and Hessians and update the DPD parameter vector $\mathbf{b}_i$ according to the Newton-Rhapson iteration.
- Iterate until convergence.
- Plug in and deploy the converged DPD coefficients in the actual data transmission.

Notice that if there are any additional constraints, such as EVM or ACLR, they can be directly included into the optimization steps by simply evaluating the output PSD at appropriate frequencies with current updated coefficients and checking if the constraints are still met. If yes, the iterations can continue, while if not, then one falls back to the previous coefficients.

V. Complexity Issues

In this section, a quantitative complexity analysis of the proposed DPD solution is presented. The primary metric used to quantify the complexity is the number of floating point operations (FLOPs) [45]. The overall DPD processing can be divided into three stages: The initial parameter estimation stage, the real-time DPD processing stage, and the parameter optimization and adaptation stage. In the following analysis, the non-linearity orders of the power amplifier and the DPD are assumed to be five and seven, respectively, in order to be consistent with the results presented in the other sections.

In the initial parameter estimation stage, a direct least-squares parallel Hammerstein (PH) identification of the PA is computed, followed by calculating the *P*th order inverse DPD coefficients. Assuming a block size of N_{bl} samples and fifth order non-linearity with three memory taps per non-linearity order, as a practical example, the number of FLOPs required by this stage is approximately $(\mathbf{81} \times N_{\mathbf{bl}} + \mathbf{243})$ for the whole block of N_{bl} samples as shown in Table I [46].

The DPD real-time running stage can be divided into two parts: The first part is the basis function generation that requires 9 FLOPs per sample [45], and the second part is the application of the estimated DPD coefficients on the generated basis functions resulting in 19 additional FLOPs per sample. Thus the total number of FLOPs in this stage is **28** FLOPs *per sample*. This stage is the most critical from the point of view of timing, hardware resources, and power consumption, especially in mobile devices, and it is *identical to classical DPD solutions*. Taking into consideration the performance gain when using our optimized coefficients, this yields a performance advantage over existing methods for any given run-time complexity, or alternatively, run-time complexity reduction for a given linearization performance.

Finally, the computations associated with the parameter optimization and adaptation stage can be divided into three main parts. The first part is the *Basis Functions Generation*, which is then used for the *PSD Evaluation* part. In the basis functions generation part, the first three sets of basis functions $x(n)|x(n)|^2$, $x(n)|x(n)|^4$ and $x(n)|x(n)|^6$ are already evaluated at every sample in the real-time DPD stage. Thus, all we need to do is to buffer N_{bl} samples from those basis functions whenever the DPD parameter optimization is needed and reuse them, while only the ninth and eleventh order basis functions need to be calculated. Finally, the last part is the *Newton Update*, where the Newton optimization coefficient update is performed. Table I summarizes the number of FLOPs required by each of these parts for a block of N_{bl} samples based on the implementation structure proposed in section IV.

To summarize the overall computational complexity required by the proposed DPD, we divide the computations into block-based and sample-based computations. The block-based computations required are in the initial acquisition and the parameter optimization and adaptation DPD stages. Using $N_{bl} = 100k$ as an example block size, the approximate number of FLOPs required in the parameter estimation stage is $(81 \times 100k + 243)$ or roughly **8.1** MFLOPs, and in the parameter optimization the corresponding number is $(44 \times 100k + 1.6k)$ or roughly **4.5** MFLOPs. These FLOPs are not computed on a frequent basis (only in the order of msecs) compared to the system sampling time which is in the order of μsecs. On the other hand, the sample-based computations in the real-time running DPD section require **28** FLOPs per sample. With an example real-time DPD processing rate of 100 MHz, this is equivalent to 2.8 GFLOPs per second. While this is already a substantial amount of processing, it is still clearly within the processing power of state-of-the-art computing platforms even in mobile devices [26].

TABLE I
Approximate number of FLOPs required in the block processing DPD stages assuming 5^{th} order non-linearity and 3 memory taps for the power amplifier, and 7^{th} order non-linearity for the DPD

Block Processing Stage	Number of FLOPs per N_{bl} samples
Initial Parameter Estimation	$(81 \times N_{bl} + 243)$
DPD Parameter Optimization	
Basis Functions Generation	$(4 \times N_{bl})$
PSD Evaluation	$(40 \times N_{bl} + 178)$
Newton Update	$1.4k$
Total Number of FLOPs	$(44 \times N_{bl} + 1.6k)$

VI. Simulation and Measurement Results

In this section, comprehensive simulation results with both memoryless and memory PA models, as well as measurements with a real commercial LTE-A mobile terminal PA with 27 dB gain and 1dB compression point of 28.5 dBm, are presented. In both simulations as well as in the measurements, the direct PA model (either memoryless or parallel Hammerstein) is first estimated via Least-Squares, as described above, and then used in the proposed DPD optimization processing. The scheme is demonstrated with different communications waveforms, including classical single-carrier 16-QAM and dual-carrier DFT-spread OFDMA LTE-A uplink waveforms. In general, the target optimization frequencies of the unwanted emission minimization cover both third-order and fifth-order regrowth or intermodulation regions, as elaborated in more details below. In general, the results are quantified using EVM, ACLR and SRR, as defined in Section II, or using IM3R and IM5R when applicable (multi-cluster and carrier aggregation transmission scenarios). Notice that the ACLR can be calculated and reported separately for left (L) and right (R) adjacent channels.

A. Simulation Results

In this sub-section, three kinds of communication waveforms are used to test and demonstrate the proposed DPD concept through simulations. The first example uses a 16-QAM single-carrier signal with root-raised cosine pulse, 22% roll-off. The second example is a multi-cluster LTE-Advanced UL transmission scenario with 1 MHz per cluster bandwidth allocation and 6 MHz cluster separation. This kind of multi-cluster uplink transmission is supported in 3GPP LTE-Advanced starting from Release'11 [34], and implies non-contiguous use of spectrum, from an individual mobile terminal perspective, inside one LTE carrier. The third example uses LTE-Advanced

UL non-contiguous intra-band carrier aggregation with asymmetric resource block allocation per component carrier, and with 15 MHz spacing between the component carriers. Non-contiguous intra-band carrier aggregation is supported in LTE-Advanced starting from Release'12 [34].

Following the presentation and developments in the previous sections, a 7th order memoryless pre-distorter is deployed, while both memoryless and Parallel-Hammerstein type memory-based PA models of 5th order are tested. A conventional 7 th order inverse solution, obtained from initial direct learning stage with 100k data samples, is always used as the starting point for the Newton optimization algorithm. In these simulations, the proposed method is deployed to reduce the emissions that fall within either the 3rd or 5th order regrowth or intermodulation region.

1) 5MHz 16-QAM Single-Carrier Example and memoryless PA: The target in this example is to optimize the DPD coefficients b_3, b_5 and b_7 such that the emission power at the right adjacent channel is minimized. To reduce the processing and optimization complexity, we keep here b_3 unchanged and only optimize b_5 and b_7. Example illustration of the convergence of the coefficients, over Newton iterations, is shown in Fig. 7 where it can be seen that 3-4 iterations are enough to reach convergence. Table II quantifies the results of the optimization along with the conventional 7th order inverse DPD by showing and comparing the ACLR, SRR and EVM values for each case. The ACLR is evaluated over the adjacent channel, with measurement bandwidth equal to the wanted channel bandwidth, while the SRR is evaluated over the second adjacent channel, with measurement bandwidth again equal to the wanted channel bandwidth. As is evident from the results, since the optimization frequency is at the center of the right adjacent channel, the biggest gains compared to conventional 7th order inverse, in the order of 5 dB, are obtained for ACLR-R.

TABLE II
VALUES OF ACLR AND SRR USING QUASI-MEMORYLESS MODELS AND 5 MHZ 16-QAM BASEBAND WAVEFORM.

	No DPD	Conventional DPD	AC Optimized DPD b_5, b_7
ACLR-R [dBc]	46.3224	57.8110	62.1449
ACLR-L [dBc]	46.2949	57.6456	61.7537
SRR-R [dBc]	65.2404	68.2239	69.1738
SRR-L [dBc]	65.1427	68.0307	68.9642
EVM [%]	0.8853	0.1968	0.0388

2) 10MHz 16-QAM Single-Carrier Example and Parallel-Hammerstein PA: We move next to a more realistic scenario where a 5th order parallel Hammerstein PA Model is deployed and the signal is 10 MHz 16-QAM single-carrier waveform. In this example, the DPD optimization target frequency is set first to the center of the right adjacent channel, and then in the second optimization scenario to the center of the second right adjacent channel being thus already at the spurious region. In both cases, b_5 and b_7 are again jointly optimized. Fig. 8 shows example PA output spectra with different optimization target frequencies. It can again be clearly seen that the proposed DPD approach indeed tunes most of the available unwanted emission suppression to the defined target frequency, in different scenarios. Also, due to the memory in the PA, the difference between left and right adjacent and second adjacent channels is even more clear, than in the previous memoryless PA example. For a more quantitative analysis and elaboration, Table III shows the obtained ACLR and SRR values in different predistortion scenarios. Again, the ACLR is evaluated over the adjacent channel(s), while the SRR is evaluated over the second adjacent channel(s), and the measurement bandwidths are again equal to the wanted channel bandwidth. The increased EVM numbers, compared to previous memoryless example case, are due to more nonlinear PA deployment and increased linear distortion introduced by the Parallel Hammerstein PA.

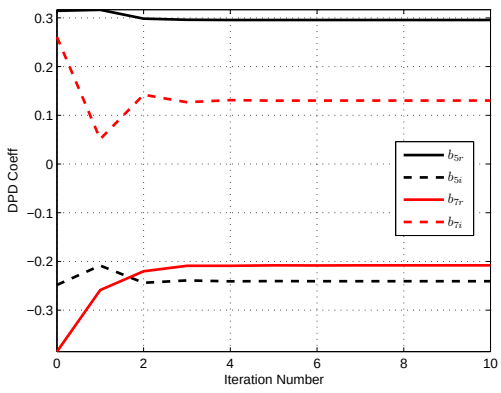

Fig. 7. Convergence of the adjacent channel optimized DPD coefficients b_5 and b_7 for a single carrier 16-QAM signal with memoryless DPD processing.

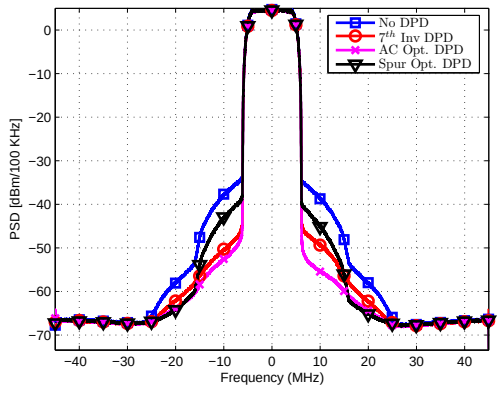

Fig. 8. Baseband equivalent power spectra of 10 MHz 16-QAM single-carrier signals with root-raised cosine pulse and 22% roll-off, with different DPD solutions and parallel Hammerstein PA model. Four cases are shown; without any DPD, using a conventional 7-th order inverse DPD, right adjacent channel (AC) optimized DPD and second right adjacent channel (Spur) optimized DPD.

TABLE III
VALUES OF ACLR AND SRR USING PARALLEL HAMMERSTEIN PA MODEL, QUASI-MEMORYLESS DPD MODEL, AND 10 MHZ 16-QAM BASEBAND WAVEFORM.

	No DPD	Conventional DPD	AC Optimized DPD	Spur Optimized DPD
ACLR-R [dBc]	44.5309	55.0876	60.9337	50.5666
ACLR-L [dBc]	43.8566	56.0416	58.1250	48.8356
SRR-R [dBc]	63.9644	67.9649	70.2154	71.0010
SRR-L [dBc]	63.8390	67.7376	69.6208	69.7659
EVM [%]	6.4619	6.3556	6.3484	6.3783

3) Multi-cluster and Carrier Aggregation Examples: For the multi-cluster and carrier aggregation uplink transmission scenarios in LTE-Advanced, the most critical nonlinear distortion is the related to intermodulation between the non-contiguous spectral allocations (i.e., the different clusters in multicluster transmission and the different component carriers in carrier aggregation) [33]. These inter-modulation products can easily violate the general spurious emission limits, or even desensitize the own receiver in FDD mode. Thus, in these example scenarios, it becomes even more vital to be able to optimize the DPD coefficients at the specific target frequencies. In this example, we thus seek to optimize the two DPD coefficients b_5 and b_7 to minimize the emissions either at the third-order or fifth-order intermodulation frequencies between the allocated non-contiguous spectral resources, referred to as IM3 and IM5, and quantified using the IM3R and IM5R reduction ratios defined in Section II. To be exact, the optimization/target frequency is set to the middle of the right-hand-side IM3 or IM5 region, respectively.

For the multi-cluster scenario, the obtained reduction in the IM3 and IM5 powers in both the left (L) and right (R) sides of the fundamental spectrum are shown in Table IV, along with the EVM values, when using a parallel Hammerstein PA Model. A corresponding example spectrum is shown in Fig. 9. As for the carrier aggregation scenario, two component carriers are used with 5 MHz and 2 MHz component carrier bandwidth allocations, respectively, and a 15 MHz separation between the component carriers. The resulting example spectra are shown in Fig. 10. It can clearly be seen that the reduction in the right IM3 band is substantially better in case of the IM3 optimized DPD compared to the conventional DPD, and the same applies for the right IM5 band, the extra gains from the optimization being in the order of 4-7 dB.

TABLE IV
VALUES OF IM3R, IM5R AND EVM USING PARALLEL HAMMERSTEIN PA MODEL, QUASI-MEMORYLESS DPD PROCESSING, AND MULTI-CLUSTER SC-FDMA BASEBAND WAVEFORM WITH QPSK DATA MODULATION.

	No DPD	Conventional DPD	IM3 Optimized DPD	IM5 Optimized DPD
IM3R-R [dBc]	41.1885	49.8385	56.7854	54.7730
IM3R-L [dBc]	40.4529	51.1442	56.0137	50.5793
IM5R-R [dBc]	54.9336	58.3671	61.6174	62.2458
IM5R-L [dBc]	55.0491	58.6405	62.1339	62.2519
EVM [%]	1.3245	1.0450	1.0054	1.0284

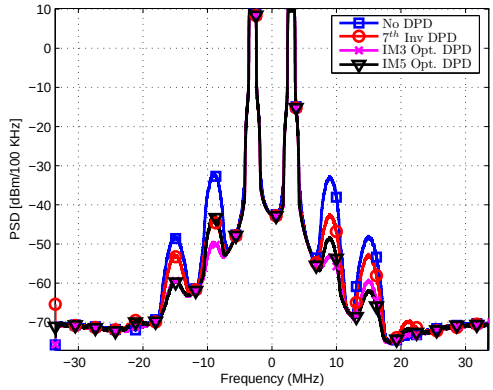

Fig. 9. Baseband equivalent power spectra of LTE-A UL signals with different DPD solutions, using multi-cluster SC-FDMA transmission, QPSK data modulation, and Parallel Hammerstein PA model. Four cases are compared; without any DPD, using a conventional DPD, and proposed IM3 and IM5 optimized DPDs.

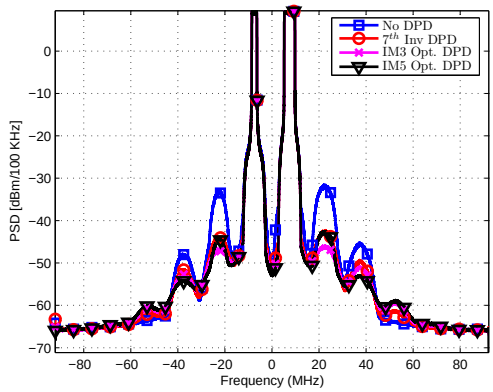

Fig. 10. Baseband equivalent power spectra of LTE-A UL carrier-aggregated signals with SC-FDMA transmission and QPSK modulation at the output of a parallel Hammerstein PA. Four cases are compared; without any DPD, using a conventional DPD, and proposed IM3 and IM5 optimized DPDs.

B. RF Measurements

In order to further elaborate and demonstrate the operation of the proposed DPD solution, it has been tested through actual RF measurements using a commercial LTE-Advanced mobile terminal power amplifier together with a vector signal generator and analyzer, and computer based processing of the measured radio signals. The overall measurement setup is shown in Fig. 11 where the signal is first generated locally on the computer, then transferred to the vector signal generator to perform I/Q modulation. The RF center-frequency used in these measurements is 1.89 GHz corresponding to LTE band 25. The generator output is then connected to the input port of the power amplifier whose output port is thereon connected directly to the vector signal analyzer, implementing

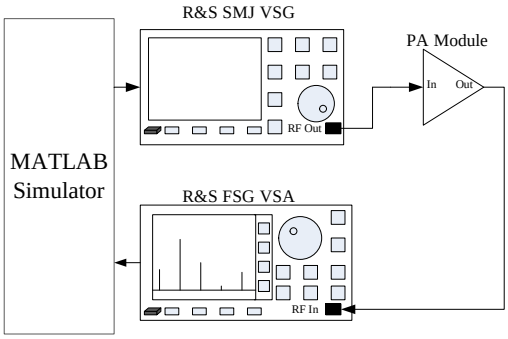

Fig. 11. Measurement Setup used in the Lab to test the proposed DPD solution against the conventional 7^{th} order inverse DPD solution. Digital signal processing is done in Matlab, while the vector signal generator and analyzer perform the RF processing to and from the PA.

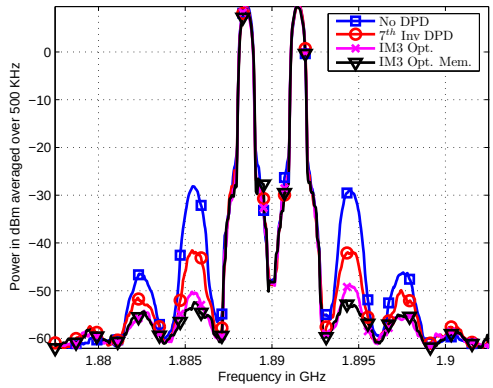

Fig. 12. RF power spectra of measured LTE-A UL signals with multi-cluster SC-FDMA transmission and QPSK data modulation at the output of a commercial mobile PA in the lab. Four cases are compared; without any DPD, using a conventional 7-th order inverse DPD, and IM3-optimized proposed DPD with both memoryless and PH-memory based PA identification in the optimization. Tx power is 15.5 dBm.

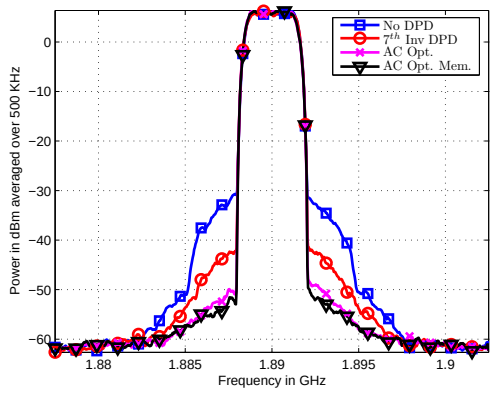

Fig. 13. RF power spectra of a 16-QAM single-carrier signal with root-raised cosine pulse, 22% roll-off at the output of a commercial mobile PA in the Lab. Four cases are compared; without any DPD, using a conventional 7-th order inverse DPD, and IM3/ACLR-optimized proposed DPD with both memoryless PA identification and PH-memory based PA identification in the optimization. Tx power is 16.5 dBm.

the observation receiver for direct model identification as well as measuring the true PA output spectrum, without and with DPD processing.

As an initial step, both memoryless and Parallel Hammerstein based direct models are identified, using least squares model fitting of the measured PA output (downconverted and quantized by the vector signal analyzer) to the original baseband data. Again, 100k samples are used in the initial identification. Then, the identified memoryless PA model is used to obtain a 7th order inverse DPD solution, to be used again as a starting point for the Newton optimization. Next, both the memoryless as well as PH memory-based identified PA models as well as the original baseband data samples are used in the digital processing, to evaluate the necessary PSD derivatives in the iterative DPD optimization processing.

As a first example, we deploy multi-cluster SC-FDMA signal with QPSK data modulation, 0.5 MHz cluster bandwidth allocation and 3 MHz separation between the clusters. The target optimization frequency is set to right IM3 frequency, and the resulting spectra are shown in Fig. 12, including DPD optimization both with memoryless and with memory-based identified direct PA models. Clearly the proposed optimization solution can provide around 8 dB gain at right IM3 frequency, already with purely memoryless optimization, while then incorporating the identified PA model with memory brings in this example an additional 3-4 dB gain. Another measured RF spectrum is shown in Fig. 13 using a 16-QAM single-carrier signal with 3 MHz BW, and the optimization frequency is set to the center of the right adjacent channel. In both RF measurement examples, it can clearly be seen that the proposed DPD solutions clearly outperform the conventional reference solution. While these first measurement studies give clear indication of the applicability of the proposed DPD concept, our future work will be directed to carrying out more extensive measurement experimentations.

VII. Conclusions

This article proposed a novel digital predistortion (DPD) approach, specifically designed and tailored to reduce power amplifier (PA) out-of-band or spurious emissions at any specified frequency in the PA output spectrum. The proposed solution relies on analyzing the power spectral density of the PA output signal, while assuming very simple memoryless DPD processing. The mathematical derivation procedures of the proposed DPD solution were presented for quasi-memoryless and parallel Hammerstein nonlinear PA models. Building on a one-shot direct model identification, through ordinary least-squares model fitting, as a starting point, the final optimized DPD coefficients are obtained iteratively such that the unwanted emission at the target frequency is minimized. Simulation results related to examining the proposed processing with

both single carrier and multicarrier/carrier aggregation type transmit waveforms were reported and compared in terms of different emissions and inband waveform quality. Furthermore, example RF measurements with commercial LTE-Advanced mobile terminal power amplifier were also reported. Both the simulation and measurement results show that the proposed method can effectively reduce the emissions at and around the pre-specified frequency, with both single and dual-carrier transmissions. The proposed DPD solution may find important applications for example in non-contiguous multi-carrier or multi-band transmitters, where the intermodulation spurs may easily be overlapping with the device's own receiver band, or generally violating the spurious emission limits. Another application is cognitive radio devices, in situations when the PA emissions would otherwise interfere with primary user transmissions. In general, the proposed approach and reported results can be seen as a first initiative towards frequency-optimized type of predistortion, opposed to classical full bandwidth linearization.

REFERENCES

[1] G. Fettweis, M. Löhning, D. Petrovic, M. Windisch, P. Zillmann, and W. Rave, "Dirty RF: a new paradigm," *International Journal of Wireless Information Networks*, vol. 14, no. 2, pp. 133–148, 2007.

[2] S. C. Cripps, *RF Power Amplifiers for Wireless Communications*. Artech House, Inc., 2006.

[3] G. Zhou and J. Kenney, "Predicting spectral regrowth of nonlinear power amplifiers," *IEEE Transactions on Communications*, vol. 50, no. 5, pp. 718–722, May 2002.

[4] "Radio transmission and reception (release 9)., 3GPP TS 36.101 version 9.3.0 3GPP. 3rd generation partnership project."

[5] "IEEE standard for information technology– local and metropolitan area networks– specific requirements– part 22: Cognitive wireless ran medium access control (MAC) and physical layer (PHY) specifications: Policies and procedures for operation in the TV bands," *IEEE Std 802.22-2011*, pp. 1–680, July 2011.

[6] A. Flores, R. Guerra, E. Knightly, P. Ecclesine, and S. Pandey, "IEEE 802.11af: a standard for TV white space spectrum sharing," *IEEE Communications Magazine*, vol. 51, no. 10, pp. 92–100, October 2013.

[7] A. Wyglinski, "Physical layer loading algorithms for indoor wireless multicarrier systems," Ph.D. dissertation, McGill University, 2004.

[8] P. Chan, E. Lo, R. Wang, E. Au, V. Lau, R. Cheng, W.-H. Mow, R. Murch, and K. Letaief, "The evolution path of 4G networks: FDD or TDD?" *IEEE Communications Magazine*, vol. 44, no. 12, pp. 42–50, Dec 2006.

[9] Ericsson and ST-Ericsson, "R4_123797, UE reference sensitivity requirement with two UL carriers." [Online]. Available: http://www.3gpp.org/ftp/tsg_ran/WG4_Radio/TSGR4_64/Docs

[10] A. Kiayani, L. Anttila, and M. Valkama, "Digital suppression of power amplifier spurious emissions at receiver band in FDD transceivers," *IEEE Signal Processing Letters*, vol. 21, no. 1, pp. 69–73, Jan 2014.

[11] M. Omer, R. Rimini, P. Heidmann, and J. Kenney, "A compensation scheme to allow full duplex operation in the presence of highly nonlinear microwave components for 4G systems," in *Microwave Symposium Digest (MTT), 2011 IEEE MTT-S International*, June 2011, pp. 1–4.

[12] M. Majidi, A. Mohammadi, and A. Abdipour, "Analysis of the power amplifier nonlinearity on the power allocation in cognitive radio networks," *IEEE Transactions on Communications*, vol. 62, no. 2, pp. 467–477, February 2014.

[13] A. Goldsmith, S. Jafar, I. Maric, and S. Srinivasa, "Breaking spectrum gridlock with cognitive radios: An information theoretic perspective," *Proceedings of the IEEE*, vol. 97, no. 5, pp. 894–914, May 2009.

[14] A. Katz, "Linearization: Reducing distortion in power amplifiers," *IEEE Microwave Magazine*, vol. 2, no. 4, pp. 37–49, 2001.

[15] G. Breed, "An overview of common techniques for power amplifier linearization," *High Frequency Electronics*, pp. 44–46, 2010.

[16] J. K. Cavers, "Amplifier linearization by adaptive predistortion," sep 17 1991, US Patent 5,049,832.

[17] A. D'Andrea, V. Lottici, and R. Reggiannini, "RF power amplifier linearization through amplitude and phase predistortion," *IEEE Transactions on Communications*, vol. 44, no. 11, pp. 1477–1484, Nov 1996.

[18] L. Anttila, P. Händel, and M. Valkama, "Joint mitigation of power amplifier and I/Q modulator impairments in broadband direct-conversion transmitters," *IEEE Transactions on Microwave Theory and Techniques*, vol. 58, no. 4, pp. 730–739, April 2010.

[19] H. Yang, P. F. M. Smulders, and E. Fledderus, "Comparison of single- and multi-carrier block transmissions under the effect of nonlinear HPA," in *2007 14th IEEE Symposium on Communications and Vehicular Technology in the Benelux*, Nov 2007, pp. 1–7.

[20] Z. Fu, L. Anttila, M. Valkama, and A. M. Wyglinski, "Digital predistortion of power amplifier impairments in spectrally agile transmissions," in *2012 35th IEEE Sarnoff Symposium (SARNOFF)*, May 2012, pp. 1–6.

[21] Y. Ma, Y. Yamao, Y. Akaiwa, and K. Ishibashi, "Wideband digital predistortion using spectral extrapolation of band-limited feedback signal," *IEEE Transactions on Circuits and Systems I: Regular Papers*, vol. PP, no. 99, pp. 1–10, 2014.

[22] C. Yu, L. Guan, E. Zhu, and A. Zhu, "Band-limited volterra series-based digital predistortion for wideband RF power amplifiers," *IEEE Transactions on Microwave Theory and Techniques*, vol. 60, no. 12, pp. 4198–4208, Dec 2012.

[23] S. Zhang, W. Chen, F. Ghannouchi, and Y. Chen, "An iterative pruning of 2-D digital predistortion model based on normalized polynomial terms," in *2013 IEEE MTT-S International Microwave Symposium Digest (IMS)*, June 2013, pp. 1–4.

[24] D. Morgan, Z. Ma, J. Kim, M. Zierdt, and J. Pastalan, "A generalized memory polynomial model for digital predistortion of RF power amplifiers," *IEEE Transactions on Signal Processing*, vol. 54, no. 10, pp. 3852–3860, Oct 2006.

[25] T. Gotthans, G. Baudoin, and A. Mbaye, "Comparison of modeling techniques for power amplifiers," in *Radioelektronika (RADIOELEKTRONIKA), 2013 23rd International Conference*, April 2013, pp. 232–235.

[26] M. Abdelaziz, L. Anttila, J. Boutellier, T. Lähteensuo, X. Lu, J. R. Cavallaro, S. S. Bhattacharyya, M. Juntti, and M. Valkama, "Mobile transmitter digital predistortion: Feasibility analysis, algorithms and design exploration," in *2013 Conference Record of the Forty Seventh Asilomar Conference on Signals, Systems and Computers (ASILOMAR)*, Nov 2013.

[27] P. Roblin, S. K. Myoung, D. Chaillot, Y.-G. Kim, A. Fathimulla, J. Strahler, and S. Bibyk, "Frequency-selective predistortion linearization of RF power amplifiers," *IEEE Transactions on Microwave Theory and Techniques*, vol. 56, no. 1, pp. 65–76, Jan 2008.

[28] S. Bassam, F. Ghannouchi, and M. Helaoui, "2-D Digital Predistortion (2-D-DPD) architecture for concurrent dual-band transmitters," *IEEE Trans. Microw. Theory Tech.*, vol. 59, pp. 2547–2553, Oct. 2011.

[29] M. Abdelaziz, L. Anttila, A. Mohammadi, F. Ghannouchi, and M. Valkama, "Reduced-complexity power amplifier linearization for carrier aggregation mobile transceivers," in *IEEE International Conference on Acoustics, Speech, and Signal Processing (ICASSP'14)*, Florence, Italy, May 2014.

[30] H. Jiang and P. Wilford, "Digital predistortion for power amplifiers using separable functions," *IEEE Transactions on Signal Processing*, vol. 58, no. 8, pp. 4121–4130, Aug 2010.

[31] W. Pan, Y. Liu, and Y. Tang, "A predistortion algorithm based on accurately solving the reverse function of memory polynomial model," *IEEE Wireless Communications Letters*, vol. 1, no. 4, pp. 384–387, August 2012.

[32] *International Telecommunication Union Radio Communication Sector, Recommendation ITU-R SM.329-12 Unwanted emissions in the spurious domain. http://www.itu.int/dms_pubrec/itur/rec/sm/R-REC-SM.329-12-201209-I!!PDF-E.pdf*, Std.

[33] E. Dahlman, S. Parkvall, and J. Skold, *4G LTE/LTE-Advanced for Mobile Broadband.* Elsevier Ltd., 2011.

[34] *3GPP Evolved Universal Terrestrial Radio Access (E-UTRA); User Equipment (UE) radio transmission and reception. http://www.3gpp.org/ftp/Specs/html-info/36101.htm*, Std.

[35] *3GPP TS 34.121 Terminal conformance specification, Radio transmission and reception (FDD)*, Std.

[36] A. Yonis, M. Abdullah, and M. Ghanim, "LTE-FDD and LTE-TDD for cellular communications," *Proc. Prog. Electromagn. Res. Sym*, pp. 1467–1471, 2012.

[37] C. Chatfield, *The analysis of time series: an introduction*. CRC press, 2013.

[38] L. Ding, G. Zhou, D. Morgan, Z. Ma, J. Kenney, J. Kim, and C. Giardina, "A robust digital baseband predistorter constructed using memory polynomials," *IEEE Transactions on Communications*, vol. 52, no. 1, pp. 159–165, Jan 2004.

[39] M. Isaksson, D. Wisell, and D. Ronnow, "A comparative analysis of behavioral models for RF power amplifiers," *IEEE Transactions on Microwave Theory and Techniques*, vol. 54, no. 1, pp. 348–359, Jan 2006.

[40] H. Ku and J. Kenney, "Behavioral modeling of nonlinear RF power amplifiers considering memory effects," *IEEE Transactions on Microwave Theory and Techniques*, vol. 51, no. 12, pp. 2495–2504, Dec 2003.

[41] A. V. Oppenheim and R. W. Schafer, *Discrete-Time Signal Processing, Third Edition*. Prentice Hall Signal Processing, 2009.

[42] M. Bartholomew-Biggs, *Nonlinear optimization with engineering applications*. Springer, 2008, vol. 19.

[43] K. Kreutz-Delgado, "The complex gradient operator and the CR-calculus," 2009. [Online]. Available: http://arxiv.org/abs/0906.4835

[44] P. J. Schreier and L. L. Scharf, *Statistical Signal Processing of Complex-Valued Data*. Cambridge, UK: Cambridge University Press, 2010.

[45] A. Tehrani, H. Cao, S. Afsardoost, T. Eriksson, M. Isaksson, and C. Fager, "A comparative analysis of the complexity/accuracy tradeoff in power amplifier behavioral models," *IEEE Transactions on Microwave Theory and Techniques*, vol. 58, no. 6, pp. 1510–1520, June 2010.

[46] G. H. Golub and C. F. Loan, *Matrix Computations, Third Edition*. Johns Hopkins University Press, 1996.

Dr. Zhu Fu is a senior engineer working at Qualcomm, San Jose, CA, USA. Dr. Fu received her Bachelor's and Master's degrees from Beijing Institute of Technology, and her Ph.D. degree from Worcester Polytechnic Institute (WPI) in May 2014, all in Electrical Engineering. Dr. Fu's research interests include Digital Pre-Distortion, Spectrally Agile Waveforms and Radio Frequency (RF) Front End Characterization.

Lauri Anttila (S'06, M'11) received his M.Sc. degree and D.Sc. (Tech) degree (with honors) from Tampere University of Technology (TUT), Tampere, Finland, in 2004 and 2011. He has published over 40 articles in international peer-reviewed journals and conferences, as well as two book chapters. Currently, he is a postdoctoral Research Fellow at the Department of Electronics and Communications Engineering at TUT. His research interests include statistical and adaptive signal processing for communications, digital front-end signal processing in flexible radio transceivers, power-efficient transmitter structures, and full-duplex radio systems.

Mahmoud Abdelaziz received his B.Sc. degree (with honors) and M.Sc. degree in Electronics and Electrical Communications Engineering from Cairo University, Egypt, in 2006 and 2011. He is currently pursuing the Doctoral degree at Tampere University of Technology, Finland where he works as a researcher with the Department of Electronics and Communications. From 2007 to 2012 he has been working as a communication systems and signal processing engineer at Newport Media Inc. (currently acquired by Atmel), as well as other companies in the wireless industry. His research interests include statistical and adaptive signal processing in flexible radio transceivers, wideband digital pre-distortion, and cognitive radio systems.

Mikko Valkama was born in Pirkkala, Finland, on November 27, 1975. He received the M.Sc. and Ph.D. Degrees (both with honors) in electrical engineering (EE) from Tampere University of Technology (TUT), Finland, in 2000 and 2001, respectively. In 2002, he received the Best Ph.D. Thesis -award by the Finnish Academy of Science and Letters for his dissertation entitled "Advanced I/Q signal processing for wideband receivers: Models and algorithms". In 2003, he was working as a visiting researcher with the Communications Systems and Signal Processing Institute at SDSU, San Diego, CA. Currently, he is a Full Professor and Department Vice-Head at the Department of Electronics and Communications Engineering at TUT, Finland. He has been involved in organizing conferences, like the IEEE SPAWC'07 (Publications Chair) held in Helsinki, Finland. His general research interests include communications signal processing, estimation and detection techniques, signal processing algorithms for software defined flexible radios, cognitive radio, full-duplex radio, radio localization, 5G mobile cellular radio, digital transmission techniques such as different variants of multicarrier modulation methods and OFDM, and radio resource management for ad-hoc and mobile networks.

Dr. Alexander M. Wyglinski (S'99, M'05, SM'11) is an Associate Professor of Electrical and Computer Engineering at Worcester Polytechnic Institute (WPI), Worcester, MA, USA and Director of the Wireless Innovation Laboratory (WI Lab). Dr. Wyglinski received his B.Eng. and Ph.D. degrees in 1999 and 2005 from McGill University, and his M.Sc.(Eng.) degree from Queens University in Kingston in 2000, all in Electrical Engineering. Throughout his academic career, Dr. Wyglinski has published over 35 journal papers, over 75 conference papers, 9 book chapters, and two textbooks. Dr. Wyglinskis current research activities include wireless communications, cognitive radio, software-defined radio, dynamic spectrum access, spectrum measurement and characterization, electromagnetic security, wireless system optimization and adaptation, and cyber physical systems. He is currently being or has been sponsored by organizations such as the Defense Advanced Research Projects Agency (DARPA), the Naval Research Laboratory (NRL), the Office of Naval Research (ONR), the Air Force Research Laboratory (AFRL) - Space Vehicles Directorate, The MathWorks, Toyota InfoTechnology Center U.S.A., and the National Science Foundation. Dr. Wyglinski is a Senior Member of the IEEE, as well as a member of Sigma Xi, Eta Kappa Nu, and the ASEE.

Publication 5

M. Abdelaziz, L. Anttila, A. Mohammadi, F. Ghannouchi, and M. Valkama, "Reduced-complexity power amplifier linearization for carrier aggregation mobile transceivers," in *Proc. IEEE International Conference on Acoustics, Speech and Signal Processing (ICASSP)*, Florence, 2014, pp. 3908-3912.

REDUCED-COMPLEXITY POWER AMPLIFIER LINEARIZATION FOR CARRIER AGGREGATION MOBILE TRANSCEIVERS

Mahmoud Abdelaziz[1], Lauri Anttila[1], Abbas Mohammadi[2], Fadhel Ghannouchi[3] and Mikko Valkama[1]

[1]Department of Electronics and Communications Engineering, Tampere University of Technology, Tampere, Finland
[2]Department of Electrical Engineering, Amirkabir University of Technology, Tehran, Iran
[3]iRadio Lab, Department of Electrical and Computer Engineering, University of Calgary, Alberta, Canada
E-mails: mahmoud.abdelaziz@tut.fi, lauri.anttila@tut.fi, abm125@aut.ac.ir, fghannou@ucalgary.ca, mikko.e.valkama@tut.fi

ABSTRACT

Spurious intermodulation components have recently been identified as a major problem in carrier aggregation mobile transmitters with multi-band power amplifiers (PAs). This article presents novel adaptive digital predistortion (DPD) solutions with reduced complexity in both the predistortion processing and the feedback paths, to tackle this problem. Compared with conventional DPDs which aim to linearize the whole transmit bandwidth, the proposed technique aims at mitigating only those intermodulation components which are most problematic from the spurious emission limit perspective. The proposed technique is verified with extensive simulations in various 3GPP LTE-A carrier aggregation scenarios, showing that the intermodulation spurs can be efficiently mitigated below the spurious emission limit with relatively small back-offs.

Index Terms— Carrier aggregation, power amplifier, intermodulation, digital predistortion, LTE-Advanced, mobile transmitter

1. INTRODUCTION

One of the major implementation concerns in radio transmitters is the ability to control unwanted spectral emissions. In carrier aggregation (CA) mobile transmitters with a single multi-band power amplifier (PA) [1], some of the intermodulation distortion components created by a nonlinear PA will fall on the spurious region, and may seriously violate the spurious emission limits [2], [3]. To satisfy the stringent emission requirements in such multi-band transmission scenarios, devices may need to considerably back off their transmit power from the nominal maximum value (e.g., +23 dBm in 3GPP LTE uplink). This is called Maximum Power Reduction (MPR) in 3GPP LTE context. However, reducing the transmit power (increasing MPR) in order to fulfill the emission mask will necessarily reduce the uplink coverage. This problem is illustrated e.g. in [3] by showing a measured RF spectrum of an LTE-A Release 12 intraband CA signal with two fully allocated 5 MHz carriers separated by 30 MHz, driving a multi-band PA. The PA nonlinearity creates strong 3rd order spurious intermodulation components at 45 MHz from the center of the whole transmission bandwidth. In this example, more than 11 dB of MPR was needed to keep these intermodulations below the spurious emission limit.

An intriguing alternative solution to power back-off is to use digital predistortion (DPD) linearization for reducing the unwanted spectral emissions [4–8]. In CA transmit scenarios in battery-powered mobile devices, however, conventional DPDs which take the composite dual-carrier digital signal as input (”full-band DPD”), are not feasible for transmit signal bandwidths exceeding a few tens of MHz, due to the high computational power and sample rate required [5]. In LTE-A with interband CA, for example, the total transmit signal bandwidth can be several hundreds of MHz, thus exemplifying the need for alternative linearization approaches.

In [6], a DPD technique with separate processing for the fundamental bands and the third-order intermodulation (IM3) bands in a dual-carrier transmitter was introduced. This work relied on quasi-memoryless DPD for each subband, and the parameter estimation was non-adaptive, carried out off-line with a large-signal network analyzer (LSNA). In [7], this work was extended to predistort also the fifth-order intermodulation bands with up to three component carriers, still relying on the memoryless modeling and off-line estimation with an LSNA. Memory polynomial based DPD linearization of dual-band PAs, focusing on the spectral regrowth mitigation of the component carriers only, was in turn proposed in [9]. This approach was extended to include also the IM3 bands in [8] but including only memoryless processing. This work represents the current state-of-the-art in the field. The works [6–9] predistort each band separately, thus having much lower sample rate requirements compared to conventional full-band DPDs. In [8] and [9], the DPD parameter estimation is also simplified, since only the linearized bands need to be sampled in the feedback loop. Furthermore, in [6], [7], and [8], the IM3 band distortion compensation is based on injecting a signal with equal magnitude but 180 degree phase shift compared to the estimated IM3 terms, into the input of the transmitter. This approach is here referred to as the 3rd order inverse approach.

In this article, we develop a fully adaptive reduced complexity DPD scheme to specifically target the IM3 bands. In contrast to the previous works in [6], [7], and [8] which utilize the 3rd order inverse solution, we aim to tune the amplitude and phase of the injected signal adaptively, by decorrelating the considered IM3 band signal of the PA output with appropriate basis functions stemming from our analysis and signal modeling. This approach is shown to yield superior results compared to the previous works, while having very low computational and instrumentation complexity. In general, we consider the main objective of the predistorter to keep the spectral emissions below the regulated spectral and spurious emission limits. For the spurious emissions, at RF frequencies over 1 GHz, this limit is -30dBm over a 1 MHz measurement bandwidth [10], [11].

This work was funded by the Finnish Funding Agency for Technology and Innovation (Tekes, under the CREAM project), the Academy of Finland (under the project #251138) and the Austrian Competence Centre in Mechatronics (ACCM).

2. REDUCED-COMPLEXITY DIGITAL PREDISTORTION

2.1. Spurious IM3 Component Modeling and Analysis

In this Section, we first analyze the output of a third-order memoryless PA when excited with a dual-carrier LTE-A UL type signal. A principal scenario illustration is given in Fig. 1. The analysis is carried out at composite baseband equivalent level, and the two component carriers (CC) are assumed to be separated by $2f_{IF}$. Thus, the composite baseband equivalent PA input and output signals, $x(n)$ and $y(n)$, read

$$x(n) = x_1(n)e^{j2\pi\frac{f_{IF}}{f_s}n} + x_2(n)e^{-j2\pi\frac{f_{IF}}{f_s}n} \quad (1)$$

$$y(n) = \beta_1 x(n) + \beta_3|x(n)|^2 x(n) \quad (2)$$

where β_1 and β_3 are unknown PA coefficients, and $x_1(n)$ and $x_2(n)$ are the baseband equivalents of the input CCs. Through direct substitution of (1) in (2), the baseband equivalent positive and negative IM3 terms, located in the composite BB equivalent at three times the IF frequency, can be easily extracted and read

$$\begin{aligned} y_{IM3_+}(n) &= \beta_3(x_2^*(n)x_1^2(n)) \\ y_{IM3\_}(n) &= \beta_3(x_1^*(n)x_2^2(n)) \end{aligned} \quad (3)$$

While the PA output contains also other signal and distortion terms, our objective is to develop a low-complexity DPD solution that can in particular reduce the above IM3 components and thus assist the mobile transceiver to fulfill the spurious emission mask with smaller MPR. This is formulated next at structural level in Section 2.2 while the actual parameter optimization and estimation through decorrelation principle are addressed then in Section 3.

2.2. Proposed IM3 Reduction DPD

To simplify the presentation, we focus below on canceling only the $IM3_+$ term in (3). In short, the idea is to inject a proper additional low-power cancellation signal to (1), located at three times the IF, such that $IM3_+$ at PA output is reduced. Stemming from the signal structure in (3), natural injection is of the form $x_2^*(n)x_1^2(n)$ but should be scaled properly with a complex DPD coefficient, say α. Thus, incorporating such DPD processing, the composite baseband equivalent PA input signal reads now

$$\begin{aligned} \tilde{x}(n) =& x_1(n)e^{j2\pi\frac{f_{IF}}{f_s}n} + x_2(n)e^{-j2\pi\frac{f_{IF}}{f_s}n} \\ &+ \alpha(x_2^*(n)x_1^2(n))e^{j2\pi\frac{3f_{IF}}{f_s}n} \end{aligned} \quad (4)$$

Here, and in the continuation, we use $\tilde{(.)}$ variables to indicate DPD-based processing and corresponding signals. Substituting now $\tilde{x}(n)$ in (2), the fundamental CCs and IM3 components at PA output read

$$\begin{aligned} \tilde{y}_+(n) =& \beta_1 x_1 + \beta_3|x_1|^2 x_1 + 2\beta_3|x_2|^2 x_1 \\ &+ 2\beta_3\alpha|x_1|^2|x_2|^2 x_1 + 2\beta_3|\alpha|^2|x_1|^4|x_2|^2 x_1 \end{aligned} \quad (5)$$

$$\begin{aligned} \tilde{y}_-(n) =& \beta_1 x_2 + \beta_3|x_2|^2 x_2 + 2\beta_3|x_1|^2 x_2 \\ &+ \beta_3\alpha^*|x_1|^4 x_2 + 2\beta_3|\alpha|^2|x_1|^2|x_2|^2 x_1 x_2 \end{aligned} \quad (6)$$

$$\begin{aligned} \tilde{y}_{IM3_+}(n) =& (\beta_3 + \beta_1\alpha)x_2^* x_1^2 + 2\beta_3\alpha(|x_1|^2 + |x_2|^2)x_2^* x_1^2 \\ &+ \beta_3|\alpha|^2\alpha|x_1|^4|x_2|^2 x_2^* x_1^2 \end{aligned} \quad (7)$$

$$\tilde{y}_{IM3\_}(n) = \beta_3 x_1^* x_2^2 + 2\beta_3\alpha^*|x_1|^2 x_1^* x_2^2 \quad (8)$$

Notice that in above, we have excluded the discrete-time arguments (n) in the signal variables to simplify the presentation. This notational convention is deployed also in the continuation. In addition to above components, the injection of the DPD signal at three times the IF produces then also fifth- and seventh-order IM (IM5 and IM7) terms at the PA output. These are given by

$$\begin{aligned} \tilde{y}_{IM5_+}(n) =& \beta_3\alpha^2|x_1|^2 x_1^3 x_2^{*2} \\ \tilde{y}_{IM5\_}(n) = \beta_3\alpha^* x_1^{*2} x_2^3,\ & \tilde{y}_{IM7_+}(n) = \beta_3\alpha^2 x_1^4 x_2^{*3} \end{aligned} \quad (9)$$

These are, however, typically much weaker than the third-order components which tend to limit the spurious emission performance [10], [11].

As (7) shows, the strength of the considered IM3 at the PA output depends directly on, and can thus be controlled by, the DPD coefficient α. Hence, the optimization and feedback-based low-complexity estimation of α for efficient IM3 cancellation is addressed next in Section 3.

3. DPD PARAMETER OPTIMIZATION AND ESTIMATION

Below we address the DPD parameter optimization and practical estimation. As in the previous Section, we focus mostly on the positive IM3 spurious band to keep the notations compact. Similar processing and optimization can be directly developed then also for the corresponding negative IM3 spurious band. This will also be illustrated in the simulation results section.

3.1. Third-Order Inverse Reference Solution

We start our coefficient optimization by shortly investigating the so-called third-order inverse solution for reference. From (7), it is clear that choosing α such that $\beta_3 + \beta_1\alpha = 0$ or

$$\alpha_{inv} = -\beta_3/\beta_1, \quad (10)$$

the third-order distortion term at positive IM3 band is fully eliminated. This is called here third-order inverse solution. This solution is very intuitive, as injecting $-(\beta_3/\beta_1)x_2^* x_1^2$ at PA input will approximately yield $-\beta_3 x_2^* x_1^2$ at the output, thus suppressing the IM3, since the injection is a very low power signal exiting only the PA linear gain. However, as the PA is anyway a fundamentally nonlinear device, some intermodulation will remain at the positive IM3 band. This can be analyzed more closely by substituting $\alpha_{inv} = -\beta_3/\beta_1$ in (7). This yields directly

$$\begin{aligned} \tilde{y}_{IM3_{+,inv}}(n) =& -(\beta_3^2/\beta_1)x_2^* x_1^2[2(|x_1|^2 + |x_2|^2) \\ &+ (|\beta_3|^2/|\beta_1|^2)|x_1|^4|x_2|^2)] \end{aligned} \quad (11)$$

Thus we can see that the remaining intermodulation at positive IM3 band contains higher-order terms with structural similarity and correlation with $x_2^* x_1^2$. This will be deployed in Section 3.2 where the proposed decorrelation-based DPD parameter optimization and estimation is formulated. More specifically, denoting the statistical expectation operator by $\mathbf{E}(.)$ and assuming that the CCs x_1 and x_2 are statistically independent, the correlation can be written explicitly as

$$\begin{aligned} &\mathbf{E}(\tilde{y}_{IM3_{+,inv}}(n) \times (x_2^*(n)x_1^2(n))^*) = \\ &-\frac{\beta_3^2}{\beta_1}\left[2\mathbf{E}|x_1|^6\mathbf{E}|x_2|^2 + 2\mathbf{E}|x_1|^4\mathbf{E}|x_2|^4 + \frac{|\beta_3|^2}{|\beta_1|^2}\mathbf{E}|x_1|^8\mathbf{E}|x_2|^4\right] \end{aligned} \quad (12)$$

thus implying non-zero correlation.

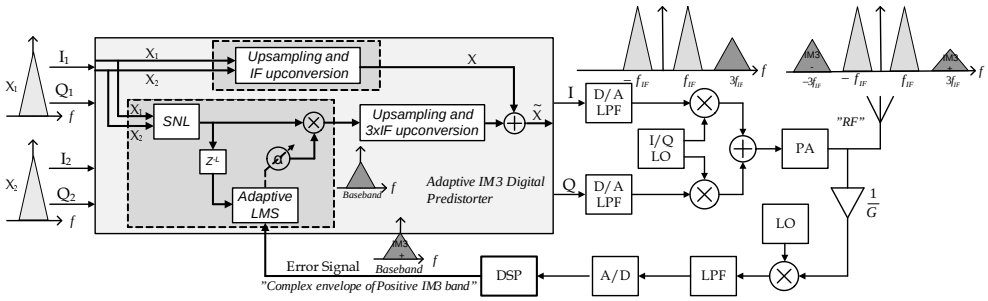

Fig. 1. Principal adaptive DPD system architecture for third-order spurious intermodulation reduction in a dual-carrier transmitter. Also essential composite baseband equivalent spectra are shown.

3.2. Decorrelation-based Parameter Optimization and Practical Adaptive Estimation

As formulated above, the third-order inverse solution in (10) needs explicit estimation of the PA parameters β_1 and β_3. Furthermore, even with perfect estimation, the remaining distortion has correlation with the essential distortion basis of the form $x_2^* x_1^2$, as was shortly shown above. Hence, opposed to third-order (or more generally Pth-order) inverse processing, we formulate the DPD parameter optimization task here as minimizing the correlation between the considered IM3 spurious band and the distortion basis $x_2^* x_1^2$. This will then also imply very simple instrumentation complexity for the feedback receiver, for parameter learning with unknown PA characteristics, as only *narrowband feedback* capturing the considered IM3 spurious band is needed. This is conceptually illustrated in Fig. 1. As formulated in more details below, this will then also enable directly tracking, e.g., possible time-variations in the PA characteristics due to temperature changes and other possible sources like device ageing. Furthermore, very low-complexity practical learning algorithms can be deployed without, e.g., matrix inversion typically encountered in Least-Squares (LS) based block-processing.

We start the mathematical formulation by deploying the *error signal notation*, depicted also in Fig. 1. This error signal, $e(n)$, is defined as the baseband feedback signal from the PA output measured at the considered IM3 spurious band, here the positive one. We also define the cancellation signal basis, also called filter input signal, here as $u(n) = x_2^*(n)x_1^2(n)$ as the focus is on positive IM3 spurious band. We emphasize that this can be generated directly from the baseband signals of the individual component carriers, $x_1(n)$ and $x_2(n)$, at baseband. Then, the idea is find α that minimizes the correlation between $e(n)$ and $u(n)$ and thus orthogonalizes the error signal with the input signal, i.e. sets $E(e(n)u^*(n) = 0)$. To shortly derive this decorrelation solution, we first write the essential instantaneous signal expressions as

$$\begin{aligned} e(n) &= \tilde{y}_{IM3_+}(n) \\ &= (\beta_3 + \beta_1\alpha)x_2^* x_1^2 + 2\beta_3\alpha(|x_1|^2 + |x_2|^2)x_2^* x_1^2 \\ &\quad + \beta_3|\alpha|^2\alpha|x_1|^4|x_2|^2 x_2^* x_1^2 \qquad (13) \\ u(n) &= x_2^*(n)x_1^2(n) \qquad (14) \end{aligned}$$

$$\begin{aligned} e(n)u^*(n) &= \beta_3|x_1|^4|x_2|^2 + \beta_1\alpha|x_1|^4|x_2|^2 \\ &\quad + 2\beta_3\alpha(|x_1|^6|x_2|^2 + |x_1|^4|x_2|^4) + \alpha|\alpha|^2\beta_3|x_1|^8|x_2|^4 \qquad (15) \end{aligned}$$

Then, we can directly operate with the statistical expectation operator $\mathbf{E}(.)$ to (15), yielding

$$\begin{aligned} \mathbf{E}(e(n)u^*(n)) &= \beta_3\mathbf{E}|x_1|^4\mathbf{E}|x_2|^2 \\ &\quad + \alpha\left[\beta_1\mathbf{E}|x_1|^4\mathbf{E}|x_2|^2 + 2\beta_3(\mathbf{E}|x_1|^6\mathbf{E}|x_2|^2 + \mathbf{E}|x_1|^4\mathbf{E}|x_2|^4)\right] \qquad (16) \end{aligned}$$

where it has been assumed that the component carrier signals x_1 and x_2 are statistically independent and also the expectation of the last term in (15) has been neglected as it is vanishingly small compared to other terms. Now, setting this expression to zero yields the optimal decorrelating DPD parameter, denoted with α_o, as

$$\alpha_o = \frac{-\beta_3}{\left[\beta_1 + 2\beta_3\left(\frac{\mathbf{E}|x_1(n)|^6}{\mathbf{E}|x_1(n)|^4} + \frac{\mathbf{E}|x_2(n)|^4}{\mathbf{E}|x_2(n)|^2}\right)\right]} \qquad (17)$$

Interestingly, the derived solution depends on the PA parameters and higher-order statistics of the component carrier signals. As the PA parameters β_1 and β_3 are assumed unknown, this solution cannot be directly evaluated. However, it serves as the reference solution and its derivation also forms directly the basis for developing the actual sample-adaptive practical learning algorithm.

Next, as the PA parameters are assumed unknown, a sample-adaptive or instantaneous decorrelation solution is pursued where only the feedback observation is needed and DPD parameter α is adapted continuously. This can be obtained directly using the instantaenous sample correlation $u(n)e^*(n)$ to update the DPD parameter α. We formulate this as

$$\begin{aligned} e(n) &= \tilde{y}_{IM3_+}(n) \qquad (18) \\ u(n) &= x_2^*(n)x_1^2(n) \qquad (19) \\ \alpha^*(n+1) &= \alpha^*(n) - \frac{\mu}{|u(n)|^2}u(n)e^*(n) \qquad (20) \end{aligned}$$

where learning step-size normalization is also deployed. This resembles closely Normalized Least-Mean-Square (N-LMS) type adaptive filtering but with nonlinear transmitter inside the learning loop, which from the learning perspective is the mapping from DPD injection to IM3 band reference receiver output. In practical implementations, as already depicted in Fig. 1, the delay of the transmitter and feedback receiver chains should also be incorporated in

Table 1. Required MPRs to meet the Spurious Emission Limit with minimum of 95% success rate with different numbers of allocated LTE-A RBs per CC

Number of RBs	MPR, no DPD	MPR, proposed DPD
1	6.4 dB	2.7 dB
10	6.2 dB	2.2 dB
50	4.8 dB	1.5 dB

the learning recursion. This type of learning algorithm can also be interpreted as a stochastic Newton root search in the function $J(\alpha) = \mathbf{E}[u(n)e^*(n)]$ (i.e., (16)), with the inverse of the gradient of $J(\alpha)$ approximated with the (positive) scalar $\mu/|u(n)|^2$. This is plausible since the gradient of (16) is indeed positive when the PA total output signal is still dominated by linear signal terms.

4. SIMULATION RESULTS AND ANALYSIS

A dual-carrier LTE-A UL SC-FDMA signal is deployed to test and demonstrate the proposed DPD concept. The CCs are separated by 60 MHz and 25 resource blocks (RB) are allocated at each CC deploying QPSK subcarrier modulation. The IIP3 of the 3rd-order PA model is 17 dBm and the PA output power is +21dBm. As can be seen in Fig. 2, the proposed decorrelation-based DPD provides better results compared to the 3rd-order inverse solution, even when the sample-adaptive practical learning is deployed. Fig. 3 shows the corresponding convergence of the DPD coefficient, together with the derived optimum value α_0.

For more realistic performance assessment, a 5th-order PA model is next deployed while still carrying out the linearization with IM3 emphasis and sample-adaptive decorrelation-based learning. Furthermore, both IM3+ and IM3- bands are linearized implying parallel learning and processing with separate coefficients, say α_+ and α_-. The results in terms of transmitter output spectra are illustrated in Fig. 4. Clearly, the existence of 5th-order terms have certain impact on the linearization performance but the transmitter emission requirements are still fulfilled with +22dBm output power. To address shortly the impact of 5th-order distortion at IM3 band, and assuming a polynomial PA model of the form $y(n) = \beta_1 x(n) + \beta_3|x(n)|^2x(n) + \beta_5|x(n)|^4x(n)$, one can easily show that without DPD processing, the positive IM3 band baseband equivalent observation is equal to $\beta_3(x_2^*x_1^2) + 3\beta_5|x_2|^2(x_2^*x_1^2) + 2\beta_5|x_1|^2(x_2^*x_1^2)$. Thus, the IM3 bands contain additional signal terms, due to 5th-order distortion in the PA. Compared to the 3rd-order term, these terms are clearly correlated and thus have an impact on the predistortion coefficient learning. Extending the pre-distortion processing to adaptively decorrelate the higher-order distortion terms at IM3 bands is thus an important topic for future work.

Finally, we elaborate on the ability of the developed DPD solution to relax the MPR requirements in different RB allocation scenarios, using the 5th-order PA model. Table 1 shows the required MPRs, without and with DPD, in order to ensure meeting the spurious emission mask defined in [10] and [11] in large number of parallel realizations with at least 95% success rate. It is evident that the proposed DPD allows using lower MPRs, by at least 3-4 dB, depending on the number of allocated RBs. This directly reflects on the UL network coverage.

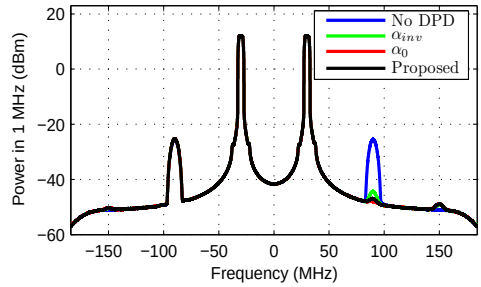

Fig. 2. Dual-carrier LTE-A mobile transmitter power spectra without and with DPDs. PA with 17 dBm IIP3 and output power of +21 dBm.

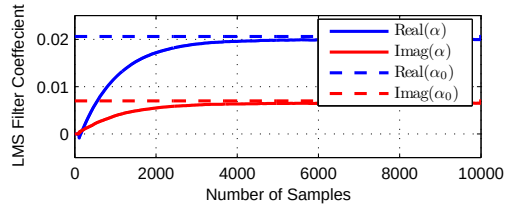

Fig. 3. Illustration of sample-adaptive decorrelation coefficient convergence and the corresponding optimum coefficient.

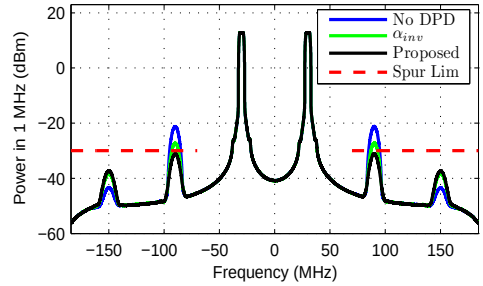

Fig. 4. Dual-carrier LTE-A mobile transmitter power spectra without and with DPD. 5th-order PA model having 1-dB compression point of 26 dBm and output power of +22 dBm.

5. CONCLUSIONS

In this paper, reduced-complexity adaptive digital pre-distortion solution was developed to specifically suppress third-order intermodulation in non-contiguous dual-carrier mobile transmitters. Sample-adaptive parameter learning algorithm deploying only narrowband feedback was formulated, and the whole DPD concept was shown to outperform the existing third-order inverse solutions. This can help dual-carrier mobile devices to reduce their power back-off while still fulfilling the spurious emission requirements. Future work will include extending the DPD processing and parameter learning to high-order PAs with memory.

6. REFERENCES

[1] S.A. Bassam, Wenhua Chen, M. Helaoui, and F.M.Ghannouchi, "Transmitter architecture for CA: Carrier Aggregation in LTE-Advanced systems," *IEEE Microwave Magazine*, vol. 14, 2013.

[2] V. Lehtinen, T. Lähteensuo, P. Vasenkari, A. Piipponen, and M. Valkama, "Gating factor analysis of maximum power reduction in multicluster LTE-A uplink transmission," in *Proc. IEEE Radio and Wireless Symposium (RWS), Austin, TX*, Jan. 2013.

[3] T. Lähteensuo, "Linearity requirements in LTE Advanced mobile transmitter," M.S. thesis, Tampere University of Technology, Tampere, Finland., May 2013. http://dspace.cc.tut.fi/dpub/handle/123456789/21504.

[4] J. Thorebäck, "Digital predistortion the evolution of linearized transmitters for radio basestations," in *Signal Processing for Amplifiers Workshop, Chalmers, Sweden*, Nov. 2012.

[5] M. Abdelaziz et al., "Mobile transmitter digital predistortion: Feasibility analysis, algorithms and design exploration," in *47th Asilomar Conf. Signals Systems Computers, Pacific, Grove, CA, USA*, Nov. 2013.

[6] P. Roblin, S. K. Myoung, D. Chaillot, Y. G. Kim, A. Fathimulla, J. Strahler, and S. Bibyk, "Frequency-selective predistortion linearization of RF power amplifiers," *IEEE Transactions on Microwave Theory and Techniques*, vol. 56, pp. 65–76, Jan. 2008.

[7] J. Kim, P. Roblin, D. Chaillot, and Z. Xie, "A generalized architecture for the frequency-selective digital predistortion linearization technique," *IEEE Transactions on Microwave Theory and Techniques*, vol. 61, pp. 596–605, Jan. 2013.

[8] S.A. Bassam, M. Helaoui, and F.M. Ghannouchi, "Channel-selective multi-cell digital predistorter for multi-carrier transmitters," *IEEE Transactions on Microwave Theory and Techniques*, vol. 60, pp. 2344–2352, Aug. 2012.

[9] S.A. Bassam, M. Helaoui, and F.M. Ghannouchi, "2-D Digital Predistortion (2-D-DPD) architecture for concurrent dual-band transmitters," *IEEE Transactions on Microwave Theory and Techniques*, vol. 59, pp. 2547–2553, Oct. 2011.

[10] "3GPP Evolved Universal Terrestrial Radio Access (E-UTRA); User Equipment (UE) radio transmission and reception. http://www.3gpp.org/ftp/specs/html-info/36101.htm," .

[11] "International telecommunication union radio communication sector, recommendation ITU-R SM.329-12 unwanted emissions in the spurious domain. http://www.itu.int/dms_pubrec/itur/rec/sm/R-REC-SM.329-12-201209-i!!PDF-E.pdf," .

Publication 6

M. Abdelaziz, L. Anttila, J. R. Cavallaro, S. S. Bhattacharyya, A. Mohammadi, F. Ghannouchi, M. Juntti, and M. Valkama, "Low-complexity digital predistortion for reducing power amplifier spurious emissions in spectrally-agile flexible radio," in *Proc. International Conference on Cognitive Radio Oriented Wireless Networks and Communications (CROWNCOM)*, Oulu, 2014, pp. 323-328.

Low-Complexity Digital Predistortion For Reducing Power Amplifier Spurious Emissions in Spectrally-Agile Flexible Radio

Mahmoud Abdelaziz[1], Lauri Anttila[1], Joseph R.Cavallaro[2], Shuvra S. Bhattacharyya[3], Abbas Mohammadi[4], Fadhel Ghannouchi[5], Markku Juntti[6] and Mikko Valkama[1]
[1]Department of Electronics and Communications Engineering, Tampere University of Technology, Tampere, Finland
[2]Rice University, ECE Department, Houston, TX
[3]University of Maryland, ECE Department, College Park, MD
[4]Department of Electrical Engineering, Amirkabir University of Technology, Tehran, Iran
[5]iRadio Lab, Department of Electrical and Computer Engineering, University of Calgary, Alberta, Canada
[6]University of Oulu, Dept. Communications Engineering, Oulu, Finland
E-mail: mahmoud.abdelaziz@tut.fi

***Abstract*—Increasing the flexibility in spectrum access is a key to enhanced efficiency in radio spectrum utilization. Non-contiguous carrier aggregation (CA) is one enabling technology towards more flexible spectrum access, but can also lead to serious implementation challenges in terms of transmitter linearity. Especially when a single power amplifier (PA) is deployed for all carriers, serious intermodulation components will rise which can easily limit the maximum transmit power. In this paper, a low-complexity digital predistortion (DPD) solution is developed to reduce the most critical spurious components at the PA output, opposed to more classical full bandwidth linearization. The developed concept and associated parameter learning and optimization are particularly tailored towards mobile devices, building on limited narrowband feedback receiver with reduced instrumentation complexity and reduced-rate DPD processing. The developed DPD solution can handle PAs with substantial memory effects, and is verified with extensive simulation examples in various non-contiguous carrier aggregation scenarios and practical PA models with memory.**

***Index Terms*—Carrier aggregation, cognitive radio, digital predistortion, flexible spectrum access, intermodulation, LTE-Advanced, mobile transmitter, power amplifier**

I. Introduction

Cognitive radio (CR) systems seek to increase the efficiency of radio spectrum utilization by allowing secondary user (SU) access to spatially and/or temporally unused spectral chunks in limited geographical areas such that interference towards primary users (PUs) is kept within the specified limits [1], [2]. At physical layer, this calls for frequency-agile flexible radio transceivers which can transmit and receive spectrally well-contained waveforms, including also non-contiguous transmission with multiple simultaneous carriers. Similar non-contiguous or scattered spectrum access scenarios are also emerging in 3GPP mobile cellular radio, most notably in LTE-Advanced in terms of non-contiguous intra-band and inter-band carrier aggregation (CA) [3].

In above-kind flexible spectrum access scenarios, the linearity of transceiver circuits, and especially transmit power amplifier (PA), is one key challenge [4]. Especially with single PA based transmitter architecture, non-contiguous transmission can result in severe intermodulation components stemming from the nonlinear characteristics of the PA. These spurious components, if not properly controlled, can easily violate the SU-PU interference constraints in cognitive radio systems [5] or the spurious emission limits of commercial mobile cellular radio such as 3GPP LTE-Advanced [6], [7]. One alternative to reduce the spurious emissions is simply to back-off the transmit power, called Maximum Power Reduction (MPR) in 3GPP LTE uplink context. As shown through actual RF measurements in [7] with an LTE-Advanced Release 12 intraband CA signal composed of two fully allocated 5 MHz carriers and 30 MHz separation, the needed MPRs can be even in the order 10-15 dB, which has then a very big impact on the achievable transmission rate and coverage.

Instead of backing-off the power, a fascinating alternative is to deploy digital predistortion (DPD) for suppressing the unwanted spurious emissions [8]–[12]. In CA transmitters, however, the total bandwidth of the digital signal is already very high and running classical full-bandwidth DPD processing may not be feasible, especially in mobile devices [9]. Thus, alternative reduced-complexity DPD solutions are needed. In the existing literature, some works towards sub-band specific linearization have been reported in the recent years. In [10] and [11], DPD solutions with separate processing for the fundamental bands and the higher-order intermodulation (IM) bands in CA transmitter context were developed. Quasi-memoryless model for each subband was assumed and the

This work was supported in part by the US National Science Foundation under grants CNS-1265332 and CNS-1264486 as well as by the Finnish Funding Agency for Technology and Innovation (Tekes) through the TRIAL programme under the project "Cross-Layer Modeling and Design of Energy-Aware Cognitive Radio Networks (CREAM)". The work was also funded by the Academy of Finland under the project #251138 "Digitally-Enhanced RF for Cognitive Radio Devices" and the Linz Center of Mechatronics (LCM) in the framework of the Austrian COMET-K2 programme.

parameter estimation was based on off-line measurements with a large-signal network analyzer (LSNA). Memory polynomial type predistortion of dual-band PAs, focusing on the spectral regrowth mitigation of the component carriers only, was in turn proposed in [13], and then extended to cover also the third-order IM bands in [12] but including only memoryless processing. All these works allow lowering the sample rate in the DPD processing, compared to classical full-bandwidth solutions. In [12] and [13], also the feedback receiver instrumentation is simplified as only the linearized sub-bands need to be measured. The reported solutions are, however, limited either to simple memoryless processing or assume offline measurements and parameter optimization.

In this article, opposed to offline measurements based parameter estimation, we develop an online reduced complexity predistortion solution, specifically tailored to suppress third-order spurious IM components in non-contiguous CA transmitters. First, detailed modeling for the spurious components is carried out assuming a general case of PA with memory effects. Then, stemming from this modeling, a specific cancellation signal is injected into the transmit path such that the third-order spurious IM component at PA output is suppressed. The properties of this injected cancellation signal are adaptively controlled, deploying a decorrelation-based adaptive learning algorithm and narrowband observation receiver with reduced instrumentation complexity. Compared to the previous works in [10], [11], and [12], explicit knowledge of the PA properties is then not needed. Comprehensive simulation experiments are also reported, with practical wideband PA models, evidencing efficient suppression of the selected spurious components. The developed solution thus offers an efficient low-complexity DPD solution for reducing PA-induced spurious emissions in spectrally-agile flexible radio systems.

II. Spurious Component Modeling and Digital Predistortion

A. Spurious IM3 Component Modeling for Power Amplifiers with Memory

In [14], modeling of the spurious IM3 component of a third order memoryless PA was performed. This analysis established the basis for the memoryless decorrelating DPD using the relevant third order basis functions, and it is shortly reiterated next. The modeling is carried out at composite baseband equivalent level, and the two component carriers (CC) are assumed to be separated by $2f_{IF}$. Defining the composite baseband equivalent input and output signals of the PA respectively as

$$x(n) = x_1(n)e^{j2\pi\frac{f_{IF}}{f_s}n} + x_2(n)e^{-j2\pi\frac{f_{IF}}{f_s}n} \quad (1)$$

$$y(n) = \beta_1 x(n) + \beta_3|x(n)|^2x(n), \quad (2)$$

the PA output signals at the spurious IM3 bands centered at +/- $3f_{IF}$ read

$$\begin{aligned} y_{IM3_+}(n) &= \beta_3(x_2^*(n)x_1^2(n)) \\ y_{IM3_-}(n) &= \beta_3(x_1^*(n)x_2^2(n)). \end{aligned} \quad (3)$$

Here, β_1 and β_3 are the (unknown) memoryless PA coefficients, and $x_1(n)$ and $x_2(n)$ are the baseband equivalents of the input CCs.

Now, in order to extend this analysis to power amplifiers exhibiting memory effects, we shall assume a third order Parallel Hammerstein (PH) PA model excited with the same dual-carrier signal. The PA output signal in this case is

$$y(n) = f_1(n) \star x(n) + f_3(n) \star |x(n)|^2x(n), \quad (4)$$

where $f_1(n)$ and $f_3(n)$ are the filters in the main and third order PH branches, respectively, and $\star$ is the convolution operator. Through direct substitution of (1) in (4), the baseband equivalent positive and negative IM3 terms, located in the composite BB equivalent at three times the IF frequency, can be easily extracted and read

$$\begin{aligned} y_{IM3_+}(n) &= f_3^+(n) \star (x_2^*(n)x_1^2(n)) \\ y_{IM3_-}(n) &= f_3^-(n) \star (x_1^*(n)x_2^2(n)). \end{aligned} \quad (5)$$

Here, $f_3^+(n)$ is the baseband equivalent response of $f_3(n)$ at the positive $IM3$ band ($+3f_{IF}$), and similarly, $f_3^-(n)$ is the baseband equivalent response of $f_3(n)$ at the negative $IM3$ band ($-3f_{IF}$). These are formally defined as

$$f_3^+(n) = LPF\{e^{-j2\pi\frac{3f_{IF}}{f_s}n} f_3(n)\} \quad (6)$$

$$f_3^-(n) = LPF\{e^{j2\pi\frac{3f_{IF}}{f_s}n} f_3(n)\}, \quad (7)$$

with $LPF\{.\}$ denoting an ideal low pass filtering operation, with a passband 3 times the bandwidth of the wider CC. While the PA output signal contains also other signal and distortion terms, our objective is to develop a low-complexity DPD solution that aims at reducing only these particular IM3 components, and thus assist the mobile transceiver to fulfill the spurious emission mask with a smaller MPR. This is formulated next at structural level in Section II-B while the actual parameter optimization and practical estimation through the decorrelation principle are addressed in Section III.

B. Proposed DPD Structure for Dedicated Spur Reduction

To simplify the presentation, the following analysis will focus on canceling only the $IM3_+$ term in (5). In short, the idea is to inject a proper additional low-power cancellation signal to (1), located at $+3f_{IF}$, such that the level of the $IM3_+$ term at PA output is reduced. Stemming from the signal structure in (5), a natural injection signal is a filtered version of $x_2^*(n)x_1^2(n)$ using a filter $\alpha(n)$ composed of a set of N+1 taps $\alpha_0, \alpha_1, ...\alpha_N$. Incorporating such DPD processing, the composite baseband equivalent PA input signal now reads

$$\begin{aligned} \tilde{x}(n) =& x_1(n)e^{j2\pi\frac{f_{IF}}{f_s}n} + x_2(n)e^{-j2\pi\frac{f_{IF}}{f_s}n} \\ &+ \left[\alpha(n) \star (x_2^*(n)x_1^2(n))\right] e^{j2\pi\frac{3f_{IF}}{f_s}n}. \end{aligned} \quad (8)$$

Here, and in the continuation, we use $\tilde{(.)}$ variables to indicate DPD processing and corresponding predistorted signals.

Substituting now $\tilde{x}(n)$ in (4), the most dominant terms at the positive IM3 band at the PA output read

$$\tilde{y}_{IM3_+}(n) = (f_3^+(n) + f_1^+(n) \star \alpha(n)) \star x_2^*(n)x_1^2(n) + 2f_3^+(n) \star \left[(|x_1(n)|^2 + |x_2(n)|^2)(\alpha(n) \star x_2^*(n)x_1^2(n))\right]. \quad (9)$$

From (9), it can be shown that the strength of the considered IM3 band at the PA output depends directly on, and can thus be controlled by, the DPD coefficients $\alpha_0, \alpha_1, ...\alpha_N$. In the next section, we address practical feedback-based adaptive learning of $\alpha(n)$ for efficient online IM3 mitigation.

III. Adaptive Decorrelation-Based Learning of DPD Parameters

Below we address the practical estimation of the DPD parameters. As in the previous section, we focus mostly on the positive IM3 spurious band to keep the notations compact. Similar processing and estimation can be directly developed then also for the corresponding negative IM3 spurious band.

A. 3rd Order Inverse Solution

Examining (9), it can be seen that the solution that nulls the third order term is simply obtained by setting the first line of the equation to zero, i.e., $f_3^+(n) + f_1^+(n) \star \alpha_{inv}(n) = 0, \ \forall n$. Unlike in the memoryless scenario, in order to solve this equation for the DPD filter $\alpha(n)$, it is easier to transform the expression to the frequency domain where convolutions are turned into multiplications. Consequently, the 3rd order inverse solution for $\alpha(n)$ in the frequency domain becomes

$$A_{inv}(e^{j\frac{2\pi f}{f_s}}) = -\frac{F_3^+(e^{j\frac{2\pi f}{f_s}})}{F_1^+(e^{j\frac{2\pi f}{f_s}})}, \quad (10)$$

where $F_1^+(e^{j\frac{2\pi f}{f_s}})$ and $F_3^+(e^{j\frac{2\pi f}{f_s}})$ are the baseband equivalent frequency responses of the PH filters $f_1(n)$ and $f_3(n)$ at the positive IM3 band (i.e. $+3f_{IF}$). After that, an IDFT operation can be performed on $A_{inv}(e^{j\frac{2\pi f}{f_s}})$ in order to obtain the impulse response of the DPD filter $\alpha_{inv}(n)$.

Clearly, the 3rd order inverse solution implies estimating $F_1^+(e^{j\frac{2\pi f}{f_s}})$ and $F_3^+(e^{j\frac{2\pi f}{f_s}})$, which is not a simple task in practice. Such estimation for a memoryless DPD was proposed in [10], [12]. In this article, instead of explicitly trying to estimate the 3rd order inverse solution, we propose multi-tap adaptive decorrelation-based DPD as an effective solution. The actual estimation procedure is addressed next.

B. Decorrelation-Based Adaptive Parameter Estimation

Examining the first line of (9), the dominant term in the positive IM3 expression is $(f_3^+(n) + f_1^+(n) \star \alpha(n)) \star x_2^*(n)x_1^2(n)$. As shown in the previous subsection a suitable linear filter $\alpha_{inv}(n)$ can remove the dominant third-order term. However, applying predistortion always creates higher-order IM products on the IM3 bands, such as the fifth order term seen on the second line of (9), that the 3rd order inverse solution cannot suppress. This fifth order term can be seen to be strongly correlated with the dominant third order basis function $x_2^*(n)x_1^2(n)$. We therefore conjecture, that *decorrelating* the IM3 band signal at the PA output with $x_2^*(n)x_1^2(n)$ and its delayed replicas could give superior performance compared to the 3rd order inverse solution. This approach was originally developed in [14] for a memoryless DPD and PA. There, the adaptive decorrelation algorithm was shown to clearly improve the IM3 band reduction compared to the 3rd order inverse solution, and was also shown to work under 5th order PA nonlinearity. The memoryless solution from [14] is here generalized to a multi-tap solution, aiming for improved spur reduction with practical wideband PAs exhibiting substantial memory effects.

As implicated by the analyses in Sections II-B and III-A, the proposed multi-tap adaptive decorrelation DPD is formulated as a multi-tap adaptive filter which filters the locally generated Static Non-Linear (SNL) basis function $x_2^*(n)x_1^2(n)$, with the objective of decorrelating it with the IM3 band signal at the PA output. Consequently, the adaptive decorrelation coefficient update reads as follows:

$$e(n) = \tilde{y}_{IM3_+}(n) \quad (11)$$

$$u(n) = x_2^*(n)x_1^2(n) \quad (12)$$

$$\underline{u}(n) = [u(n) \ u(n-1) \ ... \ u(n-N)]^T \quad (13)$$

$$\underline{\alpha}(n) = [\alpha_0(n) \ \alpha_1(n) \ ... \ \alpha_N(n)]^T \quad (14)$$

$$\underline{\alpha}^*(n+1) = \underline{\alpha}^*(n) - \frac{\mu}{||\underline{u}(n)||^2 + C} \underline{u}(n)e^*(n). \quad (15)$$

Where N+1 denotes the filter length. The scaling factor $||\underline{u}(n)||^2 + C$ of the adaptation constant μ in (15) corresponds to the Normalized Least Mean Square (NLMS) scaling factor and the constant C is added to avoid numerical problems when the energy in the current set of samples is very small.

The proposed adaptive learning structure is shown in Fig. 1. Notice that the learning and the actual main DPD path filtering are separated, to be able to handle the delay of the predistortion feedback loop. This delay is denoted by the block z^{-L} in front of the 'Adaptive Decorrelator' block.

C. Computational and Hardware Complexity

Compared to conventional full-band DPD, the proposed technique has many benefits. First, the computational requirements of the DPD processing are greatly reduced. Full-band DPD with nonlinearity order 3 would need to run at a sample rate 3 times the composite dual-carrier signal bandwidth, which quickly becomes impossible when increasing carrier separation. The minimum sample rate for the proposed technique is only 3 times the bandwidth of the wider component carrier. To give an example, assume a CA scenario with two 10 MHz carriers separated by 100 MHz. The minimum sample rate with 3rd order full-band DPD would be 330 MHz, whereas with the proposed technique, it is only 30 MHz.

Second, the proposed technique implies very simple instrumentation complexity for the feedback receiver, which is needed for parameter learning with unknown PA characteristics, as only *narrowband feedback* capturing the considered IM3 spurious band is needed. Using the same numerical example as above, and the feedback structure shown in Fig.

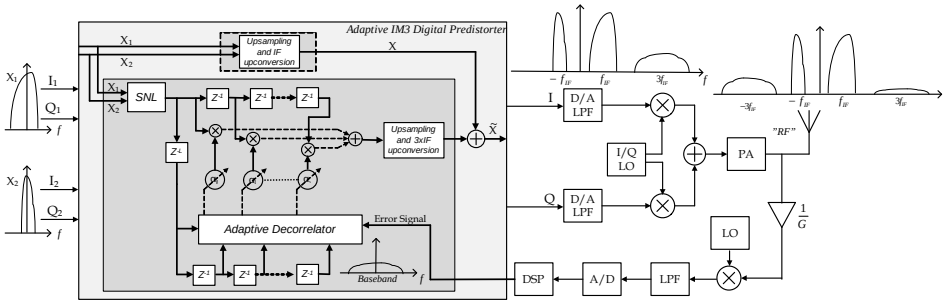

Fig. 1. Principal adaptive DPD system architecture for third-order spurious intermodulation reduction in a dual-carrier transmitter. Also essential composite baseband equivalent spectra are shown.

1, conventional full-band DPD would need an ADC with a minimum sample rate of 660 MHz, while the proposed technique needs only a 60 MHz ADC.

Third, the complexity of the proposed structure could be further reduced, if the signal injection, which in Fig. 1 is fully digital, would be implemented in the analog domain using an extra DAC and I/Q modulator for each injected signal. This would also enable using separate DAC's for the component carriers instead of a single wideband DAC. Sample rate requirements at the digital side and DAC stage would thus be reduced, which would otherwise inevitably become a bottleneck if the carrier separation was increased beyond couple of tens of MHz. This approach, however, implies complex cost-related trade-offs between digital and analog instrumentation, and requires careful study to find the carrier separation after which analog injection becomes cheaper. Such a discussion is out of the scope of this article and remains an important topic for future work.

To shortly demonstrate the differences in hardware complexity between the fully digital implementation shown in Fig. 1 and the analog injection technique, assume again a CA scenario with two 10 MHz carriers separated by 100 MHz. The fully digital injection would need a dual DAC running at a minimum of 330 MHz, and on the digital side, three complex upsamplers to bring the sample rate to 330 MHz, plus two adders running at this frequency. Using analog injection, one would need a dual DAC at 110 MHz for the combined main carriers (or alternatively two 10 MHz dual DAC's for the main carriers separately), one dual DAC at 30 MHz for the injection signal, plus one to three analog I/Q modulators and one or two adders, depending on the main carriers' DAC implementation.

IV. Simulation Results and Analysis

A. Simulation Scenarios

So far, the theoretical foundation of the decorrelating DPD algorithm has been established along with an implementation proposal for linearizing power amplifiers exhibiting memory effects as shown in Fig. 1. In this section, a non-contiguous dual-carrier signal is used to test the proposed DPD concept. As a concrete example, the two carriers are separated by 60 MHz and both are deploying QPSK carrier modulation with flexible carrier bandwidth. This models an example flexible spectrum access scenario, applicable already in 3GPP LTE-Advanced Release 12.

The DPD analysis and derivations in section II were formulated for a parallel Hammerstein power amplifier model. However, for a more general and realistic testing scenario in which there is a mismatch between the PA model in the analysis and actual verification simulations, we will also deploy a Wiener power amplifier model, in addition to parallel Hammerstein, in our simulations. Furthermore, the channel bandwidth assignment of the two carriers is varied in order to test the performance of the proposed DPD algorithm in flexible channel assignment scenarios where the bandwidth allocation of the two CCs can be symmetrical or asymmetrical.

For simplicity, we focus in the forthcoming examples mostly on the positive IM3 band, but like mentioned already in the previous sections, the negative IM3 band can also be considered and processed similarly by just changing the SNL basis in Fig. 1 from $x_2^*(n)x_1^2(n)$ to $x_1^*(n)x_2^2(n)$ and then upconverting the DPD injection signal to the negative IM3 band instead of the positive one. Finally, in the feedback path, appropriate downconversion and filtering to observe the negative IM3 signal from the PA output, instead of the positive one, is then obviously also needed. An example of this is given in subsection C below.

B. Simulation Results with 3rd Order PA

First, a third-order Wiener amplifier is tested with an IIP3 of +17 dBm and transmission power of +22 dBm thus implying only 1 dB back off (MPR) from the maximum 3GPP LTE class 3 UE transmission power (+23 dBm). Asymmetric spectrum access is considered, with 5 MHz and 10MHz carrier bandwidths. Fig. 2 shows the PSD of the PA output signal under three different conditions. First, without using any DPD, then using the single-tap decorrelating DPD, and finally using the proposed multi-tap decorrelating DPD with five taps. The learning in the adaptive DPD solutions is iterated for approx-

imately 300 microseconds before freezing the coefficients. As the figure demonstrates, there is a clear gain in the suppression of the positive IM3 band when the multi-tap algorithm and processing is deployed, compared to the single tap one. This is mainly because the single-tap DPD cannot process frequency-dependent IMD within the IM3 band, imposed by PA memory.

Another simulation scenario is next considered and demonstrated where the PA model is a parallel Hammerstein one. In this case, for demonstration purposes, very long memory is imposed in the PA model corresponding to high frequency selectivity within the IM3 band. In this scenario, both access carriers have an identical bandwidth of 5 MHz. Again the DPDs are adapted for approximately 300 microseconds, and the corresponding output spectra are shown in Fig. 3. Again the proposed multi-tap processing yields substantially improved reduction of the considered spurious component, compared to memoryless processing.

C. Simulation Results with 5th Order PA

Real-world practical PAs usually exhibit higher-order nonlinearities than just the third order. Using similar notation as in the previous sections, the wideband output signal of a 5-th order parallel Hammerstein PA model is of the form

$$y(n) = f_1(n) \star x(n) + f_3(n) \star |x(n)|^2 x(n) + f_5(n) \star |x(n)|^4 x(n), \quad (16)$$

where in addition to $f_1(n)$ and $f_3(n)$, $f_5(n)$ is now the filter in the fifth order PH branch. One can then easily show that without any DPD processing, the positive IM3 band baseband equivalent reads

$$\begin{aligned} y_{IM3_+}(n) = & f_3^+(n) \star (x_2^*(n)x_1^2(n)) \\ & + 3f_5^+(n) \star (|x_2(n)|^2(x_2^*(n)x_1^2(n))) \\ & + 2f_5^+(n) \star (|x_1(n)|^2(x_2^*(n)x_1^2(n))). \end{aligned} \quad (17)$$

Here, $f_5^+(n)$ is the baseband equivalent response of $f_5(n)$ at the positive $IM3$ band ($+3f_{IF}$). Thus, the IM3 band clearly now contains other signal terms in addition to the third order term $x_2^*(n)x_1^2(n)$ as a result of the fifth order distortion in the PA. However, we can also see that the additional fifth order terms in the IM3 band have a significant correlation with delayed replicas of the SNL basis function $x_2^*(n)x_1^2(n)$, thus justifying the application of the decorrelating solution also with higher-order PA models. A more extensive study for analyzing the output of a fifth order PA when the DPD injection is inserted is left for future work and here below we simply focus on experimental verification and demonstration.

Stemming from above, in order to shortly elaborate the applicability of the proposed multi-tap decorrelating DPD, a fifth-order Wiener PA model is now deployed in the simulator. The used PA model has +17 dBm IIP3 and +26.5 dBm 1dB compression point, and includes clear memory effects. As in the third-order PA example, both the single and multi-tap DPD solutions are tested. The resulting convergence curves of the five-tap filter coefficients are shown in Fig. 4. Again, after approximately 300 microseconds, the coefficients are converged and can thus be frozen. The corresponding PA output PSD results are shown in Fig. 5, where it is again evident that the proposed multi-tap DPD solution outperforms the single-tap counterpart also in this practical scenario with higher-order PA model. In this example, both positive and negative IM3 spurious components are suppressed. We also show in the figure the general ITU spurious emission mask [15], namely -30dBm over 1 MHz measurement bandwidth. As the figure illustrates, the proposed five-tap DPD solution clearly allows the device to meet the spurious emission limits which in turn are violated not only without DPD but also with memoryless DPD processing. Notice also that as the DPD processing is optimized for third-order IMD reduction, the fifth-order spurs at IM5 bands are somewhat increased but still well within the spurious emission limits.

V. Conclusions and Discussion

A low complexity digital predistortion technique for wideband power amplifiers with memory was proposed, specifically designed for spectrum-agile mobile devices deploying non-contiguous carrier aggregation. The predistortion processing mainly targets to suppress the third-order intermodulation components which can fall into the critical spurious emission region when the component carriers are, e.g., a few tens of MHz apart. Novel parameter learning and optimization based on a narrowband observation receiver and decorrelating principle was devised, covering frequency-dependent multi-tap processing against PA memory within the spur bandwidth. The overall DPD concept was succesfully tested and demonstrated with different power amplifier models exhibiting memory effects. In addition, flexible bandwidth assignments for the transmitted component carriers were tested and demonstrated, which is an essential element in emerging flexible spectrum access and cognitive radio scenarios. In cognitive radio context, successful spur reduction, through DPD processing, allows for improved coexistence with other higher priority primary users while still meeting the interference limits imposed on the mobile transmitter output at adjacent channels and other protected parts of the spectrum. Without sufficient spectral containment of the secondary user signals, due to e.g. spurious emissions of the PA, SU-PU interference constraints may considerably compromise the deployment possibilities of dynamic spectrum access and in particular non-contiguous spectrum access. Thus, embedding an adaptive low-complexity DPD into the devices to improve the spectral containment of the signals is one of the enabling elements of dynamic and flexible spectrum access in the future. Our future work will focus on more comprehensive testing and performance evaluations of the proposed DPD concept, including both real-time hardware demonstrations and practical RF measurements.

References

[1] S. Haykin, "Cognitive radio: brain-empowered wireless communications," *IEEE J. Sel. Areas Commun*, vol. 23, no. 2, pp. 201–220, Feb. 2005.

[2] I. Akyildiz, W.-Y. Lee, M. Vuran, and S. Mohanty, "Next generation/dynamic spectrum access/cognitive radio wireless networks: A survey," *Computer Networks*, vol. 50 no.13, pp. 2127–2159, Sept. 2006.

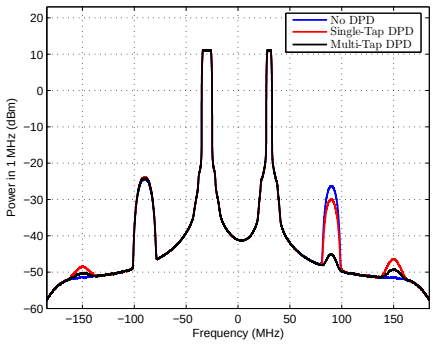

Fig. 2. Dual-carrier mobile transmitter baseband equivalent power spectra with asymmetrical channel BW assignments. 5 and 10 MHz are allocated to the first and second CC respectively. The memoryless single tap and the proposed multi-tap adaptive DPD are compared. Third order Wiener PA is used, with +17 dBm IIP3 and output power of +22 dBm.

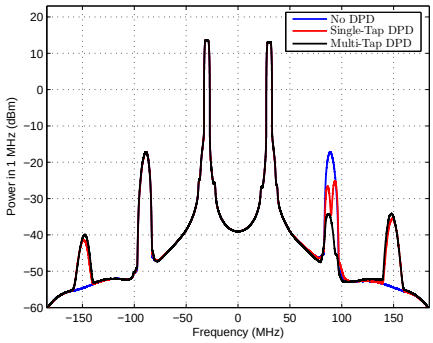

Fig. 3. Dual-carrier mobile transmitter baseband equivalent power spectra with symmetrical 5 MHz allocation per CC. The memoryless single tap and the proposed multi-tap adaptive DPD are compared. Third order PH PA is used with output power of +22 dBm.

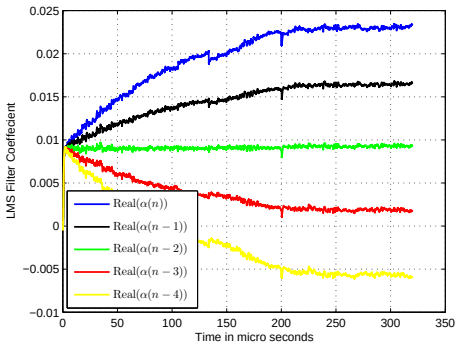

Fig. 4. Convergence of the multi-tap adaptive DPD coefficients in case of fifth-order Wiener PA.

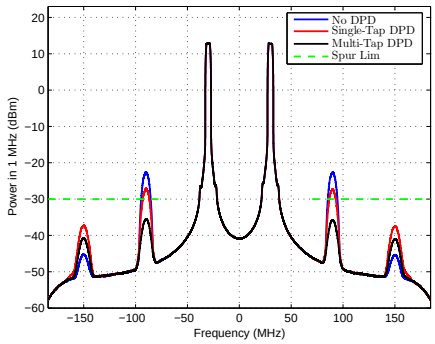

Fig. 5. Dual-carrier mobile transmitter baseband equivalent power spectra with symmetrical 5 MHz allocation per CC. The memoryless single tap and the proposed multi-tap adaptive DPD are compared. Fifth order Wiener PA is used, with +17 dBm IIP3, +26.5 dBm 1dB compression point and output power of +22 dBm.

[3] *3GPP Evolved Universal Terrestrial Radio Access (E-UTRA); User Equipment (UE) radio transmission and reception. http://www.3gpp.org/ftp/Specs/html-info/36101.htm*, Std.

[4] B. Razavi, "Cognitive radio design challenges and techniques," *IEEE J. Solid-State Circuits*, vol. 45, no. 8, p. 15421553, 2010.

[5] R. Zhang, "On peak versus average interference power constraints for protecting primary users in cognitive radio networks," *IEEE Trans. Wireless Commun.*, vol. 8, no. 4, pp. 2112–2120, April 2009.

[6] V. Lehtinen, T. Lähteensuo, P. Vasenkari, A. Piipponen, and M. Valkama, "Gating factor analysis of maximum power reduction in multicluster LTE-A uplink transmission," in *Proc. IEEE Radio and Wireless Symposium (RWS), Austin, TX*, Jan. 2013.

[7] T. Lähteensuo, "Linearity requirements in LTE Advanced mobile transmitter," Master's thesis, Tampere University of Technology, Tampere, Finland., May 2013. http://dspace.cc.tut.fi/dpub/handle/123456789/21504.

[8] J. Thorebäck, "Digital predistortion the evolution of linearized transmitters for radio basestations," in *Signal Processing for Amplifiers Workshop, Chalmers, Sweden*, Nov. 2012.

[9] M. Abdelaziz, A. Ghazi, L. Anttila, J. Boutellier, T. Lähteensuo, X. Lu, J. Cavallaro, S. Bhattacharyya, M. Juntti, and M. Valkama, "Mobile transmitter digital predistortion: Feasibility analysis, algorithms and design exploration," in *47th Asilomar Conf. Signals Systems Computers, Pacific, Grove, CA, USA*, Nov. 2013.

[10] P. Roblin, S. K. Myoung, D. Chaillot, Y. G. Kim, A. Fathimulla, J. Strahler, and S. Bibyk, "Frequency-selective predistortion linearization of RF power amplifiers," *IEEE Trans. Microw. Theory Tech.*, vol. 56, pp. 65–76, Jan. 2008.

[11] J. Kim, P. Roblin, D. Chaillot, and Z. Xie, "A generalized architecture for the frequency-selective digital predistortion linearization technique," *IEEE Trans. Microw. Theory Tech.*, vol. 61, pp. 596–605, Jan. 2013.

[12] S. Bassam, M. Helaoui, and F. Ghannouchi, "Channel-selective multicell digital predistorter for multi-carrier transmitters," *IEEE Trans. Microw. Theory Tech.*, vol. 60, pp. 2344–2352, Aug. 2012.

[13] S. Bassam, F. Ghannouchi, and M. Helaoui, "2-D Digital Predistortion (2-D-DPD) architecture for concurrent dual-band transmitters," *IEEE Trans. Microw. Theory Tech.*, vol. 59, pp. 2547–2553, Oct. 2011.

[14] M. Abdelaziz, L. Anttila, A. Mohammadi, F. Ghannouchi, and M. Valkama, "Reduced-complexity power amplifier linearization for carrier aggregation mobile transceivers," in *Proc. IEEE International Conference on Acoustics, Speech and Signal Processing (ICASSP '14), Florence, Italy*, 2014, (Accepted).

[15] *International Telecommunication Union Radio Communication Sector, Recommendation ITU-R SM.329-12 Unwanted emissions in the spurious domain. http://www.itu.int/dms_pubrec/itur/rec/sm/R-REC-SM.329-12-201209-I!!PDF-E.pdf*, Std.

Publication 7

M. Abdelaziz, L. Anttila, and M. Valkama, "Digital predistortion for mitigating transmitter-induced receiver desensitization in carrier aggregation FDD transceivers," in *Proc. IEEE Global Conference on Signal and Information Processing (GlobalSIP)*, Washington, DC, 2016, pp. 694-698.

DIGITAL PREDISTORTION FOR MITIGATING TRANSMITTER-INDUCED RECEIVER DESENSITIZATION IN CARRIER AGGREGATION FDD TRANSCEIVERS

Mahmoud Abdelaziz, Lauri Anttila, and Mikko Valkama

Department of Electronics and Communications Engineering,
Tampere University of Technology, Tampere, Finland

ABSTRACT

In frequency division duplexing (FDD) transceivers, the intermodulation distortion (IMD) created by a nonlinear transmit power amplifier can easily interfere with the receiver (RX) band. This is a particular concern in various carrier aggregation scenarios, and can cause severe own RX desensitization. In this paper, a spur-injection based sub-band digital predistortion (DPD) solution is proposed to mitigate this problem. Compared to earlier works, the proposed DPD parameter learning is performed using the main RX of the device, and thus it does not require any auxiliary observation RX, which implies reduced costs and size. The proposed DPD is tested using computer simulations with practical models for the transmitter (TX) power amplifier and the TX/RX duplexer filters. The TX-induced IMD is suppressed by up to 25dB at the own RX band, demonstrating a significant improvement in the RX signal-to-interference-and-noise-ratio (SINR).

***Index Terms*—** 5G, carrier aggregation, digital predistortion (DPD), frequency division duplexing (FDD), long term evolution (LTE)-Advanced, receiver desensitization.

1. INTRODUCTION

Carrier aggregation (CA) in 3GPP long term evolution (LTE)-Advanced combines multiple component carriers (CCs) at different RF frequencies. The CCs are combined either within the same RF band (intraband CA), or at different RF bands (interband CA) [1]. Power efficiency is improved when the CCs are combined at the power amplifier (PA) input, whenever feasible, compared to combining them after the PA [1]. However, this leads to additional unwanted spurious emissions at the PA output, which may violate the emission limits regulated by the standardization bodies, e.g., ITU-R [2]. These unwanted emissions can interfere with other users in the same band or at different RF bands. In general, aggressive adoption of CA and flexible duplexing technologies are expected to be key ingredients in the emerging 5G radio networks, in particular at lower center-frequencies below 6 GHz [3, 4].

In FDD devices, in addition to violating the general spurious emission limits, the generated spurious components can also overlap with the device's own receive band, causing own receiver desensitization, in particular in mobile devices [5–9]. This becomes particularly problematic in CA scenarios, due to limited duplexing distance, as well as finite TX-RX duplexer isolation (50-60 dB). Straightforward solutions for this problem are: increasing the duplexing distance, increasing the duplexer isolation, and reducing the TX power. However, increasing the duplexing distance reduces the system spectral efficiency, and thus degrades the overall network capacity. Increasing the duplexer isolation, on the other hand, significantly increases the cost, complexity, and size of the duplexer filters, which becomes impractical, especially for mobile devices. Finally, reducing the TX power will end up yielding a significantly lower PA efficiency, as well as a substantial reduction in the network coverage. Thus, there is a need for other solutions to this transmitter-induced RX desensitization problem, that do not have such drawbacks.

Digital cancellation algorithms in the receiver have been proposed in [7–9] for canceling the transmitter-induced spurious emissions at the RX band in CA scenarios. On the other hand, digital predistortion (DPD), on the transmitter side, is considered an effective method for mitigating these harmful emissions as well. Recently, some DPD techniques have been developed for mitigating the TX spurious emissions explicitly while not necessarily focusing on the other emissions [10–13]. These spur-injection DPD techniques are based on injecting dedicated cancellation spurs at the PA input, properly phased, such that the selected unwanted emissions are suppressed at the PA output. In general, DPD solutions have an extra advantage compared to RX cancellation algorithms, since they do not impose any additional dynamic range constraints on the RX, in particular the ADC. However, DPDs typically require an extra auxiliary receiver in order to estimate the PA nonlinearity characteristics, which then adds to the overall costs and size of the transceiver.

In this paper, a novel spur-injection sub-band DPD solution is proposed which uses directly the device's own RX for learning, and thus does not require any extra auxiliary RX. At the same time, the spurious emissions at the PA output, falling at the own RX band, are suppressed and thus the RX dynamic range can be fully utilized for the desired RX signal. This implies that the DPD processing and parameter learning have to consider the RF duplex filters' frequency responses for proper parameter estimation and predistortion. The proposed DPD learning solution is based on evaluating and minimizing the correlation between the observed spurious emissions at the RX band, and specific locally generated basis functions representing these emissions. The parameter learning approach is very simple and does not require any computationally intensive operations, such as matrix inversions, typically encountered in most DPD and digital cancellation methods. Thus, the proposed DPD concept offers a novel, efficient, low cost, and simple solution for protecting the own RX from the TX-induced spurious emissions in future LTE-Advanced and 5G CA networks.

This paper is organized as follows. Section 2 presents the TX-induced spurious component modeling at the RX band, along with the proposed DPD processing principle. Section 3 describes the proposed block-adaptive DPD parameter learning. Section 4 then presents comprehensive simulation results of the proposed DPD using realistic PA and duplexer models. Finally, section 5 concludes

This work was supported by the Finnish Funding Agency for Technology and Innovation (Tekes), by the Academy of Finland under the projects 251138 and 284694, and by the Linz Center of Mechatronics (LCM) in the framework of the Austrian COMET-K2 programme.

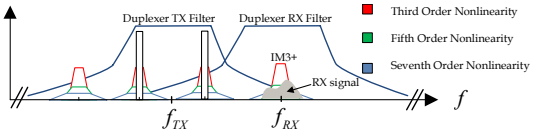

Fig. 1. PSD at the PA output when excited with a dual carrier signal. Spurious emissions at the IM3+ sub-band can easily overlap with the RX band and desensitize own RX.

the paper.

2. TX-INDUCED SPURIOUS COMPONENT MODELING AT RX BAND AND PROPOSED DPD PROCESSING

In this section, modeling of the spurious intermodulation distortion (IMD) at the own RX band, due to TX power amplifier nonlinearity, is carried out in case of a CA FDD transceiver. Fig. 1 shows the PSD when a dual carrier signal is applied to a nonlinear PA. The IMD at the IM3+ sub-band, for example, can lie at the own RX band and lead to own receiver desensitization. This problem can be shortly quantified, numerically, as follows. Assuming the IM3+ spur is at -30dBm/MHz at the PA output [14], and the duplexer isolation is 60 dB [15], the unwanted spurious leakage at the RX band can be around -90dBm/MHz. This is 15dB above the RX thermal noise floor (assuming 9dB RX NF [14]), which is a significant self-interference and can completely block the RX. The proposed DPD structure and basic processing for mitigating this problem is also presented in this section, while the actual DPD parameter estimation is explained in section 3 in more details. For notational simplicity, we solely focus on dual-carrier transmission and assume that the IM3 sub-band is located at own receive band.

2.1. TX-induced spurious component modeling at RX band

The modeling is carried out at composite baseband equivalent level, where the two component carriers are assumed to be separated by normalized frequency $2f_{IF}$. A P^{th} order Parallel Hammerstein (PH) model is adopted for characterizing the PA nonlinearity. The I/Q modulators at the TX and RX are assumed to be ideal. The TX/RX duplexer filters then model the signal path towards the RX frontend. Finally, the TX-induced leakage signal at the RX is extracted at the output of the digital channel selection filter (CSF), as illustrated also in Fig. 2. The RX LNA is assumed to be linear since the signal levels are close to the reference sensitivity level in our problem. Furthermore, LNA gain is normalized to one, without loss of generality.

The composite baseband equivalent input and output signals of the PA, with monomial nonlinearities and FIR branch filters in the assumed PH model, then read

$$x(n) = x_1(n)e^{j2\pi f_{IF}n} + x_2(n)e^{-j2\pi f_{IF}n}, \tag{1}$$

$$y(n) = \sum_{p=1,p\text{ odd}}^{P} f_{p,n} \star |x(n)|^{p-1}x(n), \tag{2}$$

where $x_1(n)$ and $x_2(n)$ are the baseband component carrier signals, $f_{p,n}$ denotes the PH branch filter impulse responses of order p, and $(\star)$ is the convolution operator. Direct substitution of (1) in (2) allows extracting the baseband equivalent distortion terms at the IM3+ sub-band, for example, which, through straight-forward manipulations, yields

$$y_{3+}(n) = \sum_{p=3,p\text{ odd}}^{P} f_{p,n}^{3+} \star u_p(n). \tag{3}$$

Here, $f_{p,n}^{3+}$ denotes the baseband equivalent impulse response corresponding to the wideband PH PA model filters $f_{p,n}$, evaluated at the IM3+ sub-band, formally defined as

$$f_{p,n}^{3+} = LPF\{e^{-j2\pi 3 f_{IF}n} f_{p,n}\}, \tag{4}$$

with $LPF\{.\}$ denoting an ideal low pass filtering operation with a passband width P times the bandwidth of the wider CC. Furthermore, $u_p(n)$ are the corresponding p^{th} order static nonlinear (SNL) basis functions, related to the nonlinear distortion at the IM3+ sub-band. Assuming a 7^{th} order PA model (i.e., $P = 7$), as a practical example, the IM3+ sub-band basis functions read

$$u_3(n) = x_2^*(n)x_1^2(n), \tag{5}$$

$$u_5(n) = u_3(n)(2|x_1(n)|^2 + 3|x_2(n)|^2), \tag{6}$$

$$u_7(n) = u_3(n)(3|x_1(n)|^4 + 6|x_2(n)|^4 + 12|x_1(n)|^2|x_2(n)|^2). \tag{7}$$

In FDD transceivers, the PA output signal passes through the duplexer filters before the receiver frontend. A duplexer is composed of two band pass filters. In the transmitter path, the TX filter tries to attenuate the unwanted emissions outside the transmit band. The RX filter then attenuates the transmitter passband signal leaking into the receiver chain. With finite attenuation of duplexing filters, TX-induced spurious IMD is not completely suppressed and can cause self-interference at the RX band. At the receiver input, the baseband equivalent IM3+ component leaking into the RX band, after passing through the cascade of TX and RX duplexer filters, then reads

$$y_{3+}^D(n) = h_n^D \star y_{3+}(n). \tag{8}$$

The cascaded duplexer filter response from TX-RX leakage perspective, denoted by h_n^D in the above equation, is defined as

$$h_n^D = h_n^{RX} \star \left(h_n^{TX} e^{-j2\pi 3 f_{IF}n}\right), \tag{9}$$

where h_n^{TX} and h_n^{RX} represent the baseband equivalent lowpass models of the bandpass TX and RX duplexer filters, respectively. Finally the RX CSF stage filters the leakage signal after the duplexer, which then reads

$$y_{3+}^L(n) = h_n^{CSF} \star y_{3+}^D(n). \tag{10}$$

From (3), (8), and (10), the final leakage signal at the RX, denoted with $y_{3+}^L(n)$, can be expressed as a filtered version of the SNL basis functions $u_p(n)$ as follows

$$y_{3+}^L(n) = \sum_{p=3,p\text{ odd}}^{P} h_{p,n}^L \star u_p(n), \tag{11}$$

where $h_{p,n}^L = f_{p,n}^{3+} \star h_n^D \star h_n^{CSF}$ is the equivalent filter representing the cascaded p^{th} order PA PH filter, TX/RX duplexer filters, and CSF respectively.

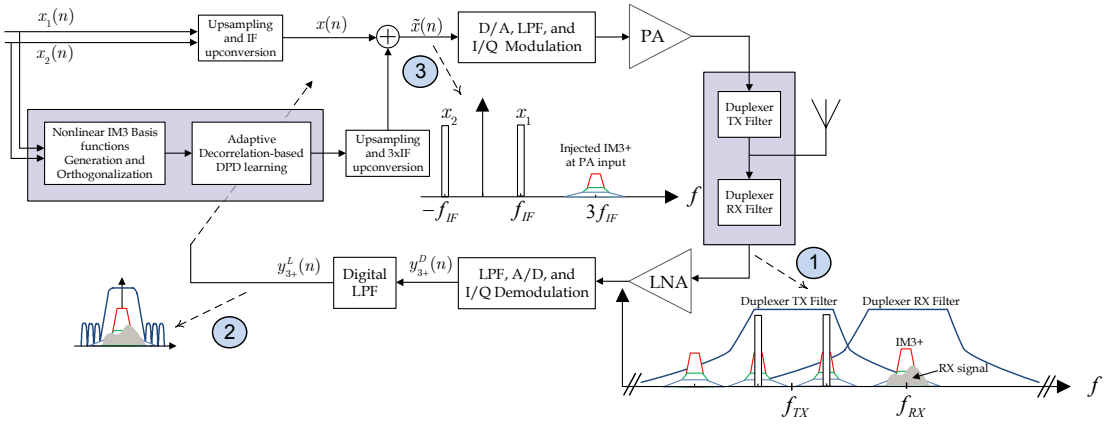

Fig. 2. Block diagram of the proposed sub-band DPD solution which uses the main RX for learning the DPD coefficients.

2.2. Proposed Sub-band DPD Processing

The key idea of the proposed DPD is to inject a proper additional low-power cancellation signal, with structural similarity to (11) and located at $+3f_{IF}$, into the PA input, such that the level of the IM3+ TX-induced leakage at the RX is reduced. Now, stemming from the IMD structure in (11), an appropriate digital injection signal can be obtained by adopting the IM3+ basis functions $u_p(n)$ in (5)-(7), combined with proper filtering using a bank of DPD filters $\alpha_{p,n}$. Incorporating such DPD processing with polynomial order Q, the composite baseband equivalent PA input signal reads

$$\tilde{x}(n) = x(n) + \left[\sum_{p=3,p\ \text{odd}}^{Q} \alpha_{p,n} \star u_p(n)\right] e^{j2\pi 3 f_{IF} n} \tag{12}$$

Here, and in the continuation, we use $\tilde{(.)}$ variables to indicate DPD processing and the corresponding predistorted signals. This DPD processing principle is illustrated in Fig. 2 at a conceptual level, while the actual DPD parameter learning algorithm is described in the next section.

3. DPD PARAMETER LEARNING FOR MITIGATING TX-INDUCED SPURS AT RX BAND

The p^{th} order DPD coefficients $\alpha_{p,n}$ in (12) are obtained such that the correlation is minimized between the TX-induced IMD observed at the RX, and the nonlinear basis functions in (5)-(7). However, those basis functions are highly mutually correlated, and thus they are first orthogonalized to obtain a new set of basis functions $s_p(n)$ for better convergence properties [16]. A block-adaptive DPD parameter learning solution can then be formulated, where the following vector based notations are adopted:

$$\boldsymbol{\alpha}_p(m) = [\alpha_{p,0}(m)\ \ \alpha_{p,1}(m)\ \ ...\ \ \alpha_{p,N}(m)]^T \tag{13}$$

$$\bar{\boldsymbol{\alpha}}(m) = [\boldsymbol{\alpha}_3(m)^T\ \ \boldsymbol{\alpha}_5(m)^T\ \ ...\ \ \boldsymbol{\alpha}_Q(m)^T]^T \tag{14}$$

$$\mathbf{s}_p(n_m) = [s_p(n_m)\ \ s_p(n_m-1)\ \ ...\ \ s_p(n_m-N)]^T \tag{15}$$

$$\bar{\mathbf{s}}(n_m) = [\mathbf{s}_3(n_m)^T\ \ \mathbf{s}_5(n_m)^T\ \ ...\ \ \mathbf{s}_Q(n_m)^T]^T \tag{16}$$

$$\bar{\mathbf{S}}(m) = [\bar{\mathbf{s}}(n_m)\ \ ...\ \ \bar{\mathbf{s}}(n_m+M-1)] \tag{17}$$

$$\mathbf{e}(m) = [\tilde{y}^L_{3+}(n_m)\ \ ...\ \ \tilde{y}^L_{3+}(n_m+M-1)]^T \tag{18}$$

Here, N denotes the DPD filter memory depth, n_m denotes the first sample of block m, with block size M, and $\tilde{y}^L_{3+}(n)$ denotes the baseband equivalent TX-induced leakage at the RX band with the current DPD coefficients. Consequently, the decorrelation-based DPD block-adaptive parameter learning rule then reads

$$\bar{\boldsymbol{\alpha}}(m+1) = \bar{\boldsymbol{\alpha}}(m) - \mu\, \bar{\mathbf{S}}(m)\mathbf{e}^*(m), \tag{19}$$

where $\mathbf{e}^*(m)$ is the element-wise conjugated error signal vector, while $\bar{\mathbf{S}}(m)$ denotes the filter input data matrix, all within the processing block m. The obtained new DPD coefficients $\bar{\boldsymbol{\alpha}}(m+1)$ are then applied on the next block of samples in a block-adaptive manner, as illustrated also in [17] in the context of using an auxiliary RX for sub-band DPD learning. The learning rate parameter μ provides a natural tradeoff between the speed of convergence and the steady state error of the proposed block-adaptive sub-band DPD.

4. SIMULATION RESULTS AND ANALYSIS

In order to demonstrate the effectiveness of the proposed DPD, practical simulations are presented in this section using realistic models of power amplifiers and duplexer filters. In the simulations, the TX waveform is composed of two 10MHz LTE-A UL SC-FDMA component carriers with QPSK subcarrier modulation, and the CC spacing is 50MHz. The PA model, in turn, is a PH fifth-order model whose parameters have been identified using a true mobile PA transmitting at +23dBm. The simulation framework is setup according to Fig. 2, assuming ideal I/Q modulators and demodulators. A linear LNA with normalized unit gain is also assumed, with the signal levels at the LNA input being close to the reference sensitivity (REFSENS) level. The desired RX signal at the RX antenna is assumed to be a 10MHz OFDM LTE-A DL signal with QPSK subcarrier modulation.

The block-adaptive decorrelation-based DPD uses the observed IM3+ spur after the digital CSF stage at the RX for learning the DPD parameters, as shown in Fig. 2. The fifth-order DPD has a memory depth equal to four, and 130 sample blocks are used for estimation, with block size $M = 10k$. The final obtained coefficients are then applied in the actual performance evaluation phase, to quantify the amount of obtained spur suppression at the own RX band.

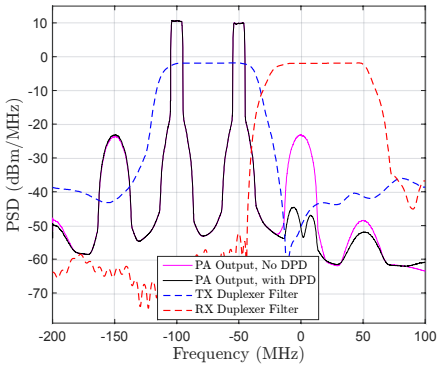

Fig. 3. PSD at the PA output with and without DPD. TX power is +23dBm. Two 10MHz LTE UL signals, with 50MHz carrier spacing are used.

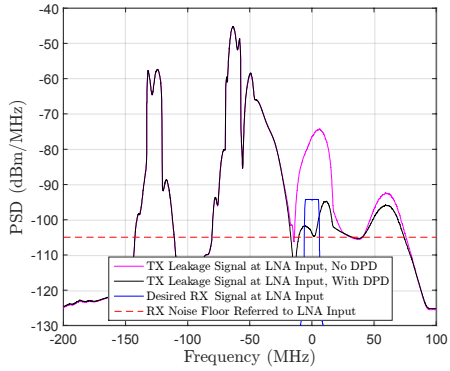

Fig. 4. PSD after the TX/RX duplexer filters at the RX LNA input, with and without DPD. TX power is +23dBm. Two 10MHz LTE UL signals, with 50MHz carrier spacing are used. The desired RX signal PSD is also shown, which is 10dB above REFSENS level.

Fig. 3 shows the baseband equivalent PSD at the PA output with and without using the proposed DPD, where the frequency axis is normalized such that zero refers to the considered RX center frequency. The TX and RX duplexer filter responses are also shown, indicating the total TX and RX bands. Fig. 4 then shows the output PSDs after the duplexer filters at the input of the LNA in the own RX. The desired RX signal is also shown in this figure, where it is assumed that the RX signal is 10dB above the reference sensitivity level [14]. The RX noise floor is also shown in the same figure, where 9dB RX noise figure (NF) is assumed [14]. Fig. 5 shows the stable convergence of the DPD coefficients, while using the main RX for learning. Finally, Fig. 6 demonstrates the gain in the signal to interference and noise ratio (SINR) at the own RX obtained by using the proposed DPD. Up to 25dB gain in SINR is achieved when operating at +23dBm, thus significantly improving the performance, without sacrificing the TX power efficiency, cost, or size of

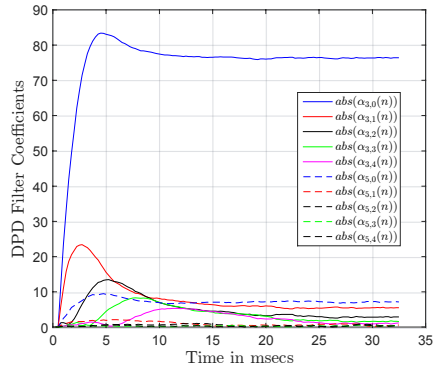

Fig. 5. Convergence of the DPD coefficients with fifth order nonlinearity, and memory depth four.

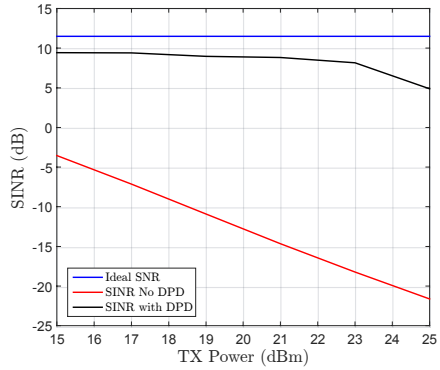

Fig. 6. Own RX SINR versus TX power with and without the proposed DPD. Desired RX signal is assumed to be 10dB above the reference sensitivity level.

the overall transceiver.

5. CONCLUSIONS

In this paper, a novel DPD solution was proposed to protect the own RX from TX-induced unwanted emissions in future FDD CA networks. Instead of adopting an additional observation receiver, the proposed solution uses directly the main RX observation for learning the DPD parameters, reducing the costs and size of the overall transceiver. Moreover, the dynamic range at the RX input is relaxed in presence of a TX-induced spurious leakage signal, compared to existing RX cancellation-based solutions. The performance of the proposed solution was evaluated using extensive simulations, showing up to 25dB improvement in the own RX SINR compared to the no DPD case. Efficient self-interference suppression methods, like the one proposed in this paper, are some of the key ingredients to enhance the carrier aggregation and duplexing flexibility in the future 5G radio networks, particularly at frequencies below 6 GHz.

6. REFERENCES

[1] S.A. Bassam, W. Chen, M. Helaoui, and F.M. Ghannouchi, "Transmitter architecture for CA: Carrier Aggregation in LTE-Advanced systems," *IEEE Microw. Mag.*, vol. 14, 2013.

[2] *International Telecommunication Union Radio Communication Sector, Recommendation ITU-R SM.329-12 Unwanted emissions in the spurious domain. Available at: https://www.itu.int/.*

[3] H. Bogucka, P. Kryszkiewicz, and A. Kliks, "Dynamic spectrum aggregation for future 5G communications," *IEEE Commun. Mag.*, vol. 53, no. 5, pp. 35–43, May 2015.

[4] N. Bhushan, J. Li, D. Malladi, R. Gilmore, D. Brenner, A. Damnjanovic, R. T. Sukhavasi, C. Patel, and S. Geirhofer, "Network densification: the dominant theme for wireless evolution into 5G," *IEEE Commun. Mag.*, vol. 52, no. 2, pp. 82–89, February 2014.

[5] C. Park, L. Sundström, A. Wallen, and A. Khayrallah, "Carrier aggregation for LTE-advanced: Design challenges of terminals," *IEEE Commun. Mag.*, pp. 76–84, Dec. 2013.

[6] Ericsson and ST-Ericsson, "R4-123797, UE reference sensitivity requirements with two UL carriers. Available at: http://www.3gpp.org/," Tech. Rep., 3GPP, Feb. 2013.

[7] A. Kiayani, M. Abdelaziz, L. Anttila, V. Lehtinen, and M. Valkama, "DSP-based suppression of spurious emissions at RX band in carrier aggregation FDD transceivers," in *2014 22nd European Signal Processing Conference (EUSIPCO)*, Sept 2014, pp. 591–595.

[8] A. Kiayani, M. Abdelaziz, L. Anttila, V. Lehtinen, and M. Valkama, "Digital Mitigation of Transmitter-Induced Receiver Desensitization in Carrier Aggregation FDD Transceivers," *IEEE Trans. Microw. Theory Tech.*, vol. 63, no. 11, pp. 3608–3623, Nov 2015.

[9] Chao Yu, Wenhui Cao, Yan Guo, and A. Zhu, "Digital Compensation for Transmitter Leakage in Non-Contiguous Carrier Aggregation Applications With FPGA Implementation," *IEEE Trans. Microw. Theory Tech.*, vol. 63, no. 12, pp. 4306–4318, Dec 2015.

[10] S.A. Bassam, M. Helaoui, and F.M. Ghannouchi, "Channel-selective multi-cell digital predistorter for multi-carrier transmitters," *IEEE Trans. Microw. Theory Tech.*, vol. 60, pp. 2344–2352, Aug. 2012.

[11] J. Kim, P. Roblin, D. Chaillot, and Z. Xie, "A generalized architecture for the frequency-selective digital predistortion linearization technique," *IEEE Trans. Microw. Theory Tech.*, vol. 61, pp. 596–605, Jan. 2013.

[12] M. Abdelaziz, L. Anttila, A. Mohammadi, F. Ghannouchi, and M. Valkama, "Reduced-complexity power amplifier linearization for carrier aggregation mobile transceivers," in *IEEE International Conference on Acoustics, Speech, and Signal Processing*, May 2014.

[13] M. Abdelaziz, Z. Fu, L. Anttila, A. M. Wyglinski, and M. Valkama, "Digital predistortion for mitigating spurious emissions in spectrally agile radios," *IEEE Commun. Mag.*, vol. 54, no. 3, pp. 60–69, March 2016.

[14] *LTE Evolved Universal Terrestrial Radio Access (E-UTRA) RF system scenarios, 3GPP TR 36.942 V10.2.0 (Release 10)*, May 2011.

[15] *Avago Band 25 LTE-Advanced UE Duplexer, ACMD-6125. Available at: http://docs.avagotech.com/docs/AV02-4214EN.*

[16] W. Hoffmann, "Iterative algorithms for Gram Schmidt orthogonalization," *Computing*, vol. 41, no. 4, pp. 335–348, 1989.

[17] M. Abdelaziz, C. Tarver, K. Li, L. Anttila, M. Valkama, and J. Cavallaro, "Sub-band digital predistortion for noncontiguous transmissions: Algorithm development and real-time prototype implementation," in *49th Asilomar Conf. Signals, Systems, and Computers, Pacific, Grove, CA, USA.*, Nov. 2015.

Tampereen teknillinen yliopisto
PL 527
33101 Tampere

Tampere University of Technology
P.O.B. 527
FI-33101 Tampere, Finland

ISBN 978-952-15-3988-6
ISSN 1459-2045